Martin Gade
Heinrich Hühnerfuss
Gerald Korenowski
Editors

Marine Surface Films

Chemical Characteristics, Influence on Air-Sea Interactions and Remote Sensing

Springer

Martin Gade, Heinrich Hühnerfuss, Gerald Korenowski

Marine Surface Films

Martin Gade
Heinrich Hühnerfuss
Gerald Korenowski (Eds.)

Marine Surface Films

Chemical Characteristics, Influence on Air-Sea Interactions and Remote Sensing

With 126 Figures, 4 in colour

Springer

EDITORS:

DR. MARTIN GADE
UNIVERSITÄT HAMBURG
ZENTRUM FÜR MEERES- UND
KLIMAFORSCHUNG
INSTITUT FÜR MEERESKUNDE
BUNDESSTR. 53
20146 HAMBURG, GERMANY

E-mail: gade@ifm.zmaw.de

PROF. DR. HEINRICH
HÜHNERFUSS
UNIVERSITÄT HAMBURG
INSTIUT FÜR ORGANISCHE
CHEMIE
MARTIN-LUTHER-KING-PLATZ 6
20146 HAMBURG, GERMANY

E-mail: huehnerfuss@chemie.
uni-hamburg.de

PROF. DR. GERALD M.
KORENOWSKI
DEPARTMENT OF CHEMISTRY &
CHEMICAL BIOLOGY
RENSSELAER POLYTECHNIC
INSTITUTE
120 COGSWELL
110 8TH STREET
TROY, NY 12180, USA

E-mail: koreng@rpi.edu

ISBN 10 3-540-33270-7 **Springer Berlin Heidelberg New York**
ISBN 13 978-3-540-33270-1 **Springer Berlin Heidelberg New York**

Library of Congress Control Number: 2006924570

Springer is a part of Springer Science+Business Media
springeronline.com

Printed in The Netherlands

Cover design: E. Kirchner, Heidelberg
Production: A. Oelschläger
Typesetting: Camera-ready by the Editors

Printed on acid-free paper 30/2132/AO 543210

Preface

Marine surface films are encountered at many places of the world's oceans, particularly in marginal seas and coastal regions. Their impact on basic processes at the air-water interface is well known since ancient times and has been a matter of scientific research ever since. There has been, however, a lack of a comprehensive compendium that provides the state-of-the-art knowledge on the chemical nature of marine surface films, with particular emphasis on their influence on air-sea interaction processes.

Since the 1960s natural surface films ("sea slicks"), that tend to exhibit thicknesses of one molecule only, have been in the focus of interdisciplinary research that required input by various disciplines such as oceanography, meteorology, physics and chemistry. Albeit the thickness of such monomolecular surface films is small compared to that of mineral oil films their wave damping capability and, thus, their influence on air-sea interactions is comparable. Consequently, they are still often mixed up with mineral oil films ("oil spills"), particularly in the frame of remote sensing applications. It is the aim of the present book to provide a scientific basis that allows avoiding such misinterpretation in the future.

This book is organized in four scientific chapters that are preceded by a general section. The latter provides a historical survey of more than two thousand years of marine surface film research. A biography of Carlo Marangoni, who formed a basis for the modern sea slick research, is followed by a tribute to Erik John Bock who contributed to this book, but died before its publication. The first scientific chapter provides information on the chemical characteristics of both sea slicks and oil spills, thereby putting more emphasis on monomolecular surface films. Chapter 2 and 3 summarize theoretical and experimental work on air-sea exchange processes in the presence of surface films, and on numerical modelling with emphasis on remote sensing of marine surface films. Finally, Chapter 4 describes remote sensing applications that benefit from a deeper knowledge of the results from the previous chapters.

The editors sincerely hope that the present contributed book will conserve existing knowledge and help to avoid misinterpretations of data, or even misplanning of experiments in the future.

January 2006

Martin Gade
Heinrich Hühnerfuss
Gerald M. Korenowski

Contents

Adresses of Corresponding Authors

Nicole Braun

Radarhydrographie (Dept. KOR)
Institut für Küstenforschung
GKSS Forschungszentrum
Max-Planck-Straße 1
21502 Geesthacht
Germany
Phone : +49 (0)4152 87 1899
Fax : +49 (0)4152 87 2818
E-Mail : NBraun@gkss.de

Kristian B. Dysthe

University of Bergen
Department of Mathematics,
Johannes Brunsgate 12,
5008 Bergen,
Norway
Phone : +47 55 58 48 57
Fax *:* +47 55 58 96 72
E-Mail : Kristian.Dysthe@mi.uib.no

Stanislav A. Ermakov

Institute of Applied Physics
Russian Academy of Sciences
46, Ul'janova st.
603950, Nizhny Novgorod
Russia
Phone : +7 8312 164935
Fax : +7 8312 365976
E-Mail : stas.ermakov@hydro.appl.sci-nnov.ru

Guido Ferraro

European Commission
Joint Research Centre
Institute for the Protection and Security of the Citizen
21020 Ispra
Italy
Phone : +39 0332 789488
Fax : +39 0332 785469
E-Mail : guido.ferraro@jrc.it

Nelson M. Frew

Woods Hole Oceanographic Institution
Marine Chemistry & Geochemistry Dept.
360 Woods Hole Road
Mailstop #4
Woods Hole, MA 02543
USA
Phone : +1 508 289 2489
Fax : +1 508 457 2164 (Fye Lab)
E-Mail : nfrew@whoi.edu

Martin Gade

Universität Hamburg
Zentrum für Meeres- und Klimaforschung
Institut für Meereskunde
Bundesstraße 53
20146 Hamburg
Germany
Phone : +49 (0)40 42838 5450
Fax : +49 (0)40 42838 7471
E-Mail : gade@ifm.zmaw.de

Christine P. Gommenginger

Laboratory for Satellite Oceanography
Ocean Circulation and Climate
National Oceanography Centre, Southampton (NOCS)
European Way
Southampton, SO14 3ZH
United Kingdom
Phone : +44 (0)23 80 596411 (direct)
Fax : +44 (0)2380 596400
E-Mail : cg1@noc.soton.ac.uk

Harm Greidanus

European Commission
Joint Research Centre (JRC)
TP 266
Via Fermi 1
21020 Ispra (VA)
Italia
Phone : +39 0332 78 9739
Fax : +39 0332 78 9658
E-Mail : harm.greidanus@jrc.it

Heinrich Hühnerfuss

Institut für Organische Cheme
Universität Hamburg
Martin-Luther-King-Platz 6
20146 Hamburg
Germany
Phone : +49 (0)40 42838 4240
Fax : +49 (0)40 42838 2893
E-Mail : huehnerfuss@chemie.uni-hamburg.de

Paul A. Hwang

Oceanography Division
(on assignment at Remote Sensing Division)
Naval Research Laboratory
Bldg. 2, Room 244E
4555 Overlook Avenue SW
Washington DC 20375
USA
Phone : +1 202 767 0800
Fax : +1 202 767 5599
E-Mail : phwang@ccs.nrl.navy.mil

Gerald M. Korenowski

Department of Chemistry & Chemical Biology
Science Center 2W14
Rensselaer Polytechnic Institute
110 8th Street
Troy, NY 12180
USA
Phone : +1 518 276 8480
Fax : +1 518 276 4887
E-Mail : koreng@rpi.edu

Konstantin Litovchenko

Russian Institute of Space Device Engineering
Aviamotornaya str. 53
111024 Moscow
Russia
E-Mail: litov@rniikp.ru

Giuseppe Loglio

Department of Organic Chemistry
University of Florence
Polo Scientifico
Via della Lastruccia, 7 – 13
50019 Sesto Fiorentino (Firenze , Italy)
Phone : +39 055 457 3487
Fax : +39 055 457 3531
E-Mail : loglio@unifi.it

Sean P. McKenna

E-Mail : smckenna@alum.mit.edu

Leonid M. Mitnik

Satellite Oceanography Department
V.I. Il'ichev Pacific Oceanological Institute
Far Eastern Branch
Russian Academy of Sciences
43 Baltiyskaya St.
690041 Vladivostok
Russia
Phone : 7-4232-312-854
Fax : 7-4232-312-573
E-Mail : mitnik@poi.dvo.ru

Boris A. Noskov

Department of Colloid Chemistry
St.Petersburg State University
Universitetskij pr. 26
198504 St.Petersburg - Petrodvorez
Russia
Phone +7-812-4284093
Fax : +7-812-4286939
E-Mail : boris@bn1664.spb.edu

Uwe Schimpf

Institut für Umweltphysik
Universität Heidelberg
Im Neuenheimer Feld 229
69120 Heidelberg
Phone : +49 (0)6221 54 6542
Fax : +49 (0)6221 54 8850
E-Mail : Uwe.Schimpf@iwr.uni-heidelberg.de

David K. Woolf

National Oceanography Centre
Southampton
SO14 3ZH
UK
Phone : +44 23 80596401
Fax : +44 23 80596400
E-Mail : dkw@noc.soton.ac.uk

Oliver Zielinski

Hochschule Bremerhaven
Maritime Technologien
An der Karlstadt 8
27568 Bremerhaven
Germany
Phone : +49 (0)471 4823 546
Fax : +49 (0)471 4823 346
E-Mail : ozielinski@hs-bremerhaven.de

General Section

Oil on troubled waters – a historical survey

Heinrich Hühnerfuss

Institute of Organic Chemistry, University of Hamburg,
Hamburg, Germany

1 Early observations and applications

Damping of water waves by "oil films" has already been appreciated since ancient times, however, knowledge regarding the causes of this effect has progressed only very slowly since the first attempted explanations in classical times. The first to describe this phenomenon was Aristotle in his *Problemata Physica*:

Why is it that the sea, which is heavier than fresh water, is more transparent? Is it because of its fattier composition? Now oil poured on the surface of water makes it more transparent, and the sea, having fat in it, is naturally more transparent.

Furthermore, Plutarch in his *Moralia: Quaestiones Naturales* ascribed to Aristotle (probably from lost parts of that author's *Problemata*):

Is it, as Aristotle says, that the wind, slipping over the smoothness so caused, makes no impression and raises no swell? ..... They say that when (sponge) divers take oil into their mouths and blow it out in the depths they get illumination and see through the water. Surely it is impossible to adduce slipping of the wind as the cause there.

In addition to these astonishingly correct explanations Plutarch offered alternative but relatively obscure interpretations.

Another practical application of organic surface films added to the sea surface was reported by Pliny the Elder (77 A.D.) describing the seamen's practice of calming water waves in a storm by pouring oil onto the sea, in order to prevent shipwrecking. A similar utilisation of oil was reported by Bede (Baeda Venerabilis ≡ The Venerable Bede) who spent most of his life at the monastery Jarrow where he wrote the first comprehensive history book on British history *Historia Ecclesiastica Brittanorum*. He gives an account of one of Aidan´s miracles, as told to him by Cynemund, a priest of Jarrow. A priest named Utta,

making a long sea journey, was instructed to pour oil on the sea in the event of a storm:

.... and the wind will immediately drop, giving you a pleasant, calm voyage.....He .... poured some of it over the sea, which immediately ceased its raging as Aidan had foretold (cited in the translation after Scott 1979).

Further early reports on wave damping by oil can be found in manuscripts by St. Germanus, Theophilact Simocrate, St. Nicholas, Erasmus Roterdamus, H. Canisius, S. Maiolus, M. Martin, V. Donati, T. Pennant, and L. Poinsinet de Sivry. The exact references are summarised in the bibliography by Scott (1979), presumably the most comprehensive one with regard to this subject.

From a scientific point of view, Benjamin Franklin was the first to perform experiments with "oils" on natural waters. On June 20th, 1757, a convoy of ships set sail northwards from New York, bound for Louisburg, a French fortress near the eastern tip of Cape Breton Island, northeast of Nova Scotia (Giles 1969). The convoy consisted of transports carrying British troops, their escorting frigates, and some vessels carrying civilian passengers. One of these passengers happened to be watching the accompanying fleet when something unusual in the appearance of the sea around a vessel attracted his attention. This passenger was Benjamin Franklin, who had been appointed by the American House of Assembly in Philadelphia as their agent to petition George II against the action of the Proprietors of Pennsylvania. After a frustrating wait of nearly three months in New York until permission was given for the fleet to sail, he set out with about 40 others, passengers included, in one of three packet boats, which for protection sailed in convoy with the fleet and steered for England. The incident, which captured his attention, led to the first scientific recognition of the importance of surface films on water. Some years later he described it, and its sequel, in these words (Franklin 1774):

In 1757, being at sea in a fleet of 96 sail bound against Louisburg, I observed the wakes of two of the ships to be remarkably smooth, while the others were ruffled by the wind, which blew fresh. Being puzzled with the differing appearance, I at last pointed it out to our captain, and asked him the meaning of it? "The cooks", says he, "have, I suppose, been just emptying their greasy water through the scuppers, which has greased the sides of those ships a little"; and this answer he gave me with an air of some little contempt as to a person ignorant of what everybody else knew. In my own mind I at first slighted his solution, tho' I was not able to think of another. But recollecting what I had formerly read in Pliny, I resolved to make some experiment of the effect of oil on water, when I should have opportunity.....

At length being at Clapham where there is, on the common, a large pond, which I observed to be one day very rough with the wind, I fetched out a cruet of oil, and dropt a little of it on the water. I saw it spread itself with surprising swiftness upon the surface..... I then went to the windward side, where (the

waves) began to form; and there the oil, though not more than a teaspoonful, produced an instant calm over a space several yards square, which spread amazingly, and extended itself gradually till it reached the lee side, making all that quarter of the pond, perhaps half an acre, as smooth as a looking glass (1 acre = 43 560 sq. feet = 63 x 63 m^2).

After this, I contrived to take with me, whenever I went into the country, a little oil in the upper hollow joint of my bamboo cane, with which I might repeat the experiment as opportunity to succeed..... In these experiments, one circumstance struck me with particular surprize. This was the sudden, wide and forcible spreading of a drop of oil on the face of the water, which I do not know that anybody has hitherto considered. If a drop of oil is put on a polished marble table, or on a looking-glass that lies horizontally; the drop remains in its place, spreading very little. But when put on water it spreads instantly many feet around, becoming so thin as to produce the prismatic colours, for a considerable space, and beyond them so much thinner as to be invisible, except in its effect of smoothing the waves at a much greater distance. It seems as if a mutual repulsion between its particles took place as soon as it touched the water, and a repulsion so strong as to act on other bodies swimming on the surface, as straws, leaves, chips, etc., forcing them to recede every way from the drop, as from a center, leaving a large clear space. The quantity of its force and the distance at which it will operate, I have not yet ascertained, but I think it a curious enquiry, and I wish to understand whence it arises.....

Benjamin Franklin's experiments with a "teaspoonful of oil" on Clapham pond in 1773 inspired many investigators to consider sea surface phenomena or to conduct experiments with oil films. This early work was reviewed by Scott (1979), Giles (1969), Giles and Forrester (1970), and Tanford (1989). Franklin's studies with experimental slicks can be regarded as the beginning of surface film chemistry. His speculations on the wave damping influence of oil induced him to perform the first qualitative experiment with artificial sea slicks at Portsmouth (England) in October of 1773. Although the sea was calmed and very few "white caps" appeared in the oil-covered area, the swell continued through the oiled area to Franklin's great disappointment.

2 Early laboratory experiments and theories

In addition to early experiments on the open sea, basic studies were performed in the laboratory, in order to gain basic insight into the wave damping mechanism induced by surface-active oil film materials ("slicks"). The first to carry out systematic wave tank investigations appears to have been Achard in the year 1778 who used a trough 4.3 m long, 1.2 m wide, and 1.2 m deep, in which standing waves were generated by a hand-cranked

rotating-cylinder assembly (Achard 1778). The effect of the waves on a model ship, 15 cm long, was observed, and the action of an oil film in suppressing the breaking of waves over the ship was demonstrated. The effect of oil was, however, not remarkable, and the greater wave-suppressing action of air-filled glass spheres tethered to the model ship led the author to the conclusion that the effect of both oil and floating solid bodies was a result of the mass they added to the surface.

Otto (1798) gave perhaps the earliest comprehensive account of the classical and medieval authors, and in his descriptions of uses he draws heavily on Franklin and Lelyveld (see Scott 1979). In explaining the effect he favours the hypothesis that the oil discourages the natural affinity of water for air, and prevents the force of the wind from being transmitted to the water. He does not, however, reject the hypothesis of Achard that floating solid bodies may have a similar, and more permanent, calming effect. Kries (1799) described his reasons for scepticisms regarding all of the mechanisms so far proposed for explaining the action of oil on waves: Achard's work with a model system is criticised as unrealistic; Otto`s belief in the chemical effect, waves being generated by the affinity between water and air, was thought to be unlikely compared with the mechanical effect of the fluctuating force of the wind, and Müller's suggestion (see Scott 1979) that the viscous skin on the surface hinders wave breaking, although felt to be plausible, was seen to require more experiments to determine whether the oil layer is sufficiently strong for this effect. Principally concerned with explaining the damping of large amplitude waves observed by Franklin at an oil/water interface, Robinet (1807) suggested that an oil film can only exert a marked effect on waves whose amplitude is less than the film thickness. Since all waves must start from small amplitudes, however, he considered that the effect on storm waves is credible. By the way of contrast, Weber and Weber (1825) conjectured that an oil layer does not adhere to the water, and thus absorbs the horizontal component of the wind stress. Van Beek (1842) concurred with Franklin and Aristotle that the effect of oil is in the prevention of small waves which would allow the wind to grip the breakers. He attempted to explain this damping action, his argument being based on some effect of the oil on horizontal components of the wind velocity.

The basis for our present models describing wave damping by monomolecular surface films was formed by a paper published by Marangoni in 1872:

Spargendo dell'olio sul mare si sostituische alla superficie elastica dell'aqua la superficie non elastica dell'olio; sicche il vento smuoverá localmente le particelle dell'olio senza che il movimento venga a communicarsi per una grande estensione, e di qui il cessare dell'increspamento della superficie coll'effusione dell'olio.

Marangoni described investigations which showed that motions of bodies at the surface of a liquid may be opposed by elastic forces associated with a sur-

face layer. The conclusion of Plateau that such effects are due to an increased viscosity of the surface layer was shown to be inadequate. The importance of the surface elasticity (or more precise visco-elasticity in modern terms) in the damping of wind waves was pointed out (*Abbonacciamento delle onde, pp 268-270*) and the explanation of the effect that the change of elasticity associated with the oil is sufficient to prevent excitation of waves by the wind, is essentially that still held today. However, it should be noted that Marangoni´s conclusions are rather confused from a modern point of view, the water being found to be *elastic* and the oil surface *not elastic*. On the other hand, Marangoni´s views inspired many models related to the influence of surface-active chemical compounds on the motion of fluids (*Marangoni effect, Marangoni damping*), including models in the field of Applied and Technical Chemistry. It may also be of interest to the readers that several observations of daily life are closely associated with the Marangoni effect. For example, if wine is poured into a wine glass, and then moderately shaken around such that the wine is moving along the outer parts of the glass, one can observe the wine creeping up the walls. This upward movement is driven by surface tension gradients (Marangoni effect) caused by different intense evaporation of ethanol at the lower and upper parts of the walls.

A more precise interpretation of water wave damping through the elastic nature of a spread oil film was given by Reynolds (1880). The full text is as follows:

The paper contained a short account of an investigation from which it appeared that the effect of oil on the surface of water to prevent wind-waves and destroy waves already existing, was owing to surface-tension of the water over which the oil spread varying inversely as the thickness of the oil, thus introducing tangential stiffness into the oil-sheet, which prevented the oil taking up the tangential motion of the water beneath. Several other phenomena were also mentioned. The author hopes shortly to publish a full account of the investigation.

This full account apparently never appeared, except for a few lines given in Reynolds 1884 (see Scott 1979).

Lord Rayleigh carried out very detailed laboratory experiments, which showed the damping of wind-excited *ripples* by a drop of oil. The phenomenon was explained in terms of the resistance to wave motion associated with the differences in surface tension, which arise during the periodic extensions and contractions of the surface. Related experiments on the properties of soap films and the spreading of organic materials were also described. The very comprehensive work was published in three papers (Rayleigh 1890a, 1890b, 1890c).

The first to perform wave-damping measurements in a kind of *Langmuir trough*, i.e., under different compression status of the monolayer, was Agnes Pockels (1891). Ironically, she described for the first time an apparatus that was

later also used by Langmuir and named after him (according to a publication in 1917). Pockels performed relatively delicate experiments on the contamination of water surfaces by organic materials. A shallow trough divided by a movable barrier was used to vary the area of a water surface and thus the compression status of the monolayer, and marked variations of the damping of ripples were found. A rapid increase in damping with increasing surface concentration was found.

The earliest available hydrodynamic theory of water wave damping by elastic surface films was published by Lamb (1895). He refers to Reynolds (1880) and the experiments by Aitken (see Scott 1979, Giles and Forrester 1970), but prior publication of the detailed theory is not indicated. All but the outline of the theory was omitted from later editions of this book, and it is likely that Lamb assumed that damping was greatest with an inextensible film, and that intermediate elasticities, therefore, had less effect (cited after Scott 1979). This conclusion was shown by Dorrestein (1951) to be incorrect. The paper by Levich (1940) was the first to present in detail the linearised hydrodynamics of waves on a water surface with surface dilational elasticity. The only cases considered in detail concern insoluble films, and represent the clean and incompressible-film-covered surface. A detailed treatment of the hydrodynamic theory of surface waves, including the effect of an elastic surface film, was published by Levich in 1962. In addition, the damping caused by dissolved surface-active material was considered. Further laboratory experiments performed until 1978 were briefly reviewed by Scott (1979).

3 Utilisation for basic studies of air-sea interactions

Giles (1969) reviewed the literature published after Franklin's experiments and found 17 authors discussing wave damping by oil prior to 1951. But apart from some experiments on wave quelling by John Shields in the harbours of Peterhead and Aberdeen (Scotland) in 1882, 70 years passed again, before surface films again became of interest as a tool for the practical modification of air-sea interaction processes, when Mansfield and several other authors started large-scale investigations on the retardation of evaporation by monomolecular surface films (La Mer 1962). Basically, long-chain saturated alkanols and carboxylic acids are able to reduce the rate of evaporation of water from lakes and reservoirs in hot, arid regions where the amount of water lost by evaporation may exceed the amount regularly used. In other terms, evaporation may lower the level of a reservoir by as much as ten feet annually. In order to reduce this evaporation by using only a monolayer of surface-active compounds, has not only the advantage that quite small amounts are required, but also that the oxygen

necessary to support life can still diffuse into the water, and stagnation of the lake is thereby avoided (Davies and Rideal 1963). The reason that enough oxygen penetrates a quiescent surface covered with a monolayer lies in the high diffusional resistance R_L encountered in the aqueous solution subjacent to the surface: compared with this resistance, the monolayer has a small effect. If, however, a thick film layer such as a crude oil spill were used to retard evaporation, its enormous resistance would become dominant in retarding the entry of oxygen. Under natural conditions the exchange both of water and oxygen between a reservoir and the air is aided by the wind. However, in the presence of , e.g., hexadecanol monolayers the exchange rates may be influenced. While the evaporation retardation may thus attain values of about 90 %, the oxygen content may be reduced to 80 % of saturation only (Davies and Rideal, 1963). This has little effect on living organisms. The experiments carried out in the 50ties and 60ties of the last century supplied sufficient evidence that these assumptions are realistic. However, it turned out that continuous application of surface films on reservoirs was ineffective, if winds were blowing with ≥ 5 ms^{-1}. On the other hand, many insights gained during evaporation retardation experiments carried out at reservoirs supplied deepened insights into ocean/air exchange processes as well.

In recent years, experimental sea slicks are being utilised for basic studies of air-sea interaction processes including wind wave generation (Hühnerfuss and Garrett 1981, Hühnerfuss et al. 1981a, 1981b, 1983, 1987, Alpers and Hühnerfuss 1989, Barger et al. 1970, Mallinger and Mickelson 1973), wind-induced drift response of the ocean surface (Lange and Hühnerfuss 1978), and gas exchange (Brockmann et al. 1982) as well as for the investigation of the modification of remote sensing signals by biogenic and anthropogenic surface-active chemicals on the ocean surface (Hühnerfuss et al. 1994, 1996, Gade et al. 1998a, 1998b).

4 References

Achard FC (1778) Mémoire sur la manière de calmer l'agitation d'une partie de la surface d'un fluide,... (Concerning the means of reducing the motion of part of the surface of a fluid...). Nouveaux Mémoires de l'academie Royale des Sciences et Belles-Lettres, Berlin, 19-26 (in French)

Alpers W, Hühnerfuss H (1989) The damping of ocean waves by surface films: A new look at an old problem. J Geophys Res 94: 6251-6265

Aristotle, Problemata Physica , Book XXIII "Problems connected with salt water and the sea", No. 38

Barger WR, Garrett WD, Mollo-Christensen EL, Ruggles KW (1970) Effects of an artificial sea slick upon the atmosphere and the ocean. J Appl Meteorol 9: 396-400

Brockmann UH, Hühnerfuss H, Kattner G, Broecker H-Ch, Hentzschel G (1982) Artificial surface films in the area near Sylt. Lymnol Oceanogr 27: 1050-1058

Davies JT, Rideal EK (1963) Interfacial Phenomena. Academic Press, New York and London

Dorrestein R (1951) General linearised theory of the effect of surface films on water ripples. Proceedings, Koninklijke Nederlandse Akademie van Wetenschappen, Series B, Vol. 54: 260-272

Franklin B (1774) Of the stilling of waves by means of oil. Phil Trans Roy Soc 64: 445-460

Gade M, Alpers W, Hühnerfuss H, Masuko H, Kobayashi T (1998a) Imaging of biogenic and anthropogenic ocean surface films by the multifrequency/multipolarization SIR-C/X-SAR. J Geophys Res 103: 18851-18866

Gade M, Alpers W, Hühnerfuss H, Wismann VR, Lange PA (1998b) On the reduction of the radar backscatter by oceanic surface films: scatterometter measurements and their theoretical interpretation. Rem Sens Environ 66: 52-70

Giles CH (1969) Franklin's teaspoonful of oil. Studies in the early history of surface chemistry, part 1. Chem Ind 1616-1624

Giles CH, Forrester SD (1970) Wave damping: the Scottish contribution. Studies in the early history of surface chemistry, part 2. Chem Ind 80-87

Hühnerfuss H, Garrett WD (1981) Experimental sea slicks: their practical applications and utilization for basic studies of air-sea interactions. J Geophys Res 86: 439-447

Hühnerfuss H, Alpers W, Jones WL, Lange P, Richter K (1981a) The damping of ocean surface waves by a monomolecular film measured by wave staffs and micro-wave radars. J Geophys Res 86: 429-438

Hühnerfuss H, Alpers W, Lange PA, Walter W (1981b) Attenuation of wind waves by artificial surface films of different chemical structure. Geophys Res Lett 8: 1184-1186

Hühnerfuss H, Alpers W, Garrett WD, Lange PA, Stolte S (1983) Attenuation of capillary and gravity waves at sea by monomolecular organic surface films. J Geophys Res 88: 9809-9816

Hühnerfuss H, Walter W, Lange PA, Alpers W (1987) Attenuation of wind waves by monomolecular sea slicks and the Marangoni effect. J Geophys Res 92: 3961-3963

Hühnerfuss H, Gericke A, Alpers W, Theis R, Wismann V, Lange PA (1994) Classification of sea slicks by multi-frequency radar techniques: new chemical insights and their geophysical implications. J Geophys Res 99: 9835-9845

Hühnerfuss H, Alpers W, Dannhauer H, Gade M, Lange PA, Neumann V, Wismann V (1996) Natural and man-made sea slicks in the North Sea investigated by a helicopter-borne 5-frequency radar scatterometer. Int J Remote Sensing 17: 1567-1582

Kries FC (1799) Einige Bemerkungen über J.F.W. Otto's Aufsatz: das Öl, ein Mittel die Wogen des Meeres zu besänftigen (Some comments on J.F.W. Otto`s article: Oil as a means of calming waves at sea). Allgemeine Geographischen Ephemeriden, Vol 3: 242-251 (in German)

Lamb H (1895) The calming effect of oil on water waves. Hydrodynamics, 2nd Edition, Cambridge University Press, Article 304, 552-555

La Mer VK (1962) Retardation of evaporation by monolayers: transport processes. Academic Press, New York

Lange P, Hühnerfuss H (1978) Drift response of monomolecular slicks to wave and wind action. J Phys Oceanogr 8: 142-150

Levich VG (1940) The damping of waves by surface-active materials. Zhurnal Eksperimentalnoi i Teoretcheskoi Fiziki Vol. 10, No. 11: 1296-1304 (in Russian). (English language version: Acta Physiochimica URSS, Vol.14: 307-328 (1941))

Levich VG (1962) Waves on a liquid surface. Physicochemical Hydrodynamics, Prentice Hall, Chapter 11, 591-626

Mallinger WD, Mickelson TP (1973) Experiments with monomolecular films on the surface of the open sea. J Phys Oceanogr 3: 328-336

Marangoni C (1872) Sul principio della viscosita superficiale dei liquidi stabilito dal sig. J. Plateau (On the principle of the surface viscosity of liquids, established by J. Plateau), Nuovo Cimento, Series 2, Vol. 5/6: 239-273 (in Italian). (Further evidence was given Marangoni in Nuovo Cimento, Series 3, Vol. 3: 50-68, 97-115, 193-211

Otto JFW (1798) Das Öl, ein Mittel die Wogen des Meeres zu besänftigen (Oil as a means of calming waves at sea). Allgemeine Geographischen Ephemeriden, Vol. 2: 516-527 (in German)

Plinius Secundus C (Pliny the Elder), Historia Naturalis, Book 2, Chapter 49 (completed A.D. 77) (see also C. Plinius Secundus, Historia Naturalis, Book 2, Chapter 106). Scott J C (1979) Oil on troubled waters. A bibliography on the effects of surface-active films on surface-wave motions. Multi-Science Publishing Co. Ltd, The Old Mill, Dorset Place, London, 1979. ISBN 0 906522 00 5

Plutarch, Moralia: Quaestiones Naturales. Vol. 11, No. 12. (see also Plutarch, Moralia: De Primo Frigido, No. 950)

Pockels A (1891) Surface tension. Nature 43: 437-439

Rayleigh, Lord (1890a) Foam. Proceedings of the Royal Institution Vol. 13: 85-97

Rayleigh, Lord (1890b) On the superficial viscosity of water. Proceedings of the Royal Society Vol. 48: 127-140

Rayleigh, Lord (1890c) On the tension of water surfaces, clean and contaminated, investigated by the emthod of ripples. Philosophical Magazine, Vol. 30: 386-400

Reynolds O (1880) On the effect of oil in destroying waves on the surface of water. Report of the British Association for the Advancement of Science, 489-490

Robinet (1807) Explication d'un phénomène d'hydrostatique observè par Franklin (Explanation of a hydrostatic phenomenon observed by Franklin). Journal de Physique, de Chimie et d'Histoire Naturelle, 277-282 (in French)

Tanford C (1989) Ben Franklin stilled the waves. Duke University Press, Durham and London

van Beek A (1842) Mémoir concernant la propriété des huiles de calmer les flots, et de rendre la surface de l'eau parfaitement transparente (Memoir concerning the property of oils to calm waves, and to make the surface of water perfectly transparent). Annales de chimie et de Physique, 3^{me} Série, Vol 4: 257-289

Weber EH, Weber W (1825) Über die Besänftigung der unter dem Einflusse des Windes erregten Wellen durch die Ausbreitung von Ölen auf der Oberfläche von Wasser (On the calming of wind-generated waves by the spreading of oil on the surface of water). Wellenlehre, auf Experimente gegründet. Leipzig, 60-90 (in German)

Carlo Marangoni and the Laboratory of Physics at the High School "Liceo Classico Dante" in Firenze (Italy).

Giuseppe Loglio

Dipartimento di Chimica Organica, Universita degli Studi di Firenze, Sesto Fiorentino, Firenze, Italy

Since 1869 until 1910, during 41 years, Carlo Marangoni continuously held the Chair of Physics at the High School *Liceo Classico Dante* at Florence. In the course of his long permanence, Marangoni to a large extent developed the ancient laboratory of Physics of the "Liceo".

At Pavia, where he was born in 1840, Carlo Marangoni studied Physics including all courses until the University Degree in Physics (*Laurea di fisica*), which he obtained after defending a thesis on the phenomena occurring in liquids due to the action of surface tension, under the advice of Professor G. Cantoni (1). In 1868, Marangoni moved to Florence and joined the *Specola*, a section of the *Istituto di Studi Superiori* (2). Here, he focused his attention upon meteorological research subjects. In this field, a very short note is particularly worth mentioning, published in *Nuovo Cimento* in the year 1868 at page 318, entitled *The thermometer of Mr. Marchi, with maximum and minimum values*. Later on, Marangoni equipped the Laboratory of Physics of the *Liceo* with this kind of instrument, which he judged especially accurate.

Furthermore, Marangoni always showed particular attention and devotion to Acoustics, a typical science of the Nineteenth Century. The rich collection of acoustic instruments, present in the High School, testimonies the above-mentioned devotion. Moreover, an article (3) about physiologic acoustics, executed in the Laboratory of Physics of the *Istituto Tecnico* at Firenze, was published in collaboration with Emilio Villari.

In 1869, Marangoni started his teaching activity at the *Liceo Classico Dante* (4), accompanied by research activities, as documented by numerous and important articles in *Nuovo Cimento* (5,6) and in *Rendiconti dell'Accademia dei Lincei*. In Ref. 5, Carlo Marangoni and Pietro Stefanelli, teachers in the *Regio Liceo Classico Dante* and in the *Scuola Tecnica Dante* at Firenze, respectively, wrote that they used a good "Sine Galvanometer" that was present in the Laboratory. This galvanometer, showing a

label "made by Officina Galileo", is up to now in a good functioning state and it represents one among the earliest products of the Officina Galileo.

Fig. 1. Carlo Marangoni, year 1909

In Ref. 6, the fore-mentioned authors described the transport phenomena occurring in liquids due to surface tension gradients. During his active life, Carlo Maragoni also devoted his time to the preparation of laboratory experiments, to devising new instruments and he participated in thorough and state-of-the-art discussions on the principal developments of scientific research at the end of the Nineteenth Century, as documented by his collaboration with the journal *Rivista Scientifico-Industriale* edited by Mr. Vimercati.

The continuous work of Marangoni, during more than 40 years, is reflected by the instrumentation of the Laboratory of Physics, which attained a high qualitative and quantitative level under his direction. Such an important achievement was, in addition to the prestigious quality of Maran-

goni as a teacher and as a scientist, also due to the widely held intention of the contemporary governments for remedying the large scientific lag of the country. Actually, during the second part of the Nineteenth Century, a great part of the scientific research was conducted in the laboratories of the high school institutes. Moreover, numerous teachers had available comparable (if not better) laboratories as compared with university laboratories and performed an appreciable and, as much as possible, advanced experimental activity.

Note. The present short biography of Marangoni is available on the Web-site of the *Liceo Classico Dante*. The text has been edited and translated into English by Giuseppe Loglio. Figure 1 is cropped out from the image of a group of professors and students, celebrating the final High School Degree, in the year 1909. The original photograph belongs to a private collection (Dr. Valleri). A photographic reproduction of the original photograph is deposited in the archive of *Liceo Classico Dante* (by a courtesy of the Rector of the High School and of Prof. Maria Teresa Aristodemo Renzi).

References

1. G. Cantoni (1818-1897), was the successor of Giuseppe Belli on the Chair of Physics of the University of Pavia, which formerly was the Chair of Alessandro Volta
2. The "Istituto di Studi Superiori" changed its name into "Universita' degli Studi di Firenze" at the beginning of the Twentieth Century.
3. "Ricerche sul limite della percezione dei suoni in riguardo alla loro durata"; del prof. Emilio Villari e del dottor C. Marangoni; Nuovo Cimento serie 2, vol I, pp. 382-397, 1869.
4. Liceo Classico Dante is still operative in the original building, Via Francesco Puccinotti n. 55, 50129 Firenze (Italy), Tel.: +39-055-490268, Web-site : http://www.liceoclassicodante.fi.it
5. "Sulle proprietà che hanno vari liquidi di impedire o far cessare talune reazioni tra acidi e metalli"; ricerche sperimentali dei professori C. Marangoni e P. Stefanalli, Nuovo Cimento, serie 2, vol. IV , pp.373-389, 1871.
6. "Monografia sulle bolle liquide"; dei professori C. Marangoni e P. Stefanelli, insegnanti nel R. liceo e nella scuola Tecnica Dante di Firenze, Nuovo Cimento, serie 2, vol. VII-VIII, pp. 301-356, 1872; serie 2, vol. IX pp.236-256, 1873.

Tribute to Erik John Bock

Nelson Frew

Department of Marine Chemistry and Geochemistry, Woods Hole Oceanographic Institution, Woods Hole, USA

The oceanographic and remote sensing communities recently lost a valued colleague. Dr. Erik John Bock, of the University of Heidelberg, Germany. Erik died unexpectedly near his home in Obrigheim, Germany on June 25, 2001, of injuries suffered in a bicycle accident. He was 39 years old.

Erik was bom in Buffalo, New York on November 2, 1961 and grew up in Cheektowaga and Boston, New York. An avid Boy Scout and early achiever, he attained the rank of Eagle Scout and was Salutatorian of his Orchard Park High School Class of 1980. Erik went on to study chemistry at the Renssalaer Polytechnic Institute in Troy, New York, earning a B.S. in chemistry (*magna cum laude*) in 1984, an M.S. in Chemistry in 1986, and then his Ph.D. in Chemistry in 1987. Following three years as Research Assistant Professor at Renssalaer, Erik joined the Woods Hole Oceanographic Institution as Assistant Scientist in 1990, becoming an Associate Scientist in 1994. In 1998, he moved to the University of Heidelberg as Guest Scientist to work with B. Jähne in the new Aeolotron wind-wave facility.

Erik's research focused on the interfacial properties of the ocean surface, and, in particular, how the chemistry of the air-sea interface affects the dynamics of short waves, nearsurface flows and interfacial fluxes of heat, mass and momentum. During his short career, he contributed to over 30 scientific publications in this area. His doctoral research, carried out under the tutelage of well-known colloid and surface chemist, Sydney Ross, concerned the propagating characteristics of surface waves in the presence of adsorbed films. That work was eventually published as a series of seminal papers on capillary ripples, and his theoretical treatment of ripple propagation and a corrected dispersion relation for surface waves in the presence of a surface dilational modulus (with J. Adin Mann, Jr.) still stand as the definitive word on the subject.

Erik considered himself first and foremost a surface chemist, although the timely relevance of his work to ocean wave dynamics and to remote sensing questions pushed him strongly in the direction of ocean physics.

He became a leading expert in designing and deploying instruments to measure small-scale ocean waves, which play an important role in many air-sea exchange processes. Increasing interest in the high frequency tail of the ocean wave spectrum and the role of small-scale waves in the scattering of microwave radar led him to develop novel optical slope gauges that provided ripple frequency spectra and later, full three-dimensional frequency-wavenumber spectra of ripples. These instruments played a central role in numerous field campaigns to study radar imaging of the sea surface and the role of surface roughness in boundary layer processes. In collaboration with colleagues at Woods Hole, Heidelberg, and the University of Rhode Island, Erik explored the relationship between the mean square slope of small-scale waves and air-sea gas transfer velocity, work that subsequently led to estimation of global gas transfer velocity fields using satellite altimeters. In the laboratory, he continued his interest in interfacial phenomena, including the influence of surface films on near-surface vortical flows, the subject of a contribution with S. McKenna in this volume.

Erik was mentor and teacher to several postdoctoral investigators, graduate students and undergraduates, who benefited from his clear explanations of physical phenomena and his competent engineering advice. Erik made a huge contribution to the field of ocean physics by providing detailed spatiotemporal spectra of small-scale ocean waves. His colleagues and the community-at-large will sorely miss his keen insight and jovial presence.

Erik J. Bock. Picture taken during the Gasex 2001 expedition in February, 2001.

Chapter 1:

Chemical Characteristics of Sea Slicks and Oil Spills

Basic physicochemical principles of monomolecular sea slicks and crude oil spills

Heinrich Hühnerfuss

Institute of Organic Chemistry, University of Hamburg,
Hamburg, Germany

1. Introduction

During the 60ties until the 80ties of the last century several working groups comprised oceanographic, meteorological, remote sensing, and chemical experts that were able to carry out interdisciplinary research on a safe basis, taking into account state-of-the-art knowledge of the involved disciplines. This was particularly important for the study of air-sea interaction processes, their modification by organic chemical compounds as well as the investigation of these aspects by airborne and satellite-borne remote sensors. In the last decade, however, an increasing number of papers slipped into scientific journals or are being presented at international conferences that report studies on sea slicks or oil spills violating basic and well-known principles of organic and physicochemistry. For example, every textbook on basic physicochemistry describes the fact that surface-active compounds form monomolecular surface films, while nonpolar chemical compounds that represent the main constituents in crude oils are distributed on water surfaces by forming thick layers. In spite of this clear background, several papers were presented in which authors describe theoretical and experimental approaches that aim at the determination of different thicknesses of, e.g., vegetable oil films at the air/sea interface. It is being ignored that the components of vegetable oils are surface-active and never spread over each other, but form monomolecular films that stand in equilibrium with the thicker source spot, which comprises the relatively small and negligible area, where the vegetable oil was poured onto the sea surface. Furthermore, a Babylonic confusion can be found in the actual literature with regard to the nomenclature of slick and spill phenomena, which on one hand side are clearly defined in surface chemistry, however,

on the other hand are mixed-up or ignored by authors not caring of the clear and internationally obligatory nomenclature.

This situation forms the background of the present paper that aims at summarising the main physicochemical principles of sea slicks and oil spills, including the chemical structures of film-forming compounds, their interaction with the adjacent water layer, their spontaneous distribution at the water surface and their potential influences on air-sea interaction processes, thus forming a link to the subsequent reports of this monograph that describe detailed research on the modification of air-sea interaction processes and remote sensing signals by sea slicks and oil spills.

2. The chemical structure of slick- and spill-forming chemical substances

Sea slicks are being formed by surface-active organic compounds the chemical structure of which consists of a hydrophobic part (*hydor = Greek word for water; phobos = Greek for fear*) and a hydrophilic part (*philos = Greek word for love/strong preference*). This ambiphilic structure, i.e., strong tendency both towards and against water, leads to the consequence that surface-active molecules are spontaneously arranged at the air/water interface such that the hydrophobic part is directed into the air, while the hydrophilic head group dips into the interfacial water layer (Figure 1).

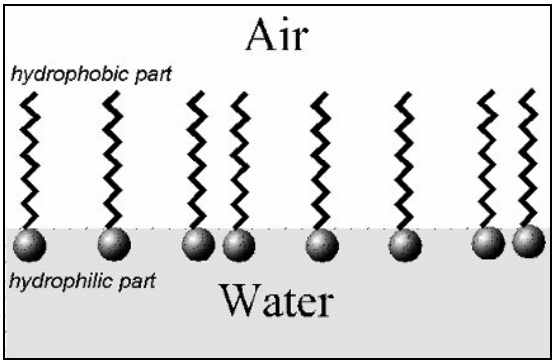

Fig. 1. Schematic sketch of a monomolecular surface film being formed by surface-active compounds that consist of a hydrophobic and a hydrophilic part

Specific surface-active substances that have often been used for the generation of slicks at the sea surface, in order to simulate biogenic sea slicks and their potential influence on air sea interaction processes and on remote sensing signals, include oleyl alcohol (Z-9-octadecen-1-ol; OLA), oleic

acid methyl ester (methyl *Z*-9-octadecenoate; OLME), and methyl palmitate (methyl hexadecanoate; PME), see Figure 2.

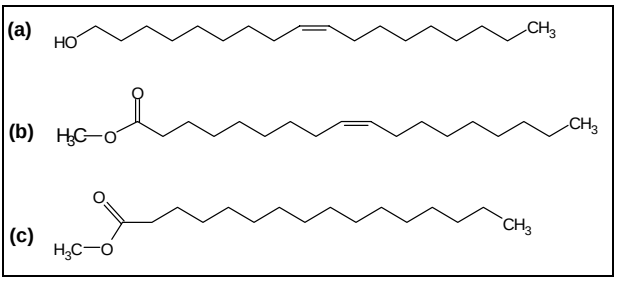

Fig. 2. Chemical structures of typical slick-forming compounds, a.) oleyl alcohol (*Z*-9-octadecen-1-ol; OLA), b.) oleic acid methyl ester (methyl *Z*-9-octadecenoate; OLME), and c.) methyl palmitate (methyl hexadecanoate; PME)

By the way of contrast, crude oil spills mainly consist of alkanes ("*paraffins*"), cycloalkanes, and aromatic compounds, i.e., chemicals that exclusively exhibit a hydrophobic character, because no hydrophilic head group is present. As a consequence, a small drop of high-boiling paraffin oil, placed onto the water surface, maintains its form as a drop, floating in a depression as shown in Figure 3. Depending on the amount and the viscosity of the crude oil mixture as well as on the specific environmental conditions the drop will leave this idealised form, flattens out and becomes thinner. However, the final thicknesses thus achieved still remain orders of magnitude larger than those of a monomolecular film shown in Figure 1.

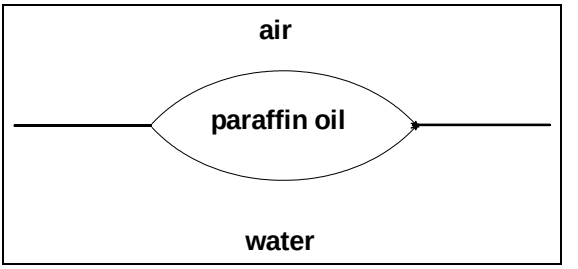

Fig. 3. Simplified representation of a drop of high-boiling (= long-chain) paraffin oil lying on a water surface

3. Distribution of slick- and spill-forming substances on the water surface

All surface-active molecules, once placed at one point onto the water surface ("point source"), show a strong tendency to attain the optimum arrangement illustrated in Figure 1. Therefore, all molecules *spread* from the point source towards all sides as a monomolecular film. The thermodynamic equations describing the spreading effect can be found in every basic physicochemical textbook, e.g., Davies and Rideal (1963), Gaines (1966). If no wind, waves and currents were active (just an ideal, non-real assumption) the slick would spread symmetrically in a circle around the point source. Wind and/or currents will give rise to elongations of the slick (Lange and Hühnerfuss 1978). Close to the point source we encounter spreading velocities of typically around 6 to 18 cm/s, depending on the exact chemical structure. Then, the velocity decreases exponentially with the distance from the point source. This is exemplarily shown in Figure 4 for OLA and OLME that induce strong and weak water wave damping, respectively.

As long as we try to generate a sea slick from a point source it may take several hours to have the complete bulk material spread as a monomolecular film. However, during the ongoing spreading procedure, nearly the complete slick area is monomolecular, where this area stands in equilibrium with the source which just covers a negligibly small area (in comparison to the monomolecular area). This means that the thickness of nearly the complete slick area must not be measured by sophisticated theoretical and experimental approaches, because it can be safely assumed that it exhibits the usual thickness of a monomolecular film consisting of molecules with C16 to C18 chain lengths, i.e., the actual thickness is about 2.4 - 2.7 nm. In connection with sea slick investigations slight deviations of this value (± a few tenth of nm) due to a slight variation of the angle of the alkyl chain with respect to the water surface does not play any role for this discussion. This aspect has to be taken into account when investigating the influence of morphology effects (see the paper by Hühnerfuss et al., this monograph).

The decrease in spreading velocity with increasing distance from the source has consequences for the optimum strategy for the generation of artificial sea slicks aiming at the simulation of potential influences of biogenic slicks on air sea interaction processes and remote sensing signals. A very effective generation was described by Hühnerfuss and Garrett (1981) who distributed frozen chunks of slick material (ca 80 g each) from a helicopter within a sea area of 0.5 to 2.5 km^2. Thus about 100 to 300 point

sources allowed spreading of a corresponding number of single slicks that were easily connected to one large slick after about 10 to 15 min.

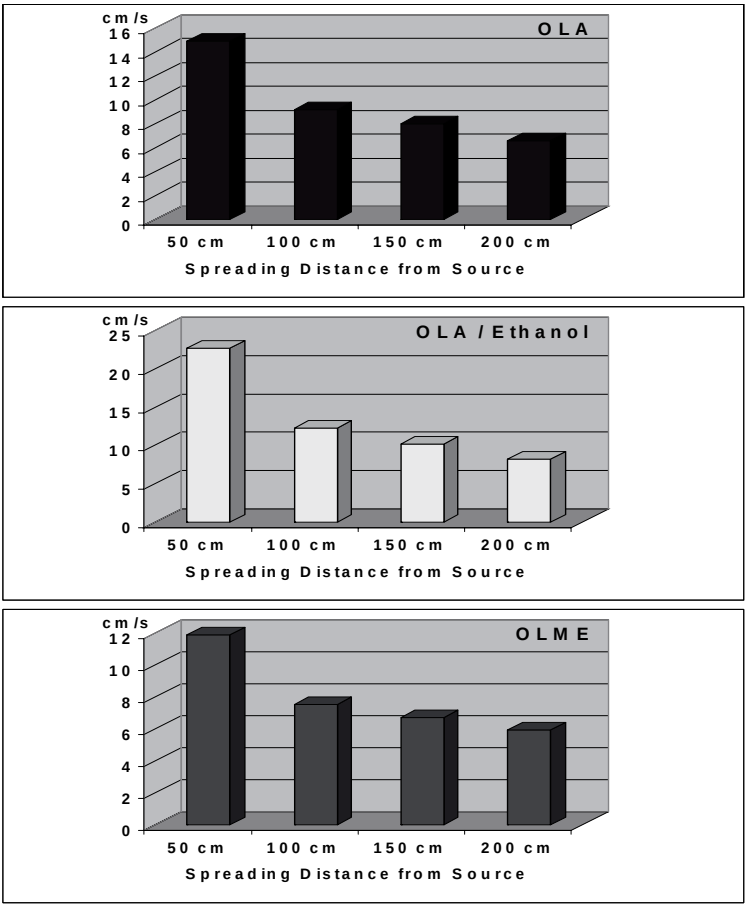

Fig. 4. Spreading velocities [cm/s] in dependence on the distance from the source [cm] for pure oleyl alcohol (OLA; top), a 75 mmol solution of OLA in ethanol (OLA/ethanol; middle), and pure oleic acid methyl ester (OLME; bottom); note the different ordinate scales

Furthermore, potential holes within the slick that may have been caused by strong winds or waves are easily repaired by respreading of material present as surplus material at the nearest point sources. While theoretically about 2 mg of the slick material are needed per square metre, it is advisable to use a tenfold surplus because of these repair mechanisms. As a consequence, 10 to 30 litres of the respective slick materials such as OLA or OLME are sufficient to generate slick sizes of 0.5 to 2.5 km^2. Care has

to be applied that the helicopter flies sufficiently high, in order to avoid disturbance of the water wave field by the downwash-effect of the helicopter.

If no helicopter is available, fluid slick-forming substances may also be distributed on the sea surface from aboard a boat. However, in this case the bulk material must be poured overboard very close to the water surface, in order to get optimum spreading conditions. Furthermore, the boat should be moved very slowly backwards out-of the developing slick, while additional slick material is being poured continuously onto the sea surface. During this procedure, propeller-induced water turbulence should be avoided as far as possible.

Several particularly strongly wave damping substances such as PME (see Figure 2) are solid and must be solved prior to their application, because solid PME crystals will not spread on the sea surface. The choice of an appropriate solvent is important for the spreading procedure, which determines the morphology of the developing slick and thus the influence on the water wave spectrum. The latter aspect is discussed in a separate paper by Hühnerfuss et al. in this monograph. In many cases, ethanol is assumed to be an excellent choice as a solvent. Its potential influence on the spreading velocity of the respective surface-active compound is shown for OLA in Figure 4. However, it has to be stressed that the application of organic solvents requires specific safety precautions, which in each country may be based on different safety regulations.

The distribution of crude oil mixtures on the water surface is dominated by the viscosity of the crude oil mixture as well as on the specific environmental conditions (currents, wind and water wave directions and magnitudes). As crude oil spills will form layers that remain orders of magnitude thicker than those of monomolecular slicks, considerably higher amounts of oil material are needed to generate experimental crude oil spills. Typically some cubic metres of crude oil have to be pumped onto the sea surface, i.e., three to four orders of magnitude more than in the case of artificial sea slicks. Furthermore, caution should be applied with the application of crude oils, because the transformation of the chemical constituents is much slower than that of the components of quasi-biogenic sea slicks. Furthermore, regulations of the respective countries have to be checked.

4. Damping of water waves by sea slicks or oil spills

The different water wave damping mechanisms of sea slicks and crude oil spills can be understood on the basis of their different influences on the structure and physicochemical characteristics of the air/water interface.

Monomolecular surface films change the structure of the uppermost water layer within a thickness of around some micrometers to possibly some hundred micrometers (Hühnerfuss and Alpers 1983, Hühnerfuss 1986). For example, "ice-like" clathrate structures are induced by OLA films in a water layer of $d \leq 190$ μm. Furthermore, the surface potential of pure water of about – 180 mV becomes positive and may approach values of ≥ 400 mV (Gericke and Hühnerfuss 1989), and the dilational surface viscosity is drastically increased (Hühnerfuss 1985). The relaxation time for disturbances of the surface film order τ_{comp} attains values of around 10 to 20 min, which are about 10^{13} times larger than the relaxation time τ_s of the water molecules (Hühnerfuss and Alpers 1983).

Wave-induced compression and dilation of a monomolecular surface film lead to concentration gradients, which in turn give rise to surface tension and surface potential gradients (Hühnerfuss 1986, Lange and Hühnerfuss 1984). A viscoelastic surface film changes the free surface boundary condition in the tangential direction, i.e., longitudinal waves are formed, and it thus strongly modifies the flow pattern in the boundary layer. As a consequence, wave energy is dissipated by enhanced viscous damping in the short-gravity-wave region due to large velocity gradients induced in the viscous boundary layer. This phenomenon is called the *Marangoni effect*. Marangoni damping denotes resonance-type wave damping of water waves in the short-gravity-wave region, which is connected with the fact that viscoelastic surfaces can carry two kinds of waves, the well-known gravity-capillary waves and the Marangoni waves. The latter waves are predominantly longitudinal waves in the boundary layer which are heavily damped by viscous dissipation. When these two waves are in resonance, the surface waves experience maximum damping. The fact that the Marangoni waves are strongly damped is the reason why these waves have long escaped detection. Their existence was verified experimentally only in 1968. A detailed presentation of the theory is given in Hühnerfuss (1986) and Alpers and Hühnerfuss (1989). In summary, water wave damping by monomolecular sea slicks can be attributed to the Marangoni effect and to slick-induced modification of nonlinear wave-wave interaction, by means of which wave energy is transferred from the longer waves to the energy sink in the Marangoni resonance region.

By the way of contrast, a water surface covered with a freshly spilled crude oil exhibits quite different physicochemical characteristics. No surface tension gradients will be generated by the undulating water surface and thus the Marangoni effect plays no role. On the other hand, the crude oil layer may also dampen short gravity waves due to its relatively high viscosity as compared with a pure water surface.

Both water damping effects, Marangoni damping and viscous damping, may be observed in parallel, if crude oil spills drifted on the sea surface for many days, weeks or even months. Then, the alkanes, cycloalkanes and aromatics will be subject to photochemical and microbial transformation processes (the so-called *weathering process*), by means of which surface-active compounds may be formed, which in turn may spread and thus form large area monomolecular slicks around the smaller areas of thicker crude oil layers. Within the outer areas of monomolecular regimes Marangoni damping with its resonance-type damping characteristics may be observed (Alpers and Hühnerfuss 1988), while within the thick crude oil layers viscous damping will still dominate.

As a consequence of the slick- or spill-induced water wave field various remote sensing signals and several air/sea exchange processes such as gas exchange and exchange of inorganic and organic chemical substances will be modified. These aspects will be further pursued in specific articles of the present monograph.

In conclusion, the main differences in slick and spill characteristics as well as the implications for the respective nomenclature are summarised in Table 1.

5. Comparative studies of slicks and spills

Comparative studies of sea slicks and crude oil spills are scarce, in particular investigations, in the course of which both spills and slicks were generated within the same sea area, at the same time, overflown by the same airborne or spaceborne remote sensors. It would be beyond the scope of this chapter, which actually intended to supply the basic chemical background information for the interpretation of remote sensing signals, to give a detailed appreciation of the few comprehensive slick/spill studies reported in the literature. Herein, only a brief summary as well as references can be given that will allow the reader to dive deeper into this aspect by consulting the original reports and papers.

Table 1: Summarising characteristics and nomenclature for sea slicks and crude oil spills.

	Sea Slicks	**Crude Oil Spills**
Chemical constituents	*surface-active substances* consisting of a *hydrophilic* head group and a *hydrophobic* tail	alkanes, cycloalkanes and aromatics with *preferentially hydrophobic* character, no hydrophilic head group
Distribution at the water surface	a.) substances *spread* on the water surface; b.) substances *are being spread* on the water surface c.) a sea slick *is generated (or produced)* at the sea surface	a.) crude oil *is spilled* at the sea surface b.) a crude oil spill *is generated (or produced)* at the sea surface
Thicknesses	*monomolecular*, typically 2.4 – 2.7 nm (2.4×10^{-9} – 2.7×10^{-9} m)	thicker layers, typically μm-range until mm-range, if freshly spilled even cm-range (in connection with accidents)
Origin	both biogenic (secreted by plankton or fish) and man-made	nearly in all cases man-made, in few cases oil seeps (e.g., Gulf of Mexico)
Water wave damping mechanisms	resonance-type wave damping in the short-gravity-wave region, (*Marangoni damping*)	damping by an interfacial layer of higher viscosity
Microbial or photochemical transformation of constituents	relatively fast: time scale hours or few days (⇒ soluble, highly polar substances that disappear in the bulk water)	very slow: several months (⇒ *weathered oil spills* ⇒ formation of surface active compounds ⇒ *slick* formation around thick spill centres)

5.1. Generation of crude oil spills

Several drawbacks related to the generation of crude oil spills on the sea surface have to be taken into account. While the spreading of artificial, but quasi-biogenic, sea slicks such as oleyl alcohol slicks is absolute harmless as they are part of natural processes at the sea surface, the spilling of crude

oil on the open sea requires an official permission that will be different for each country. Furthermore, the chemical composition of crude oils as outlined in Chapter 2 has the consequence that the strong van-der-Waals interactions between the long alkyl chains give rise to three-dimensional thick layers. The crude oil has to be pumped from a ship onto the sea surface, where it forms thick layers, dependent on the viscosity of the crude oil sort or fraction applied. After the campaign, intensive efforts should be undertaken to recover the remainder of the oil from the sea surface by oil combating ships.

In order to illustrate the range of application strategies (*chocolate mousse, fuel oil spill* etc.) that are closely related to the chemical structures of the respective crude oil fractions, examples are summarised in Table 2 that stem from the ARCHIMEDES experiments carried out in the German Bight in 1983 and 1985 (Commission 1985).

Table 2: Characteristics of the crude oil fractions used during ARCHIMEDES 1 in 1983 in the German Bight (Commission 1985)

Sort of spill	Fractions included	Density [kg m^{-3}]	Viscosity [m^2 s^{-1}]	Evaporation [%]
# 1 Mousse spill *chocolate mousse*	fuel oil: 11.3 m^3 gas oil: 4.0 m^3 sea water: 34.7 m^3	990	0.0022 (i.e. 2200 cSt)	20
#2 Pure fuel oil spill	fuel oil: 40.0 m^3 gas oil: 6.7 m^3	895	0.00075 (i.e. 750 cSt)	20

After the combating exercise some samples were taken and analysed: For spill #1 the viscosity and the water content turned out to be 0.055 m^2 s^{-1} and 75 %, respectively, while for spill #2 the viscosity and the water content attained 0.035 m^2 s^{-1} and 70 %, respectively. 18 hours after the spillage for both spills a total amount of about 20 m^3 of pure oil was evaporated, and to be combated at the sea surface remained 7.3 m^3 oil in spill #1, and 28 m^3 fuel oil in spill #2. In total, 30 m^3 were actually recovered by the combating vessels.

5.2. Comparison of different remote sensors flown over sea slicks and spills

In the literature, comparison of sensors that were flown over slicks and spills, which had been produced at different locations, can be found occasionally, and in some few experiments slicks and spills were generated within the same sea area and overflown with the same sensor systems, be it air or spaceborne (Table 3).

Table 3: References comparing the performance and signal responses of remote sensors to different slicks and spills; OLA ≡ oleyl alcohol; DIEOISO ≡ di(ethylenglycol)mono-*iso*-stearyl ether; OLME ≡ methyl oleate; TOLG ≡ triolein; DP ≡ Discrimination Potential

Campaign	Slicks	Spills	Sensors	DP	Ref.
MARSEN (1979)	OLA	artificial crude oil*	passive microw. L-band and S-band	+ -	Blume et al. 1983
MARSEN (1979)	OLA	Murban crude oil*	Lidar (381, 414, 482, 500 nm)	- +	Hühnerfuss et al. 1986a
SPILL 84 (1984)	OLA ISEO2 OLME	North Sea crude oil	RAR X-band; IR sensor	- -	Hühnerfuss et al. 1986b
Archimedes 2 (1985)	OLA ISEO2 OLME	Ekofisk cr, chocolate mousse, heavy fuel, med. fuel	five RAR X-band systems;	-	Hühnerfuss et al. 1986c, 1987
Review article	OLA ISEO2 OLME	Murban crude oil; North Sea crude oil	RAR x-band; Lidar 381, 414, 482, 500 nm; IR sensor	- + -	Hühnerfuss and Alpers 1987
Archimedes 2a (1988)	OLA ISEO2 OLME	heavy fuel	RAR X-band and K_a-band; passive microw. L-band**	- ?	Hühnerfuss et al. 1990
SIR-C/ X-SAR (1994)	OLA OLME TOLG	heavy fuel	L-, C-, and X-band SAR; 5-frequency HELISCAT	- - +	Gade et al. 1996, 1997, 1998a,b

* same sensor system, however, different experimental areas for spills and slicks
** passive microw. L-band signals disturbed by interference with Schiphol airport

As can be inferred from Table 3, some remote sensors appear to bear a potential for the discrimination of sea slicks and crude oil spills. The most promising approach was published by Hühnerfuss et al. (1986) who showed evidence that both Lidar and passive microwave L-band sensors may be able to discriminate between slicks and spills (Figure 5).

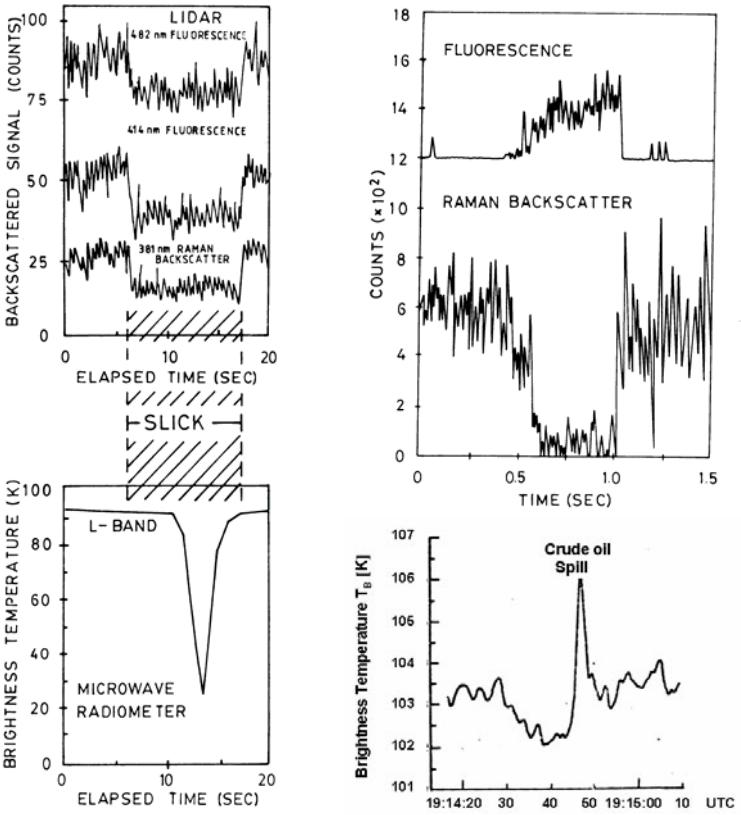

Fig. 5. Top left: Laser-induced Raman backscatter (381 nm) and two fluorescence return signals (414, 482 nm) measured during an overflight over an oleyl alcohol slick and adjacent *clean* sea areas; **bottom left:** the simultaneously obtained passive microwave L-band data; **top right:** same lidar sensor, Raman backscatter (381 nm) and fluorescence return signal at 500 nm during an overflight over a Murban crude oil spill and adjacent *clean* sea areas; **bottom right:** same passive microwave sensor, over an artificial oil spill in the New York Bight.

With regard to the Lidar measurements, the presence of an OLA slick at the ocean surface caused a decrease in both the Raman backscatter at 381 nm and of the fluorescent bands at 414 and 482 nm, while in the presence of a thick crude oil spill the Raman depression at 381 nm was accompanied by a simultaneous increase in the longer wavelength bands. During the same overflights a dramatic decrease in the passive microwave L-band signals was observed in the presence of an OLA slick (Blume et al. 1983), while in the presence of a crude oil spill an increase in the same band is encountered. Unfortunately, a verification of the latter conclusions is still

due, because during subsequent Archimedes 2a experiments off the Dutch coast (Table 3) the radar signals of Schiphol airport interfered with the DFVLR passive microwave L-band sensor thus spoiling the data set.

Conceivable explanations for the potential of lidar and passive microwave L-band sensors for the discrimination between slicks and spills can be given on the basis of the chemical structures of the respective film-forming compounds: Crude oil always contains aromatic compounds, and as a consequence, an increase in fluorescent signals around 500 nm can be taken for verification. The relative amount of such aromatic compounds may vary in dependence on the origin of the crude oil. High resolution evaluation of lidar data may even shed light on the sort and the origin of crude oils. The present state-of-the-art of this technique is being discussed in this monograph by Zielinski et al. By the way of contrast, in biogenic and nearly all anthropogenic monomolecular sea slicks the content of aromatic and other fluorescent compounds is negligible.

The chemical background of the different signal characteristics of a passive microwave L-band sensor in the presence of slicks and spills was discussed by Hühnerfuss and Alpers (1983). Monomolecular sea slicks induce ice-like clathrate structures within the uppermost water layer thus giving rise to a significant reduction of the relaxation time of water molecules by an order of magnitude, while crude oil represents a layer of completely different dielectric constant. These two different phenomena are being reflected by a decrease in the brightness temperature in the presence of slicks and an increase in the signal in the presence of crude oil spills.

6. References

Alpers W, Hühnerfuss H (1989) The damping of ocean waves by surface films: A new look at an old problem. J Geophys Res 94: 6251-6265

Alpers W, Hühnerfuss H (1988) Radar signatures of oil films floating on the sea surface and the Marangoni effect. J Geophys Res. 93: 3642-3648

Blume H-JC, Hühnerfuss H and Alpers W (1983) Variation of the microwave brightness temperature of sea surfaces covered with mineral and monomolecular oil films. IEEE Trans Geosci Remote Sensing GE-21: 295 - 300

Commission of the European Communities (1985) The Archimedes 1 Experiment. Gillot RH and Toselli F eds. Report **Eur 10216 EN**

Davies JT, Rideal EK (1963) Interfacial Phenomena, Academic Press, New York and London.

Gade M, Alpers W, Bao M and Hühnerfuss H (1996) Measurements of the radar backscattering over different oceanic surface films during the SIR-C/X-SAR campaigns. Proc

Gade M, Alpers W, Hühnerfuss H and Wismann V (1997) Radar signatures of different oceanic surface films measured during the SIR-C/X-SAR missions. Proceed 16th EARSEL Symp, Malta, May 20-23, 1996, p. 233 – 240

Gade M, Alpers W, Hühnerfuss H, Masuko H, Kobayashi T (1998a) Imaging of biogenic and anthropogenic ocean surface films by the multifrequency/multipolarization SIR-C/X-SAR. J Geophys Res 103: 18851 – 18866

Gade M, Alpers W, Hühnerfuss H, Wismann VR, Lange PA (1998b) On the reduction of the radar backscatter by oceanic surface films: scatterometter measurements and their theoretical interpretation. Rem Sens Environ 66: 52 - 70

Gaines, GL (1966) Insoluble Monolayers at Liquid-gas Interfaces, Interscience Publishers/John Wiley & Sons Inc., New York

Gericke A, Hühnerfuss H (1989) Thermal anomalies of the surface potential induced by monomolecular surface films. J Colloid Interface Sci 131: 588-591

Hühnerfuss H., Garrett WD (1981) Experimental sea slicks: their practical applications and utilization for basic studies of air-sea interactions. J Geophys Res 86: 439-447

Hühnerfuss H, Alpers W (1983) Molecular aspects of the system water/monomolecular surface film and the occurrence of a new anomalous dispersion regime at 1.43 GHz. J Phys Chem 87: 5251-5258

Hühnerfuss H (1985) Surface viscosity measurements - a revival of a nearly forgotten surface chemical method ? J Colloid Interface Sci 107: 84 - 95

Hühnerfuss H (1986) The molecular structure of the system water/monomolecular surface film and its influence on water wave damping. Habilitation thesis, University of Hamburg, Hamburg 1986, 245 pp

Hühnerfuss H, Garrett WD and Hoge FE (1986a) The discrimination between crude oil spills and monomolecular sea slicks by an airborne lidar. Int J Remote Sensing **7**: 137 – 150

Hühnerfuss H, Alpers W and Richter K (1986b) On the discrimination between crude oil spills and monomolecular sea slicks by airborne radar and infrared radiometer - possibilities and limitations. Int J Remote Sensing **7**: 1001 – 1013

Hühnerfuss H, Alpers W, Fäst O, Lange PA, Loffet A, Richter K, Schriel RC, Skou N and Witte F (1986c) On the discrimination between crude oil spills and monomolecular sea slicks by airborne remote sensors - todays possibilities and limitations. Proc Intern Geosci Remote Sens Symp (IGARSS `86) Vol III: 1359 – 1364

Hühnerfuss H, Alpers W, Fäst O, Lange PA, Loffet A, Richter K, Schriel RC, Skou , and Witte F (1987) The discrimination between crude oil spills and monomolecular sea slicks by airborne remote sensors. In: *Environment and quality of life. The Archimedes 2 Experiment.* R.H. Gillot ed., Commission of the European Communities, **Eur 11249 EN**: 167 – 177

Hühnerfuss H and Alpers W (1987) On the detection and classification of organic chemical compounds on the sea surface by airborne remote sensors. In: *Proceedings of the 1987 International Colloquium on Remote Sensing of Pollution of the Sea, Oldenburg (FRG).* Reuter R and Gillot RH eds., Commission of the European Communities, **S.P.I. 87.46**: 441 – 455

Hühnerfuss H, Grüner K and Witte F (1990) The discrimination between crude oil and monomolecular sea slicks by microwave sensors. In: *Environment and quality of life. The Archimedes 2A Experiment.* Bekkering JA ed., Commission of the European Communities, **Eur 12674 EN**: 65 - 72

Lange P, Hühnerfuss H (1978) Drift response of monomolecular slicks to wave and wind action. J Phys Oceanogr 8, 142-150

Lange PA, Hühnerfuss H (1984) Horizontal surface tension gradients induced in monolayers by gravity water wave action. J Phys Oceanogr 14: 1620-1628

New chemical insights into the structure and morphology of sea slicks and their geophysical interpretations

Heinrich Hühnerfuss[1], Frank Hoffmann[1], Johannes Simon-Kutscher[1], Werner Alpers[2] and Martin Gade[2]

[1]Institute of Organic Chemistry, University of Hamburg, Hamburg, Germany
[2]Institute of Oceanography, University of Hamburg, Hamburg, Germany

Abstract. The different morphology of palmitic acid methyl ester (PME) slicks spread from *n*-hexane or ethanol was studied by 'Brewster Angle Microscopy' [BAM]. In the latter case, already at large areas per molecule a foam-like structure is being formed on the water surface, i.e., a two-dimensional network which appears to be comparable with the morphological structure of biogenic sea slicks. In line with this assumption, both the magnitudes of the radar backscatter damping ratios and the characteristics of the damping ratio/wave number curves were comparable for the PME slick spread from ethanol and for the biogenic slicks, while in the presence of the PME slick spread from *n*-hexane lower damping ratios were determined. In the first instance, we were able to simulate the water wave damping characteristics of the biogenic sea slicks very well. Furthermore, the relaxation of alkanoic acid esters, which are often being found in biogenic sea slicks, was investigated by 'Infrared Reflection-Absorption Spectroscopy' [IRRAS]. It turned out that the ester group is continuously hydrated and dehydrated during compression and dilation on an undulating water wave field. It can be safely assumed that the strong water wave damping induced by these chemical compounds is centrally related to this phenomenon.

1. Introduction

Thus far, different model substances have been used in the open sea to simulate biogenic sea slicks with the aim of studying their influence on various remote sensing signals (Alpers and Hühnerfuss 1989, Hühnerfuss 1986, Hühnerfuss and Garrett 1981, Hühnerfuss et al. 1982, 1984, 1987). The choice of these chemicals was largely based on their physico-chemical

characteristics and/or their wave damping potential as inferred from wind wave tunnel investigations. In recent experiments during the SIR C/X-SAR campaign, it turned out that the spreading procedure, be it from frozen chunks or be it with the help of spreading solvents, may give rise to significantly different distribution patterns (the so-called „morphology“) on the sea surface and thus to different influences on remote sensing signals.

Morphology effects reflect the phenomenon that the same film-forming compound may be arranged and distributed at the air/water interface in the following different manners:

- The molecules may be spread homogeneously.
- The molecules may form ‘islands’, so-called domains, of different sizes between microns and several hundred microns in diameter (Benvegnu and McConnel 1992).
- The hydrophobic alkyl chains may be arranged vertically with respect to the water surface (i.e., 90°) or at a specific angle of less than 90°. The hydrophobic alkyl chains may exhibit kinks, i.e., the linear arrangement of the alkyl chain is disturbed by irregularities. The head group structure may vary in dependence on the compression status. For more details on these aspects the reader is referred to (Hühnerfuss 1986, Hühnerfuss et al. 1984, 1994).

The clear correlation between morphology effects and remote sensing signals inspired us to perform systematic laboratory investigations on the influence of the spreading procedure on the surface viscosity, the surface potential and on the morphology. The latter aspect, which will be discussed further in this paper, is being studied with the help of ‘Brewster Angle Microscopy’ [BAM], while the molecular structure of the slick/ adjacent water layer system is being investigated by ‘Infrared Reflection-Absorption Spectroscopy’ [IRRAS]. Both methods allow *in situ* investigations of the monolayer at the air water interface without disturbing the structure and morphology of the film. Comparison with scatterometer results obtained over biogenic and man-made sea slicks during the SIR C/X-SAR campaign will illustrate the morphology aspects and their importance for the simulation of biogenic sea slicks.

2. Methods

In the present study, the water surface is being surveyed by two optical methods, i.e., ‘Brewster Angle Microscopy’ [BAM] and ‘Infrared Reflection-Absorption Spectroscopy’ [IRRAS]. A schematic sketch of the BAM

setup is shown in Fig. 1a, while the experimental approach is depicted in Fig. 1b.

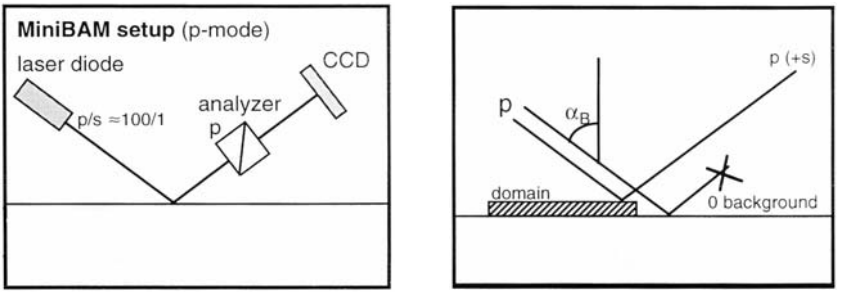

Fig. 1a, left. Schematic sketch of the BAM setup; **1b, right:** Schematic sketch of the experimental approach

If the incidence angle of *p*-polarised radiation is equal to the Brewster angle α_B, the reflectivity from the pure (i.e., slick-free) water surface is close to zero. As a consequence, the water surface appears to be dark. In the presence of a film-forming substance, however, the slick patches represent a different optical medium that gives rise to a measurable reflectivity, which in turn makes the slick domains visible by their lighter appearance. This effect can be recorded by a Charge-Coupled-Device [CCD]-camera.

The infrared reflection-absorption spectroscopy was performed on a Bruker IFS 66 spectrometer (Karlsruhe, Germany) equipped with a MCT detector and a modified external reflection attachment P/N 19650 of SPECAC (Orpington, UK). This included a miniaturized Langmuir-trough, permitting thermostatic measurements. An extensive description of the method can be found in Gericke et al. (1993). The IRRAS set-up as well as the experimental approach can be inferred from the schematic sketch shown in Fig. 2.

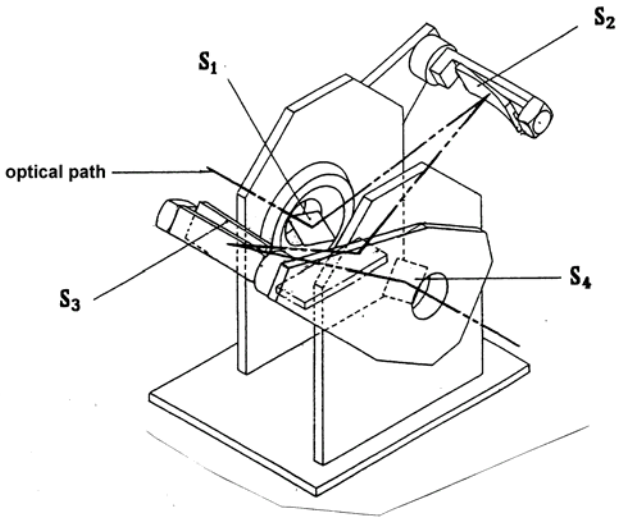

Fig. 2. Schematic sketch of the IRRAS setup: S_1, S_2, S_3, and S_4 are mirrors

3. Results and Discussion

As an illustration of the versatility of BAM, examples of the investigation of two problems will be given:

- the morphology changes during the compression of a slick on an undulating water surface.
- the different morphologies attained by different spreading procedures of slick-forming material.

A sequence of BAM images obtained in the course of compression of a slick consisting of hexadecanoic acid methyl ester (Palmitic acid Methyl Ester = PME) is shown in Figs. 3-5. At large area per molecule, relatively small domains prevail (Fig. 3), which, under compression, combine so that kidney-like shapes are being formed (Figs. 4 and 5). A completely different situation is encountered when the same slick material is being spread from ethanol (Fig. 6). Already at large areas per molecule a foam-like structure is being formed, i.e., a two-dimensional network that is expected to exhibit quite different viscoelastic characteristics compared to those of the morphological structures of the PME film displayed in Figs. 3-5.

The versatility of IRRAS for the *in situ* investigation of slick structures on the air/ water interface is demonstrated in Fig. 7, which summarizes the results of a relaxation experiment: a PME monolayer was generated at a water surface and then compressed to 0.272 nm^2/molecule. In the course of

the compression procedure, some disorder is induced within the monolayer. After stopping the compression, the molecules tend to arrange themselves such that an optimum order of the alkyl chains and of the head groups is attained. This is largely the relaxation process that is also encountered on a slick-covered undulating water surface. With regard to the PME films, it is well-documented [4] that the ester head group performs a "flip-flop"-like change in its orientation (the so-called *E/Z*-isomerisation). As a consequence, the head group is prevented from hydration by the adjacent water layer during compression of the monolayer, and, *vice*

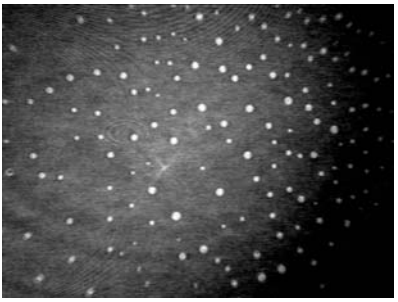

Fig. 3. Morphology of a PME-film spread of *n*-hexane as determined by BAM; compression status 0.34 nm^2/molecule; 1 mm = 100 μm

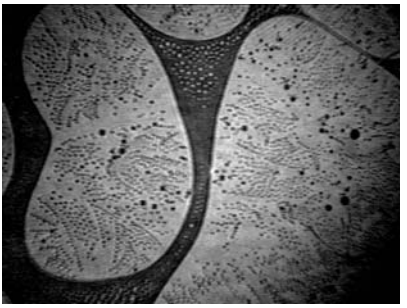

Fig. 4. Same as Fig. 3, but compression status 0.24 nm^2/molecule

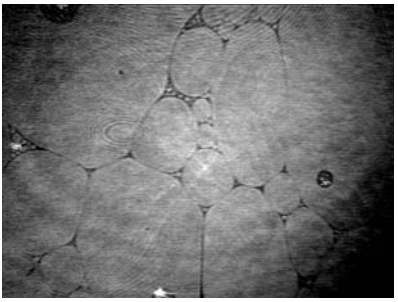

Fig. 5. Same as Fig. 3, but compression status 0.20 nm^2/ molecule

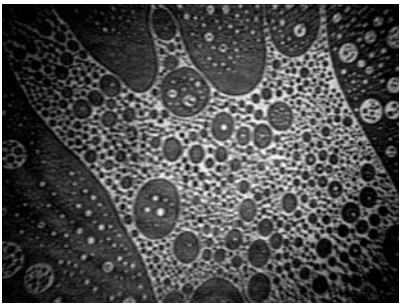

Fig. 6: Morphology of a PME-film spread of ethanol as determined by BAM; compression status 0.415 nm^2/ molecule; 1 mm = 100 μm

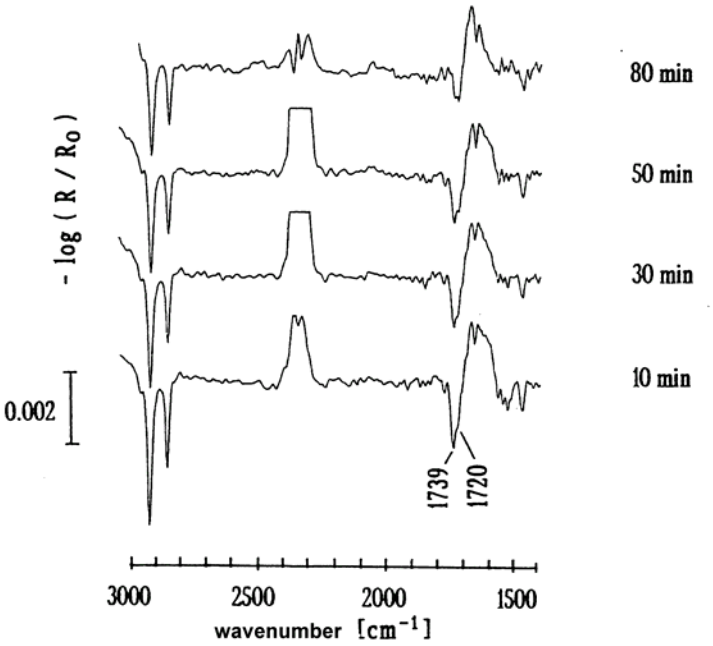

Fig. 7. IR reflection-absorption spectra for a PME slick at the air/water interface after compression to 0.272 nm^2/molecule and subsequent relaxation, from bottom to top after 10, 30, 50, and 80 min, respectively

versa, accessible to water molecules during dilation of the film. The same hydration effect can also be observed during the increasing ordering of the film molecules, i.e., a higher order means more space per molecule and thus an increased possibility for a hydration of the head group. This phenomenon can be followed by IRRAS: In the spectra shown in Fig. 7, a strong band is observed at 1739 cm^{-1} directly after spreading and also 10 min thereafter. This band represents the C=O vibration of an unhydrated carbonyl group. In the course of the relaxation procedure (Fig. 7, $t > 10$ min), a second band appears at 1720 cm^{-1} which indicates the C=O vibration of a hydrated carbonyl group. This results shows that alkanoic acid esters, which are often being found in biogenic sea slicks, are continuously hydrated and dehydrated during compression and dilation on an undulating water wave field. It can be safely assumed that the strong wave damping effect of these compounds is centrally related to this phenomenon.

With the aim of simulating biogenic sea slicks, we generated PME slicks at the sea surface by distributing the film-forming material with the help of different spreading solvents, i.e., by the application of ethanol or *n*-hexane. These man-made sea slicks were overflown by a helicopter carry-

ing a five-frequency multi-polarization radar scatterometer, the so-called HELISCAT of the University of Hamburg. During the same flight, we also overflew biogenic sea slicks, which had been forming sufficiently close to this sea area, under the same meteorological and oceanographic conditions. It turned out that both the magnitudes of the damping ratios as well as the characteristics of the damping ratio/wave number curves determined for the PME slick spread from ethanol (Fig. 8) and for the biogenic slicks (Fig. 9) were very comparable, while in the presence of the PME slick spread from *n*-hexane lower damping ratios were determined.

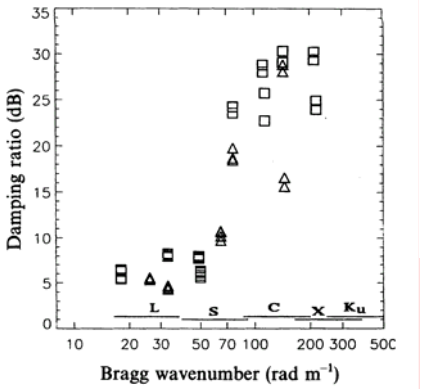

Fig. 8. Damping ratio, i.e., reduction of the backscattered radar power (in dB) induced by a PME slick, which was spread from ethanol, as a function of the Bragg wave-number. The measurements were performed at *L*-, *S*-, *C*-, *X*-, and K_u-band using both *VV*- and *HH*-polarisations (up- [tri-angles] and downwind [squares] look directions)

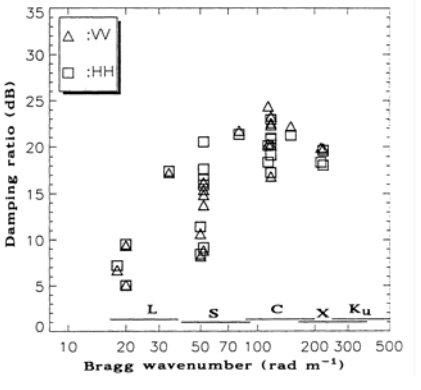

Fig. 9. Damping ratio, i.e., reduction of the backscattered radar power (in dB) induced by natural sea slicks, as a function of the Bragg wave number. The measurements were performed at *L*-, *S*-, *C*-, *X*-, and K_u-band using both *VV*- [triangles] and *HH*-polarisations [squares]

Obviously, we were able to simulate the water wave damping characteristics of the biogenic sea slicks, in this case largely secreted from *phaeocystis globosa*, as well as their influence on backscattered radar signals very exactly by spreading PME from ethanol. This result is conceivable, because biogenic slicks are being formed from microdroplets that are secreted by plankton, i.e., many tiny point sources will appear at the sea surface, if the wind speed and thus the turbulence of the upper water layer will be sufficiently reduced, say below about 7 m/s wind velocity. Furthermore, many alkanoic acid esters have been found in biogenic sea slicks,

i.e., chemical compounds exhibiting structures very similar to PME. Therefore, it can be safely assumed that very comparable morphological structures are prevailing in biogenic sea slicks and in PME slicks spread from ethanol.

4. References

Alpers W and Hühnerfuss H (1989) The damping of ocean waves by surface films: a new look at an old problem. J Geophys Res 94: 6251-6265

Benvegnu DJ and McConnell HM (1992) Line tension between liquid domains in lipid monolayers. J Phys Chem 96: 6820-6824

Gericke A, Michailov AV, and Hühnerfuss H (1993) Polarized external infrared reflection-absorption spectroscopy at the air/water interface: comparison of experimental and theoretical results for different angles of incidence. Vib Spectroscop 4: 335-348

Hühnerfuss H and Garrett WD (1981) Experimental sea slicks: their practical applications and utilization for basic studies of air-sea interactions. J Geophys Res 86: 439-447

Hühnerfuss H, Lange P, and Walter W (1982) Wave damping by monomolecular surface films and their chemical structure. Part I: Variation of the hydrophobic part of carboxylic acid esters. J Mar Res 40: 209-225

Hühnerfuss H, Lange P, and Walter W (1984) Wave damping by monomolecular surface films and their chemical structure. Part II: Variation of the hydrophilic part of the film molecules inluding natural substances. J Mar Res 42: 737-759

Hühnerfuss H (1986) The molecular structure of the system water/monomolecular surface film and its influence on water wave damping, Habilitationsschrift, Fachbereich Chemie, Universität Hamburg, Germany

Hühnerfuss H, Walter W, Lange PA, and Alpers W (1987) Attenuation of wind waves by monomolecular sea slicks and the Marangoni effect. J Geophys Res 92: 3961-3963

Hühnerfuss H, Gericke A, Alpers W, Theis R, Wismann V, and Lange PA (1994) Classification of sea slicks by multifrequency radar techniques: new chemical insights and their geophysical implications. J Geophys Res 99: 9835-9845

Hühnerfuss H, Alpers W, Dannhauer H, Gade M, Lange PA, Neumann V, and Wismann V (1996) Natural and man-made sea slicks in the North Sea investigated by a helicopter-borne 5-frequency radar scatterometer. Int J Remote Sensing 17, 1567-1582

Sea slicks: variability in chemical composition and surface elasticity

Nelson M. Frew, Robert K. Nelson and Carl G. Johnson

Department of Marine Chemistry and Geochemistry, Woods Hole Oceanographic Institution, Woods Hole, USA

Abstract. Surface-active organic matter collected from the air-sea interface is examined using mass spectrometry. The mass spectra reveal significant spatio-temporal variability in the chemical composition of sea slick materials. This compositional variability leads to differences in observed surface pressure-elasticity relationships.

1. Introduction

Biogenous marine surfactant films or sea slicks play a significant role in modulating physical exchange processes across the air-sea interface, including mass, heat, and momentum transfer (Herr and Williams 1986). Sea slicks are prominent features in microwave imagery of the ocean surface (Vesecky and Stewart 1982, Hühnerfuss et al. 1983, 1994, Alpers et al. 1982, Alpers and Hühnerfuss 1989, Gade et al. 1998, Marmorino et al. 1998) since they modulate the spectral density of centrimetric-scale waves *via* the Marangoni effect (Bock and Mann 1989). The intensity of the modulation of these processes depends on the elasticity of the film-influenced sea surface and, therefore, on film surface concentration and specific chemical composition. The occurrence, spatial distribution, concentration and composition of sea surface films, however, are not well known (Williams et al. 1985, Romano 1996, Frew 1997, Gašparović et al. 1998, Frew and Nelson 1999).

Sources of surface-active organic matter (SAOM) are varied and include primarily phytoplankton, zooplankton and their degradation products (Zutic et al. 1981, Williams et al. 1985, Henrichs and Williams 1985), but also marine bacteria (Sieburth et al. 1976, Hardy 1982, Carlucci et al. 1985, Van Vleet and Williams 1983), rivers and estuaries (both natural and anthropogenic organic matter) and atmospheric volatiles and dust (Peltzer and Gagosian 1989). Sea surface films are, therefore, complex mixtures of

surface-active compounds spanning a wide range of polarity, molecular weight and chemical structure (Frew and Nelson 1992a,b). As multicomponent systems, microlayer films exhibit a more complex rheological response to surface straining than monolayers of single pure compounds (Bock and Frew 1993, Krägel et al.1995, Kozarac et al. 2000).

This paper discusses studies of sea surface films observed and collected in the southern California Bight and the U. S. Middle Atlantic Bight. The goals of these studies were to understand the relationship between chemical composition and surface elasticity in these complex natural films and to determine the range of surface elasticity typical of the ocean surface. Mass spectrometry was the principal analytical tool because of its capacity to characterise and identify chemical structures for many compound classes and to provide a quick assessment of compounds enriched in sea surface films. We present typical variations in SAOM chemical composition as reflected in mass spectral patterns and show the effect of these compositional variations on the film elasticity.

2. Methodology

2.1. Microlayer Sampling and Extraction

The sea surface microlayer was sampled with a surface skimmer of a design similar to that of Carlson et al. (1988). The sampler consisted of a partially submerged, rotating glass cylinder supported by a small catamaran. The rotating cylinder collected a thin layer of water (40-60 μm thickness) by viscous retention. The theoretical basis for the sampling mechanism was described by Levich (1962) and verified experimentally by Cinbis (1992). The sampler was used to collect large volume (20 L) samples of the microlayer and subsurface water (10 cm nominal depth). The SAOM was extracted from microlayer and bulk seawater samples using bubble adsorption in a foam tower apparatus (Wallace et al. 1972). Briefly, samples were filtered through pre-combusted Whatman glass fiber filters (GF/F 1 μm nominal pore size) under low nitrogen pressure to remove particulate matter and organisms; 6.5 L of the filtered samples were then loaded into the foam tower. A plume of ultrahigh purity nitrogen bubbles generated by a frit in the tower base was used to adsorb and strip surfactants from the large volume samples, producing a surfactant-enriched foam that was collected at the top of the apparatus. The concentrated SAOM in the foam was then fractionated by extraction into a series of increasingly polar solvents to provide three SAOM fractions designated F1 (1:1 *n*-hexane/dichloromethane), F2 (2:1 trichloromethane/methanol) and F3 (10:9:1

trichloromethane/methanol/methanoic acid). The resulting fractions were used to explore the effects of changing composition on surface elasticity. SAOM was also isolated using a solid phase extraction technique described in Frew and Nelson (1992a) in which samples were acidified to pH 5.0 and pumped through SepPak-Plus tC_{18} cartridges (Waters Associates, Milford, Massachusetts) to remove SAOM. The cartridges were then rinsed with distilled water and the adsorbed surfactants were eluted with methanol. All extracts were stored at -40 °C until analysed.

2.2. Mass Spectrometric Analysis

Sample extracts were analysed in triplicate by desorption-electron ionisation (DEI) mass spectrometry (Boon 1992). Data were acquired on a Micromass Autospec-Q hybrid mass spectrometer equipped with a low energy electron ionisation source and a modified direct chemical ionisation probe. The original wire desorption coil on the probe was replaced by a 1.5 turn, 1 mm diameter loop of 0.005" platinum wire. Aliquots (1-5 μL) of the extracts containing ~1 μg dry weight SAOM were applied to the loop and allowed to dry before inserting the probe into the mass spectrometer ion source. Samples were desorbed by resistively heating the platinum loop with current programming from 0.0 to 1.5 A at a rate of 1.0 A min^{-1}. The ion source was operated at 185 °C with 16 eV electron ionisation and 8 kV acceleration voltage and was tuned only to nominal resolution. The magnet was scanned from 800 to 40 Da at 1.15 sec $decade^{-1}$ and data were acquired in centroid mode. The resulting mass spectra represented the composite signal from desorbed volatile components and pyrolysed (thermally dissociated) involatile polymeric components.

2.3. Film Elasticity Measurements

Elasticities were estimated quasi-statically from surface pressure-area (Π/A) isotherm measurements in a KSV 2200 Langmuir film balance (Frew and Nelson 1992a). Aliquots of film extracts containing ~20 μg of SAOM were uniformly spread on clean seawater at pH 8.1 ± 0.2. The seawater substrate was Sargasso seawater (1000 m depth) that had previously been stripped of surfactants in the foam tower; the substrate exhibited low surface activity and generally gave surface pressure readings comparable to high purity distilled water blanks ($\leq$0.25 mN m^{-1}) at maximum compression. The SAOM film was allowed to stabilize for 20 minutes and then compressed at a rate of 50 mm min^{-1} from an initial surface area of 725 cm^2 to a final area of 58 cm^2. Instrument sensitivity was ±10 μN m^{-1}; the

estimated maximum uncertainties in film pressure (Π) and static elasticity ($\varepsilon_o = - d\Pi/d\ln A$) were ± 0.4 mN m^{-1} and ± 0.9 mN m^{-1}, respectively.

3. Results and Discussion

Coherent slicks were observed in both coastal and oligotrophic waters under low to moderate wind stress conditions, indicating that sufficient surface-active organic material was usually present to form localised surface features whenever organised water motions were favourable for concentrating organic material at the surface. Wind stress and subsurface water motions play a strong role in controlling the degree of enrichment of the surfactant classes that dominate microlayer surface elasticity (Moum et al. 1990, Bock and Frew 1993). Thus, the spatial distribution of surface film enrichments can be extremely 'patchy' or inhomogeneous (Frew et al. 2002). Mass spectrometry provided the means to visualise these variations in enrichment. The DEI-MS spectra of foam extracts (fraction F2) of a slicked surface microlayer and a bulk seawater sample collected at a station in oligotrophic waters (35° 24' N; 73° 41' W) are compared in Figure 1. Differences in mixture composition are evident from a comparison of the relative intensities at each mass-to-charge ratio (*m/z*) in the spectra. Specific surface-active lipids, including fatty acids (*e.g. m/z* 256, 270, 284), sterols and other tetracyclic/pentacylic lipids (*m/z* 370-470) and β-carotene (*m/z* 536) are relatively enriched in the microlayer spectrum. Highly oxygenated surfactant compounds similar to synthetic poloxamers (*m/z* 58, 59, 160, 161, 333) are relatively more abundant in the spectrum of the subsurface sample, although the absolute concentrations (not shown) are lower in the subsurface water than in the microlayer. Less prominent in the spectra of both samples are mass fragments that arise from pyrolysis (thermal dissociation) of peptide, protein and carbohydrate components, and a background of degraded polymeric (humic) materials. Additional analyses using electrospray ionisation mass spectrometry indicated that the bulk of the surface-active materials in these samples exhibit molecular weights below 2000 Da, with a maximum abundance in the 700-1000 Da range.

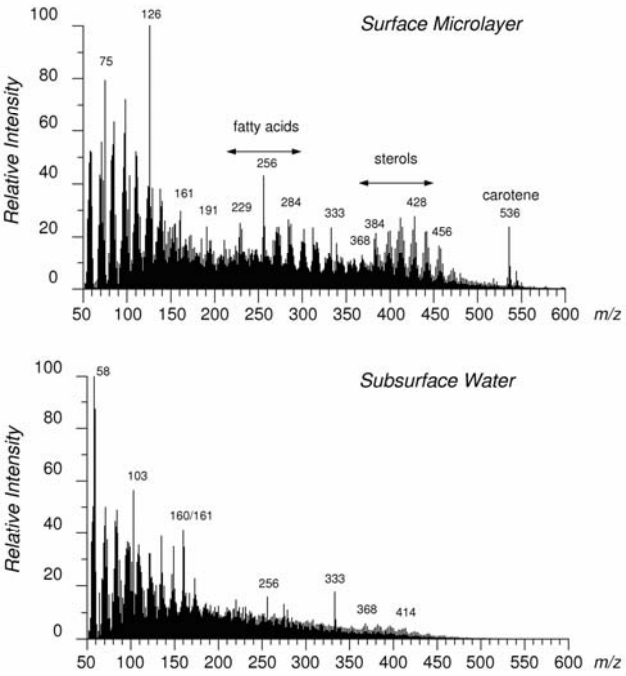

Fig. 1. Comparison of DEI-MS spectra of a marine microlayer F2 foam extract (2:1 v/v trichloromethane-methanol) with that of the underlying seawater. The spectra highlight the microlayer enrichments of several classes of lipid compounds, including fatty acids, sterols and carotenoids

The mass spectra indicated that some compound classes tended to become enriched in the microlayer regardless of spatial considerations (perhaps reflecting autochthonous marine sources), while enrichment of other compound classes depended strongly on distance offshore (reflecting terrigenous sources). In certain cases, systematic variations in microlayer composition were observed along cruise transects due to changing organic matter composition in the underlying bulk water. In the Middle Atlantic Bight, for example, bulk seawater concentrations of coloured dissolved organic matter (primarily terrigenous humic materials) decreased roughly 20-fold from the Delaware River estuary to the continental slope. The signature of this humic material in the microlayer mass spectra also decreased strongly with distance from the estuary. Figure 2 presents a sequence of mass spectra of microlayer SAOM (SepPak isolates) from three stations, progressing south-eastward from Delaware Bay across the continental shelf. The spectrum for the sample at 37.85 °N 74.90 °W, which was within the Delaware River plume, was dominated by a broad background of fragments at every

m/z value, characteristic of pyrolysis spectra of coloured humic materials (Little and Jacobus 1985). This background decreased rapidly and other individual components became prominent in the spectra with increasing distance offshore.

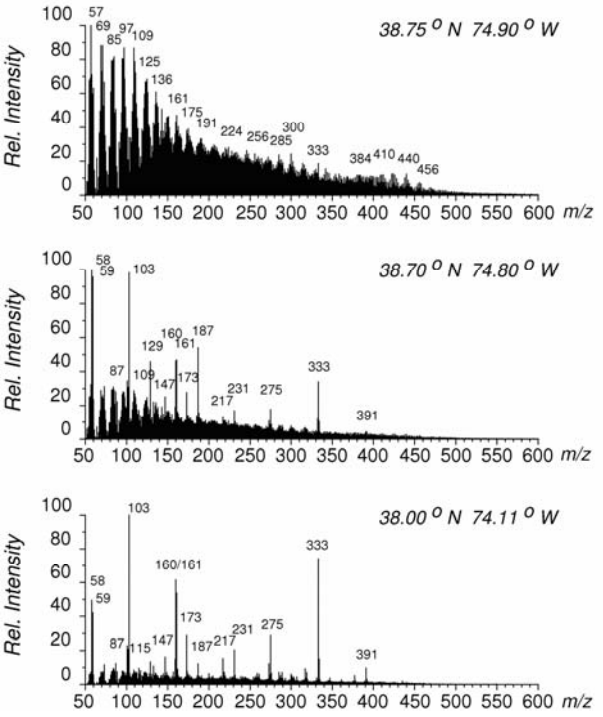

Fig. 2. Variations in surface microlayer chemical composition as shown by DEI-MS spectra for three microlayers (SepPak eluates) collected along a cruise track from Delaware Bay south-eastward across the continental shelf. Spectral intensities are normalised to the most abundant *m/z* intensity. The spectrum of the sample in the upper panel, which was collected within the Delaware River plume, is dominated by the presence of humic compounds that characteristically pyrolyse to produce mass fragments at every *m/z* value. The contribution from humic materials decreases markedly with distance from the estuary

Qualitatively, the Middle Atlantic Bight samples were very similar to those collected in the California Bight. The predominant components were the same in both locales, suggesting that a limited number of compound classes are dominant in microlayer films, but present in varying proportions. The specific mixtures of surfactants in the microlayers sampled in this study strongly influenced air-sea interfacial quasi-static elasticity. Pre-

vious field work comparing small-scale wave spectra in slicked and unslicked regions (Bock and Frew 1993) has suggested that sea-surface films exhibit a complex surface response to compressional-dilational straining, dependent on chemical composition. In this work we used static elasticity as representative of dynamic elasticity, recognising that *in situ* measurements of dynamic elasticity, although preferable, were not feasible. Recent laboratory work on the dynamic behaviour of sea surface films (Mass and Milgram 1998) suggests that static elasticities predict dynamic elasticities accurately, since the time scales for interfacial exchange processes are long relative to the time scales for surface straining by capillary waves. The strong influence of chemical composition on interfacial elasticity is illustrated by comparing mass spectra of selected samples with their respective ε_o-Π characteristics. The mass spectra of three surfactant mixtures isolated by bubble adsorption and *n*-hexane/dichloromethane extraction (fraction F1) from (1) a surface bulk water sample, (2) an unslicked microlayer, and (3) a heavily slicked microlayer are presented in Figure 3. The mass spectrum of the bulk seawater sample is dominated by intense ions from only a few compounds, whose structures we have shown to be similar to poloxamers (mixed ethylene oxide-propylene oxide copolymers), most likely of anthropogenic origin. In the spectrum of the visibly unslicked microlayer, additional low intensity ions are observed in the *m/z* 80-150, 200-300, and *m/z* 350-470 regions, representing the presence of small amounts of adsorbed lipid materials, primarily free and bound fatty acids, steroids, and terpenoids, along with the poloxamers. The spectrum of the third sample indicates that these lipid components, seen in minor amounts in the unslicked microlayer, are heavily enriched in the slicked microlayer relative to the poloxamers. The effect of this changing composition on interfacial elasticity is shown in Figure 4, in which measured static surface elasticities are plotted as a function of film surface pressure for the same three samples. Film balance measurements of surface elasticities of films composed of poloxamers isolated from coastal seawater and purified by gas chromatography have shown that these compounds have intrinsically low elasticity at a given surface pressure. This is reflected in Figure 4 by the ε_o *vs.* Π curve for the bulk water sample, which exhibited the lowest elasticity as a function of film pressure. Increasing amounts of the lipid components in the microlayer samples had a measurable effect on surface elasticity, increasing it up to a factor of four in the most concentrated slicks.

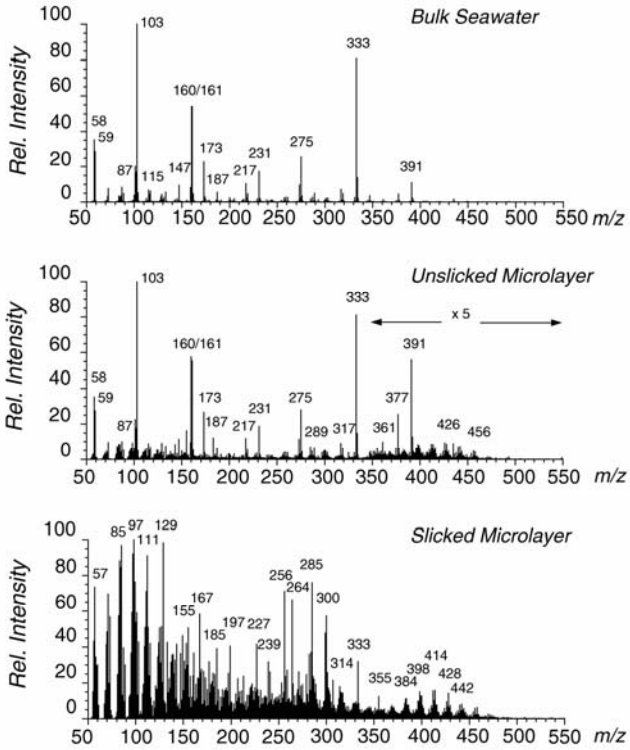

Fig. 3. Examples of mass spectra of *n*-hexane/dichloromethane (F1) extractable surfactants isolated by foam tower stripping from a bulk surface seawater sample (upper), an unslicked microlayer (centre), and a heavily slicked microlayer (lower). The spectra show the dominance of polyoxy components in the bulk seawater surfactants and different degrees of enrichment of more hydrophobic lipid surfactants in the microlayer. Note that these particular spectra were chosen to illustrate the range of composition observed and the impact on surface elasticity (see Figure 4), not to represent bulk seawater, unslicked and slicked microlayers generally

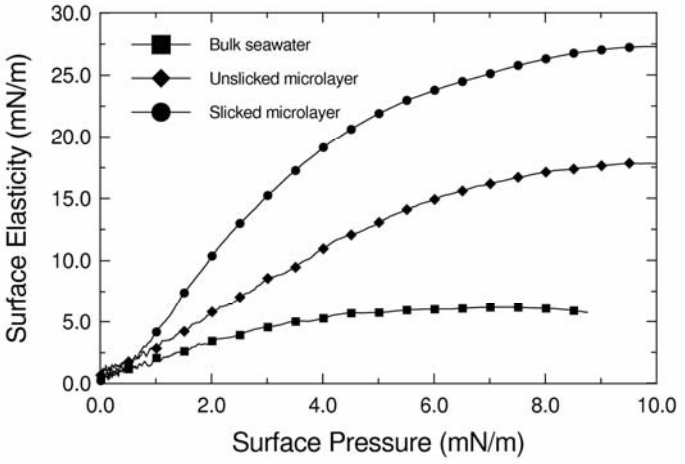

Fig. 4. The variation of static surface elasticity (ε_o) with surface pressure (Π) for air-seawater interfacial films with compositions corresponding to the F1 extracts and mass spectra of Figure 3. The highest elasticities at a given film surface pressure were observed for films dominated by lipid surfactants; lowest elasticities were observed for films dominated by polyoxy surfactants

4. Summary

Surface microlayer films sampled in both coastal and oligotrophic waters exhibited variable enrichments of surface-active compounds, including lipids, biological and synthetic polymers, and humic materials. The relative proportions of these compound classes in the films were shown to influence the overall film elasticity. Although the elasticity measurements in this study were carried out on surface films reconstructed from artificially fractionated film materials, the observed elastic moduli were very similar to those reported for spontaneous films formed from unfractionated seawater (Barger and Klusty, cited in Peltzer et al. 1992); the latter exhibited maximum elastic moduli of ~26 mN m^{-1} at surface pressures <10 mN m^{-1}. In some of the few dynamic elasticity estimates made *in situ*, Lombardini et al. (1989) reported elasticities generally ranging from 10 to 25 mN m^{-1}. They also suggested that variations in elasticity were caused by varying proportions of water-soluble and water-insoluble surfactants, based on parametric fits to a wave damping model. Thus, it is likely that elasticity variations are coupled to compositional differences in films *in situ*.

Acknowledgments. This research was sponsored by the U. S. Office of Naval Research under grants N00014-94-1400 and N00014-98-10593. We also thank the officers and crews of the R/V Cape Henlopen and R/V New Horizon for their cooperation in meeting our sampling needs during their respective cruises.

5. References

Alpers W, Hühnerfuss H (1989) The damping of ocean waves by surface films: a new look at an old problem. J Geophys Res 94: 6251-6265

Alpers W, Blume H-J, Garrett WD, Hühnerfuss H (1982) The effect of monomolecular surface films on the microwave brightness temperature of the sea surface. Int J Remote Sensing 3: 457-474

Bock EJ, Frew NM (1993) Static and dynamic response of natural multicomponent oceanic surface films to compression and dilation: laboratory and field observations. J Geophys Res 98: 4599-14617

Bock EJ, Mann JA, Jr. (1989) On ripple dynamics. II. A corrected dispersion relation for surface waves in the presence of surface elasticity. J Colloid Interface Sci. 129: 501-505

Boon, J (1992) Analytical pyrolysis mass spectrometry: new vistas open by temperature-resolved in-source PYMS. Int J Mass Spectrometry and Ion Processes 118/119: 55-787

Carlson DJ, Canty JL, Cullen JJ (1988) Description of and results from a new surface microlayer sampling device. Deep-Sea Res35: 205-1212

Carlucci, AF, Craven DB, Henrichs SM (1985) Surface film microheterotrophs: amino acid metabolism and solar radiation effects on their activities. Mar Biol 85: 3-22

Cinbis, C (1992) Non-contacting techniques for measuring surface tension of liquids. Ph. D. Dissertation, Stanford University, EL Ginzton Laboratory Report No. 4931

Frew, NM (1997) The role of organic films in air-sea gas exchange. In: Liss P, Duce R (eds) The Sea Surface and Global Change, Cambridge University Press, Cambridge, pp. 121-172

Frew, NM, Nelson RK (1992a) Isolation of marine microlayer film surfactants for ex situ study of their surface physical and chemical properties. J Geophys Res 97 5281-5290

Frew, NM, Nelson RK (1992b) Scaling of marine microlayer film surface pressure-area isotherms using chemical attributes. J. Geophys. Res. 97:5291-5300

Frew, NM, Nelson RK (1999) Spatial mapping of sea surface microlayer surfactant concentration and composition. In: T.I. Stein (ed) Proceedings of the 1999 International Geoscience and Remote Sensing Symposium, IEEE Publications, Piscataway, pp. 1472-1474

Frew, NM, Nelson RK, McGillis WR, Edson JB, Bock EJ, Hara T (2002) Spatial variations in surface microlayer surfactants and their role in modulating air-

sea exchange. In: Gas Transfer at Water Surfaces, Geophysical Monograph Series, 127, AGU, Washington, DC, pp. 153-159

Gade, M, Alpers W, Hühnerfuss H, Wismann V, Lange PA (1998) On the reduction of the radar backscatter by oceanic surface films: scatterometer measurements and their theoretical interpretation. Remote Sens Environ 66: 52-70

Gašparović, B, Kozarac Z, Saliot A, Ćosović B, Möbius D. Physicochemical characterization of natural and ex-situ reconstructed sea-surface microlayers. J Colloid Interface Sci 208: 191-202

Hardy, JT (1982) The sea surface microlayer: biology, chemistry and anthropogenic enrichment. Prog Oceanog 141: 307-328

Henrichs, SM, Williams PM (1985) Dissolved and particulate amino acids and carbohydrates in the sea surface microlayer. Mar. Chem 17: 141-163

Herr FL, Williams J (eds) (1986) ONRL Workshop Proceedings – Role of Surfactant Films on the Interfacial Properties of the Sea Surface, ONRL Report C-11-86, U.S. Office of Naval Research, London

Hühnerfuss H, Alpers W, Cross A, Garrett WD, Keller WC, Lange PA, Plant WJ, Schulde F (1983) The modification of X and L band radar signals by monomolecular sea slicks. J Geophys Res 88: 9817-9822

Hühnerfuss H, Gericke A, Alpers W, Theis R, Wismann V, Lange PA (1994) Classification of sea slicks by multifrequency radar techniques: new chemical insights and their geophysical implications. J Geophys Res 99: 9835-9845

Levich VG (1962) Physico-Chemical Hydrodynamics, Prentice-Hall International, Englewood Cliffs

Lombardini PP, Fiscella B, Trivero P, Cappa C, Garrett WD (1989) Modulation of the spectra of short gravity waves by sea surface films: slick detection and characterization with a microwave probe. J Atmos Oceanic Technol 6: 882-890

Little B, Jacobus J (1985) A comparison of two techniques for the isolation of dissolved organic material from seawater. Org Geochem 8: 27-33

Marmorino GO, Lyzenga DR, Kaiser JAC (1998) Comparison of airborne synthetic aperture radar imagery with in-situ surface slope measurements across Gulf Stream slicks and a convergent front. J Geophys Res 104: 1405-1422

Mass JT, Milgram JH (1998) Dynamic behavior of natural sea surfactant films. J Geophys Res 103: 15695-15715

Moum JN, Carlson DJ, Cowles TJ (1990) Sea slicks and surface strain. Deep-Sea Res 37: 767-775

Peltzer ET, Gagosian RB (1989) Organic geochemistry of aerosols over the Pacific Ocean. In: Duce RA (guest ed) Riley JP, Chester R, (eds) Chemical Oceanography, 10, Academic Press, London, pp. 281-228

Peltzer RD, Griffin OM, Barger WR, Kaiser JAC (1992) High-resolution measurement of surface-active film redistribution in ship wakes. J Geophys Res 97: 5231-5252

Romano J-C (1996) Sea-surface slick occurrence in the open sea (Mediterranean, Red Sea, Indian Ocean) in relation to wind speed. Deep-Sea Res 43: 411-423

Sieburth J McN, Willis PJ, Johnson KM, Burney CM, Lavoie DM, Hinga KR, Caron DA, French III FW, Johnson PW, Davis PG (1976) Dissolved organic

matter and heterotrophic microneuston in the surface microlayers of the North Atlantic. Science 194: 1415-1418

Van Vleet ES, Williams PM (1983) Surface potential and film pressure measurements in seawater systems. Limnol Oceanogr 28: 401-414

Vesecky JF, Stewart RH (1982) The observation of ocean surface phenomena using imagery from the Seasat synthetic aperture radar: an assessment. J Geophys Res 87: 3397-3430

Wallace GT, Loeb GI, Wilson DF (1972) On the flotation of particulates in sea water by rising bubbles. J Geophys Res 77: 5293-5301

Williams PM, Carlucci AF, Henrichs SM, Van Vleet ES, Horrigan SG, H. Reid FM, Robertson KJ (1985) Chemical and microbiological studies of sea-surface films in the southern Gulf of California and off the west coast of Baja California. Mar. Chem. 19: 17-98

Zutic VB, Cosovic B, Marcenko E, Bihari N (1981) Surfactant production by marine phytoplankton. Mar Chem 10: 505-20

Correlation studies of mass spectral patterns and elasticity of sea-slick materials

Nelson M. Frew, Robert K. Nelson and Carl G. Johnson

Department of Marine Chemistry and Geochemistry, Woods Hole Oceanographic Institution, Woods Hole, USA

Abstract. Variations in the chemical composition of surfactants from natural sea slicks are compared to variations in surface elasticity using mass spectrometry, Langmuir film balance measurements, and multivariate statistical techniques. It is shown that the information on chemical class and molecular structure contained in the mass spectra is strongly correlated with measured static elasticity and can be used to estimate film elasticity at a given surface pressure.

1. Introduction

The surface physical properties of a surfactant are strongly dependent on molecular structure (Gaines 1966). As multicomponent systems, microlayer films exhibit a more complex rheological response to surface straining than monolayers of single pure compounds (Bock and Frew 1993). Since the composition of these mixed films is too complex to allow rigorous modelling of surface rheology based on individual component properties, an empirical approach is suggested. The mass spectral fingerprints of sea-slick materials may contain information not only about chemical composition and molecular structure, but also the surface elasticity. Thus, it may be possible to use the mass spectra of microlayer organics not only to identify the structural classes that control elasticity but also to predict elasticity. We explore this hypothesis by applying chemometric techniques to the mass spectra. We show, through the use of multivariate analysis, the effect of these compositional variations on the film elasticity.

2. Methodology

The mass spectral data selected for multivariate analysis represented a suite of 30 microlayer and bulk surface seawater surfactant samples (fraction F1; Frew et al. (2006)) including seven from waters off Monterey and Santa Barbara, California and 23 collected along a transect from Delaware Bay on the U. S. east coast to the Sargasso Sea. Sample extracts were analysed in triplicate by desorption-electron ionisation (DEI) mass spectrometry (Boon 1992; Frew et al. 2006). Individual DEI mass scans were summed over the full desorption/pyrolysis interval, reduced to integer masses, and averaged for processing by multivariate analysis. Elasticities were estimated quasi-statically from surface pressure-area (Π/A) isotherm measurements in a KSV 2200 Langmuir film balance (Frew et al. 2006). The elasticity data were subsampled at fixed surface pressure intervals (0.5 mN m^{-1}) for comparison with the results of the multivariate analysis.

Linear discriminant analysis (LDA) was applied to the resulting 90 mass spectra using a MATLAB-based (MATLAB™, The Mathworks, Inc., Natick, Massachusetts) chemometrics routine 'Chemometricks' (developed at FOM-AMOLF, Amsterdam; www.amolf.nl). This LDA routine was implemented using a two-step principal component analysis (Hoogerbruge et al. 1983) that reduced the number of variables relative to the number of classes. Classes were defined in two ways: by allowing each set of sample replicates to represent one class, yielding 30 classes, or by arbitrarily binning samples with similar elasticity values at Π = 6.5 mN m^{-1}. The seven classes resulting from the latter method are listed in Table 1. Discriminant functions were then developed that minimised and maximised the within-class and between-class variance (Windig et al. 1983) respectively, and the discriminant function scores for each spectrum were evaluated. The possible relationship between the mass spectral patterns and elasticity was then evaluated by computing the correlation matrix for the static surface elasticities measured for each surface film at each surface pressure interval and the corresponding discriminant scores, resulting in linear relations between elasticity and discriminant score for each surface pressure interval. A quantitative description of microlayer films covering different dynamic and physical conditions in a variety of geographic and productivity regimes was thus developed. In this initial report, LDA results are presented for fraction F1 extracts only. Similar LDA analyses of fractions F2, F3 and the SepPak isolates from this sample suite are in progress and will be reported elsewhere.

Table 1. Seven elasticity classes obtained by binning samples with similar elasticity at $\Pi = 6.5$ mN m^{-1}

	Elasticity Class						
Class ID	***1***	***2***	***3***	***4***	***5***	***6***	***7***
Bin elasticity range (mN m^{-1})	6.1 -7.7	8.5 -9.4	9.6 -10.6	11.2-13.5	14.7 -15.6	21.2	24.5 -26.1
# Samples in class *	18	12	15	21	9	3	12
Mean elasticity for class (mN m^{-1})	7.2 ±0.7	8.9 ±0.3	10.3 ±0.4	12.2 ±0.9	15.2 ±0.5	21.2	25.6 ±0.8
Mean D1 Score for class	-0.097	-0.063	-0.056	-0.013	+0.040	+0.199	+0.222
Std. deviation of D1 score for class	±0.001	±0.019	±0.006	±0.007	±0.007	n. a.	±0.003

*Individual mass spectrum/elasticity pairs

3. Results and Discussion

The Chemometricks analysis developed discriminant functions that distinguished each sample or sample class from every other based on the principal mass components of the spectra. Applied to individual spectra, the discriminant functions yielded a function score that reflected the abundance of those chemical components in the sample mixture that distinguished the sample or class from the others. Experimentally measured static elasticities for the samples were then compared with the discriminant scores to determine the degree of correlation between the spectral patterns and surface elasticity.

In Figures 1-3, we present the results of the LDA analysis of the 30 F1 surfactant extracts for the case where classes were defined by binned elasticity. Trends were roughly similar whether the spectral classes were defined by replicates or by binned elasticity value. The Chemometricks algorithm was not given any information about the elasticity values other than which samples exhibited similar elasticities at a fixed surface pressure, yet

the analysis demonstrated that variations in the mass spectra were systematically and strongly correlated with observed variations in elasticity. The five top-ranked discriminant functions (D1-D5) explained roughly 41% of the between-class spectral variance. It was found that elasticities were most strongly correlated with the scores of the first-ranked discriminant D1 (Table 1). The graphical representation of D1 is given in Figure 1. This discriminant represented 30 % of the variance in the original spectral data and had a between-class to within-class variance ratio of 110. The discriminant function is shown as a reconstructed mass spectrum with both positive and negative sides, where the intensities represent the loadings for each particular mass-to-charge ratio (*m/z*) used to calculate scores from individual sample spectra.

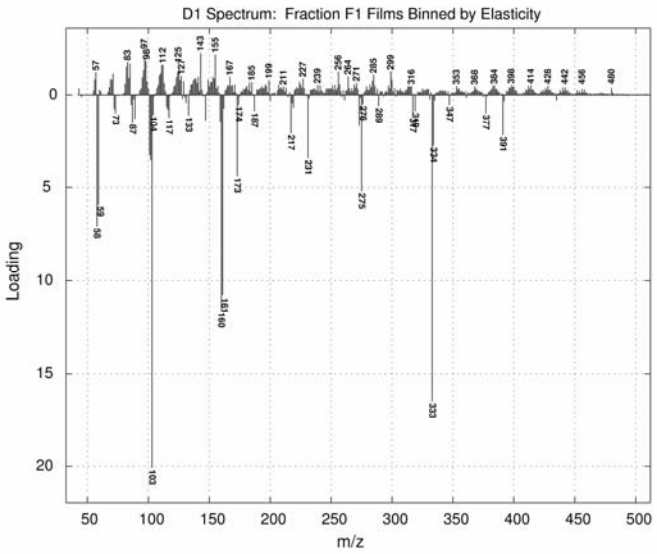

Fig. 1. Graphical representation of discriminant function D1 derived from the chemometric analysis of mass spectral signatures of 30 microlayer and bulk seawater film extracts (F1). Intensities at each *m/z* represent the loadings for that particular *m/z* variable used to calculate the D1 discriminant function score. Prominent *m/z* variables include those representative of fatty acids, acyl lipids, sterols, poloxymers and humic compounds

Note that since the mean spectrum was subtracted from each individual spectrum in the initial stage of the discriminant analysis, the resulting discriminants reflect only the variations in the spectra that distinguished one sample class from another. The positive portion of D1 (D1+) was domi-

nated by lipid components, particularly free fatty acids (*e.g. m/z* 256, 270, 284), bound acyl lipids, including wax esters and glycerides (*m/z* 227, 239, 271, 285, 299), and sterols (*m/z* 368, 384, 398, 412). The negative portion of D1 (D1-) was dominated by the highly oxygenated poloxymers (*m/z* 160, 161, 333, 391). The averaged D1 scores for the 30 sample extracts are shown plotted against corresponding average surface elasticities at a surface pressure Π = 6.5 mN m^{-1} in Figure 2. A strong linear correlation (r = 0.9875) is evident. Microlayers enriched in D1+ components (higher D1 scores) had higher elasticities than those enriched in D1- components (lower D1 scores). Somewhat analogous to the characteristic water masses that define a salinity mixing curve, the D1+ and D1- discriminants describe the extreme or 'end member' compositions that control variations in mixed film rheology.

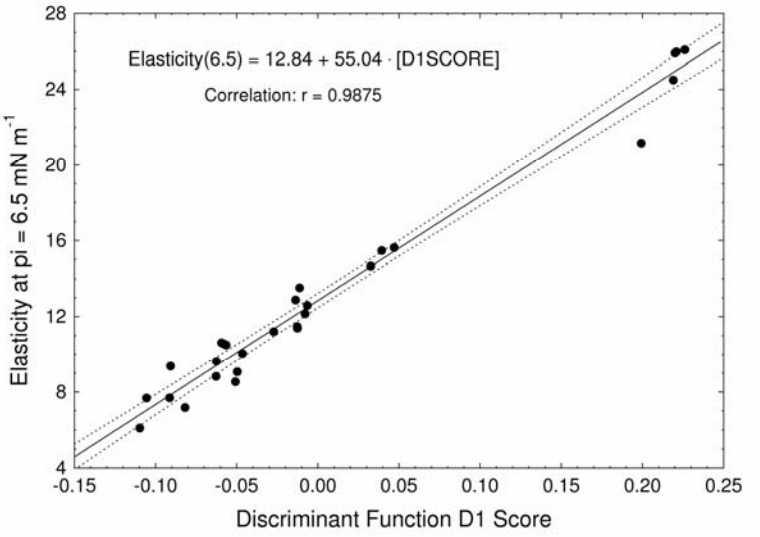

Fig. 2. Correlation of static surface elasticity (ε_0) at a film pressure of 6.5 mN m^{-1} with discriminant function D1 score for 28 films formed from microlayer and subsurface seawater F1 surfactant extracts

The mass spectra contained sufficient information to predict film elasticities. Linear regressions were evaluated at each 0.5 mN m^{-1} surface pressure interval in the range 0.5 - 7.5 mN m^{-1} from the correlation matrix. The resulting coefficients for the linear fits are given in Table 2 along with the correlation coefficients. Correlation coefficients were greatest at high surface pressures and decreased toward low surface pressures, for which the measurement uncertainty becomes significant. The regression coefficients

can be used to predict static elasticity from the mass spectrum, if the surface pressure (or surface tension) is known. This is illustrated in Figure 3 where we plot the predicted and measured ε_o *vs.* Π curves for the three samples of Figure 3 of Frew et al. (2006). The results suggest that the D1 scores and the resulting regression relations can be used to predict surface elasticities at a given surface pressure reasonably accurately (to within 20 %) for the F1 fraction. Deviations of the predicted elasticities from the measured values are mainly due to the fact that only D1 was used in the prediction, thus ignoring information in lower ranked discriminants. In the future, a more comprehensive approach using canonical correlation techniques may improve this by incorporating multiple discriminant functions.

Table 2. Linear fit coefficients a and b, respectively, and correlation coefficient r at an elasticity (Π) = a [D1 Score] + b

Π (mN m^{-1})	**a**	**b**	**r (df)***
0.5	2.59	1.38	0.557 (28)
1.0	7.96	2.39	0.910 (28)
1.5	15.19	3.62	0.944 (28)
2.0	22.33	4.75	0.957 (28)
2.5	28.38	5.86	0.960 (27)
3.0	34.11	6.93	0.969 (27)
3.5	38.83	7.94	0.969 (27)
4.0	43.53	8.88	0.976 (27)
4.5	46.69	9.79	0.982 (27)
5.0	49.36	10.64	0.983 (27)
5.5	51.19	11.47	0.984 (26)
6.0	53.33	12.19	0.987 (26)
6.5	55.04	12.84	0.988 (26)
7.0	56.18	13.43	0.987 (26)
7.5	57.26	13.99	0.985 (25)

*Degrees of freedom = n-2

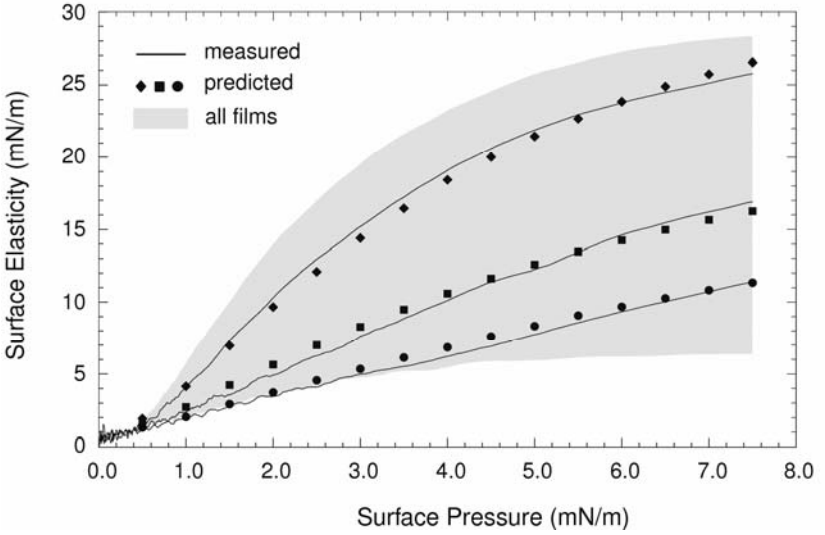

Fig. 3. Measured static surface elasticity (solid lines) as a function of surface pressure for the three surface films of Figures 3 and 4. Solid symbols are elasticity values predicted for the three films from their mass spectra using the LDA-derived D1 scores and the linear relations in Table 2. The shaded area indicates the overall range of elasticity values observed for the suite of 30 microlayer

4. Summary

In the absence of a rigorous theoretical model for multicomponent surface films, an empirical method for relating the composition and molecular structure of complex natural surface films to interfacial physical properties has been explored. The method combines chemical and structural data with statistical analysis. The advantages of this approach are that (1) it facilitates identification of the end-member components in complex mixtures that determine the elasticity of microlayer films and (2) allows reasonably accurate estimates of static elasticity from surface pressure and the mass spectrum of the microlayer SAOM. This approach will be extended in future work to *in situ* mapping of slick composition and surface elasticity by coupling advanced ion trap mass spectrometers, which are capable of detecting and measuring individual film components in unresolved mixtures, with continuous microlayer sampling.

Acknowledgments. This research was sponsored by the U. S. Office of Naval Research under grants N00014-94-1400 and N00014-98-10593. The authors wish to acknowledge G. B. Eijkel and J. J. Boon of FOM-AMOLF, Amsterdam, Netherlands, for making the Chemometricks program available, and W. S. Little of Woods Hole Oceanographic Institution for his help modifying the program to improve its utility. We also thank the officers and crews of the R/V Cape Henlopen and R/V New Horizon for their cooperation in meeting our sampling needs during their respective cruises.

5. References

Bock EJ, Frew NM (1993) Static and dynamic response of natural multi-component oceanic surface films to compression and dilation: laboratory and field observations. J Geophys Res 98: 14599-14617

Boon J (1992) Analytical pyrolysis mass spectrometry: new vistas open by temperature-resolved in-source PYMS. Int J Mass Spectrometry and Ion Processes 118/119: 755-787

Frew NM, Nelson RK, Johnson CG (2006) Sea-slicks: variability in chemical composition and surface elasticity. This volume.

Gaines GL Jr. (1966) Insoluble Monolayers at Liquid-Gas Interfaces, Wiley Interscience, New York

Hoogerbruge R, Willig SJ, Kistemaker PG (1983) Discriminant analysis by double stage principal component analysis. Anal Chem 55: 1710-1712

Windig, W, Haverkamp J, Kistemaker PG (1983) Interpretation of sets of pyrolysis mass spectra by discriminant analysis and graphic rotation. Anal Chem 55: 81-88

On surface renewal and sea slicks

Kristian B.Dysthe

Department of Mathematics, University of Bergen, Norway

Abstract. Interaction between a current and surface-active material is considered. Some simple cases where the substrate motion is steady and 2D is analysed using standard boundary layer theory. Questions like: how is the transversal dimension of a slick related to the film pressure and the substrate convergence? and how strong substrate motion does it take to break up a surface film?, are addressed. It is pointed out that the answers depend on whether the film can be considered stagnant, or develops self-organised motion. It is further pointed out how small scale thermal convection at the ocean surface is easily suppressed by a slick.

1. Introduction

The surface motion of the sea takes place on a variety of scales from mm capillary waves to mesoscale eddies. At low wind conditions it seems that there are some scales that dominate with regard to slick-formation. They give rise to long filamentary structures observed on optical- as well as SAR-images of the sea surface, where they have a transverse dimension of the order of 100 m and longitudinal coherence for several kilometres (Scully-Powers 1986).

Also readily observed on satellite images are the ship-wakes, which may extend over large distances (wake-lengths of approximately 70 km have been reported). Again, the reason why they are visible seems to be connected to the ability of the ship wake to trap surface-active material and to produce a coherent film (Peltzer et al. 1992).

At the other end of the relevant scales is the surface motion caused by shallow convection. Gemmerich and Hasse (1992) demonstrated its role in renewal of the sea surface at low and moderate winds (less than 6 m s^{-1} say). Their study indicated a time scale for the renewal of the sea surface under these conditions of the order of 10 seconds.

The present paper considers some simple case studies with surface film and substrate motion in search for some criteria for construction and de-

struction of a coherent film-covered surface. It is shown using the data of Gemmerich and Hasse (1992) that a slick can easily suppress small-scale convective motion in the surface layer. Thus the heat transport through the sea surface is influenced by surface films, as found experimentally (Jarvis 1962).

2. Some "simple" case studies

In order to understand how surface slicks are formed and how they are broken up, it is necessary to take into account a number of elementary processes and how they work in combination. This paper does not pretend to present anything like a complete list of these processes, nor does it have much to say about their interaction. What is intended is a simple-minded discussion on a few effects that are felt to be of importance to establish a more coherent description of slicks.

In the following three case studies with simplified geometry and flow are considered. Two of them are simple theoretical investigations using standard hydrodynamic theory, while the third one is based on a very interesting experiment carried out by Mockros and Krone (1968).

2.1. Tearing of a continuous film

Consider a piece of the ocean covered with a monolayer with film pressure $\Pi \equiv \sigma_w - \sigma$, where σ_w and σ are the surface tensions of pure water and film, respectively. We further assume that the film is stagnant. Beneath the film, however, there is a horizontal motion (taken to be in the x-direction) with a corresponding boundary layer. Consequently, there is a tangential viscous stress, τ_{visc} , on the film which must be balanced by a gradient in Π.

$$\tau_{visc} = \frac{d\Pi}{dx} = -\frac{d\sigma}{dx} \tag{1}$$

We take the motion below the boundary layer to be spatially periodic with up-welling and down-welling zones, and model the flowfield **v** just below the boundary layer as

$$\mathbf{v} = U_k (\sin kx,\, 0,\, kz \cos kx) \tag{2}$$

where z is the vertical coordinate (see Figure 1), and there stagnation lines parallel to the y-axis at $kx = 0, \pm\pi, \pm 2\pi$..... are assumed.

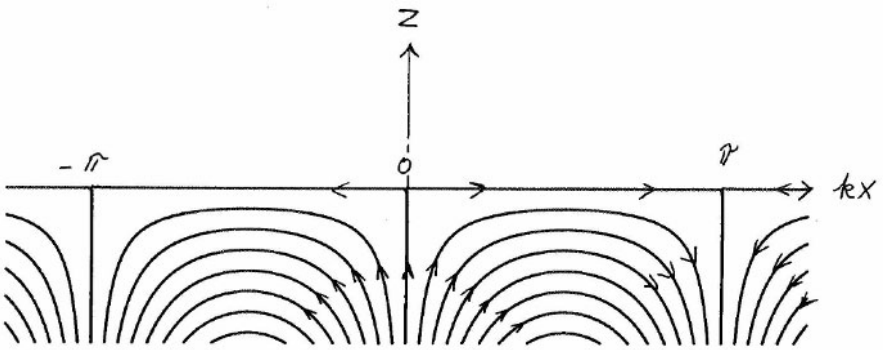

Fig. 1. Periodic surface current

In this steady state the film is stagnant and acts as a "wall". The corresponding boundary layer can be calculated by standard methods. We have used an approximative method due to Twaites (White 1991). Starting from the up-welling stagnation line at $x = 0$ there is an acceleration zone up to $kx = \pi/2$. Then, a deceleration zone up to the down-welling stagnation line at $kx = \pi$ can be assumed. Separation, according to the approximate theory, occurs at the point $kx \cong 1.8$. Integrating the viscous stress from the up-welling stagnation line to the line of separation we obtain

$$\int_{stagn.}^{sep.} \tau_{visc}\, dx \cong 0.93\rho\left(\frac{\nu U_k^3}{k}\right)^{1/2} \tag{3}$$

By equation (1) this is balanced by the difference in film pressure between the same two lines. If Π_{max} is the maximum available film pressure, the *condition for tearing the film* becomes

$$\Pi_{max} \le 0.93\rho\left(\frac{\nu U_k^3}{k}\right)^{1/2} \tag{4}$$

If the condition (4) is satisfied, a steady state with the film covering the whole area is no longer possible. Instead, the film is split up into periodic bands (slicks) centred on the down-welling stagnation lines. We consider next such a down-welling zone in some more detail.

2.2. Accumulation near a stagnation line

We now consider a two-dimensional down-welling zone with a stagnation line at $x = 0$. The flow field below the boundary layer is taken to be

$$\mathbf{v} = \alpha(-x, 0, z) \tag{5}$$

which is a simplified version of the flow around $x = \pi$ in the example above, if $\alpha = kU_k$ (see (2)). There is now a *surface convergence* $\nabla\cdot\mathbf{u} = -\alpha$ so that surface active material may collect starting from the stagnation line $x = 0$ (see Fig. 2). Here $\mathbf{u}$ is the horizontal component of $\mathbf{v}$. Let us assume that the film has grown to a width $2L$. Again assuming that there is no motion in the film, it may be considered as a "rigid" boundary. The boundary layer for such a situation has been worked out by Howarth (1937). He found that the deceleration towards the stagnation line caused separation to occur at a distance of $\approx 0.12L$ downstream of the edges. The force per lateral length acting on the film from an edge to the corresponding separation line, can be worked out from Howarths results to be

$$\int_{film\_edge}^{sep.} \tau_{visc}\, dx \cong 0.17\rho L^2 \nu^{1/2}\alpha^{3/2} = 0.17\rho(kL)^2\left(\frac{\nu U_k^3}{k}\right)^{1/2} \tag{6}$$

where the last equation follows by the substitution $\alpha = kU_k$. The film pressure Π exhibits a maximum, and σ a corresponding minimum at the line of separation. If the force (6) exceeds the maximum sustainable film pressure Π_{max} the film growth will stop.

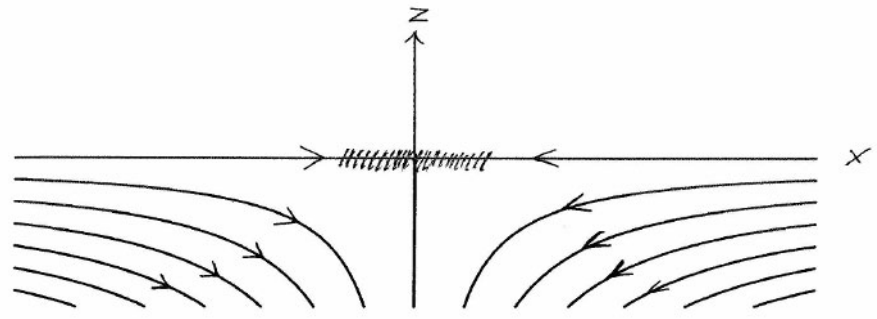

Fig. 2. Down-welling zone with accumulation of film

Therefore, the maximum width of the film becomes

$$L_{\max} \cong 2.4\left(\frac{\Pi_{\max}}{\rho}\right)^{1/2} \nu^{-1/4}\alpha^{-3/4} \tag{7}$$

As a numerical example consider the parameters $\alpha = 10^{-3}\ s^{-1}$, $\nu = 0.015\ cm^2\ s^{-1}$, and $\Pi_{max} = 40\ mN\ m^{-1}$ which is not unreasonable for a slick. This gives a "slick width" according to (7) of ≅ 150 m.

In both examples above we have assumed that there is no motion in the film, so that it can be considered to act like a "rigid" plate. In the next case study we shall see that even in a steady state situation there may be a pattern of motion in the film that change the total viscous drag.

2.3. Accumulation of a surface film by flow under surface obstruction

It is commonly observed that an obstruction on the surface of water flowing gently in an open channel (with free passage underneath the obstruction) causes a spontaneous surface film to accumulate on the upstream side. Although this is not the way a surface slick is generated, there is perhaps something to be learned here.

A very interesting controlled experiment was described by Mockros and Krone (1968). Ordinary tap water was recirculated in a flume 113 cm wide 8 cm deep and 4 m long. When a shallow obstruction was placed across the full width of the channel, a surface film was observed growing. The upstream front of the film was easily visible by a small ripple, the so-called Reynolds ridge (Harper and Dixon 1974). The growth followed a power law first at a fast rate, and then at a reduced rate (Figure 3).

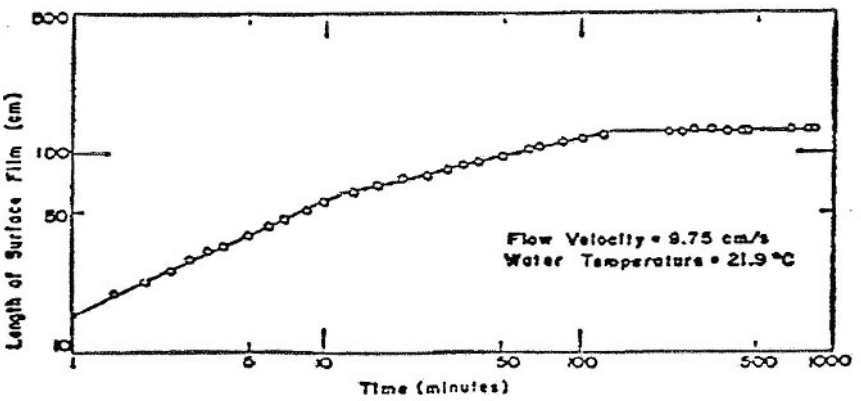

Fig. 3. Typical growth curve for the surface film (taken from Mockros and Krone 1968)

At a certain critical length, L_c, depending on the stream velocity, U, the film stopped growing. It is found that a dimensionless parameter (a "Weber number") N_w given by

$$N_w \equiv \frac{\rho}{\sigma_w - \sigma_o} L_c U^2 \tag{8}$$

is approximately constant with a value of roughly 620 in the experiment. Here σ_w and σ_o are the surface tensions upstream of the film (pure water) and at the obstruction end of the film, respectively, i.e., σ_w - σ_o is the total drop in surface tension. In the experiment this drop was always found to be around 45 mN m^{-1}. This implies that

$$L_c U^2 \approx \text{constant}$$

It was further found that the surface tension varies linearly along the film (excluding the front portion with the Reynolds ridge). Using (8) we get

$$\Delta\sigma = K\rho U^2 x \tag{9}$$

where $\Delta\sigma$ is the drop in the surface tension and x the distance from a reference level right behind the Reynolds ridge (Figure 4). Here the dimensionless number $K \cong 0.003$.

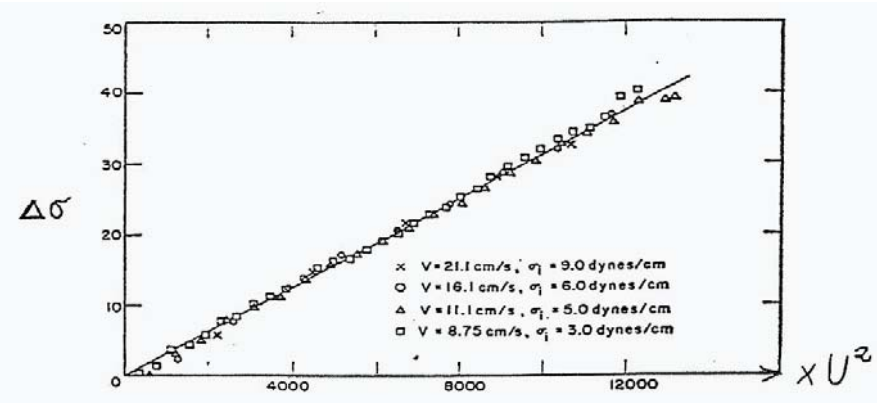

Fig. 4. Drop in surface tension $\Delta\sigma$ from a reference level behind the Reynolds ridge as a function of U^2x where x is the distance behind the same reference level (taken from Mockros and Krone 1968)

If one assumes that there is no motion in the film it acts as a "wall". Then the viscous stress τ_{visc} from standard theory would be distributed as[1]

$$\tau_{visc} \cong 0.33\rho\sqrt{\frac{U^3\nu}{x}} \tag{10}$$

where x is the distance from the front of the 'plate'.[2] The viscous stress must be balanced by a gradient in the surface tension, i.e.

$$\tau_{visc} = \frac{d\sigma}{dx}$$

Integrating over the entire film length when the film has obtained its critical length L_c one then obtains

$$\Pi_{\max} = \sigma_w - \sigma_o = 0.66\rho\sqrt{\nu U^3 L_c} \tag{11}$$

implying that $U^3L_c \approx$ constant, which is inconsistent with the experimental findings described above.

The reason for the inconsistency of the 'plate'-model is presumably the circulation pattern that was observed in the film: *a self-organized motion of regularly spaced, unsteady channels, oriented parallel to the direction of the substrate flow*. These channels, about 1 cm in width, extended most of the length of the film and alternated in direction of flow. The circulation velocity was $\leq U/2$.

It is questionable to apply the experimental results of Mockros and Krone to a field situation. This is mainly because the role of the side walls and the bottom in the formation of the streaming filaments is not known. Another question is what happens when the substrate flow is non-uniform. A new experiment is needed, looking into these questions. One possibility is to make a down-welling zone with film accumulation symmetrically around the stagnation line, and making the experiment broad enough for side wall effects to be negligible.

2.4. Dimensional arguments

One might inquire what can be obtained on purely dimensional grounds considering relations between the quantities ν,k,U_k and $\Pi_{\max}/\rho$. Since only

[1] The Reynolds number in the boundary layer is sufficiently small so that laminar flow can be assumed.

[2] Obviously this is not a good model near the front where the curvature at the Reynolds ridge modifies the stress distribution.

two independent non-dimensional quantities can be formed from them, any possible relation will be of the form

$$\frac{\Pi_{\max}}{\rho} = \frac{U_k^2}{k} f\left(\frac{U_k}{\nu k}\right)$$

where $f(x)$ is an unknown function. The relation (8) with N_w = const. corresponds to the case $f(x)$ = const, while the relation (4) corresponds to $f(x) \propto x^{-1/2}$.

3. Motion on different scales

The surface motion is of many scales, spanning from mm-waves to mesoscale eddies. In our discussion perhaps the range 10^{-1} to 10^3 meters is of interest. Surface slicks are only observed for relatively low and moderate winds. The surface motion during slick conditions may, however, be the result of earlier wind induced turbulence and Langmuir cells in the upper ocean layer. Small scale motion (of the order of 10 cm or less) is probably due to a convective motion in a shallow surface layer (Gemmerich and Hasse 1992).

Let us first consider the surface flow caused by turbulence in the bulk. While moving towards the surface, the vertical velocity fluctuations are disappearing and the horizontal ones seems to have the same wave number scaling as in the bulk (Kumar et al. 1998, Eckhardt and Schumacher 2004). If the turbulence in the bulk has an inertial range with a Kolmogorov type spectral variation, then the induced surface divergence kU_k (at a clean surface) scales like $k^{-1/3}$ i.e. a rather weak dependence on k, and the right hand side of equation (7) scales like $k^{1/4}$. On the other hand the quantity $(U_k^3/k)^{1/2}$ appearing in equation (4) would be expected to scale like $k^{-5/2}$. So over the inertial range the longest scales would be likely to dominate the tearing, while the compacting have an insignificant variation with scale in the same range.

For scales comparable or exceeding the depth of the mixed layer it seems reasonable to assume that the arrangement of surface film material is dominated by stronger and more coherent motions like Langmuir cells and fronts with downwelling. The structures seen in SAR images have a number of different scales. The basic ones being the filamentary structures with transverse dimensions of the order of 100 m and longitudinal coherence of several kilometers. Even the smaller eddies (order of 10 km) are visualized by the bending of this smaller scale striation. There is, however, an upper limit to the ocean scale induced arrangement of slicks, because a

characteristic time L/U for advection over a distance L cannot be longer than the time available with low or moderate winds.

3.1. A note on wind and waves

So far we have assumed the slick material to be collected and compacted by regions of surface convergence of the currents in the upper ocean. A wind of velocity V causes a surface drift that on the average is uniform and of the order of magnitude $0.03V$. Such a surface drift will then tend to move the surface material relative to the underlying regions of convergence and thus upset the process of compactification of film material.

In the first case study above a wind velocity V in the x-direction would remove the stagnation points, and thus the source of accumulated slick formation if $U_k < 0.03V$. For example, with $U_k = 15$ cm s^{-1} this would take a wind of velocity > 5m s^{-1}.

The waves caused by small wind velocities are damped by a slick. The momentum loss of the waves induces a wave stress gradient acting on the surface film (Foss 2001). This results in a compacting influence on the upwind side of the slick.

3.2. Surface renewal

At the short end of the scale (of the order of 10 cm) the motion may be due to convective instability in a shallow surface layer as explained by Gemmerich and Hasse (1992). They made field observations of the surface motion by spraying powdered corkwood on the surface, watching how it collected on a time scale of 10 seconds or less, into various structures depending on the condition. Lines were by far the most common structure observed. They may, for example, be caused by convective rolls along the wind drift direction.

Will a slick be able to suppress such a convectively induced surface motion? Gemmerich et al. measured characteristic lengths between the lines, and the corresponding surface velocities. One can now use the relation (4) to estimate the critical film pressure needed to cover such an area. We find using their data that a film pressure of 2 mN m^{-1} would be enough. Thus a slick easily suppresses the surface motion induced by shallow convection, causing a boundary layer over which heat must be transported by conduction rather than convection. The viscous boundary layer is thicker than a corresponding thermal layer because the kinematic viscosity is much larger than the thermal diffusivity. This lead to a reduced efficiency of heat transport through a slick that can be detected through the surface temperature signature it leaves (Jarvis 1962, MacLeish 1970).

4. Conclusions

Some simple cases of 2D current-film interaction have been studied, relating to questions like: How is the transversal dimension of a slick related to the film pressure and the substrate convergence? Possible relations were found, both through standard hydrodynamic theory and dimensional analysis. It was pointed out, referring to an interesting experiment by Mockros and Krone (1968), that the answers depend on whether the film can be considered stagnant or develops self-organised motion. It is further pointed out using the mentioned results that small-scale thermal convection at the ocean surface is easily suppressed by a slick.

5. References

Eckhardt B, Schumacher J (2004) Turbulence and passive scalar transport in a free slip surface. Physical Review E, 64: 016314

Foss M (2001) Wave damping and momentum transfer. Doctoral thesis, University of Tromsö, Norway

Gemmerich J, Hasse L (1992) Small-scale surface streaming under natural conditions as effective in air-sea gas exchange. Tellus 44B: 150-159

Howarth L (1937) On the solution of the laminar boundary layer equations. Proc Royal Soc London A 164:547-579

Jarvis NL (1962) The effect of monomolecular films on surface temperature and convective motion at the air/water interface. J.Colloid Sci. 17: 512-522

Kumar S, Gupta R, Banerjee S (1998) An experimental investigation of the characteristics of free surface turbulence in a channel flow. Physics of Fluids 10: 437-456

MacLeish W (1970) Spatial spectra of ocean surface temperatures. J Geophys Res 75: 6872-6877

Mockros LF, Krone RB (1968) Hydrodynamic Effects on an Interfacial Film. Science 161: 361-363

Peltzer RD, Griffin OM, Barger WR, Kaiser JAC (1992) High-Resolution Measurement of Surface-Active Film Redistribution in Ship Wakes. J Geophys Res 97: 5231-5252

Scully-Powers P (1986) Navy Oceanographer Shuttle Observations. NUSC Technical Doc 7611.

White FM (1991) Viscous Fluid Flow. Mc Graw-Hill, New York

Chapter 2:

Chemical Characteristics

Physicochemical effects of the marine microlayer on air-sea gas transport

Sean P. McKenna [1], Erik John Bock [2 *]

[1]Department of Applied Ocean Physics and Engineering
Woods Hole Oceanographic Institution, Woods Hole, Massachusetts, USA
[2]Interdisciplinary Centre for Scientific Computing
University of Heidelberg, Heidelberg, Germany

1 Introduction

Observations that films of surfactant material influence wave propagation date back at least two millennia (Plinius Secundus 77 AD). One of the first mathematical treatments of wave damping was that by Levich (1962), who studied the propagation of capillary waves for the limiting cases of a free interface and an interface with an infinite dilational elastic modulus. Levich analytically solved these two limiting cases and found that the time-damping coefficient of short waves was increased by a factor of approximately 1.5 for waves propagating on liquids with infinite elastic films. Levich did not investigate the case of finite surface dilational viscoelasticty, but his work launched a number of theoretical and experimental investigations.

Much of the early interest in the propagation characteristics of short waves stemmed from the increased feasibility of utilizing remotely-sensed microwave backscatter from radars to observe wide areas of the ocean surface. The primary scattering elements for these instruments are ocean surface waves having wavelengths similar to the incident electromagnetic radiation (Bragg scattering), making it necessary to understand the statistical distribution of short waves under different environmental conditions. Remote sensing data products were initially interpreted to yield fundamental geophysical estimates, including sea state and wind speed (for global weather prediction models), ship wake incidences (for ship detection and tracking), internal wave propagation (for wave interaction models), and

---

[*] In memoriam.

later, in assessing mass-transfer rates on global scales (for balancing global budgets for CO_2 and other environmentally important gases).

It became apparent that the presence of surfactant films could affect all of these estimates, but at the time when the first quantitative studies were being performed on capillary ripple propagation, many aspects of the remote sensing field were still in stages of development. For instance, supercomputers had not yet developed to the point where dense maps of wind speed could be assimilated in real time to predict global weather. Similarly, synthetic aperture radar had not yet been developed to produce the scale resolution needed for ship wake tracking or internal wave field interpretation. It was also evident that environmental issues of global warming and greenhouse gases had not yet achieved prominent recognition. These reasons accounted for the ebb in research efforts between the time of the first formulation by Levich in 1962 and the revitalisation that occurred two decades ago. The renewed interest that occurred in the 1980s was spurred by the maturation of several independent technologies, including computing power, remote-sensing capabilities, and the development of robust techniques for making short wave measurements *in situ.* This combination enabled studies to assess the amount, extent, and physical properties of the microlayer that forms at the air–sea interface from both natural and anthropogenic sources.

2 Theoretical and experimental studies

Following Levich, subsequent wave propagation studies sought to determine the extent to which surface films modify the air–water interface and its dynamics for intermediate cases of surface dilational viscoelasticity (Mann and Hansen 1963, Hansen and Mann 1964, van den Temple and van de Riet 1965, Lucassen-Reynders and Lucassen 1969, Cini and Lombardini 1978, Hühnerfuss et al. 1982, Bock and Mann 1989). Theory predicted, and laboratory studies validated, that damping enhancements could exceed two orders of magnitude under some circumstances. The bulk of the experimental data was obtained from measurements of the distance-damping characteristics of short ripples. The wavelengths studied ranged from roughly 0.01 cm to 10 cm using waves induced by mechanical, electro-capillary, active thermal, and passive thermal techniques (Sohl et al. 1978, Bock 1987, Stenvot and Langevin 1988).

Other experimental efforts focused on the collection of ocean surface samples in order to investigate properties of the marine microlayer in the laboratory. Samples were retrieved using either inert screens (Garrett 1965) or drum-type samplers (Carlson et al. 1988, Frew and Nelson 1992).

Because these samplers physically disturb the natural state of the marine microlayer, *in vitro* results obtained from collected samples could not be proven to represent films in their natural state. Despite this limitation, these studies resulted in characterisation of quasi-static film elasticities and led to parameterisations that adequately define bounds within which the marine microlayer typically ranges. By setting such bounds, these works provided constraints for laboratory experiments (e.g., Hirsa et al. 1995, McKenna 1997, Saylor 1997). At the same time, techniques for making short wave measurements *in situ* were developed by independent researchers (Hwang 1989, Bock and Hara 1995), and others have followed (Zhang 1995, Suoja 2000).

Field measurements of the microlayer and its effects on air–sea processes have advanced with the use of specialized sampling and measurement platforms. Carlson et al. (1988) developed a small catamaran platform (SCUMS, Self-Contained Underway Microlayer Sampler) for making measurements of the extent of chemical enrichment (using an in-line fluorometer and UV-absorbance detector), near-surface microstructure (using high-resolution, fast-response temperature sensors), and surface wave statistics (using a simple laser slope gauge). This platform was refined to incorporate a fixed-point slope gauge capable of measuring temporal wave spectra and was deployed during several field programs in the Atlantic and Pacific Oceans. A scanning laser slope gauge (Bock and Hara 1995) was integrated later to allow full three-dimensional wave spectral measurements of capillary and capillary-gravity waves (wavelengths between 7.9×10^{-3} and 3.1×10^{-1} m could be measured), as well as an array of capacitive wire wave gauges to measure longer gravity waves (wavelengths greater than 10 m). A recent configuration of this platform (shown in Fig. 1) was used in the Coastal Ocean Processes field experiments conducted off Southern California and in the Northwestern Atlantic Ocean in 1995 and 1997. This research catamaran has the capability of simultaneously measuring short and long wave spectra, surface chemical enrichment, wind stress, and near-surface turbulence.

Fig. 1. Research catamaran during 1997 Coastal Ocean Processes experiment. The catamaran is shown here after deployment from R/V Oceanus in the Northwestern Atlantic Ocean. The platform is manoeuvred autonomously and is controlled remotely from the ship. During this experiment, the catamaran was equipped to measure long and short wave spectra, sub-surface turbulence, chemical enrichment, and various meteorological parameters. A system to measure vertical profiles of dimethylsulfide above the ocean surface was also incorporated into the catamaran measurement suite

One of the most important findings of these studies and parallel laboratory efforts was that surface wave roughness (a parameter that can be remotely-sensed) was found to correlate well with gas-transfer rates across the air–sea interface (Frew et al. 1995, Hara et al. 1995). Results obtained in both laboratory and field experiments indicate that the range of wavelengths pertinent to gas transport may be restricted to wavelengths of millimetres to centimetres. While the correlation between surface roughness and gas transport is robust under differing environmental conditions, the specific mechanisms of interfacial transport have yet to be adequately elucidated and are the topic of recent research (e.g., McKenna 2004).

3 Mechanisms of air–water gas transport

The enhancement of air–sea gas transport (for waterside rate-controlled gases), over that expected for pure molecular diffusion, is affected by several interrelated mechanisms that can depend on the wind and wave condi-

tions. Thus, many complex physical processes influence gas transfer, including: the interaction between the wind-driven surface shear layer and the wave field, near-surface turbulence, the modification of interfacial hydrodynamics by surface films, and breaking waves that lead to bubble formation and increased mixing. Consequently, an experiment or model that completely describes gas transfer does not exist. Estimates of gas-transfer coefficients based on wind speed have been favoured for years (e.g., Liss and Merlivat 1986, Wanninkhof 1992). Each of these formulations predicts a monotonic increase in the gas-transfer rate with increasing wind speed. The largest difference between the Liss and Merlivat model and subsequent models is the mechanistic interpretation of distinct regimes occurring under different wind conditions. Liss and Merlivat suggest a low critical wind speed below which the gas-transfer rate increases slowly with increasing wind speed owing to the lack of near-surface mixing associated with a smooth surface without waves. They also suggest a second critical wind speed that occurs when the wind over a wavy surface exceeds the threshold necessary for initiating wave breaking. Above this point, it is presumed that wave breaking, bubble entrapment, and near-surface mixing by rising bubbles contribute significantly to gas transfer. In contrast to this tri-linear model, the Wanninkhof (1992) relationship postulates a smoother enhancement of gas transfer as wind speed increases.

Several laboratory and field studies, from the early work of Broecker et al. (1978) to the more recent studies of Frew (1995), have shown that a unique relationship between the gas-transfer rate and wind speed is not likely to exist for natural waters where surfactants are influential. Fundamentally, the exchange of gases between water and air occurs through very thin boundary layers at the air–water interface where turbulent motions are suppressed giving way to molecular diffusion processes. The details of these layers — their thicknesses and the gradients across them — are determined by the aero- and hydrodynamics near the surface. For sparingly soluble gases (e.g., CO_2, O_2, N_2) the airside effect is less critical, and the transport is determined by the waterside boundary layer. The fluid flow in this boundary layer is highly sensitive to the presence of a surface film and can be modified considerably, which is the reason gas transfer exhibits a similar sensitivity. Therefore, studies of the relevant physical mechanisms of interfacial gas transport and the role of surface films are crucial to improving our understanding of the exchange process.

Conceptual models aimed at explaining the dominant processes associated with gas transfer can be generalized as being either turbulent eddy diffusivity or surface renewal models; others are based on similarity considerations with reference to experimental data. Irrespective of the model type, it may be assumed that the vertical velocity fluctuations near the sur-

face, $w'(z)$, which bring fresh fluid from the bulk to the interface for diffusion, contribute to gas-transfer enhancement. Assuming incompressibility, these velocity fluctuations can be expressed in terms of the surface divergence as $w'(z) \approx -(\nabla_h \cdot \mathbf{v}')_o z$ to first order, where the subscript 'o' indicates evaluation at the interface, $z = 0$. Expressing $w'(z)$ in such manner suggests a strong connection between the surface divergence, $(\nabla_h \cdot \mathbf{v}')_o$, and gas transport. Some models (e.g., Lamont and Scott 1970, Brumley and Jirka 1988) attempt to predict gas-transfer rates by considering surface renewal by turbulent eddies. Such a process is sketched conceptually in Fig. 2, which shows how upwelling eddies bring about a horizontal surface divergence that renews the near-surface region with bulk fluid from below. This figure also makes clear how the presence of a surfactant can influence surface renewal and divergence. A common difficulty with many gas-transfer models has been relating the model inputs (velocity, length, and/or time scales) to relevant, measurable hydrodynamic parameters. Therefore, a direct experimental measurement of the surface divergence could prove very useful. In addition, such a measurement could be used to explore the model results of Ledwell (1984) and Csanady (1990), which provide direct relationships between surface divergence and the gas-transfer rate.

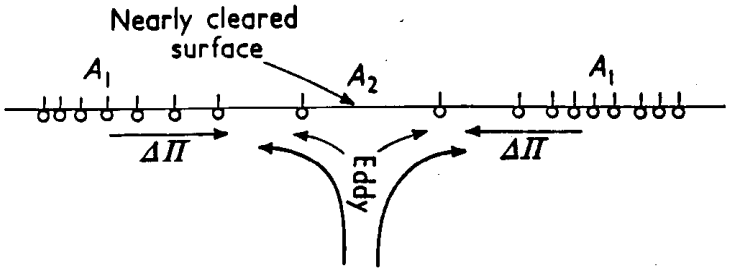

Fig. 2. Conceptualisation of surface renewal by a turbulent eddy in the presence of a surfactant. The eddy upwells fresh fluid to the surface, while the differential spreading pressure, $\Delta\Pi$, opposes the transport of new fluid to the interface. Adapted from Davies and Rideal (1963)

In order to gain insight into the impact of an interfacial film on surface divergence, the case of linear, monochromatic capillary-gravity waves was studied. Although it is generally believed that the mechanical straining of the surface due to orbital wave motions is not sufficiently large enough to bring about significant gas-transfer enhancement, this simple case provides a useful and illustrative result.

Using a formulation similar to that of Lucassen-Reynders and Lucassen (1969), the near-surface two-dimensional velocity field was numerically solved for both ideal and viscoelastic surfaces. Before considering surface divergence, Fig. 3 shows an example of the near-surface profile of the velocity component in the direction of wave propagation for three different conditions: ideal flow (irrotational and inviscid), viscous flow with zero elastic modulus, and viscous flow with a finite viscoelastic modulus. The results are for a 15 Hz water wave, with the profiles taken under a crest. The wave amplitude was set at 5% of the wavelength to accommodate linear theory, and velocities were forced to be equivalent at depth. The effect of a viscoelastic surface on the surface velocity is marked. The sharp gradient in the velocity within the upper 0.3 mm for the surfactant case is responsible for wave damping. This strong gradient is acted upon by the fluid viscosity, which dissipates the wave motion effectively. The surface divergence for the same group of conditions and for the same wave motion is shown in Fig. 4. The divergence is plotted along the phase of the wave. The considerable reduction (~50%) in divergence due to a viscoelastic surface is apparent. Reduction in surface divergence implies less surface renewal, which leads to reduced gas-transfer enhancement. In this way, the role of surface films in air–water gas exchange is revealed.

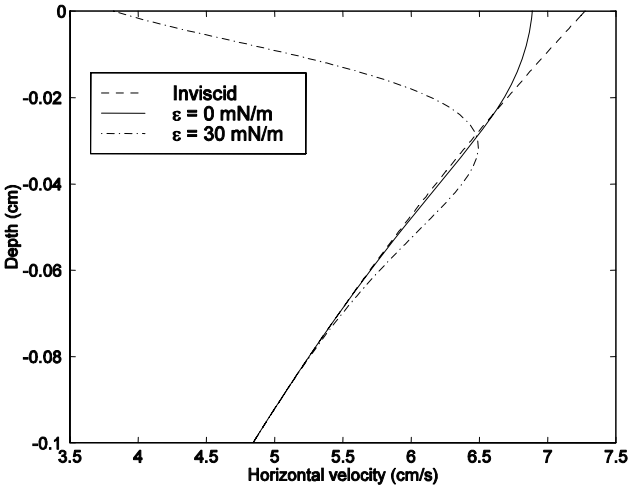

Fig. 3. Theoretical streamwise velocity profiles for a 15 Hz capillary-gravity wave. Curves are shown for an ideal inviscid flow, a real flow with zero viscoelasticity, and a surfactant flow with a finite viscoelasticity. All profiles are taken under a wave crest. The wave amplitude : wavelength ratio is 1 : 20

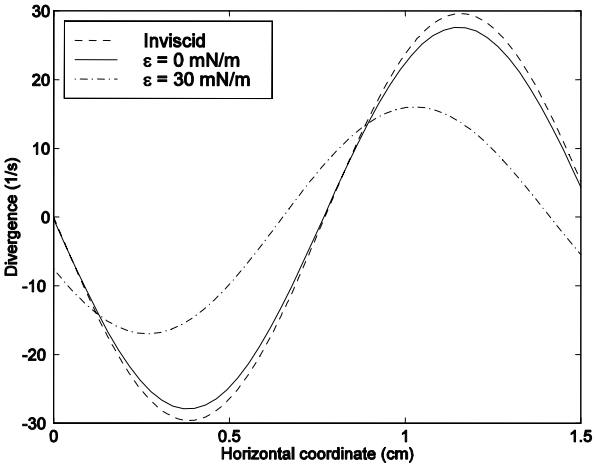

Fig. 4. Theoretical surface divergence for a 15 Hz capillary–gravity wave. Curves are shown for an ideal inviscid flow, a real flow with zero viscoelasticity, and a surfactant flow with a finite viscoelasticity. Each curve is along the phase of each wave, with the horizontal position at zero corresponding to a wave crest. The wave amplitude : wavelength ratio is 1 : 20

Next, we report results of a laboratory investigation focused on the effects of surface films on the flow field near the air/water interface. For repeatability and simplicity, we selected an axisymmetric vortex ring for the source of surface expansion and dilation (divergences) of the near surface. A detailed description of the experimental apparatus can be found in McKenna (1997). In summary, the technique relied on forcing a small slug of fluid from the mouth of a knife-edged stainless steel tube vertically into a visualisation tank. Upon exit from the tube orifice, the fluid rolled up into a vortex ring and propagated upward where it then interacted with the free surface. Surfaces with varying surfactant concentration were used to examine the influence of different surfactant composition on ring impact and the ensuing hydrodynamics. Shown in Fig. 5 are flow visualisation results taken from McKenna (1997) illustrating the effect of surfactants on the near-surface flow field. Four cases are presented: (a) approach toward a free surface, (b) interaction with a nominally clean free surface, (c) interaction with a surface covered with a microlayer of stearic acid, and (d) interaction with a solid wall boundary.

(a) Approach

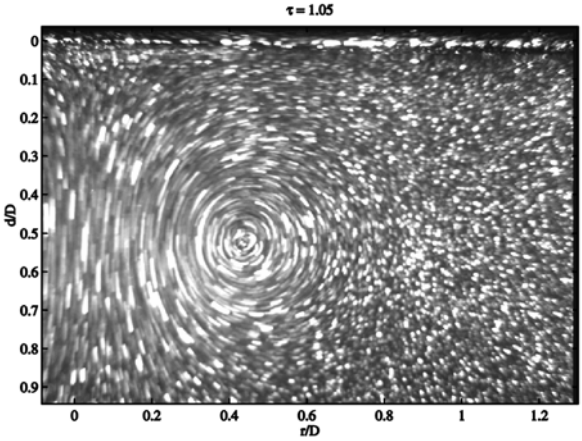

(b) Clean

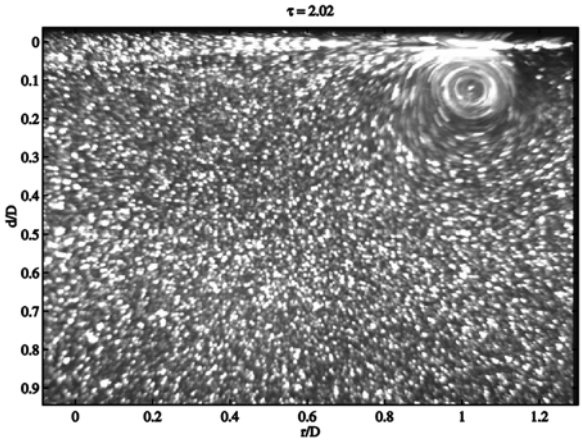

Fig. 5. Flow visualisation of vortex ring interaction with various interfaces. Each panel represents a vertical cross-section of the flow and only one half of the vortex ring is imaged. In each panel, *r* indicates the radial distance from the vertical axis of the ring, *d* measures the vertical distance from the interface, *D* is the major diameter of the ring prior to surface interaction, and τ is a dimensionless time. In this figure, panel (b) represents a surface that has not been contaminated intentionally. For this case, accompanying measurements of the spatial damping parameter (using the capillary wave technique) indicate the damping was, on average, within 7% of the theoretical value for pure water. Panels (c) and (d) follow on the next page. Taken from McKenna (1997)

(c) Microlayer

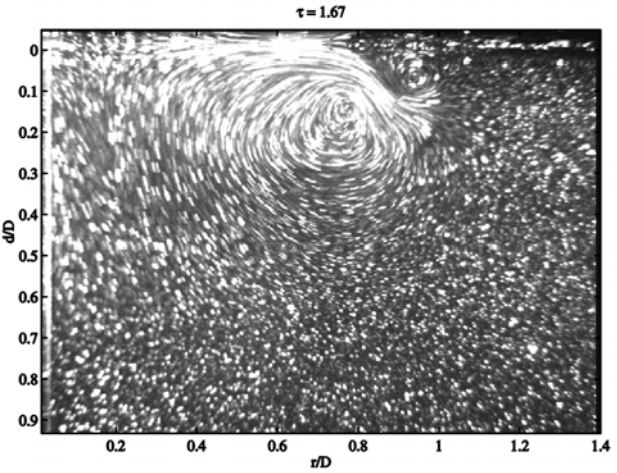

(d) Wall

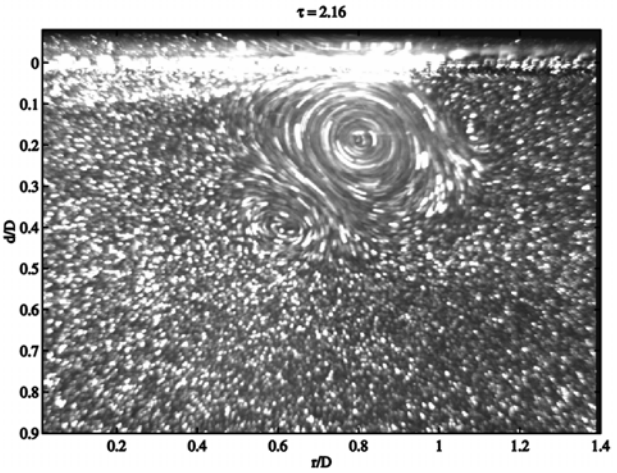

Fig. 5 (cont.). Visualisation of vortex ring interaction with various interfaces. Panel (c) is that for a stearic acid microlayer having concentration 3.5 x 10^{-10} mol cm^{-2}. Taken from McKenna (1997)

In an ideal fluid with a free surface and potential flow, a vortex ring nearing the surface will tend to dilate. This result can be rationalized by the mathematical construction of an 'image' vortex ring reflected about the interface and approaching from the opposite direction. Fig. 5b depicts the experimental observation of a physical case similar to this type of behaviour. On the other hand, when a no-slip or intermediate-slip interface is

present, the dilation of the ring major diameter is altered, as is the trajectory subsequent to surface interaction. The solid boundary demonstrates the behaviour of a no-slip interface (Fig. 5d), and the viscoelastic surface condition, obtained by spreading a surfactant film on the water surface, represents an intermediate-slip interface (Fig. 5c). A surfactant-covered surface constitutes an intermediate-slip condition because of the Marangoni effect. This effect arises from gradients in surfactant concentration that lead to gradients in surface tension, which then give rise to surface stresses and surface flows. Owing to Marangoni stresses, a surfactant surface can support a finite surface shear, whereas a free surface in the absence of any adsorbed film cannot. These Marangoni stresses develop as a result of the vortex-induced surface velocities, which act to redistribute surfactant and compress the film as the ring interacts with the surface. Such compression results in spatial gradients of the surface tension that seek to equilibrate and produce a surface flow field by themselves. These opposing flows in the surface viscous boundary layer can have strong implications for the bulk flow. Vorticity, opposite in sign to that of the primary vortex cell, can be generated in this near-surface layer. In all the cases studied, save for the clean case, coherent secondary and tertiary vortex rings were formed as a result of this newly generated vorticity. In Fig. 5c, a second vortex outside the primary cell can be seen forming very near the interface, and in Fig. 5d, two additional vortex rings are observed developing as a result of the wall interaction. Thus, a surface with an adsorbed surfactant can act intermediate between a free-slip boundary and a no-slip boundary. The ability of a surfactant surface to hydrodynamically resemble a solid boundary is widely evidenced in studies of air/water gas exchange. For mass transfer at a smooth solid boundary, the gas-transfer velocity is found to follow a -2/3 exponential Schmidt-number dependence (Deacon 1977). It has been observed (e.g., Jähne et al. 1984) that film-covered free surfaces, which inhibit formation of small-scale waves, tend to follow the same -2/3 dependence rather than a -1/2 dependence that is expected for an ideal free surface.

In order to elucidate the affects of a surfactant on the near-surface flow further, the temporal evolution of the radial component of the near-surface velocity as the vortex ring approaches the surface is plotted in Figs. 6a, b. Velocity measurements were carried out using the non-invasive full-field flow measurement technique known as digital particle image velocimetry (DPIV). In addition to a general attenuation of the tangential velocity, we observe the quasi-no-slip condition occurring outside of the vortex core for the microlayer situation. This is a direct consequence of surfactant-induced Marangoni forces that develop at the interface. These vortex ring experiments illustrate the degree to which surface films can modify near-surface

flow. By acting like a solid interface, a surfactant surface can dramatically alter the flow field at the interface. Fluid velocities at the interface are reduced, inhibiting eddy motion near the surface. This affects the degree of vertical upwelling at the surface through a reduction in the surface divergence.

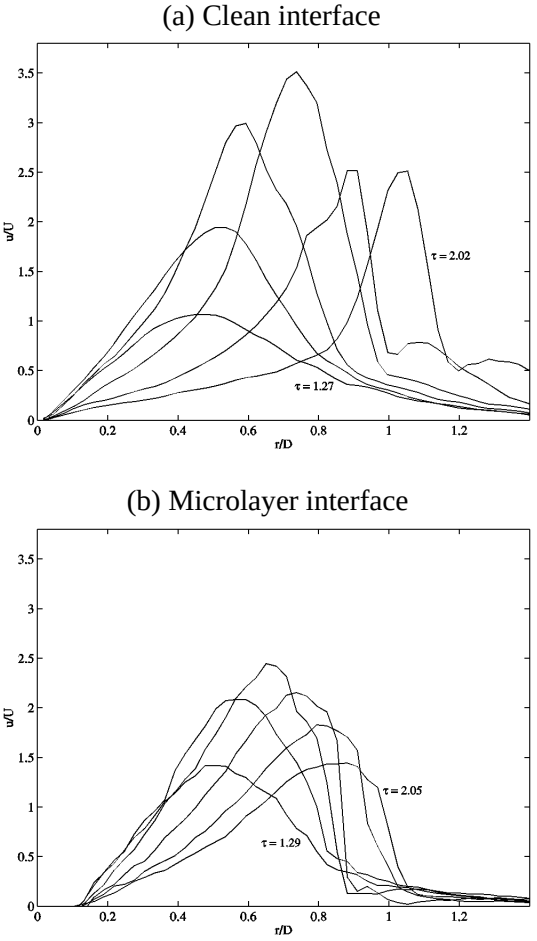

Fig. 6. Variation of the near-surface radial component of velocity. Panel (a) is for a clean interface; panel (b) is for the stearic acid microlayer. All variables are as defined in Fig. 5, u is the radial component of velocity, and U is the vertical free propagation speed of the vortex ring. Velocities are taken along a horizontal section at a depth d/D = 0.03 (0.125 cm). The temporal spacing between curves, $\Delta\tau$, is 0.15. Taken from McKenna (1997)

4 Concluding remarks

Much progress has been made in understanding the role of surface films in air–sea gas transfer. Advances in both laboratory and field techniques have provided improved measurements and needed insight into this complex and important process. Current efforts focused toward better understanding the key physical mechanisms involved in interfacial gas transfer and the role of surfactants, along with innovative and interdisciplinary field and laboratory measurements, will help to further our present knowledge.

Acknowledgements. This paper was originally presented in 1998 at EUROMECH 387, "Surface Slicks and Remote Sensing of Air-sea Interactions" in Coventry, UK. It was during the final preparation of the manuscript that Erik John Bock unexpectedly passed away. Erik was an exceptionally talented experimentalist and his passing represents a great loss to the marine sciences community. Erik was a pioneer in sea-surface measurements, most notably three-dimensional frequency-wave number spectra of ocean waves, and his contributions have been integral to many innovative air–sea interaction studies. Erik was also a supportive advisor and mentor, as well as a good friend. He will be dearly missed. –SPM

5 References

Bock EJ (1987) On ripple dynamics: I. Microcomputer-aided measurements of ripple propagation. J Colloid Interface Sci 119: 326–334

Bock EJ, Hara T (1995) Optical measurements of capillary-gravity wave spectra using a scanning laser slope gauge. J Atmos Oceanic Tech 12: 395–403

Bock EJ, Mann JA (1989) On ripple dynamics: II. A corrected dispersion relation for surface waves in the presence of surface elasticity. J Colloid Interface Sci 129: 501–505

Broeker HC, Petermann J, Siems W (1978) The influence of wind on CO_2-exchange in a wind-wave tunnel, including the effects of monolayers. J Mar Res 36: 595–610

Brumley BH, Jirka GH (1988) Air–water transfer of slightly soluble gases: turbulence, interfacial processes and conceptual models. PhysicoChem Hydrodyn 10: 295–319

Carlson DJ, Cantey LL, Cullen JJ (1988) Description of and results from a new surface microlayer sampling device. Deep-Sea Res 35: 1205–1213

Cini R, Lombardini PP (1978) Damping effect of monolayers on surface wave motion in a liquid. J Colloid Interface Sci 65: 387–389

Csanady GT (1990) The role of breaking wavelets in air-sea gas transfer. J Geophys Res 95: 749–759

Davies JT, Rideal EK (1963) Interfacial phenomena. Academic Press, New York

Deacon EL (1977) Gas transfer to and across an air-water interface. Tellus 29: 363–374

Frew NM, Nelson RK (1992) Isolation of marine microlayer film surfactants for ex situ study of their surface physical and chemical properties. J Geophys Res 97: 5281–5290

Frew NM, Bock EJ, McGillis WR, Karachintsev AV, Hara T, Munsterer T, Jähne B (1995) Variation of the air-water transfer velocity with wind stress and surface viscoelasticity. In: Jähne B, Monahan E (eds) Air–Water Gas Transfer. AEON Verlag, Heidelberg, pp 529–541

Garrett WD (1965) Collection of slick-forming materials from the sea surface. Limnol Oceanogr 10: 602–605

Hansen RS, Mann JA (1964) Propagation characteristics of capillary ripples. I: The theory of velocity dispersion and amplitude attenuation of plane capillary waves on viscoelastic films. J Appl Phys 35: 152–161

Hara T, Bock EJ, Frew NM, McGillis WR (1995) Relationship between air-sea gas transfer velocity and surface roughness. In: Jähne B, Monahan E (eds) Air–Water Gas Transfer. AEON Verlag, Heidelberg, pp 611–616

Hirsa A, Korenowski G, Logory LM, Judd CD (1995) Surfactant effects on vortex flows at a free surface and the relation to interfacial gas transfer. In: Jähne B, Monahan E (eds) Air–Water Gas Transfer. AEON Verlag, Heidelberg, pp 649–663

Hühnerfuss H, Lange P, Walter W (1982) Wave damping by monomolecular surface films and their chemical structure. Part I: Variation of the hydrophobic part of carboxylic acid esters. J Mar Res 40: 209–225

Hwang PA (1989) A scanning optical height-and-slope sensor for spatial measurements of wind-generated surface waves. STC Tech Rep 3099

Jähne B, Huber W, Dutzi A, Wais T, Ilmberger J (1984) Wind/wave-tunnel experiment on the Schmidt number dependence and wave field dependence of air/water gas exchange. In: Brutsaert W, Jirka GH (eds) Gas Transfer at Water Surfaces. D. Reidel, Minneapolis, pp 303–309

Lamont JC, Scott DS (1970) An eddy cell model of mass transfer into the surface of a turbulent liquid. AIChE J 16: 513–519

Ledwell JR (1984) The variation of the gas transfer coefficient with molecular diffusivity. In: Brutsaert W, Jirka GH (eds) Gas Transfer at Water Surfaces. D. Reidel, Minneapolis, pp 293–302

Levich VG (1962) Physicochemical hydrodynamics. Prentice-Hall, Englewood Cliffs, NJ

Liss PS, Merlivat L (1986) Air-sea gas exchange rates: Introduction and synthesis. In: Buat-Menard P (ed) The Role of Air-Sea Exchange in Geochemical Cycling. D. Reidel, Norwell, MA, pp 113–127

Lucassen-Reynders EH, Lucassen J (1969) Properties of capillary waves. Advan Colloid Interface Sci 2: 347–395

Mann JA, Hansen RS (1963) Propagation characteristics of capillary ripples. II. Instrumentation for measurement of ripple velocity and amplitude. J Colloid Sci 18: 757–771

McKenna SP (1997) The influence of surface films on interfacial flow dynamics. MS thesis, Massachusetts Institute of Technology/Woods Hole Oceanographic Institution, Cambridge, MA

McKenna SP, McGillis WR (2004) The role of free-surface turbulence and surfactants in air–water gas transfer. Int J Heat Mass Transfer 47: 539–553

Plinius Secundus C. Natural History. vol 1. Rackham H (trans), Harvard University Press, Cambridge, MA. Original text dates back to 77 AD

Saylor JR, Handler RA (1997) Gas transport across an air/water interface populated with capillary waves. Phys Fluids 9: 2529–2541

Sohl C, Miyano K, Ketterson J (1965) Novel technique for dynamic surface tension and viscosity measurements at liquid-gas interfaces. Rev Sci Instrum 49: 1464–1469

Stenvot C, Langevin D (1988) Study of viscoelasticity of monolayers using analysis of propagation of excited capillary waves. Langmuir 4: 1179–1183

Suoja NM (2000) Directional wavenumber characteristics of short sea waves. PhD thesis, Massachusetts Institute of Technology/Woods Hole Oceanographic Institution, Cambridge, MA

van den Temple M, van der Riet RP (1965) Damping of waves by surface-active materials. J Chem Phys 42: 2769–2777

Wanninkhof R (1992) Relationship between wind speed and gas exchange over the ocean. J Geophys Res 97: 7373–7382

Zhang X (1995) Capillary-gravity and capillary waves generated in a wind wave tank: Observations and theories. J Fluid Mech 289: 51–82

Static and dynamic surface tension of marine water: onshore or platform-based measurements by the oscillating bubble tensiometer

Giuseppe Loglio[1] , Boris Noskov[2], Piero Pandolfini[1], and Reinhard Miller[3]

[1]Department of Organic Chemistry, University of Florence, Florence, Italy
[2]Institute of Chemistry, St. Petersburg State University, St. Petersburg, Russia
[3]Max-Planck-Institut für Kolloid- und Grenzflächenforschung, Potsdam/Golm, Germany

Abstract. The functionality and performances of an oscillating bubble tensiometer designed for the measurement of static and dynamic surface tension of marine water samples are illustrated. The instrumentation completely works in automatic mode. Semi-continuous operation can also be easily implemented. By virtue of its geometrical configuration, the apparatus shows a relative insensitivity to external disturbances, in comparison to other measurement techniques, and consequently it can be employed even under severe environmental conditions, such as those encountered onshore or on platform-based locations. Experimental observations of the dynamic surface tension response to harmonic surface area changes are reported, for samples of sea water and for a dilute aqueous solution of a standard surfactant. The observed results are considered useful for a physical characterisation of marine water in respect to interfacial ocean-atmosphere phenomena and processes. Furthermore, the oscillating-air-bubble tensiometer mimics the real behaviour of the bubbles (ubiquitously present in the near surface of the oceans) and appears to be a suitable instrument for the assessment of the presence of natural and man-made adsorption-film-forming organic materials at the air/water interface.

1 Introduction

Interfacial properties play an important role in many natural processes occurring in the marine environment. A multitude of natural or man-made organic substances escape homogeneous distribution in the water column

and spontaneously segregate at interfaces (specifically, air-water interfaces or bottom and suspended sediment-water interfaces).

At the upper ocean microlayer and at the boundary layer confining the air bubbles, among other various physical and chemical effects, organic materials significantly alter the surface tension of water, γ. In slick covered sea surfaces, depressions of γ exceeding 20 mN m^{-1} have been observed.

Certainly, equilibrium surface tension (or surface pressure) is of basic importance. However, as regards interfacial processes in the marine environment, dynamic surface tension (time domain), $\gamma(t)$, or the surface dilational modulus (frequency domain), $\varepsilon^*(i\omega)$, is far more important than the static quantity. It is now firmly established that the existence of the dynamic quantity significantly modifies various interfacial phenomena.

In particular, organic materials at the upper ocean microlayer (sea surface slicks) are of considerable importance to the surface hydrodynamics. In fact, the presence of (adsorbed or spreading) surface films affects to a various extent the surface tension of sea water and, consequently, influences the process of capillary wave damping. The change of surface roughness in turn is reflected in the sea surface imagery, as observed in different ranges of the electromagnetic spectrum.

Extension-contraction of the sea-surface area (by wave motion, by internal waves and by convection) prevents from reaching adsorption equilibrium. Then, the surface properties in the marine environment show a large spatial and temporal variability, depending on amount and nature of the dissolved organic compounds and on the meteo-marine conditions. The actually-occurring surface properties of sea water can be evaluated by measurements at sea (either *in situ* or by remote sensing).

Laboratory tests may provide additional quantitative information on different physico-chemical properties, useful to predict the environmental behaviour of the complex mixture of natural and man-made organic compounds encountered in marine waters. In particular, in previous articles we dealt with laboratory measurements of static and dynamic surface tension of sea water samples (Loglio et al. 1986, 1987, 1998a).

Herein, our concern is to assess the suitability of the oscillating bubble tensiometer for marine purposes. Essentially, we conducted the present investigation with the aim of estimating the sensitivity of the measurement method, with respect to oceanographic studies and monitoring. In this paper we illustrate preliminary experimental results, obtained with a typical apparatus, working in an onshore laboratory.

2 Experimental

2.1 Instrument

The measuring system is the oscillating bubble tensiometer, described in detail elsewhere (Loglio et al. 1996, 1998b, 2001, Kovalchuk et al. 2001, Miller et al. 2000). Figure 1 shows a schematic drawing of the measurement assembly, which is composed of three parts: 1) the sample (20 mm x 20 mm x 40 mm) pyrex vessel, 2) the capillary (2.00 mm internal diameter stainless-steel tube with flat tip), 3) an air chamber with deformable walls (made with piezoelectric discs). Possible fluidodynamic instability of the bubble has been taken into account in the design of the bubble pneumatic circuit.

The instrument was located inside a small onshore laboratory, at the Municipal Aquarium of Leghorn (Italy). Measurement procedure, calibration and bubble profile processing were performed as previously described (Loglio et al. 1996, 1998b, 2001, Kovalchuck et al. 2001, Miller et al. 2000).

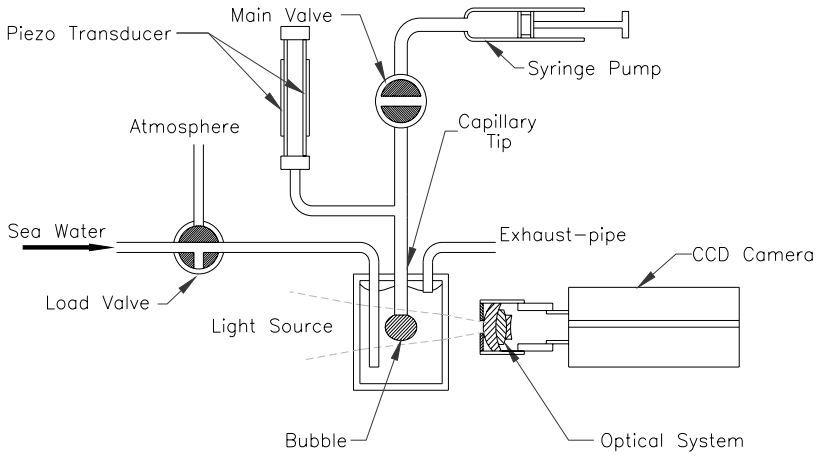

Fig. 1. Schematic diagram of the measurement assembly

2.2 Materials

Sea water samples were collected in the Tyrrhenian Sea, in front of the onshore laboratory. *n*-Dodecyl-dimethylphosphine oxide ($DC_{12}PO$) was purchased from Gamma-Service, Berlin. Water was doubly distilled from alkaline permanganate.

3 Results and discussion

3.1 Functionality of the instrument

The apparatus used in the present study is based on the axi-symmetric bubble shape analysis, i.e., a firmly established technique for the measurement of static and dynamic surface tension as well as of the geometrical properties of the bubble (Loglio et al. 1996, 2001, Kovalchuk et al. 2001, Miller et al. 2000, Rusanov and Prokhorov 1996, Neumann and Spelt 1996, Cheu et al. 1998). In essence, the shape of a bubble (or of a drop) is determined by a combination of surface tension and gravity effects. Surface forces tend to make drops and bubbles spherical whereas gravity tends to elongate them.

Drops and bubbles are indeed the same mathematical object. However, in marine water studies, the profile analysis of captive (or emerging) bubbles is preferable in respect to the analysis of drops. Actually, from the physical point of view, bubbles exhibit some differences in respect to drops: a) diffusion to the air-water interface from a semi-infinite medium (rather than from the small volume confined by the drop); b) limited evaporation; c) possibility of observing bubble properties both in quiescent hydrodynamic conditions or in laminar flow regime. Moreover, a captive bubble can be expanded to very large dimensions.

The overall instrumentation, used in the present investigation, is essentially a laboratory assembled system. Today a number of commercial setups and respective software packages exist, yielding the same quality of results as the present laboratory-assembled instrument. As an example, the drop and bubble shape tensiometer PAT1 from Sinterface Technologies Berlin, Germany, is an accurate instrument with a large number of measurement procedures. Such an equipment shows a special mode of controlling the surface area of the bubble (constant area or changing area as a function of time), which is a vital prerequisite for experiments with bubbles.

We take advantage from recent rapidly-growing developments in numerical image processing. After setting the experiment parameters for each particular run, all operations are automatically performed by a proper software (Loglio et al. 2001). At the start, an air bubble is generated at the capillary tip, inside the liquid phase, with a selected value of surface area. Then, the bubble area is continuously controlled by the computer programme, according to a predefined (transient or periodic) time function. At given (unevenly-spaced) time intervals, bubble profiles are acquired and stored; hence, the synchronous values of surface tension and surface area are determined (the Laplace equation, relating surface tension to interfacial

curvature and differential bubble pressure, is the theoretical principle of measurement (Loglio et al. 1996, 2001, Kovalchuk et al. 2001, Miller et al. 2000, Rusanov and Prokhorov 1996, Neumann and Spelt 1996, Cheu et al. 1998).

In order to describe a liquid meniscus and hence to obtain the interfacial tension from the shape of a drop or bubble the Laplace equation is used. This equation describes the mechanical equilibrium of two homogeneous fluids separated by an interface (Rusanov and Prokhorov 1996, Neumann and Spelt 1996) and relates the pressure difference across the interface to the surface tension and the curvature of the interface

$$\gamma\left(\frac{1}{R_1}+\frac{1}{R_2}\right)=\Delta P \tag{1}$$

Here R_1 and R_2 are the two principal radii of curvature, and ΔP is the pressure difference across the interface. ΔP can be expressed as a linear function of the elevation

$$\Delta P = \Delta P_0 + (\Delta\rho)gz \tag{2}$$

where ΔP_0 is the pressure difference at a reference plane, $\Delta\rho$ is the density difference between water and air, g is the gravity constant and z is the vertical height of the bubble measured from the reference plane. The earliest efforts in the analysis of axisymmetric interfaces (drops and bubbles) were those of Bashforth and Adams (1883). Later many authors improved the calculations by using computer programmes to integrate the Laplace equation. An important step ahead was the development of the Axisymmetric Drop Shape Analysis (ADSA), which allows fitting the Laplace equation to the shape of drops or bubbles obtained by a video camera (Neumann and Spelt 1996). Today, due to increased quality of the video chips, the various corrections introduced into the ADSA package became less important so that simple calibration procedures can be applied rather than a calibration with a grid covering homogenously the whole field of the screen. It has been demonstrated that a determination of the magnification by using a single sphere is usually sufficient to reach high accuracy of the measurements, typically better than 0.1 mN m^{-1}.

The oscillating bubble tensiometer, devised for marine studies, shows a particular feature, consisting of a couple of inlet and outlet tubes (Figure 1). Such conduit allows sea water to be fed either from the sampling bottle or directly from a continuously-flowing pumping system, submersed in the sea. Then, the tensiometer vessel can be initially flushed with sea water for

some minutes, prior to each measurement run. Also, the measurements can optionally be repeated on successive portions of sea water.

In this connection, considering the potential problem of surfactant loss to the apparatus, we remark that the procedure of an initial flow of sample water through the tensiometer vessel is mandatory in all circumstances when the concentration of soluble or almost-insoluble surfactants is very low. Actually, at first significant amounts of the surfactants become lost via adsorption onto the glass-vessel walls or loss of material due to adsorption at the bubble surface (Miller 2004). Consequently, the water flow through the vessel should continue until the adsorption equilibrium is reached. The instrument proved to be relatively insensitive to vibrations, as reported by Loglio et al. (1998b). Thus, the observed functionality, inside the onshore laboratory, may likely be fulfilled on a platform-based location, too.

3.2 Performances of the instrument

Figure 2 shows the surface tension response values, $\gamma(t)$, in concomitance with a trapezoidal pulse of surface area, $\Delta \ln A\,(\,t\,)$, for a sea water sample collected in the late winter. A constant value of $\gamma(\,t\,)$, as seen in the figure, indicates that no (soluble or insoluble) film is present at the bubble surface, even after a long time.

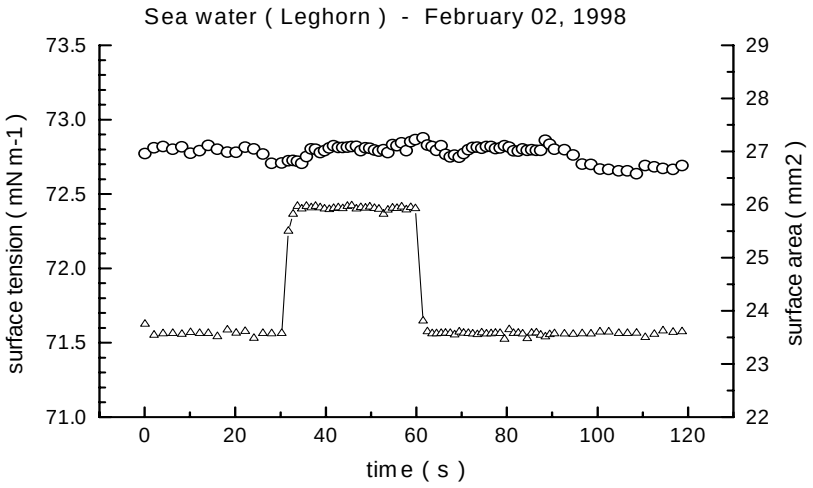

Fig. 2. Surface tension values as a function of time, $\gamma(\,t\,)$ (upper symbols), in concomitance with a trapezoidal pulse of relative surface area, $\Delta \ln A(\,t\,)$ (lower symbols), for a sea water sample collected in the Tyrrhenian Sea. Observed values after 3 hours from the instant of bubble formation. Temperature T = 22.0 °C

Figure 3 displays a sequence of responses of dynamic surface tension, excited by harmonic disturbances of the bubble surface area, for a sea water sample collected in the late summer. By keeping the bubble surface at a constant value during increasing time intervals, the $\gamma(t)$ response progressively shifts toward a lower value, but with a larger oscillation amplitude. Such behaviour manifests a slowly adsorbing organic material.

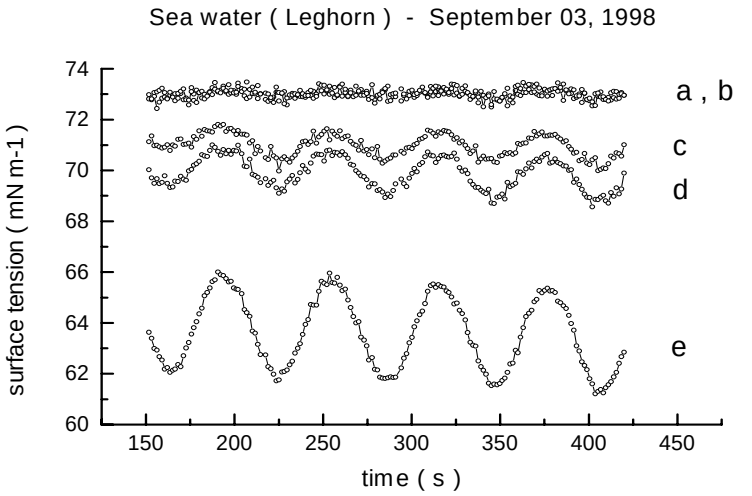

Fig. 3. Time evolution of the dynamic surface tension response, $\gamma(t)$, excited by harmonic changes of relative surface area, $\Delta \ln A(t)$, for a sea water sample collected in the Tyrrhenian Sea. Observed values at different time of bubble surface creation: **a)** fresh bubble surface; **b)** 10-minute age; **c)** 40-minute age; **d)** 1-hour age; **e)** 3-hour age. Temperature T = 20.0 °C

Figure 4 represents a (zoomed) part of the $\gamma(t)$ data of Figure 3, together with the (synchronous) surface area data. In this case, the phase angle between response and perturbation is almost zero. In other words, the film appears as purely elastic. In contrast, a viscoelastic film shows an anticipating response, as Figure 5 illustrates for example.

The relationship between dynamic surface tension, $\gamma(t)$, and surface viscoelasticity (which is one of the parameters relevant to wave damping) is well defined in the literature (Loglio et al. 1994, 1995, Dukhin et al. 1995, Noskov and Loglio 1998, Zholkovskij et al. 2000, Kovalchuk et al. 2000, 2004, 2005, Joos 1999, and references therein). Figures 2-5 also demonstrate a satisfactory sensitivity for marine applications of the measurement technique.

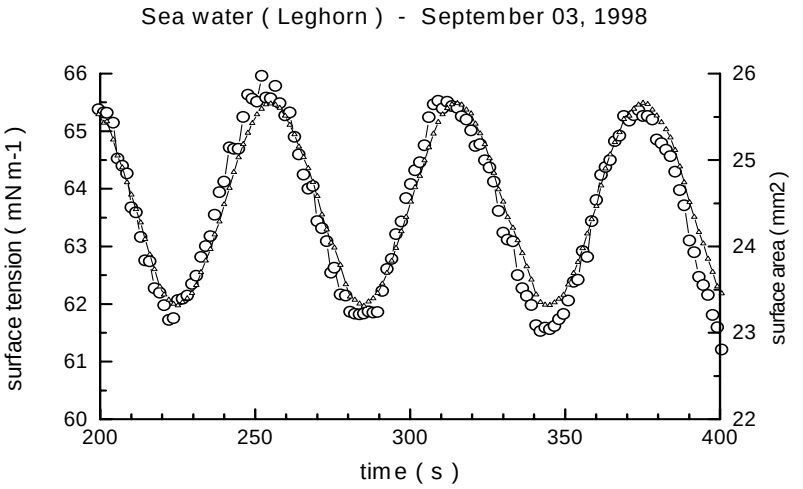

Fig. 4. Same values of dynamic surface tension as in Fig. 3, panel e) (circles, left axis scale), together with the synchronous values of surface area (small triangles, right axis scale)

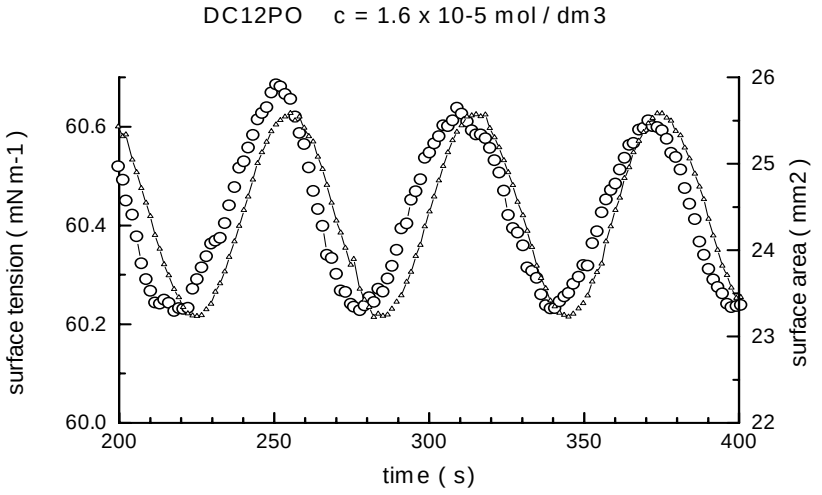

Fig. 5. Example of phase difference between dynamic surface tension response (circles, left axis scale) and input area perturbation (small triangles, right axis scale), for a submicellar aqueous solution of a standard surfactant (DC12PO), at concentration c = 1.6 x 10-5 mol dm-3. Temperature T = 22.0 °C

4 Conclusions

Considering the functionality and performances of the oscillating bubble instrument, described here, we conclude that the instrument is suitable for oceanographic studies. In particular, the obtained results allow us to assess the “availability to the surface” of adsorption-film-forming substances, on a long time scale, and to determine the surface rheological properties. In other words, we get useful information for describing and interpreting the behaviour of surfactant films (sea-slicks, formed under weak meteorological conditions), which are responsible for wave damping and reflectivity modulation over a broad range of frequencies (from the visible to the microwave regions of the spectrum).

Acknowledgements. This work was supported by the European Commission DG XII (INCO-Copernicus Contract No. ERB-IC15-CT96-0809, DG 12 - CDPE), INTAS (Ref. No. 96 -1665) and by the Italian Space Agency (Contract No. ASI ARS-96-103).

5 References

Bashforth F and Adams JC (1883) An attempt to test the capillary action, Cambridge University Press and Deighton Bell & Co., Cambridge

Chen P, Kwork DY, Prokop RM, del-Rio OI, Susnar SS and Neumann AW (1998) “Axisymmetric drop shape analysis (ADSA) and its applications”, in Drops and bubbles in interfacial research, D. Moebius and R. Miller Eds., Studies in Interface Science Series, Vol. 6, Elsevier, Amsterdam

Dukhin SS, Kretzschmar G and R. Miller R (1995) Dynamic of adsorption at liquid interfaces. Theory, experiments, applications, D. Moebius and R. Miller Eds., Studies in Interface Science Series, Vol. 1, Elsevier, Amsterdam

Joos P (1999) Dynamic Surface Phenomena, VSP, Utrecht, 1999

Kovalchuk VI, Zholkovskij EK, Krägel J, Miller R, Fainerman VB, Wüstneck R, Loglio G and Dukhin SS (2000) Bubble Oscillations in a Closed Cell. J Colloid Interface Sci 224: 245-254

Kovalchuk VI, Krägel J, Aksenenko EV, Loglio G and Liggieri L (2001) "Oscillating bubble and drop techniques", in Novel Methods to Study Interfacial Layers, Studies in Interface Science, D. Möbius and R. Miller (Eds.), Vol. 11, Elsevier, Amsterdam, pp. 485-517

Kovalchuk VI, Krägel J, Makievski AV, Ravera F, Liggieri L, Loglio G, Fainerman VB and Miller R (2004). Rheological surface properties of C12DMPO solution as obtained from amplitude- and phase-frequency characteristics of oscillating bubble system. J Colloid Interface Sci 280: 498-505

Kovalchuk VI, Miller R, Fainerman VB and Loglio G (2005). Oscillating bubble pressure experiments for dilational rheology studies. Adv Colloid Interface Sci 114-115: 303-313

Loglio G, Tesei U, Cini R (1986) Dissolved organic compounds in marine waters: Characterization of adsorption processes by means of surface dilational properties. Boll Oceanolog Teor Appl 4: 91-96

Loglio G, Tesei U and Cini R (1987) Surface thermodynamic quantities and rheological properties of the air-sea surface microlayer. Transient techniques of measurement. Boll Oceanolog Teor Appl 5: 195-205

Loglio G, Miller R, Stortini A, Tesei U, Degli-Innocenti N and Cini R (1994) Non-equilibrium properties of fluid interfaces: aperiodic diffusion-controlled regime. 1. Theory. Colloids Surfaces A 90: 251-259

Loglio G, Miller R, Stortini AM, Tesei U, Degli Innocenti N and Cini R (1995) Non-equilibrium properties of fluid interfaces: aperiodic diffusion-controlled regime 2.Experiments. Colloids and Surfaces A 95: 63-68

Loglio G, Tesei U, Pandolfini P and Cini R (1996) A software-driven apparatus designed for measuring geometrical and physical properties of a large bubble formed at a capillary tip. Colloids Surfaces A 114: 23-30

Loglio G, Pandolfini P, Miller R, Noskov B, Tesei U, Stortini AM, and Cini R (1998a), communication presented at EUROMECH Colloquium 387 “Surface Slicks and Remote Sensing of Air-Sea Interactions”, Windmill Village, Coventry, UK , April 7-9

Loglio G, Pandolfini P, Tesei U, and Noskov B (1998b) Measurements of interfacial properties with the axisymmetric bubble-shape analysis technique: effects of vibrations. Colloids Surfaces A 143: 301-310

Loglio G, Pandolfini P, Miller R, Makievski AV, Ravera F, Ferrari M and Liggieri L (2001) "Drop and Bubble Shape Analysis as Tool for Dilational Rheology Studies of Interfacial Layers", in "Novel Methods to Study Interfacial Layers", Studies in Interface Science, Vol. 11, D. Möbius and R. Miller (Eds.), Elsevier, Amsterdam, pp 439-485

Miller R, Loglio G, Tesei U and Schano K-H (1991) Surface relaxations as a tool for studying dynamic interfacial behavior. Adv Colloid Interface Sci 37: 73-96

Miller R, Fainerman VB, Aksenenko EV, Makievski AV, Kraegel J, Liggieri L, Ravera F, Wuestneck R, and Loglio G (2000) "Surfactant Adsorption Kinetics and Exchange of Matter for Surfactant Molecules with Changing Orientation within the Adsorption Layer" in Emulsion, Foams, and Thin Films, Mittal and Kumar Editors, Ch. 18, Marcel Dekker, pp. 313-327

Miller R, Fainerman VB, Makievski AV, Leser M, Michel M and Aksenenko EV (2004) Determination of Protein Adsorption by Comparative Drop and Bubble Profile Analysis Tensiometry. Colloids Surfaces B 36: 123-126

Neumann AW and Spelt JK Eds., Applied Surface Thermodynamics, Surfactant Science Series, Vol. 63, Marcel Dekker Inc., New York, 1996

Noskov B and Loglio G (1998) Dynamic surface elasticity of surfactant solutions. Colloids Surfaces A 143: 167-183

Rusanov AI and Prokhorov VA (1996) Interfacial Tensiometry, D. Moebius and Miller R eds, Studies in Interface Science Series, Vol. 3, Elsevier, Amsterdam

Zholkovskij EK, Kovalchuk VI, Fainerman VB, Loglio G, Krägel J, Miller R, Zholob SA and Dukhin SS (2000) Resonance Behavior of Oscillating Bubbles. J Colloid Interface Sci 224: 47-55

Multiple scattering of surface waves by two-dimensional colloid systems

Boris A. Noskov[1] and Giuseppe Loglio[2]

[1]St.Petersburg State University, Department of Colloid Chemistry,
St. Petersburg - Staryj Petergof, Russia
[2]Universita degli Studi di Firenze, Dipartimento di Chimica Organica,
Sesto Fiorentino, Firenze, Italy

Abstract. Propagation of capillary waves along the surface of water covered by a homogeneous insoluble film has been a subject of numerous experimental and theoretical studies. However, it has been shown only recently that real surface films contain two-dimensional aggregates, which influence the characteristics of surface waves. The problem of multiple scattering of surface waves by two dimensional viscoelastic particles is considered briefly below. The results can be compared with the experimental data for condensed films with two-dimensional bubbles of gaseous phase.

1 Introduction

Insoluble monolayers on an aqueous substrate have been investigated by means of the capillary wave method for many years. Lucassen and Hansen (1966) in their pioneering work neglected the surface viscosity and considered only pure elastic films. Subsequent studies showed that the surface elasticity of real surface films is a complex quantity, and both the equilibrium surface properties and the kinetic coefficients of relaxation processes in the films influence the characteristics of surface waves. However, it has been discovered recently that the real situation is even more complicated and the macroscopic structure of surface films influences the dependency of the damping coefficient of capillary waves on the area per molecule (Miyano and Tamada 1992, 1993, Noskov and Zubkova 1995, Noskov et al. 1997, Chou and Nelson 1994, Chou et al. 1995, Noskov 1991, 1998, Hühnerfuss et al. this issue). Some peculiarities of the experimental data can be explained, if one takes into account the capillary wave scattering by two-dimensional particles (Noskov et al. 1997).

Articles by Miyano and Tamada (1992, 1993), and Wang et al. (1994) also contain some experimental results indicating the influence of surface film heterogeneity on the propagation of capillary waves. The authors noticed that the lack of elaborate theory restrains further progress in this field. The influence of the effects of multiple scattering on the propagation velocity of surface waves is the main subject of this work.

2 Results and Discussion

At first we will consider the liquid-gas interface and linear surface waves incident on a two-dimensional particle of the radius a (Fig. 1) under the following main assumptions: the liquid is incompressible and Newtonian, the two-dimensional particle has a circular shape, the amplitude of the waves *A* is much less than the wavelength, the front of incident waves is a straight line, the excess of the energy dissipation in the transitional region at the border of the particle (Fig. 1) is negligible in comparison with the whole energy dissipation in the liquid under the two-dimensional particle.

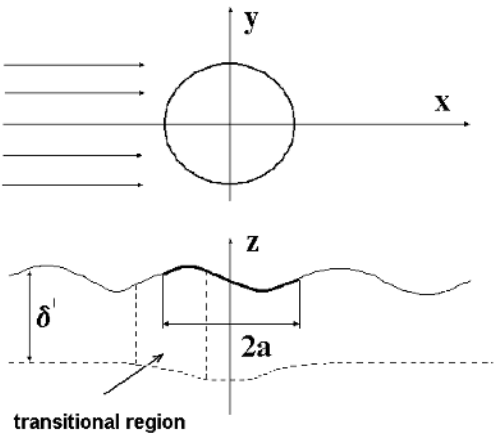

Fig. 1. Scattering of surface waves by a single two-dimensional particle

The energy of the wave motion is mainly dissipated in the vortical layer at the surface. The thickness of this layer δ depends on the wave number k and, consequently, on the surface properties, which are different in the inner and outer regions. This leads to a transitional region in the liquid at the boundary between two-dimensional phases where the liquid motion is significantly more complicated than at a distance from the boundary line.

The solution of the equations of liquid dynamics, which correspond to the propagating plane surface waves, takes the form

$$\begin{aligned} p &= -\rho g z + \mathrm{i}\omega A e^{kz+ikx+i\omega} \\ v_x &= -ikAe^{kz+ikx+i\omega} + mBe^{mz+ikx+i\omega} \\ v_z &= -kAe^{kz+ikx+i\omega} - ikBe^{mz+ikx+i\omega} \end{aligned} \tag{1}$$

where x,y,z are the cartesian coordinates, p is the pressure, v_x , v_z are the components of the liquid velocity, t is the time, g is the gravitational acceleration, ω is the angular frequency, $m^2 = (k^2 + i\omega\rho/\mu)$, $Re(m) > 0$, ρ is the density of the liquid, μ is the viscosity.

In the outer region the wave field is a superposition of the incident wave (1) and the scattered wave. The latter is described by special cylindrical functions (Hankel functions). The cylindrical functions of another type (Bessel functions) also describe the wave motion in the inner region. The conditions at the boundary line between two-dimensional phases allow us to "sew together" the solutions of the hydrodynamic equations in the inner and outer regions. The wave motion in the transitional region can be rather complicated. However, if we are not interested in the details of the liquid dynamics in the transitional region, we can continue the solutions, which were obtained at a distance from this region, up to the boundary line.

The conditions at the boundary line can be reduced to the following four equations:

1. The balance of the surface forces normal to the boundary line (the diagonal components of the surface tension tensor σ_n)

$$\sigma_n - \sigma_n^0 = \frac{\chi}{R} \tag{2}$$

   where χ is the line tension, R is the radius of the curvature, the superscript "0" indicates the inner region.
2. The balance of tangential forces.
3. The continuity equation for the normal components of the bulk pressure tensor in the liquid at the boundary line at $z = 0$.
4. The continuity of the velocity vector at the boundary line.

The scalar potential of the scattered wave φ_2 in the cylindrical coordinates r, ϑ, z takes the form

$$\varphi_2 = e^{kz+i\omega t} \sum_{n=0}^{\infty} A_{2n} H_n^1(kr) \cos n\vartheta, r > a \tag{3}$$

where H^1_n is the Hankel function of the first kind, A_{2n} are the amplitudes of the corresponding harmonics like the coefficient A in expression (1).

Using the Helmholtz theorem the vector potential of the scattered wave $\vec{\Psi}_2$ can be represented as a sum of two components

$$\vec{\Psi}_2 = \Psi_{21}\vec{e}_z + \vec{rot}(\Psi_{22}\vec{e}_z), r > a \tag{4}$$

where

$$\Psi_{2j} = e^{m_j z + i\omega t}\sum_{n=0}^{\infty} B_{nj} f_{nj} H_n(k_j r);\ \ f_{1n} = \sin n\vartheta;\ f_{2n} = \cos n\vartheta \tag{5}$$

and B_{nj} are the expansion coefficients.

One can find the wave numbers m_j from the conditions at the interface. Note that the potential ψ_{21} relates to the shear surface waves. This wave motion rapidly fades away at a short distance from the boundary between two-dimensional phases.

The boundary conditions allow us to find the scattering amplitude (the coefficients A_{2n}, B_{n2}). In the case of long waves ($ka<<1$), it is sufficient to consider only the first two harmonics. For transverse surface waves ($m>>k$, $A>>B$) the corresponding expressions for A_{20} and A_{21} as developed in Noskov (1991) take the form

$$A_{20} = -\frac{i\pi\pi^2}{4} A\left\{\left[\left(k^0\right)^2 \frac{\sigma^0}{\sigma} - k^2\right] - \frac{k^3}{m}\left(1 - \frac{\varepsilon}{\varepsilon^0 - \kappa/2a}\right)\right\}(1 - \frac{k}{m})^{-1} \tag{6}$$

$$A_{21} \approx \frac{\pi a^2 k^2}{2}\frac{\sigma^0 - \sigma}{\sigma + \sigma^0} A \tag{7}$$

where σ is the surface tension, ε is the complex longitudinal dynamic surface elasticity, which takes into account both the dilational and shear surface viscoelasticity (Noskov 1991, Noskov and Zubkova 1995).

For transverse waves the amplitudes of potential flow exceed by a few orders of magnitude the amplitudes of the vortical flow: $A_{20} >> B_{o2}$ and $A_{21} >> B_{12}$. This means that the inhomogeneities of surface tension mainly scatter the capillary waves, and the inhomogeneities of the dynamic surface elasticity play a minor role.

The obtained results allow us to calculate the scattering cross section and the corresponding effective damping coefficient. However, the real surface films usually can be considered as two-dimensional colloid sys-

tems, where one can take into account the effects of multiple scattering of surface waves.

If $A >> B$ (scattering of transversal surface waves) (Fig. 2), one can approximately consider the liquid motion to be potential and to introduce the scalar potential φ, which will satisfy the following equation

$$(\Delta + k^2)\varphi(r) = 0 \tag{8}$$

The exciting field acting upon the scatterer with the centre in the point r_1 $\varphi^E(r/r_1)$ is a sum of the incident wave φ^{inc} and the waves scattered by other particles. The contribution of the given particle depends on the distribution of the other scatterers. If the scattering is weak ($n_0 Q_s/k << 1$, where Q_s is the total scattering length and n_0 is the number density of the particles), the configurationally averaged exciting field $\left\langle \varphi^E \right\rangle$ is the solution of the following integral equation (Waterman and Truell 1961)

$$\left\langle \varphi^E(r/r_1) \right\rangle = \varphi^{inc}(r) + \int dr' n(r'/r_1) T(r') \left\langle \varphi^E(r/r') \right\rangle - R(r/r') \tag{9}$$

where $T(r')$ is the scattering operator, $n(r'/r_1)$ the conditional density of the scatterers, R a correction taking into account correlations between the scatterers. In the following we will assume that $R=0$.

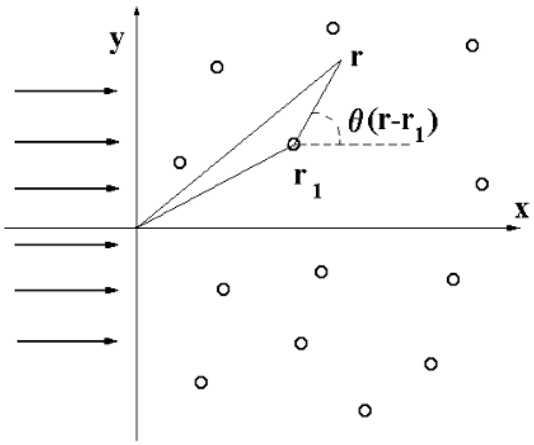

Fig.2. Scheme of multiple scattering

The solution of Eq. (9) takes the form (Noskov 1998)

$$\left\langle \varphi^E (r / r_1 \right\rangle = e^{kz+i\omega t} \sum_{n=0}^{\infty} C_n(x_1) J_n(k|r-r_1|) \cos n\vartheta(r-r_1) \tag{10}$$

where $\vartheta(r\text{-}r_1)$ is the angle between the vector $r\text{-}r_1$ and the x axis.

The scattering amplitude can be defined by the following equations

$$T(0) \xrightarrow[r\to\infty]{} f(\vartheta)\frac{e^{ikr}}{\sqrt{r}}; \qquad f(\vartheta) = \frac{1-i}{\sqrt{\pi k}} \sum_{n=0}^{\infty} \varepsilon_n \tilde{A}_n \cos n\vartheta \tag{11}$$

where $\varepsilon_0=1$, $\varepsilon_n=2$ at $n=1,2,...$; $A_{2n} = A\varepsilon_n i^n \tilde{A}_{2n}$.

Under the conditions of scattering the phase velocity of capillary waves will deviate from the value for the medium without scatterers. Therefore, it is natural to introduce an effective wave number K for the former case and to choose the following trial functions for the coefficients C_n

$$C_n(x_1) \propto e^{iKx_1} \tag{12}$$

Eqs. (9)-(12) allow us to obtain the following expression for the complex effective wave number after rather cumbersome transformations (Noskov 1998)

$$K^2 = [k + (1-i)\sqrt{\frac{\pi}{k}} n_0 f(0)]^2 - [(1-i)\sqrt{\frac{\pi}{k}} n_0 f(\pi)]^2 \tag{13}$$

where $f(0)$ and $f(\pi)$ are the forward and the backscattered amplitudes

$$f(0) = \frac{1-i}{\sqrt{\pi k}} \sum_{j=0}^{\infty} \varepsilon_j \tilde{A}_{2j}; \qquad f(\pi) = \frac{1-i}{\sqrt{\pi k}} \sum_{j=0}^{\infty} (-1)^j \varepsilon_j \tilde{A}_{2j} \tag{14}$$

Relation (13) is the main result. It allows us to determine the effective wave number at the propagation of surface waves along the interface with two-dimensional scatterers on the basis of the scattering characteristics on a single particle. As it could be expected, the difference from the three-dimensional case only consists in the form of coefficients $f(0)$ and $f(\pi)$ and also in the form of the expressions for the scattered amplitudes in themselves.

If the condition of weak scattering is satisfied and scatterers are statistically independent, Eq. (13) holds for two-dimensional particles of all sizes. The condition of "two-dimensionality" of scatterers is not too rigid. It is only important that the scattered wave approximately satisfied the Eq. (8) and it was possible to define the scattered amplitude. Probably a rather large group of particles meets these conditions, for example, three-dimen-

sional particles, which are held off at the interface by capillary forces, if the wavelength exceeds their size.

In the general case transverse surface waves have a vortical component and Eq. (8) is assumed to be an approximation only. This means that Eq. (13) does not allow to calculate the damping coefficient. However, the real part of the complex wave number K for slightly damped capillary waves ($ReK >> ImK$) can be estimated.

Both the inhomogeneities of the surface tension and of the dynamic surface elasticity scatter capillary waves. In the former case one can estimate the effects of multiple scattering if the line tension and the particle size are known. The existing experimental estimates of the line tension for the boundary between two-dimensional fluidlike phases give too low values, which cannot lead to any measurable scattering effects (Benvegnu and McConnel 1992). The larger numbers can be expected for the boundary between solid-like phases, especially under non-equilibrium conditions. In this case a noticeable influence of the multiple scattering has been predicted (Noskov 1998). Although the fluctuations of the surface elasticity usually almost do not influence the scattering of transversal waves, a special situation arises when the continuous surface film contains regions of a gaseous two-dimensional phase (two-dimensional bubbles). If the dynamic surface elasticity of the scatterer tends to zero, large multiple scattering effects can be observed (Noskov 1998).

Although the Eqs. (13), (14) do not allow us to estimate the contribution of scattering to the effective damping coefficient of surface waves within the assumptions, which have been made in this work, this can be fulfilled with the use of the total scattering length Q_s (Chou and Nelson 1994)

$$\mathrm{Im}\, K = \mathrm{Im}\, k + nQ_S / 2 \qquad (15)$$

The total scattering length was calculated in Noskov (1991). The noticeable changes of the effective damping of surface waves arise simultaneously with the corresponding changes of the wavelength. In this case it is possible to speak about a new mechanism of the wave damping: the effective damping coefficient, which can be measured experimentally, increases at the account of scattering.

Acknowledgements. This work was financially supported by the European Space Agency (FASES MAP AO-99-052). B. A. N. also gratefully acknowledges financial support from the RFFI, NSC of Taiwan (Joint Project 05-03-90580 HHC_a, Project RFFI 03-03-32366) and the grant of the President of the Russian Federation (Leading scientific schools, NSh-789.2003.3).

3 References

Benvegnu DJ and McConnel HM (1992) Line tension between liquid domains in lipid monolayers. J Phys Chem 96: 6820-6824

Chou T and Nelson DR (1994) Surface wave scattering at nonuniform fluid interfaces. J. Chem. Phys 101: 9022-9032

Chou T, Lukas SK and Stone HA (1995) Capillary wave scattering from a surfactant domain. Phys Fluids 7: 1872-1885

Lucassen J and Hansen RS (1966) Damping of waves on monolayer-covered surfaces. I. Systems with negligible surface dilational viscosity. J Colloid Interface Sci 22: 32-44

Miyano K and Tamada K (1992) Capillary wave propagation on water covered with inhomogeneous monolayers: liquid/gas coexistence films. Langmuir 8: 160-163

Miyano K and Tamada K (1993) Capillary wave propagation on water nonuniformly covered with a solid film. Langmuir 9: 508-514

Noskov BA (1991) Dynamic properties of heterogeneous surface layers. Scattering of capillary waves. Izv. AN SSSR, Ser. MZhG, N1 (1): 129-37

Noskov BA and Zubkova TU (1995) Dilational surface properties of insoluble monolayers. J Colloid Interface Sci 170: 1-7

Noskov BA, Grigoriev DO and Miller R (1997) Anomalous Damping of Capillary Waves in Systems with Insoluble Monolayers of Alkyldimethylphosphine Oxides. Langmuir 13: 295-298

Noskov BA (1998) Dynamic properties of heterogeneous surface films: Multiple scattering of capillary waves. J Chem Phys 108: 807-815

Wang Q, Feder A and Mazur E (1994) Capillary Wave Damping in Heterogeneous Monolayers. J Phys Chem 98: 1272-1276

Waterman PC and Truell R (1961) Multiple scattering of waves. J Math Phys 2: 512-537

Laboratory study of the damping of parametric ripples due to surfactant films

Stanislav A. Ermakov and Sergei V. Kijashko

Institute of Applied Physics, Nizhny Novgorod, Russia

Abstract. Laboratory studies of damping of capillary-gravity waves (CGW) due to organic films were carried out in a wide range of surfactant concentrations using a method of parametrically excited surface waves (Faraday ripples) at wave frequencies from about 15 Hz to 30 Hz. The threshold acceleration for CGW excitation and CGW wavelengths were measured and the wave damping and the surface tension coefficients were retrieved for a clean water surface and for water covered with organic films. It is obtained that the damping coefficient for ordinary surface-active substances (e.g., oleyl alcohol and oleic acid) exhibits a maximum at small surfactant concentrations, comparable with the concentrations needed for monomolecular coverage and remains practically constant at large concentrations. The damping coefficient for polymer films (poly-oxyalkylene glycol - “Emkarox”) shows two maxima, one of which is a narrow peak at small concentrations similar to the case of ordinary surfactants, and a "plateau"-like maximum at large concentrations. The dynamic film elasticities are retrieved from the measured damping coefficient using a theory of wave damping for purely elastic films. The dynamic elasticities are shown to differ strongly from the static elasticities, especially at large surfactant concentrations.

1 Introduction.

Damping of gravity-capillary waves due to organic films has been a problem of long-term interest in physico-chemical hydrodynamics (Levich 1962, Lucassen-Reynders and Lucassen 1968), the problem also is very important in oceanography, in particular, in studies of organic slicks on the ocean surface and their remote sensing using radar and optical methods (Alpers and Hühnerfuss 1989, Scott 1986, Scott and Thomas 1999 and the references therein). The most interesting aspect for remote sensing of slicks with C-, X-, K_u-, and K_a-band radars is the damping of centimetre-

millimetre-scale wind ripples with frequencies of about 5 Hz to 50 Hz. It follows from theory (Levich 1962) that the damping action of films on surface waves is determined by the dilational film viscoelasticity. This parameter depends on surface and bulk diffusion, relaxation processes, film viscosity, wave frequency etc. and its measuring is a very difficult problem. Surface films formed by insoluble surfactants, when neglecting surface diffusion and relaxation processes, can be the considered as purely elastic with a constant elasticity modulus E. The latter was measured traditionally using the Langmuir trough technique, which gives us information about "static" elasticity, corresponding to very slow film deformations. However, Hühnerfuss (1986) clearly showed that static or low-frequency elasticity values for the prediction of the damping of cm-mm-scale CGW are not adequate for insoluble surface films at monomolecular coverage (= completely covered water surface). Note, that a new method of estimating the film elasticity at low frequencies (about 1 Hz) was developed based on measurements of parameters of longitudinal waves (Bonfillon and Langevin 1993, Noskov et al. 1998). Previous wave damping measurements were carried out mostly for very short capillary waves with frequencies of about 100 Hz and higher (Lucassen-Reynder and Lucassen 1968, Noskov and Grigoriev 1996, and cited literature), and for decimetre waves with frequencies about 2.5 Hz and smaller (Hühnerfuss et al. 1984). Experimental data on the damping of cm-scale waves, however, are rather scanty at present. Among them are the measuments by Cini et al. (1987) carried out at frequencies 3 Hz – 12 Hz for one chemical at a given concentration, mainly aiming to demonstrate the existence of a maximum of the damping coefficient in the frequency domain. One can note also measurements of wave damping by Pogorzelsky et al. (1984) at a frequency of 30 Hz, and by Garrett and Zisman (1970) at a frequency of 60 Hz. The last experiments were conducted simultaneously with measurements of the film pressure in a Langmuir trough, and the measured damping coefficient was compared with theoretical predictions when using the static film elasticity (Dysthe and Rabin 1986). Qualitative agreement with theory was obtained, although the measurements were carried out with monolayers below monomolecular coverage in a comparably narrow surfactant concentration range. Scott and Stephens (1972) carried out measurements for polymer films in a wide concentration range at a wave frequency of 30 Hz and found some interesting peculiarities of wave damping, which, in particular, are studied further in this paper.

Note, that previous wave damping measurements were conducted for monomolecular films at surfactant concentrations which usually were smaller or comparable with the concentrations representing a completely covered water surface. It follows from measurements by a Langmuir

trough and by the method of longitudinal waves that a static or a low-frequency elasticity modulus tends to zero at concentrations exceeding saturated monolayer concentrations. Correspondingly, one might expect that the damping coefficient tends to its value for a clean water surface. This, however, contradicts to numerous observations of strong wave damping at large concentrations (Hühnerfuss 1986, Ermakov et al. 1995, Henderson 1998), and is also in disagreement with observations of damping in artificial slicks for which mean surfactant concentrations are often large, and which often represent saturated monolayers with microscopic drops of surfactants. Recently, Ermakov et al. (1995, 1996) addressed the problem, when estimating dynamic elasticities of some traditional surfactants at concentrations both below and above monomolecuar coverage.

Here we present an extended study of wave damping due to films of insoluble ordinary surfactants and a polymer substance for a wide surfactant concentration range. Retrieval of the film elasticity from the damping measurements has been performed, and compared with static film elasticity.

2 Experimental

The experimental apparatus comprised a small rectangular container (13.9 cm x 4 cm x 2 cm), an electromagnetic shaker, an accelerometer, and a laser slope wave gauge. Surface waves were excited at a frequency which is half the shaker frequency. In the experiments the threshold acceleration, corresponding to parametric excitation of CGW was measured, and the damping coefficient which is known to be proportional to the threshold acceleration could be retrieved. The wave excitation was detected with a laser slopemeter. The modes of parametrically excited CGW in the container could be clearly observed visually and in photographs, at CGW frequencies of about 10-15 Hz and larger the plane wave modes with longitudinal wave numbers only were mainly excited. Note, that when changing the surfactant concentration, and as a result, the surface tension coefficient, the mode number and the wavelength of CGW at a given frequency were also changed, CGW of neighboring modes could be excited, too. Therefore, to keep only one mode of CGW and thus to minimize errors in the determination of CGW wavelength and the damping coefficient, some tuning of the shaking frequency to the resonance conditions was needed. In practice, however, this tuning in the considered frequency range was quite small.

Water for experiments was carefully purified using a carbon filter, usually 10-15 purification cycles were performed for each experiment. Before measurements, the water surface in the container was cleaned several times

by skimming with paper, then auxiliary wave measurements were carried out immediately after the cleaning and 10-15 min later to check, if there were surfactants in the bulk water. Different insoluble surfactants - oleyl alcohol, oleic acid and polyoxyalkylene glykol ("Emkarox") - were tested in the present experiment. The surfactants were dissolved in ethanol to spread films at given concentrations. Note, that the viscosity coefficient of an aqueous solution of ethanol is larger, than for pure water, correspondingly ethanol can enhance the damping coefficient. Special experiments were conducted to estimate this effect and to choose proper concentrations of surfactant solutions for which the action of ethanol was small compared with the effect of the surfactants.

3 Theory

The damping coefficient of standing surface waves in a closed container can be written in the form

$$\gamma = \gamma_w + \gamma_s + \gamma_c \tag{1}$$

where γ_w , γ_s ,and γ_c denote the damping coefficients due to the container walls, the water surface and contact line effects, respectively.

The damping due to walls is connected with viscous dissipation within the boundary layers at the walls of a container and can be found easily in the boundary layer approximation (Ermakov et al. 1995)

$$\gamma_w = \sqrt{\frac{\nu\omega}{2}}\left\{\frac{1}{k^2}\left[\left(\frac{m\pi}{a}\right)^2\frac{1}{b}+\left(\frac{n\pi}{b}\right)^2\frac{1}{a}\right]\cdot\left(1+\frac{2kh}{sh(2kh)}\right)+\left(\frac{1}{a}+\frac{1}{b}\right)\cdot\left(1-\frac{2kh}{sh(2kh)}\right)+\frac{kh}{sh(2kh)}\right\} \tag{2}$$

where $k^2 = \left(\frac{m\pi}{a}\right)^2 + \left(\frac{n\pi}{b}\right)^2$, ν denotes the kinematic viscosity coefficient of water, k the wave number of a standing CGW mode with indexes (m, n), ω the frequency of a CGW mode with wave number *k*, *a* and *b* the width and the length of a rectangular container, h the water depth.

The damping coefficient due to surface, covered with an elastic film can be written as (Lucassen-Reynders and Lucassen 1969, Cini et al. 1987)

$$\gamma_s = \gamma_0 D \tag{3}$$

where $\gamma_0 = 2\nu k^2$, $D = \dfrac{1 - x + xy}{1 - 2x + 2x^2}$, $x = \dfrac{Ek^2}{\rho(2\nu)^{1/2}\omega^{3/2}}$ and $y = \dfrac{Ek}{4\rho\nu\omega}$.

Here ρ denotes the water density, *E* the film elasticity modulus.

Description of wave damping due to contact line effects needs some empirical data on meniscus velocities (Henderson 1998). Therefore, the third component in (1) is not considered here because of the lack of our knowledge about the phenomenon. One, however, can assume that the contact line effects give a small contribution to wave damping, because the dimensions of the container are large compared with the characteristic capillary scale and the wave amplitudes are small. In particular, since we study the parametric wave excitation near its threshold, i.e., at very small amplitudes, the contact line is nearly "pinned" to the walls. Then, according to Miles' theory of wave damping due to dynamic contact line, the additional wave damping, which is proportional to the speed of the contact line at small speed values (Miles 1991, Henderson 1998), is expected to be small.

4 Results and Discussion

4.1 Clean water

Wave damping in the container with clean water was measured in the frequency range 10 Hz - 32 Hz. Figure 1 shows the experimental total damping coefficients and the damping coefficients calculated for a plane wave mode (m = 1) and "mixed" modes with m = 1,2.

It can be inferred from Figure 1 that the damping coefficient values for the plane mode are practically the same as for the "mixed" modes, i.e., the wall damping coefficient mainly depends on frequency, but not on the mode structure. One, therefore, can conclude, that the mixed modes weakly affect the wave damping coefficient, even if they are excited in experiment. Furthermore, Figure 1 shows that experimental values of the damping coefficient are in reasonable agreement with theory. However, the experimental values are a little smaller than theoretically predicted, thus showing that the measured damping is smaller than a sum of the surface damping and the wall damping for free contact line. This, probably, can be due to the "pinning" of the contact line between the water surface and the walls. According to Hocking (1987) "the damping rate when this edge condition is used is probably less than that for the free-end condition because of the reduction in the movement of the interface at the contact". This assumption, however, needs further special investigations.

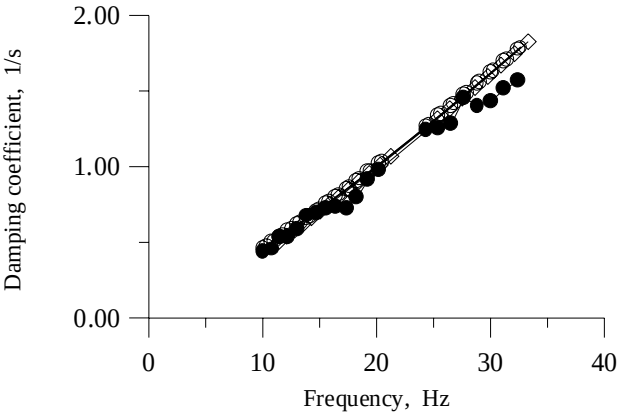

Fig.1. Damping coefficient due to walls and clean water surface. ● - experiment, ◊,○, x – theory for modes 0,1,2

4.2 Wavelengths at film-covered water surfaces

Measurements of the wavelengths of standing CGW were carried out from photographs of the wave patterns in the container. In order to reduce the influence of the meniscus on the wavelength the wave crests/troughs distances were measured for the waves not adjacent to the container walls. The results for CGW at a frequency of 25 Hz are shown in Figure 2.

The surface tension coefficient σ for the studied films can be found easily from the dispersion relationship as follows:

$$\sigma = (\omega^2 - gk)/k^3 \tag{3}$$

Corresponding film pressure values $P = \sigma_0 - \sigma(\Gamma)$ as a function of surfactant concentration Γ, calculated from the wavelength measurements are shown in Figure 3, arrow bars are shown in the last graphic. In Figure 3 the static elasticity values, estimated from the pressure-concentration curves as $E = \Gamma(dP/d\Gamma)$ are also presented (the scale for the values of elasticity and film pressure is the same).

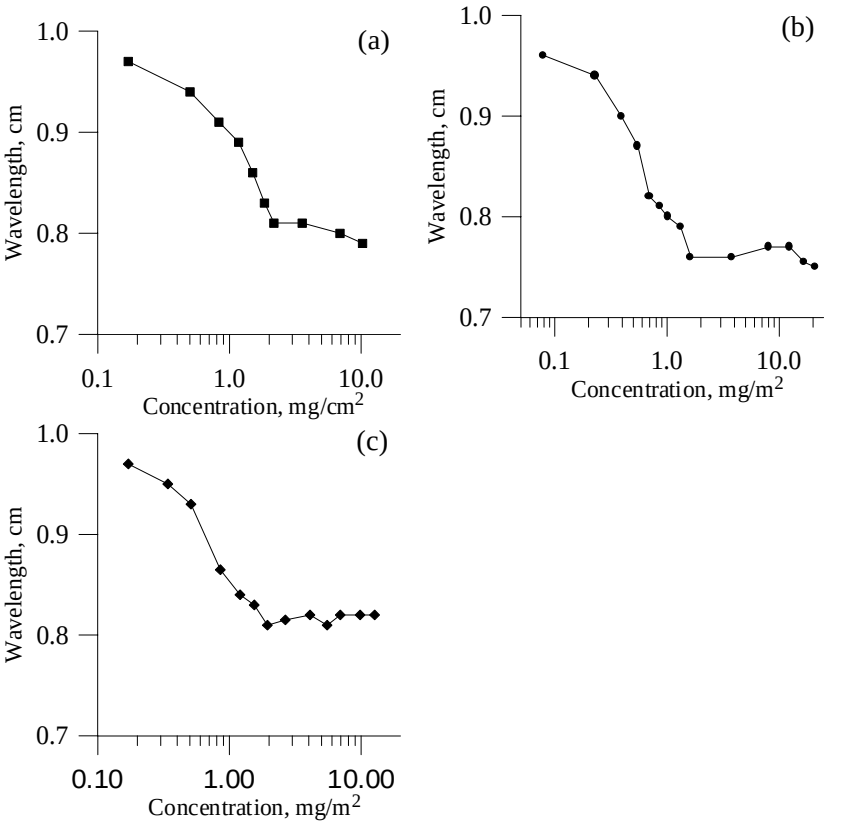

Fig. 2. Wavelength of 25 Hz waves as a function of surfactant concentration of oleyl alcohol (a), oleic acid (b) and Emkarox (c)

It follows from Figure 3 that the film pressure values increase with surfactant concentration tending to nearly constant values at large concentrations, which correspond to monomolecular films reflecting complete monomolecular coverage. The concentrations of the latter films are about (1.5 - 2) mg m^{-2}.

The behaviour of the pressure-concentration curves is analogous to the pressure-concentration curves obtained with Langmuir trough technique. Figure 4 gives examples of static isotherms for films of oleyl alcohol and Emkarox, measured at the University of Southampton with a Langmuir-Blodgett Trough “NIMA 611”. The static elasticity values shown in Figure 4 are calculated from the isotherms (the scale for the elasticity values in Fig. 4 is the same as for the film pressure values).

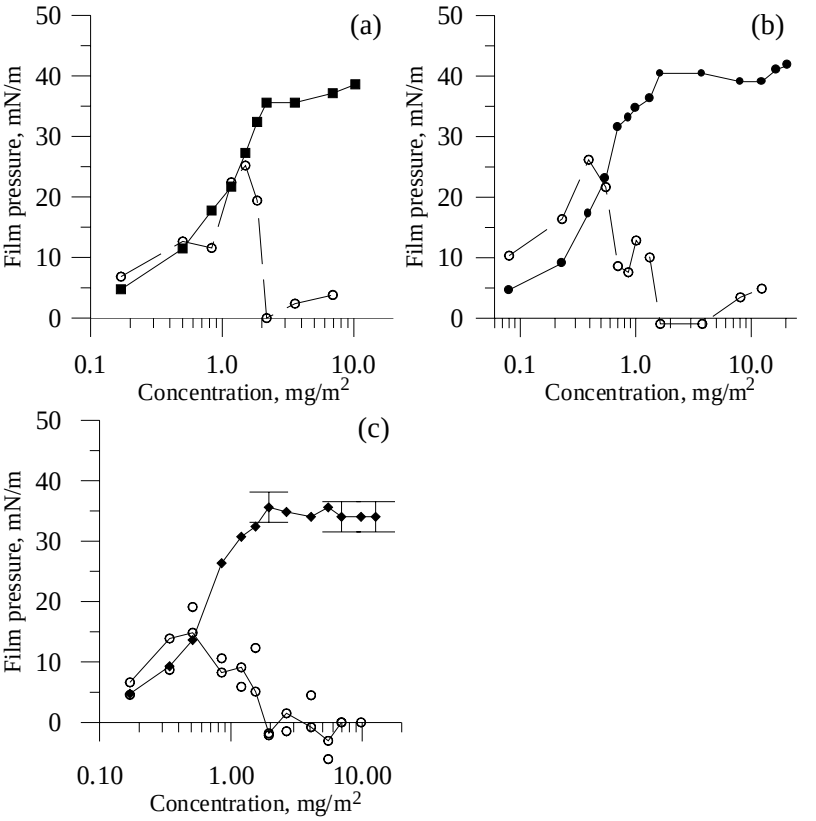

Fig. 3. Film pressure-concentration curves, retrieved from wavelength measurements for films of oleyl alcohol (a), oleic acid (b) and Emkarox (c). ○ – static elasticity values

Some differences between the isotherms and the elasticity curves in Figures 3 and 4 are worth noting. In particular, the concentrations reflecting monomolecular coverage appear to be a little smaller than for the isotherms in Figure 3, the elasticity values in Figure 3 are also smaller than those in Figure 4. This can be connected with enhanced diffusion of surfactants dissolved in ethanol from the surface to the subsurface microlayer due to parametrically excited surface waves and container vibrations.

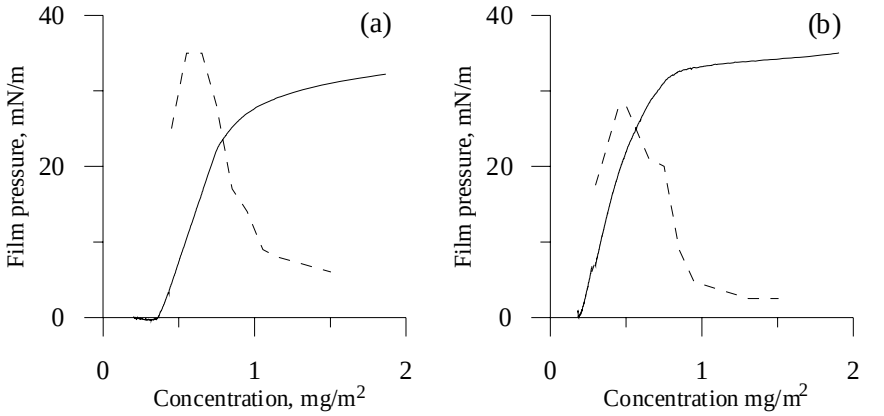

Fig. 4. Pressure-concentration curves and elasticity (dashed lines) for oleyl alcohol (a) and Emkarox (b) obtained from Langmuir trough measurements

In spite of these quantitative differences, qualitatively the behaviour of the static elasticity curves are similar in Figures 3 and 4: the elasticity achieves a maximum at small concentrations of the order of a saturated monolayer concentration and then decreases very quickly tending to small values for saturated films.

4.3 Wave damping coefficients

The measured relative damping coefficients, i.e., the damping coefficient at a given surfactant concentration, normalized by the damping coefficient γ_0 for a clean water surface is shown in Figure 5 at different wave frequencies for oleic acid, oleyl alcohol and Emkarox films.

Note, that the ranges of surfactant concentrations for all substances strongly exceeded the concentrations needed for monomolecular coverage. The damping coefficient curves for oleic acid and oleyl alcohol films exhibit one peak at monolayer concentrations below monomolecular coverage. At large concentrations the damping coefficient for these substances is practically constant. This can be explained by the fact that oleic acid and oleyl alcohol at large concentrations form monomolecular films with the excess of the surfactant material accumulated in small drops ("lenses"); at sufficiently large concentrations the drops can be seen by eye. The small drops do not strongly influence the damping of cm-scale waves, if wave scattering is weak and if the wave periods are low compared with the characteristic relaxation time of the drops. Therefore, the “oversaturated” films simply act on surface waves like a monolayer completely covering the water surface. The low increase in the damping coefficient at very high mean

concentrations for oleyl alcohol (Figure 5) is probably due to the solvent action.

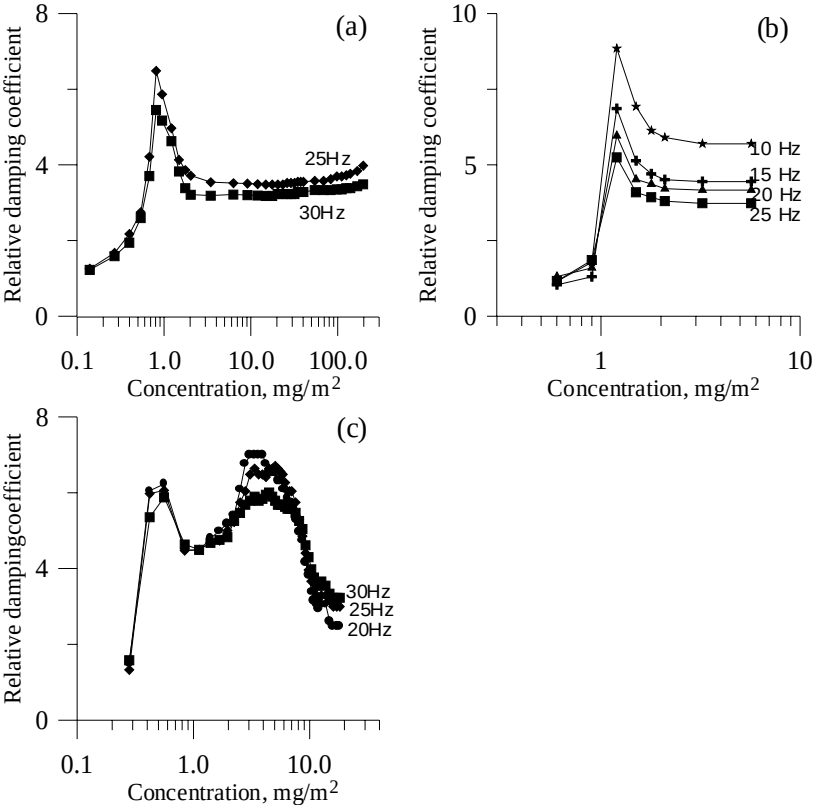

Fig. 5. Relative damping coefficients of oleyl alcohol (a), oleic acid (b) and Emkarox (c) vs. surfactant concentration

The damping coefficient curves for Emkarox films exhibit two peaks: a narrow one at low concentrations of about 0.5 mg m^{-2} and a "plateau"-like maximum in the concentration range from about 2-3 mg m^{-2} to 6-7 mg m^{-2}. The curves are similar in shape to that reported by Scott and Stephens (1971) for a film of soluble polymers. The first part of the damping coefficient curves with the first narrow maximum seems to be similar to the damping curves for monolayers of oleic acid and oleyl alcohol. Probably, polymer molecules at small concentrations unfolded and lay on the water surface interacting with water due to their hydrophilic monomer groups, so that a polymer film at this stage can to some respect be analogous to films formed by ordinary surface-active molecules. At higher concentrations the polymer chains increase the number of loops and tails and the molecules

tend to exist as coils. This can lead to a more complex behaviour of the damping curves.

4.4 Film elasticities

In order to retrieve film elasticities from the damping coefficient values we assumed that the films can be described as purely elastic and the relation between the damping coefficient and the film elasticity parameter is given by expression (3). The problem of retrival of the film elasticity from formula (3) is that there are two elasticity values (two roots) corresponding, in general, to a given damping coefficient value measured at a given wave frequency. The problem of the proper choice of retrieved elasticity values seems to be solved, if the damping coefficients will be measured at several wave frequencies. Then for purely elastic insoluble films the real elasticity value should be equal at different wave frequencies. Usually, however, both the roots for the retrieved elasticity values are different at different frequencies because of experimental errors and because a purely elastic film is only an idealization of real films. Therefore, some additional arguments have to be included to choose a physically significant elasticity value retrieved from damping measurements at a given frequency.

The film elasticity roots retrieved from the data presented in Figure 5 are shown in Figure 6. One should note that the two roots tend to each other at concentrations corresponding to the maxima of the damping coefficients. We assume that a transition of the film elasticity values from one root to another should occur. It will give us a smooth dependence of the elasticity on concentration with a continuous derivative of the elasticity on concentration, which is reasonable from a physical point of view. If to assume the elasticity as one of the roots in the whole concentration range, then the derivative of the retrieved elasticity will have a step-like behaviour at concentrations of the damping maxima.

The resulting elasticity values, using the above criterion are given in Figure 7. Obviously, the elasticity for the ordinary surfactants increases monotonously with concentration tending to some large limiting values at concentrations of the order and larger than monomolecular coverage. The physical arguments in favour of this behaviour are as those presented above. Namely, at concentrations reflecting monomolecular coverage the surface-active molecules are directed practically normal to the water surface and strongly interact with each other, so that the monolayer exhibits high elasticity. At *mean* concentrations exceeding monomolecular coverage the excess of surfactant materials will form microscopic drops. If the periods of surface waves are small compared with the characteristic times of surfactant exchange between the drops and the monolayer, then the

processes of "condensation/evaporation" of the drops when waves compress and dilate the film are insignificant and practically do not affect the resulting film elasticity. The latter is expected to be as high as for the saturated monolayer. We feel that this is the case for high-frequency gravity-capillary waves. At very slow quasistatic film deformations the opposite limiting case can be realized and the film elasticity at concentrations exceeding the saturated monolayer concentrations is nearly zero. Another argument in favour of choosing the high root values at high concentrations for the ordinary surfactants is that the relative damping coefficients slightly decrease with frequency in this concentration range. This, according to theory occurs for large elasticity values.

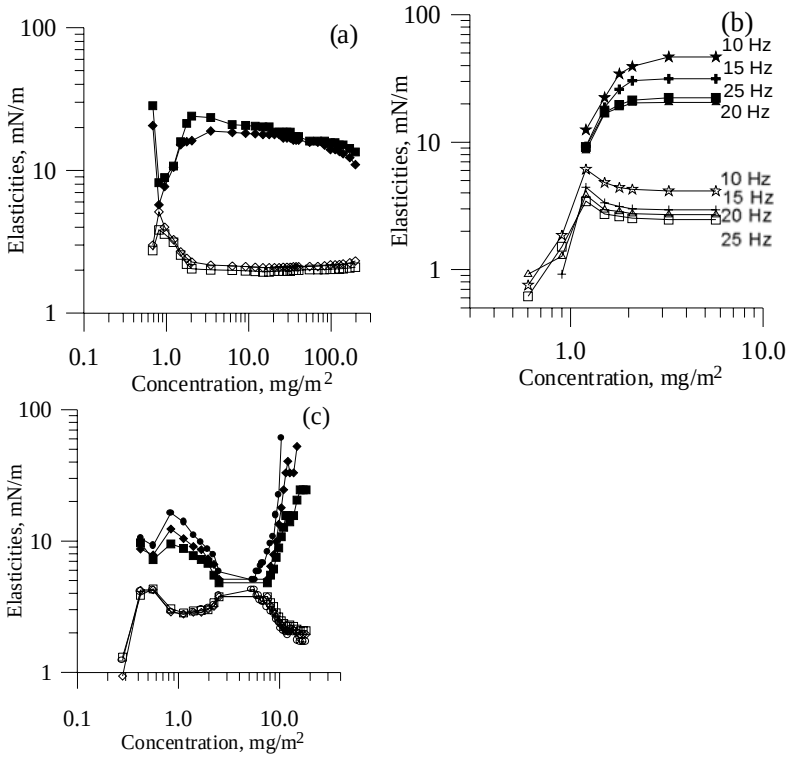

Fig. 6. Elasticity roots of oleyl alcohol (a), oleic acid (b) and Emkarox (c) films, retrieved from the damping coefficient values

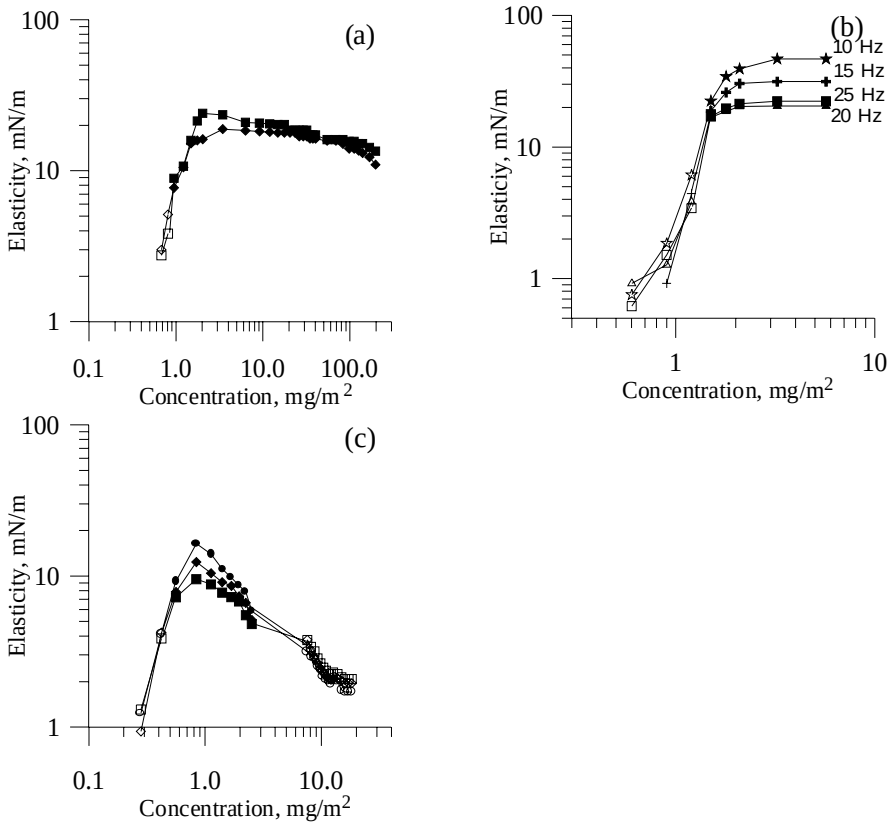

Fig. 7. Retrieved dynamic elasticities of oleyl alcohol (a), oleic acid (b) and Emkarox (c) films

For the Emkarox film at low (smaller than 0.4 mg m^{-2}) and at high (larger than 6-8 mg m^{-2}) concentrations the relative damping increases with frequency, so that we choose the smaller root. Besides, the other root gives unrealistically large values in these concentration ranges. In the intermediate concentration range the relative damping decreases with frequency, and we assume the elasticity described by the upper root. This general behavior of the elasticity of Emkarox polymer films in Figure 7 is similar to that obtained by Scott and Stephens (1972) for soluble polymer film. We hypothesize that at rather low concentrations polymer molecules lie on the water surface forming two-dimensional chains attracting to the surface due to their hydrophylic groups. When the polymer concentration increases, the polymer chains, being two-dimensional, become in stronger interaction to each other thus increasing film elasticity and wave damping. At large concentrations the polymer molecules, presumably, can form three-

dimensional coils which can be more compressible, so that the film elasticity decreases.

5 Conclusions

Laboratory measurements of the damping coefficient and wavelengths of cm-mm-scale surface waves due to ordinary surfactants (oleic acid and oleyl alcohol) and polymer (polyoxyalkylene glycol - “Emkarox”) organic films in a wide concentration range and at different wave frequencies are carried out using a method of paramertically excited waves.

It is shown that the dependencies of the damping coefficient on surfactant concentration are quite different for the ordinary surfactants and for the polymer films. For the ordinary surfactants the damping coefficient achieves a maximum at concentrations of the order of the concentration of saturated monolayers; at higher concentrations the damping coefficient is high and practically constant. For the polymer films the damping coefficient has a low-concentration peak similar to the case of ordinary surfactants and a "plateau"-like maximum at high concentrations.

The dynamic elasticities of the ordinary and polymer films are estimated from the measured damping coefficient using a theory of wave damping for purely elastic films. It is obtained that the elasticity of the ordinary surfactants at the concentrations larger that the saturated monolayer concentration is quite large and does not depend on concentration, while the static elasticity is practically zero in this concentration range. This can be explained by the fact that the ordinary surfactant films at large concentrations represent a saturated monolayer with microscopic drops. The drops weakly affect the wave damping and corresponding dynamic film elasticity in this case is as large as for saturated monolayers.

The estimated dynamic elasticity of the polymer film also differs from the static elasticity. The dynamic elasticity increases with concentration, achieving a maximum at intermediate concentrations (between the two damping coefficient maxima), and then decreases monotoniously to small values at large concentrations.

Acknowledgements. The authors thank Dr. J. Scott for his valuable remarks and discussions of this work. The work was supported by the UK Ministry of Defense through the DERA, Winfrith, UK, via the International Science and Technology Center (Project 1774p), by INTAS (Project 03-51-4987 “SIMP”), and RFBR (projects 05-05-64137, 04-05-64763).

6 References

Alpers W, Hühnerfuss H (1989) The damping of ocean waves by surface films: A new look at an old problem. J Geophys Res 94: 6251-6266

Cini R, Lombardini PP, Manfredi C, Cini E (1987) Ripples damping due to monomolecular films. J Colloid Interface Sci 119: 74-80

Dysthe K, Rabin Y (1986) Damping of short waves by insoluble surface films. In ONRL Workshop Proceedings - Role of surfactant films on the interfacial properties of the sea surface, ed. Herr FL and Williams J, U.S.Office of Naval Research, Arlington, Va, pp 187-213

Ermakov SA, Kijashko SV, Konnov IR (1995) Laboratory study of the damping of gravity-capillary waves on the water surface, covered with insoluble monomolecular films. Preprint N382, Institute of Applied Physics, Russian Academy of Sciences, Nizhny Novgorod

Ermakov SA, Kijashko SV, Konnov IR (1996) On a possibility of determination of surfactant films on a basis of measurements of damping of standing gravity-capillary waves. Izv Akad Nauk Fiz Atmos Okeana 32: 544-547

Henderson DM (1998) Effects of surfactants on Faraday-wave dynamics. J Fluid Mech 365: 89-107

Hocking LM (1987) The damping of capillary-gravity waves at rigid boundary. J Fluid Mech 179: 253-266

Hühnerfuss H (1986) The molecular structure of the system water/monomolecular surface film and its influence on water wave damping. Habilitation thesis, University of Hamburg, Hamburg 1986, 245 pp

Hühnerfuss H, Lange P, Walter W (1984) Wave damping by monomolecular surface films and their chemical structure. Part II: Variation of the hydrophylic part of the film molecules including natural substances. J Mar Res 42: 737-759

Garrett WD, Zisman WA. (1970) Damping of capillary waves on water by monomolecular films of polyorganosyloxanes. J Phys Chem 74: 1796-1805

Miles JW (1991) The capillary boundary layer for standing waves. J Fluid Mech 222: 197-205

Levich VG (1962) Physicochemical Hydrodynamics. Prentice-Hall, Elmsford Park, N.J.

Lucassen-Reynders EN, Lucassen J (1969) Properties of capillary waves. Advan Colloid Interface Sci 2: 347-395

Noskov BA, Grigoriev DO (1996) Kinetic Study of Sodium Decyl Sulfate Solutions by the Capillary Wave Method. Langmuir 12: 3399-3403

Noskov BA, Alexandrov DA, Gumennik EV, Krotov VV, Miller R (1998) Dynamic surface elasticity of solutions of dodecylsulphate Na in the frequency range 0.8Hz-5Hz. Colloid Z 60: 227-234

Pogorzelski St, Linde B, Sliwinski A (1984) Capillary wave attenuation on a water surface coated with monolayers of oil-derivative substances. Acoustics Letters 8: 5-9

Scott JC, Thomas NH (1999) Sea surface slicks - surface chemistry and hydrodynamics in radar remote sensing, in: *Wind-over-wave couplings. Perspectives*

and prospects, eds. Sajjadi, Thomas and Hunt, Clarendon Press, Oxford pp 221-229

Scott JC (1986) Surface films in oceanography, in ONRL Workshop Proceedings - Role of surfactant films on the interfacial properties of the sea surface, ed. Herr FL and Williams J, U.S.Office of Naval Research, Arlington, Va, pp187-213

Scott JC, Stephens RWB (1972) Use of moire fringes in investigating surface wave propagation in monolayers of soluble polymers. J Acoust Soc America 52: 871-878

Wave tank study of phase velocities and damping of gravity-capillary wind waves in the presence of surface films

Stanislav A. Ermakov, Irina A. Sergievskaya, Emma M. Zuikova, Vladimir Yu. Goldblat, and Yury B. Shchegolkov

Institute of Applied Physics, Nizhny Novgorod, Russia

Abstract. The wave number-frequency spectra of gravity-capillary waves were measured using two optical spectrum analysers and an artificial gradient illuminator. It was found that phase velocities of centimetre-millimetre (cm-mm) scale waves on clean water do not obey the dispersion relation of free surface waves, but they increase with fetch, while frequencies of dominant decimetre (dm)-scale wind waves decrease with fetch. This observation implies that the wind wave spectrum contains nonlinear cm-mm-scale harmonics bound to the dominant waves and propagating with the phase velocities of the dominant waves. The relation between bound and free waves can be estimated from measurements of phase velocity. Wind ripple damping was found to be maximum at wavelengths around 5-7 mm. The latter effect agrees with results of our field experiments using artificial slicks and can be explained qualitatively by a nonlinear "cascade" damping mechanism, when the damping of dm-scale dominant waves leads to strong damping of their cm-mm-scale nonlinear harmonics including damping of "parasitic" capillary ripples.

1 Introduction

It is well known that marine slicks detected by radars and optical systems may be used to characterize areas of biological productivity or pollution. In order to retrieve parameters of marine films from radar/optical observations of slicks one needs to know the physical mechanisms responsible for the damping of short wind waves. Classical linear wave damping theory (Lucassen-Reynders and Lucassen 1969 and references therein) predicts a maximum of the relative damping coefficient in the centimetre wavelength range. Our recent field experiments with artificial slicks (Ermakov et al. 1998), however, showed that the relative damping (contrast) of short wind

waves increases monotonically with wave number and achieves a maximum in the range 9-12 rad cm^{-1} (wavelengths about 5-7 mm). A nonlinear mechanism of wave damping for cm-mm-scale waves has been hypothesized, based on the assumption that nonlinearity of dm-cm-scale waves makes a significant contribution to the spectrum of cm-mm-scale waves.

Short dm-cm-scale gravity waves are characterized, even at low winds, by rather large slope values, so that nonlinear effects can determine the wind wave spectrum in the gravity-capillary range. One of the effects is connected with a non-sinusoidal profile of dm-cm-scale surface waves, which can be considered as a result of generation of "bound waves" - high-order harmonics and parasitic capillary ripples (Longuet-Higgins 1992). The bound waves move with the phase velocities of basic gravity waves, as experimentally confirmed for cm-scale waves (Yuen and Lake 1982) and for the parasitic capillary ripples (Ermakov et al.1986), generated by periodic gravity waves. The phase velocities of cm-mm-scale wind ripples are determined by free capillary-gravity waves and by bound waves. Measurements of phase velocities of wind ripples in support of this assumption are scarce and have so far been carried out in a frequency range of about 1.5-10 Hz (wavelengths 40-2.5 cm) using contact methods (Yuen and Lake 1982, Ramamonjarisoa and Giovanangeli 1978), and, also at two wavelengths of about 1.5 cm and 0.5 cm using X-band and K_a-band radar measurements (Gade et al. 1998). No other measurements of phase velocity of capillary-gravity wind waves (wavelengths smaller than 2-3 cm) have been reported, at sea or in wave tanks, although these studies are very important for the development of models of wind waves.

The amplitudes of the high-order harmonics very strongly depend on the amplitude of the basic waves. For Stokes waves, for example, the amplitude of the n-th harmonic is proportional to the n-th power of the amplitude of the basic wave. Therefore, even weak damping of dm-scale basic waves due to films can lead to strong nonlinear depression of the bound waves ("cascade" effect), the latter effect can result in a maximum of the damping in the mm-scale wavelength range.

This paper presents wave tank optical measurements of phase velocities of wind waves on clean water surfaces and on water surfaces covered with organic films and measurements of film-induced water wave damping. The results confirm the assumption that the wind wave spectrum contains nonlinear cm-mm-scale harmonics bound to the dominant wind waves, giving a strong contribution to the damping of wind waves due to films.

2 Experimental

Experiments were carried out in the oval wind wave tank of the Institute of Applied Physics. A sketch of the experimental approach is shown in Figure 1.

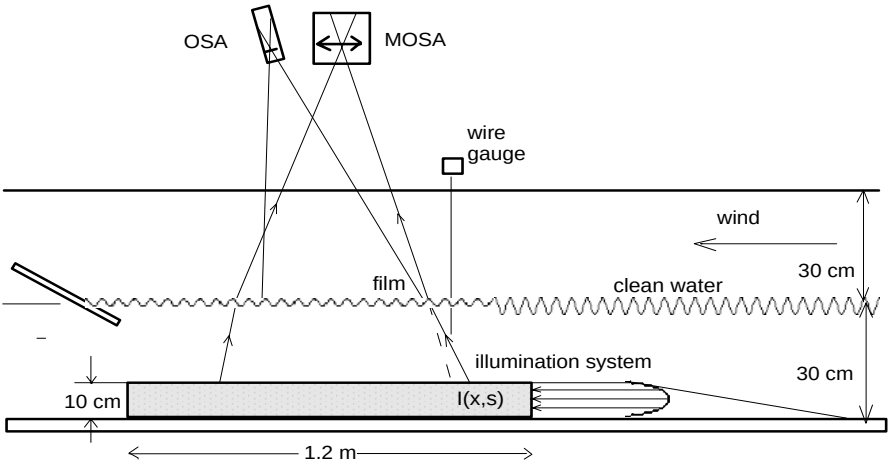

Fig. 1. Schematic diagram of the present wave tank experiment; OSA ≡ second Optical Spectrum Analyser; MOSA ≡ Multichannel ("Stroboscopic") Optical Spectrum Analyser

The phase velocities of surface waves were measured using an optical method based on the refraction of incident light by the rough water surface. Surface waves can be imaged by refracted light, as a result of both the dependencies of the refraction coefficient on the local surface slope and the nonuniformity of the light source. The latter factor is usually more important when observing the water surface at low incidence angles (near the nadir direction). If the intensity of the image of the water surface at each point is proportional to the local wave slope, the wave number spectrum of the image is linearly related to the wave number spectrum of surface waves. In order to satisfy this condition, a gradient illumination system has been designed, analogous to that reported in Keller and Gotwols (1983) and later in Jähne and Riemer (1990).

The illumination system contained a transparent plastic box, installed at the bottom of the wave tank and filled with an aqueous suspension of Latex particles with a diameter of about 0.3 μ - 0.4 μ. A nearly parallel light beam from a line-source lamp is directed into the box. Measurements with a photo receiver have shown that the resulting light intensity, in accor-

dance with first order scattering theory, decreases nearly exponentially with distance in the horizontal plane as $I_0(x) = I_0 \exp(-\alpha x)$ with a characteristic scale $1/\alpha$, depending on the Latex concentration. The light intensity weakly depends on the refracted angle except the "forward scattering angle" range, which is not the range of interest in our experiments.

The water surface is imaged by a lens with a vertically directed axis, positioned over the water surface. It can be shown (Keller and Gotwols 1983) that the light intensity in the image plane can be written in the first order approximation as follows

$$I(x,s) = I_0(x)[1 - c \cdot s + 0(s^2)] \tag{1}$$

where $I_0(x)$ is the light intensity in the absence of surface waves, and s denotes the surface wave slopes. The coefficient c in (1) for nearly isotropic light scattering and at low refraction angles is proportional to the light intensity gradient. The quadratic term in (1) is small for the conditions of the experiment (less than 0.5 % in the power slope spectrum).

The Multichannel ("Stroboscopic") Optical Spectrum Analyser (MOSA) allows us to carry out spatial Fourier analysis of the images of a ruffled water surface. One can show (see, Appendix) that the frequency spectrum $s(\omega) = < |i(\omega)|^2 >$ (<…> denotes statistical averaging) of the MOSA signal $i(t)$ can be written in the form

$$s(\omega) \sim \left|FSS\right|^2 + \sum (A_n \cdot c \cdot I_0)^2 F(nK, 0, \omega - nKV) \tag{2}$$

Here A_n denotes the Fourier coefficients describing the slit transparency function, $F(k_x,k_y,\omega)$ is the wave number-frequency slope spectrum (convolved with the spectrum of the aperture of the MOSA) at discrete wave number values $nK = n2\pi/L$, $n = 1,2,3,\ldots$, and L is the period of the slits. The reference frequency KV is determined by the slit velocity V. If surface waves obey some dispersion relation $\omega = \omega k(k_x,k_y)$, then the spectrum of the MOSA signal has the form of peaks at frequencies $nKV + \omega_k(nK,0)$ with amplitudes equal to the wave number spectrum at $k_x = nK$, $k_y = 0$. When measuring the frequency shifts of the spectrum peaks relative to the basic frequencies nKV, one can obtain the frequencies at wave numbers nK of surface waves propagating in the x-direction. The term FSS in formula (2) is due to an apparatus effect. FSS represents a system of peaks at frequencies nKV and corresponds to the undisturbed water surface. In the experiments the MOSA could detect surface waves in the wavelength range from about 10 cm down to 0.6 cm for clean water and to 1-2 cm for contaminated water (the shortest detectable wavelengths depend on the intensity of the waves exceeding the noise level of the MOSA). The second optical analyser (OSA) allowed us to measure only the wave number

spectrum water waves, but for shorter wavelengths, from about 5 cm to 2-3 mm. The two analysers were positioned over the wave tank, with co-located look areas. Co-located wave height measurements were also performed, using a wave gauge. Wind wave measurements were carried out for clean water and for water surfaces covered with surfactant films at a mean wind velocity of 2.5 m s^{-1} at a height of 15 cm and at two different fetches: 12 m and 8 m. Wind drift velocities were measured between 4 cm s^{-1} for clean water and about 3 cm s^{-1} for contaminated water using small floats.

The films were produced by spreading of 10%-solution of oleic acid in ethanol, the solvent was used to ensure better spreading of surfactants and formation of monomolecular films. Two different amounts of oleic acid were spread on the water surface for each fetch - about 1 mg and 2 mg ("film 1" and "film 2"). In the stationary wind wave regimes the films occupied a part of the tank from about 2.5 m to 3 m length, depending on the fetch and the amount of the surfactant. The surfactant concentrations ranged above those necessary for monomolecular coverage of oleic acid monolayers (which is about 1.1 mg m^{-2}), the elasticity of saturated oleic acid films can be considered as constant (Ermakov et al. 2006). Therefore, differences between wave propagation conditions in the experiments with different films could be characterized mainly by a distance from the upwind edge of the film to the look area. The largest distance from the edge of the film and, correspondingly, the most strong wave damping was for the case of "small fetch/film 2", while the case "large fetch/film 1" was characterized by the shortest distance and the weakest damping. Results below are presented for these two limiting cases.

3 Results

3.1 Clean water surface

3.1.1 Regular waves

Firstly, measurements of the wave number-frequency spectrum were conducted for steep mechanically generated waves of frequency 4.67 Hz. In order to detect the waves, the parameter L of the MOSA was chosen to be equal to 7.5 cm, i.e., equal to the basic wavelength of the steep waves. The wave amplitudes were 0.6 mm and 3 mm. The phase velocities and amplitudes of the first four harmonics in the wave number spectrum are plotted in Figure 2.

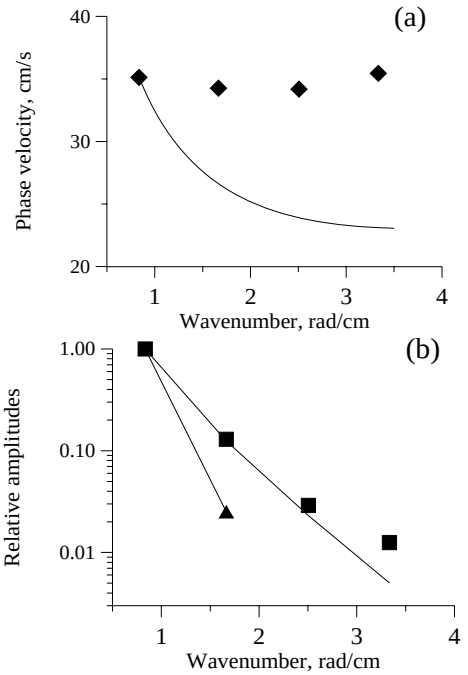

Fig. 2. Phase velocities and relative amplitudes of harmonics of a short gravity wave with a wavelength 7.5 cm. **Fig. 2a**: ♦- measured velocity, solid line –linear theory. **Fig. 2b:** wave amplitude 0.6mm (▲) and 3mm (■), solid lines – Stocks theory

Obviously, the phase velocities of high-order harmonics with wavelengths *L/n* are equal to the phase velocity of the basic harmonic (*n=1*), so that these harmonics can be considered as bound to the basic wave. The measured harmonic amplitudes for the second and third harmonics are found to be in good agreement with Stokes theory. The amplitude of the 4th harmonic a_{IV} is about 2 times larger than that in theory; this is, as we assume, because the Stokes expansion is not valid for strong gravity waves with asymmetric slopes and parasitic capillary ripples propagating along the forward wave slopes.

3.1.2 Wind waves

The wave number-frequency spectrum of wind waves was measured at low wind velocity, 2.5 m s^{-1}, and at two different fetches. Dominant dm-cm-scale wind waves are steep enough and are characterized by asymmetric profile and parasitic ripples generation even at such a low wind velocity, so that we expect that nonlinear effects can be quite strong. Co-located measurements of wave height were conducted using a wave gauge. The

wave height frequency spectra at two fetches are shown in Figure 3a, demonstrating that the frequencies of the dominant waves are different at the large and small fetches, 4.7 Hz and 5.3 Hz, respectively.

The phase velocities of wind waves obtained from measurements using the MOSA are presented as functions of the wave numbers in Figure 3b. Note that in this set of experiments the parameter L of the MOSA was chosen to be 10 cm. A theoretical dependence of the phase velocity of free surface waves accounting for the wind drift are also presented in Figure 3b at a drift velocity V_{dr} of 4 cm s^{-1}. It follows from Figure 3b that the phase velocities of cm-mm-scale wind waves do not obey the dispersion relationship for free waves, being larger and increasing more slowly with wave number in the range from about 2 rad cm^{-1} to 10 rad cm^{-1} than free waves. The phase velocities in this wavelength range also increase with fetch (one should remind that the phase velocities of the dominant waves, according to the dispersion relationship of free surface waves, are larger at the large fetch than at the small one). Both of these facts support the existence, in the wind wave spectrum, of bound harmonics which propagate with the phase velocity of the dominant waves. Note, that for better frequency resolution in the spectrum of the MOSA signal we could discriminate between peaks corresponding to free and bound waves at a given wave number. However, in our experiments we determined only weighted mean of phase velocities.

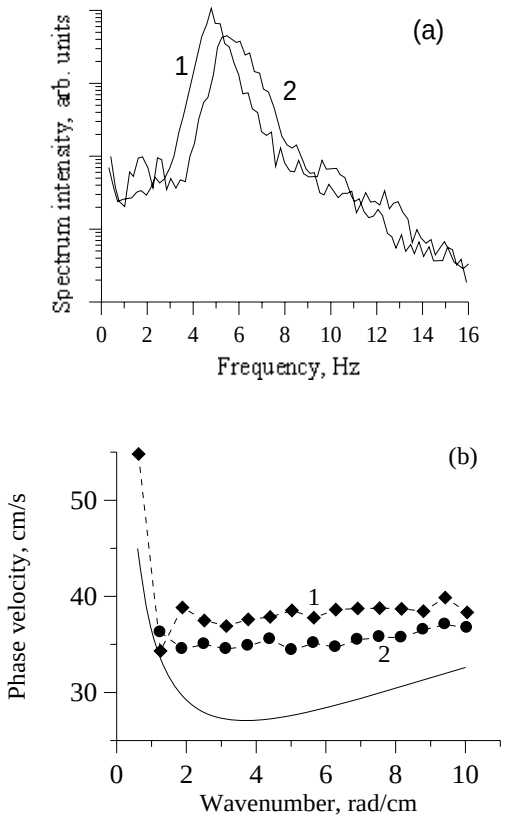

Fig. 3. Frequency spectra **(a)** and phase velocities **(b)** of wind waves at two fetches (**1** - small fetch, **2** - large fetch). Clean water, wind velocity 2.5 m/s. Solid line in Fig. 3b – phase velocity for linear gravity-capillary waves (surface tension 72 mN/m) accounting for wind drift

3.2 Contaminated water surface

Wave damping due to a film is characterized by the contrast $K(k) = F_{nsl}/F_{sl}$, where F_{nsl} and F_{sl} denote the spectra of wind waves in non-slick and slick regions at a given wave number k. The contrasts and the phase velocities measured by the optical spectrum analysers are presented in Figure 4 for the case of "large fetch/film 1" and in Figure 5 for the case of "small fetch/film 2". The contrast curves in Figures 3 and 4 show the occurrence of the maximum, which corresponds approximately to wavelengths of about 6-8 mm, which are typical wavelengths of parasitic capillary ripples (Ermakov 1986). The wavelengths of the contrast maximum

are the same as those obtained in our field experiments with artificial slicks (Ermakov 1998). This confirms our hypothesis about a nonlinear mechanism of damping of mm-scale wind ripples, connected with strong depression of parasitic ripples on the profile of basic dm-cm-scale waves due to film damping of these basic waves.

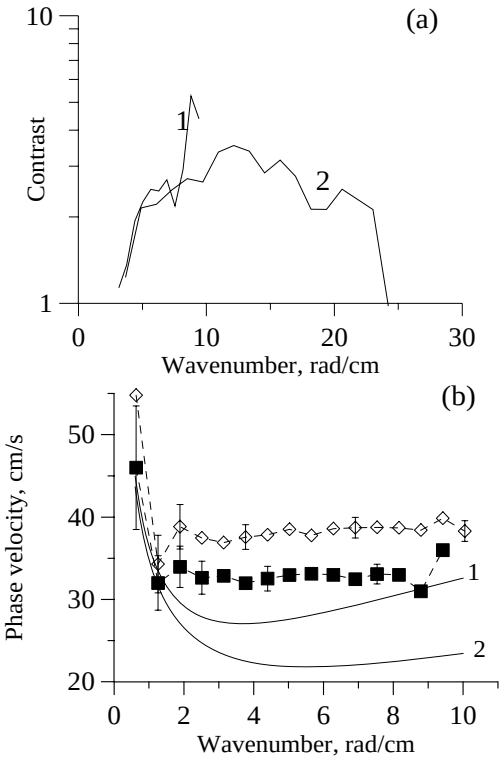

Fig. 4. Contrasts **(a)** and phase velocities **(b)** for cm-mm-scale wind waves at large fetch**. Fig. 4a**: 1 – MOSA, 2 – OSA. **Fig. 4b:** ◊- clean water, ♦- film 1, solid lines – linear theory for surface tension 72 mN m^{-1} and drift velocity 4 cm s^{-1} (curve1) and for surface tension 32 mN m^{-1} and drift velocity 3 cm s^{-1} (curve 2)

The phase velocities of cm-mm-scale waves decrease in the presence of a film and, as for clean water, do not satisfy the linear dispersion relationship, the theoretical curves for phase velocities in Figures 4b and 5b are plotted for the surface tension values of 72 mN m^{-1} and 32 mN m^{-1} for clean and contaminated water, respectively.

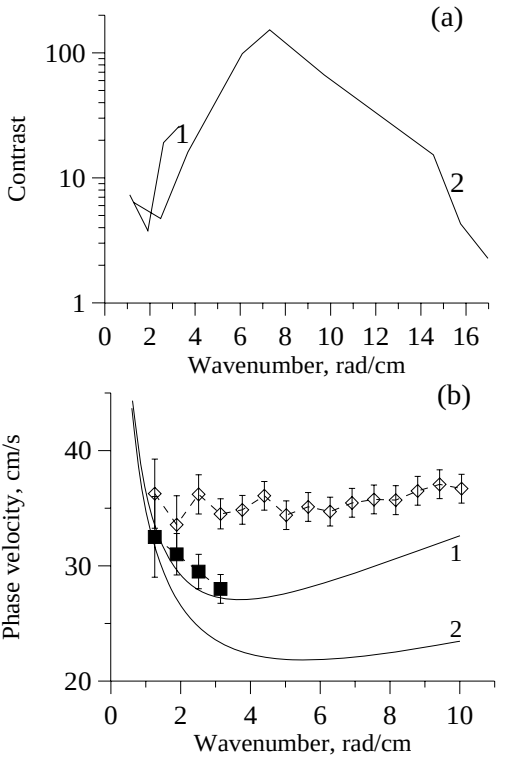

Fig. 5. Same as in Fig. 4 for film 2. Small fetch

Let us estimate the contribution of the free waves F_f to the wind wave spectrum. One can easily show that the measured phase velocity C at a given wave number k can be written as

$$C = C_k + R(C_{km} - C_k) \quad (3)$$

where R= F_b/F, F_b denotes the intensity of bound harmonics, F is the total intensity of the spectrum of wind waves at a given wave number k, $C_k=(g/k+Tk)^{1/2} + V_{dr}$ is the phase velocity of gravity-capillary waves accounting for wind drift, and km is a wave number of the dominant dm-waves.

The estimated “bound wave/total wave” ratio R is shown in Figure 6 for clean and contaminated water at the large fetch and in Figure 7 for the small fetch.

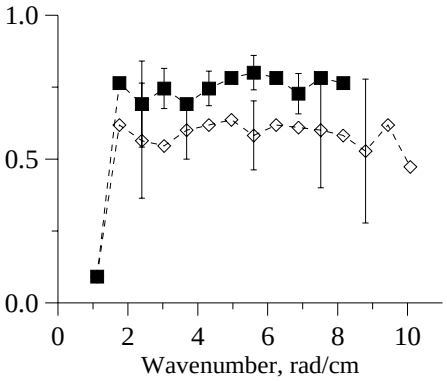

Fig. 6. Relative intensity of bound components in the spectrum of wind waves. Large fetch. ◊ - clean water, ■ – film 1

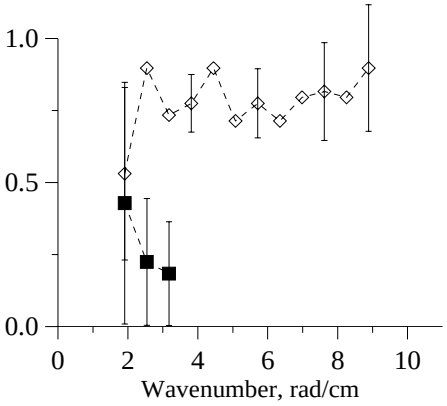

Fig. 7. Same as in Fig. 6 for film 2. Small fetch

It can be inferred from Figures 6 and 7 that the contribution of bound waves for a clean water surface for both fetches is quite large (about 0.6-0.8). In the presence of the films *R*-values increase for the large fetch and decrease for the small one. This can be explained taking into account that dominant waves for the large fetch are comparably long (wavelengths about 8 cm). Therefore, the dominant waves and corresponding bound waves are damped weakly compared with free waves. For the small fetch the dominant waves are rather short (about 5 cm) and their harmonics can be damped stronger than free waves.

4 Conclusions

Optical measurements of the wave number-frequency spectrum of wind waves in the wave tank have shown that the phase velocities of cm-mm-scale waves do not obey the linear dispersion relationship of gravity-capillary waves (GCW), both for clean water and in the presence of surfactant films, since the spectrum in this wavelength range is essentially determined by bound waves, which are nonlinear high-order harmonics of longer, dm-cm-scale waves. Nonlinear damping of "parasitic" capillary ripples on the profile of the dominant wind waves results in a contrast maximum in the mm-scale wavelength range of the spectrum. Relative intensity of bound waves in the spectrum of cm-mm-scale wind waves has been estimated from the measured phase velocities. It is obtained that the contribution of bound waves is large and can either increase or decrease in the presence of surfactant films, depending on a wind wave regime.

Note that the effect of damping of dm-waves and their nonlinear harmonics as well as free waves depend on the film elasticity. Therefore, one can expect that the resulting phase velocity of the system "free waves/bound waves" should depend on the characteristics of films. This effect will be studied in further experiments.

Acknowledgements. The authors are grateful to Dr. J. Scott for his helpful discussion and interest to this work. The work was supported by the UK Ministry of Defence through the DERA, Winfrith, UK, via the International Science and Technology Center (Project 1774p), by INTAS (Project 03-51-4987 "SIMP"), and RFBR (projects 05-05-64137, 04-05-64763).

5 References

Ermakov SA, Ruvinsky KD, Salashin SG, and Freidman GI (1986) Experimental investigation of the generation of capillary-gravity ripples by strongly nonlinear waves on the surface of a deep fluid. Izv Atmos Ocean Phys 22: 835-842

Ermakov SA, Zuikova EM, Luchinin AG, Sergievskaya IA, Schegolkovm YuB, Goldblat VYu and Scott JC (1998) Remote measurements of damping and phase velocities of short wind waves in film slicks. Proc IGARSS 5: 2562-2564

Ermakov SA and Kijashko SV (2006) Damping of capillary-gravity waves due to films of insoluble ordinary surfactants and polymers. (this issue)

Gade M, Alpers W, Ermakov SA, Hühnerfuss H, Lange PA (1998) Wind-wave tank measurements of bound and freely propagating short gravity-capillary waves. J Geophys Res 103: 21697-21710

Jähne B, Riemer KS. (1990) Two-dimensional wave number spectra of small-scale water surface waves. J Geophys Res 95: 11,531-11,546

Keller W, Gotwols BL (1983) Two-dimensional optical measurements of wave slope. Appl Opt 22: 3476-3478

Longuet-Higgins MS (1992) Capillary rollers and bores. J Fluid Mech 240: 659-679

Lucassen-Reynders EN, Lucassen J (1969) Properties of capillary waves. Adv Colloid Interface Sci 2: 347-395

Ramamonjarisoa A., Giovanangeli JP (1978) Observations de la propagation des vagues engendrees par le vent au large. C R Hebd Seances Acad Sci SerB 287: 133-136

Yuen HC, Lake BM (1982) Nonlinear dynamics of deep-water gravity waves, In Advances in Applied Mechanics (ed. Chia-Shun Yih), vol 22. Academic Press, pp.67-229

APPENDIX:
Multichannel ("Stroboscopic") Optical Spectrum Analyser

The principle of the MOSA operation was suggested by L.S. Dolin. The refracted light forming an image of the ruffled water surface in the image plane of a lens passes through a screen with narrow periodic slits. Then the light intensity of the image *I(x,y,t)* is integrated by a photo receiver. The output signal *i*(*t*) can be written in the form

$$i(t) \sim \int_{-\infty}^{\infty}\int_{-\infty}^{\infty} W(x,y)I(x,y,s)R(x-Vt)dxdy \qquad \text{(A.1)}$$

where *R(x)* describes the screen transparency (we assume that the slits are parallel to the *y*-axis), *W* is a "window function", which for a rectangular window can be written in the following form

$$W(x,y) = \left[1(x+D_x) - 1(x-D_x)\right] \cdot \left[1(y+D_y) - 1(y-D_y)\right] \qquad \text{(A.2)}$$

Here D_x and D_y are the window scales in the *x*- and *y*- directions. In (A.1) we assumed that the slits move in the *x*-direction with velocity *V*, practically it can be achieved using a rotating disk with radial slits, if the radius of the disk is large compared with the size of an analysed image. The periodic function *R(x*) can be represented by a Fourier series as

$$R(x) = \sum A_n \cdot \exp(inKx) \qquad \text{(A.3)}$$

Then it follows from (A.1)-(A.3) and (1) that the spectrum $i(\omega)$ of *i(t)* can be written in the form

$$i(\omega) \sim \sum A_n \left[\delta(\omega - nKV) \cdot F_0(-nK,0) + c\int_{-\infty}^{\infty} W(x,y)I_0(x)s(x,y,\omega - nKV)\exp(inKx)dxdy\right] \qquad \text{(A.4)}$$

Here

$$F_0(nK,0) = \int_{-\infty}^{\infty} W(x,y)I_0(x)\exp(inKx)dxdy \qquad \text{(A.5)}$$

is the wave number spectrum of the mean intensity for an undisturbed water surface multiplied by the window function *W(x,y.,* In (A.4) *s(x,y,* ω *)* is the amplitude frequency spectrum of wave slopes. The first term in the r.h.s. of (A.4) corresponds to an undisturbed water surface and does not contain information about surface waves. This "flat surface spectrum" has

a maximum at $n=0$ and decreases with wave number approximately as $\sin(nKD_x)/nKD_x$. The second term in r.h.s. of (A.4), corresponding to a signal from a rough surface, can be discriminated, in general, from the "flat surface spectrum", since it is shifted from the frequencies nKV; the shift from a given frequency nKV is equal to the frequency of surface waves with a wave number nK.

The power frequency spectrum of the MOSA signal $s(\omega) = < |i(\omega)|^2 >$ (<..> denotes statistical averaging) can be written in the form (1)

$$s(\omega) \sim \left|FSS\right|^2 + \sum (A_n \cdot c \cdot l_0)^2 F(nK,0,\omega - nKV) \tag{A.6}$$

where

$$F(nK,0,\omega - nKV) =$$
$$4 \int_0^{2D_y} dy \int_0^{2D_x} dx \cdot \left[(2D_y - y) \frac{sh\alpha(2D_x - x)}{\alpha} \cos(nKx) B(x, y, \omega - nKV) \right] \tag{A.7}$$

In (A.7) $B(x,y,\omega) = < s(x+\xi,y+\eta,\omega) \cdot s(\xi,\eta,\omega) >$ is the slope correlation function. It is easy to see that if the correlation lengths are small compared with D_x, D_y, α_1^{-1} then F in formula (A.7) in the first approximation is equal to the wave number-frequency spectrum of slopes convolved with the spectrum of the window spectrum, i.e.

$$F(nK,0,\omega - nKV) = 2D_y \frac{sh(\alpha \cdot 2D_x)}{\alpha}$$
$$\int_{-\infty}^{\infty} F(k_x, k_y, \omega - nKV) \cdot \frac{2\sin\left[2D_x(k_x - nK)\right]}{k_x - nK} \cdot \frac{2\sin\left[2D_y k_y\right]}{k_y} \cdot dk_x dk_y \tag{A.7a}$$

Laboratory measurements of artificial rain impinging on slick-free and slick-covered water surfaces

Nicole Braun, Martin Gade, and Philipp A. Lange

Institute of Oceanography, University of Hamburg, Hamburg, Germany

Abstract. Laboratory measurements with artificial rain were carried out in the wind-wave tank of the University of Hamburg, in order to gain better understanding of the radar backscattering from a slick-free and slick-covered water surface, particularly when it is agitated by strong rain. We used a coherent 9.8 GHz (X band) scatterometer at different polarisations and at an incidence angle of 28 degrees, a resistance-type wire gauge, and a two-dimensional laser slope gauge. A water surface area of 2.3 m^2 was agitated by strong artificial rain with a rain rate of 160 mm h^{-1} and rain drops of 2.9 mm diameter. The wind-speed range used in the present investigation was between 2 and 10 m s^{-1}. A monomolecular surface film was produced by deploying oleyl alcohol on the water surface. The results of the analyses of the measured radar Doppler spectra and wave amplitude and slope spectra are presented. We show that while the wind-induced surface roughness is strongly reduced in the presence of the slick, at a high rain rate (of 160 mm h^{-1}) the surface slick less strongly affects the rain-induced increase of the surface roughness (i.e., the generation of crowns, cavities, stalks, ring waves, and secondary drops).

1 Introduction

Radar signatures of rain events are often observed on synthetic aperture radar (SAR) images of the ocean surface because rain drops impinging on the sea surface change the surface roughness in at least two ways: (1) roughness is increased because the rain drops generate ring waves, crowns, cavities, and stalks, and (2) roughness is decreased because they generate turbulence in the upper water layer which in turn dampens the wind generated water waves. Moreover, oceanic surface films (be they of biogenic or anthropogenic origin) strongly influence the backscattered radar power (σ_{rel}) by damping the small-scale surface roughness, which is responsible for the radar backscattering at oblique incidence angles (between 20 and

75°, so-called Bragg waves). Figure 1 shows subsections of three SAR images of the Atlantic Ocean, north of the Azores, acquired on April 12th, 1994, at 0721 UTC by the Spaceborne Imaging Radar C/X Band SAR (SIR-C/X-SAR) at L-, C-, and X-band (from left to right), VV polarisation. The diagonal dark narrow line visible on the three images is caused by freshly spilled mineral oil, and the irregular bright spot in the image centre is caused by strong rain. This example shows the different imaging of the two counteracting phenomena (surface film and strong rain) at the different radar bands: the contrast is highest at X-band, and it is lowest at L-band. A more detailed analysis of the described phenomena can be found in Melsheimer et al. (1998) and Braun (1998), respectively.

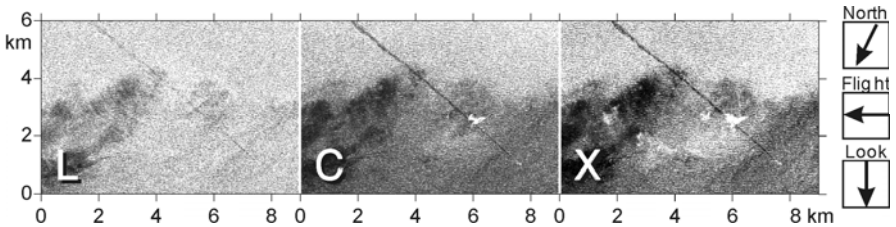

Fig. 1. Subsections of three synthetic aperture radar (SAR) images of the Atlantic Ocean, north of the Azores, acquired on April 12th, 1994, at 0721 UTC by the Spaceborne Imaging Radar C-/X-Band SAR (SIR-C/X-SAR) at L-, C-, and X-band (from left to right), VV polarisation. The diagonal dark narrow line is caused by freshly spilled mineral oil, whereas the irregular bright spot in the image centre is caused by strong rain

Braun et al. (2002) presented results from laboratory studies of the influence of artificial rain on the measured water surface elevation and slope, and, moreover, on the radar backscattering from a rain- and wind-roughened slick-free water surface. In order to complement their findings, we performed a second measurement series, where we investigated the influence of artificial rain on a slick-covered water surface. The aim of these studies was to improve the classification of signatures visible on SAR images. In particular, for an effective surface film detection the influence of rain on the visibility of oceanic surface films has to be known. *Vice versa*, if spaceborne radar data is used for the estimation of rain rates (as proposed by Melsheimer et al. (1998)), one has to know how surface films affect the radar signal of (strong) rain events over the ocean surface. First results of our studies are presented herein.

2 Instrumentation

The wind wave tank of the University of Hamburg is 26 m long and 1 m wide. It is filled with fresh water with a mean water depth of 0.5 m. The wind-tunnel height is 1 m, and the effective (maximum) fetch is 19 m. All measurements reported herein were performed at a fetch of 14.5 m and at wind speeds between 2 and 10 m s^{-1} generated by a radial blower. In the measurement and rain area, the metallic plates of the tank's roof were removed and, on the leeward side, replaced by Styrofoam panels to ensure the unattenuated transmission of the microwaves (Figure 2). At the windward side of the rain area plates of microwave absorbing material were vertically mounted in the direction of the specular-reflected radar beams.

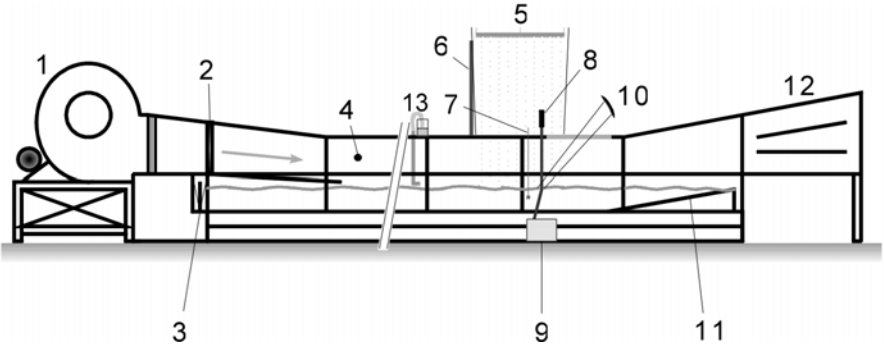

Fig. 2. Schematic side view of the wind-wave tank. 1: blower, 2: honeycomb, 3: wave flap, 4: anemometer, 5: rain generator, 6: radar absorber plates, 7: wire, 8: laser, 9: laser optics, 10: X band antennae, 11: beach and overflow baffle, 12: diffusor, 13: slick deployment.

The rain generator consists of six interconnected tubs (each 0.8 m long, 0.6 m wide, and 0.3 m high) which are mounted in an aluminum frame at a height of 4.5 m above the water surface. Approximately 2500 hypodermic needles are inserted in a triangular pattern with a distance of 3 cm into the bottoms of the tubs. The total area covered by the artificial rain is 2.3 m x 1 m. The diameter of the rain drops in our investigation was 2.9 mm and they attained an impact velocity of 8.1 m s^{-1} which is 85 % of their terminal velocity (Laws 1941). Monomolecular surface films were produced by deploying oleyl alcohol (OLA) dissolved in ethanol (75 mMol L^{-1}) on the water surface at a fetch of 5.5 m by using a pipette that was fixed a few millimetres above the water surface. The drops touched the water surface, thus allowing for optimum spreading of the monolayer without significant losses to the bulk.

The radar measurements were performed with separate upwind looking radar antennae for transmission and reception. We used a coherent continuous wave (CW) 9.8 GHz (X-band) scatterometer operating at a fixed incidence angle of 28°. The X-band microwave beam was focused on the water surface by means of a bistatic parabolic reflector construction mounted on a metal frame. The dimensions of the radar footprint on the water surface were 15 cm x 12 cm (range x azimuth). Wave heights were measured using a resistance-type wire wave gauge with a 0.075 mm diameter tungsten wire whose penetration point into the water was located at a distance of 22 cm laterally from the radar footprint (i.e., at the same fetch). Wave slopes were measured using a laser slope gauge whose footprint was at the centre of the radar footprint. The frequency resolution of the wire gauge is 30 Hz and of the laser slope gauge better than 100 Hz. The reference wind speed was measured at the wind entrance 65 cm above the mean water surface level using a propeller-type anemometer (Figure 2).

3. Results and Discussion

Various data sets were obtained by using the different sensors; however, in this paper we concentrate on results from measurements with the laser slope gauge as well as with the X-band scatterometer operating at co- (VV) and cross-polarisation (HV). In order to gain insight into the specific damping behaviour of OLA in the presence of rain, we calculated the normalised orientation ratio, NOR, which we define as

$$NOR(f) = \frac{S_y(f) - S_x(f)}{S_x(f)} \tag{1}$$

where $S_y(f)$ and $S_x(f)$ are the along-wind and crosswind wave-slope spectra, respectively. High values of the NOR denote a strong orientation of the wave field in the along-tank direction.

Some results obtained at different wind speeds are shown in Figures 3 and 4 for slick-free and slick-covered water surfaces, respectively. In both figures the NOR in the upper row were obtained without rain (rain rate 0 mm h^{-1}), and the NOR in the lower row were obtained at a rain rate of 160 mm h^{-1}. The columns denote different wind speeds (3, 5, 7, and 9 m s^{-1}, from left to right).

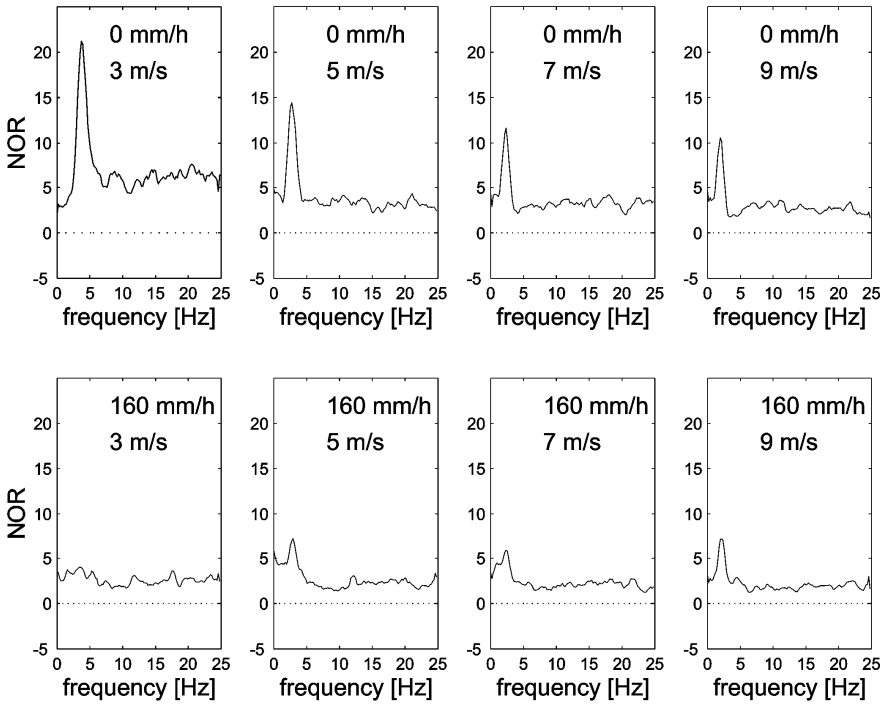

Fig. 1. Frequency dependence of the normalised orientation ratio, NOR (see (1)), measured with the two-dimensional laser slope gauge at different wind speeds (columns) without rain (upper row) and with rain at a rain rate of R=160 mm h^{-1} (lower row). The water surface was not covered with any slick.

In Figure 3 it is demonstrated how the strong rain decreases the effect of strong wave orientation, particularly at the frequency of the dominant wind wave: for each wind speed a sharp maximum of the NOR was observed without wind (upper row in Figure 3), but only a weak maximum was observed in the presence of strong rain (lower row in Figure 3). Even at high wind speeds (9 m s^{-1}) and at a rain rate of 160 mm h^{-1} the orientation of the wave field along the wind direction is still reduced.

The results shown in Figure 4 were obtained when the water surface was covered by an OLA slick. At 3 m s^{-1} (leftmost column), which is below the threshold wind speed for the first excitation of wind waves on a slick-covered water surface, only slight differences are caused by the rain (Figures 4a and e). However, at 5 m s^{-1} (Figures 4b and f) we measured strong differences: whereas a pronounced orientation of the wave field is observed from the maximum in Figure 4b (corresponding to the frequency of the dominant wave field), a less pronounced maximum was measured

when the water surface was agitated by rain (Figure 4f). The (non-oriented) ring waves, which are generated by the rain, cause a strong reduction of the NOR in the frequency range between 3 and 12 Hz (which is the characteristic frequency range of the ring-wave spectrum, see Bliven et al. (1997)).

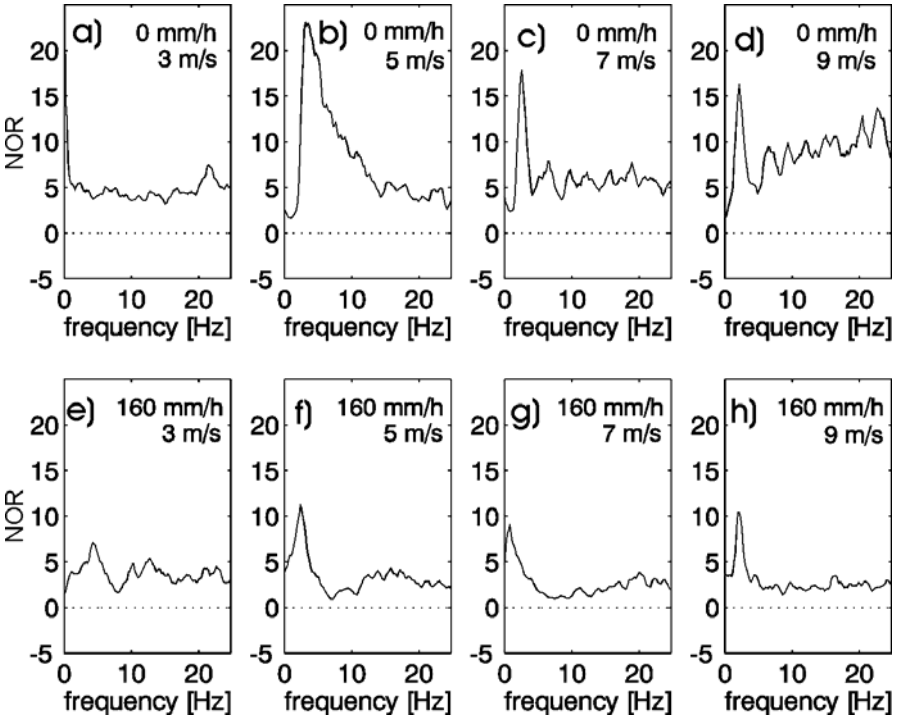

Fig. 2. Frequency dependence of the normalised orientation ratio, NOR (see (1)), measured with the two-dimensional laser slope gauge at different wind speeds (columns) without rain (upper row) and with rain at a rain rate of R = 160 mm h^{-1} (lower row). The water surface was covered with oleyl alcohol

At 7 m s^{-1} (Figures 4c and g) we measured a rain-induced decrease in the NOR also at higher frequencies (i.e., up to 25 Hz, compare Figure 4g). On the one hand, the high-frequency part of the wave-slope spectrum is strongly damped by the slick, particularly, those waves which are travelling in crosswind direction (and which are not directly generated by the wind). On the other hand, the high-frequency part of the ring-wave spectrum causes an additional reduction of the NOR at higher frequencies. Thus, the observed effect is caused by the two counteracting effects de-

scribed above (wave damping by the slicks and wave generation by the rain drops).

At 9 m s^{-1} (Figures 4d and h), again, we measured a reduction of the NOR in the presence of rain in the entire frequency range. However, we can infer from the sharp maximum in Figure 4h at about 2 Hz that at high wind speeds the wind-generated part of the slope-spectrum dominates over the rain-induced part only at low frequencies. The entire wind-wave spectrum is, therefore, more oriented than in the absence of any slick (cf. Figure 3).

Radar Doppler spectra measured at co-polarisation (VV-pol.) and at cross-polarisation (HV-pol.) are shown in Figures 5 and 6, respectively. In each figure the solid curves denote Doppler spectra acquired at a rain rate of 160 mm/h, and the dashed curves correspond to Doppler spectra acquired without rain. During the measurements the water surface was covered with a monomolecular OLA slick.

The Doppler spectra measured at VV-polarization, without rain (dashed curves in Figure 5), show that no X-band Bragg waves are generated at 2 and 4 m s^{-1} (Figures 5b, c). Moreover, at moderate wind speeds (6 and 8 m s^{-1}; Figures 5d, e) the existence of bound and freely propagating Bragg waves can be delineated from the different locations of the narrow spectral maximum (for details see Gade et al. (1998)).

The solid curves in Figure 5 (160 mm h^{-1} rain rate) show that the rain-generated ring waves are the main scatterers at wind speeds up to 8 m s^{-1}. It was already shown by Braun et al. (2002) that the occurrence of two peaks in the Doppler spectra (measured at co-polarisation) is caused by ring waves propagating towards and away from the radar antennae. These ring waves cause two separated peaks with an overall (mean) Doppler shift due to the wind-dependent surface drift.

At 10 m s^{-1}, the slicks are dispersed in both cases (wind only and wind plus rain). Thus, the Doppler spectra at co-polarisation measured with and without rain are similar and only a slight influence of the slick coverage is visible.

The Doppler spectra measured at HV-polarisation, without rain (dashed curves in Figure 6), show that no radar backscattering from a slick-covered water surface was measured up to wind speed of about 4 m s^{-1}. Moreover, at 6-8 m s^{-1} only a very weak backscattered signal was measured. At 10 m s^{-1}, where the surface film has already started to disperse, a significant radar Doppler signal was measured.

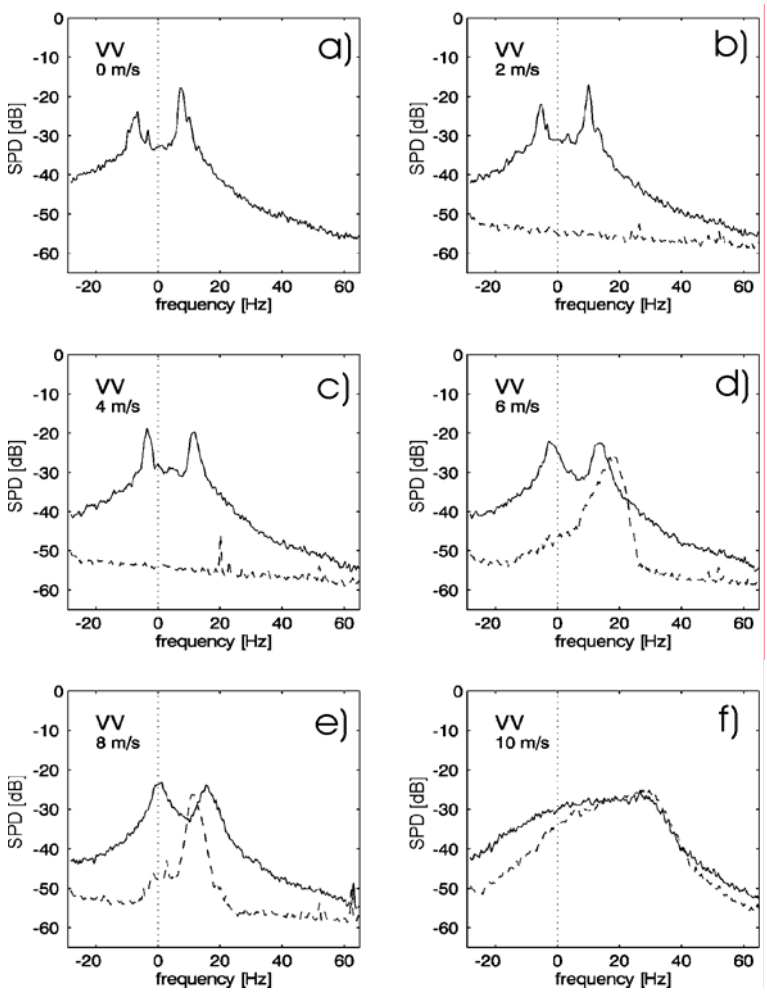

Fig. 5. Radar Doppler spectra measured at vertical polarizations (VV) and different wind speeds (0, 2, 4, 6, 8, 10 m s^{-1}, from top to bottom, left to right). The water surface was covered by an OLA slick. Dashed line: wind only, solid line: rain and wind

The Doppler spectra measured at HV-polarisation at a rain rate of 160 mm h^{-1} (solid curves in Figure 6) are very similar in the whole wind-speed range used in the present investigation: they show a symmetric, broad peak with its maximum at about -40 dB. The location of this maximum, however, depends on wind speed because of the wind-induced surface drift. From this finding we conclude that the radar backscattering at cross-polarisation from a slick-covered water surface agitated by rain is

solely caused by rain-induced effects up to wind speeds of 8 m s^{-1}. As already pointed out by Braun et al. (2002) these effects may comprise stalks and cavities, or secondary drops.

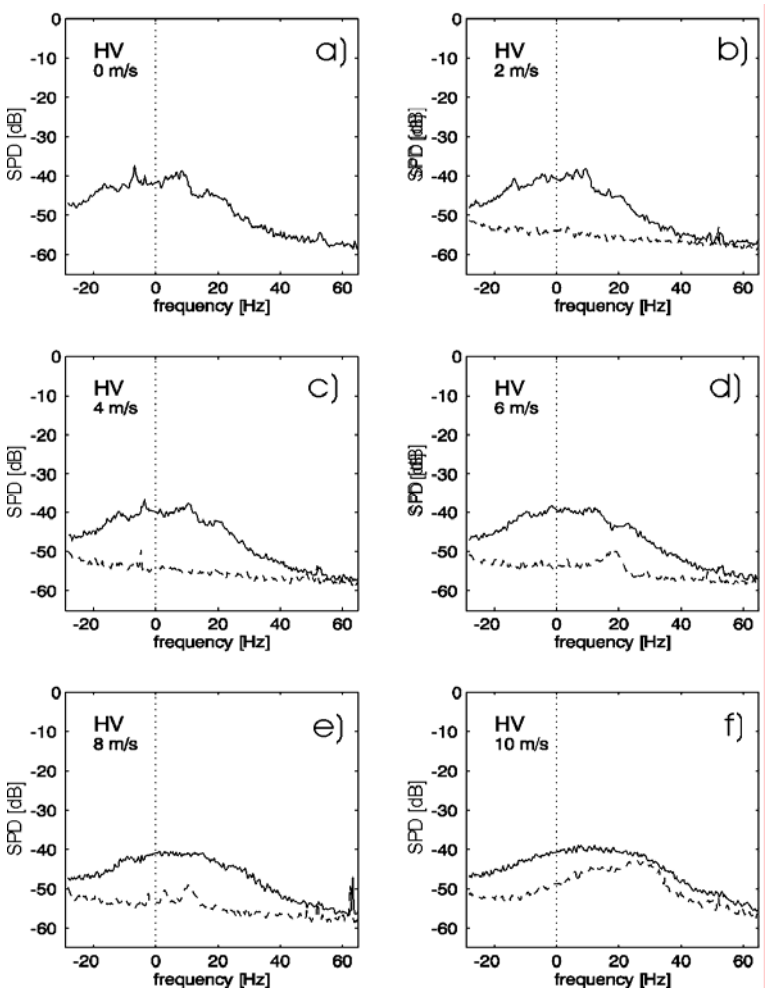

Fig. 6. Same as Figure 5, but for cross polarisation (HV)

Finally, the wind-dependence of the backscattered radar power (σ_{rel}) has been studied under different conditions. The results are shown in Figure 7, where the stars denote σ_{rel} values measured at a slick-free water surface and with rain, the circles denote σ_{rel} values measured at a slick-covered water surface and with rain, the crosses denote σ_{rel} values measured at a slick-

free water surface without rain, and the pluses denote σ_{rel} values measured at a slick-covered water surface without rain.

The upper diagram shows the measured σ_{rel} values for VV-polarisation, and the lower diagram shows the measured σ_{rel} values for cross-polarisation. It is obvious that the agitation of strong rain caused similar radar backscattering, independently of the slick coverage (see the stars and circles in Figure 7). That is, at high rain rates (like used in the present investigation) the enhancement of the radar backscattering by rain-induced effects such as ring waves, stalks, and cavities is not affected appreciably by the presence of a slick. This explains why the bright signature in the right panel of Figure 1 (X-band) is obviously not affected by the mineral oil spill.

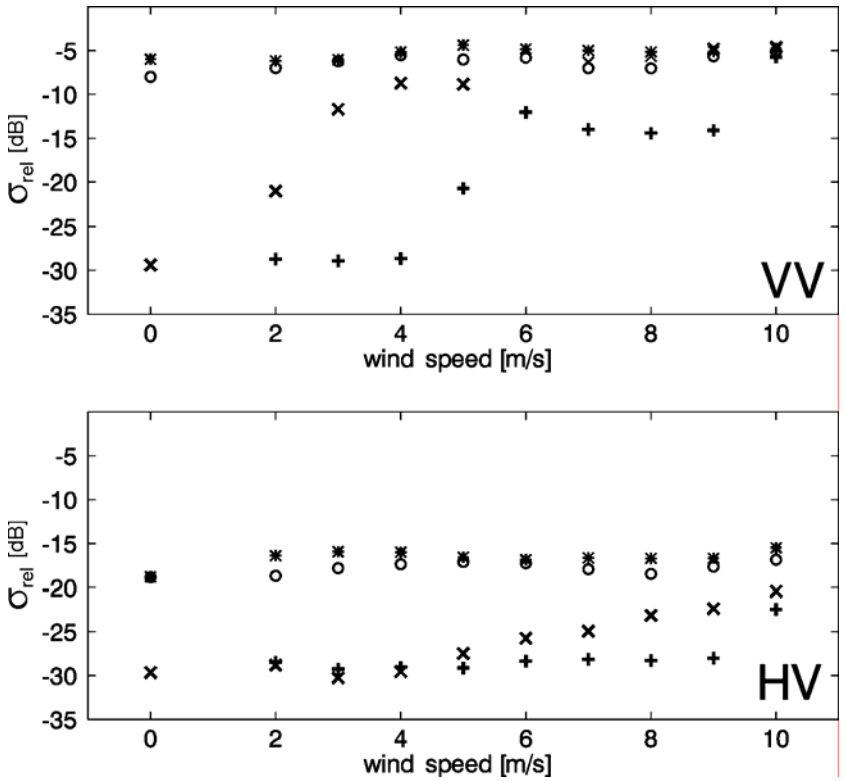

Fig. 7. Wind dependence of the relative backscattered radar power, σ_{rel}, measured under different conditions (×: slick-free, no rain; +: slick-covered, no rain; *: slick-free, with rain; o: slick-covered, with rain). Upper diagram: VV-polarization, lower diagram: HV-polarisation

The σ_{rel} values measured without rain (crosses and pluses in Figure 7, corresponding to a slick-free and to a slick-covered water surface, respectively) show that the reduction of the radar backscattering by monomolecular slicks is lower at cross-polarisation than at co-polarisation. This finding is in contrast to the results presented by Braun et al. (2002) and we suspect that this is due to an insufficient signal-to-noise ratio encountered during the herein presented measurements.

4 Summary and Conclusions

We have presented results of our laboratory measurements with artificial rain impinging on slick-free and slick-covered water surfaces. They show that the rain-induced roughness is not appreciably affected by slicks, whereas wind waves are strongly damped.

We have studied the dependence of the wave orientation ratio (measured with the two-dimensional laser slope gauge) on slick coverage and on wind speed. It can be inferred from our results that, on a slick-covered water surface, the rain-induced effects have an influence on the orientation of the wave field, particularly on the high-frequency part (up to 25 Hz), which is expected to be due to high frequency ring waves generated by the rain.

We also observed that, at wind speeds up to 8 m s^{-1}, the radar backscattering at co- and cross-polarisation is mainly caused by the rain-induced effects. Since similar results were obtained at slick-free water surfaces, we conclude that the coverage of the water surface by a monomolecular slick has no significant influence on the measured radar backscatter. However, we expect larger differences are to be found at lower rain rates.

Though our experiments were performed in a wind wave tank, where volume scattering at rain drops is negligible (cf. Melsheimer et al. 1998), our results may be transformed to lower radar frequencies. The splash products may strongly affect the radar backscattering at C-band, but volume scattering occurs only at very high rain rates. Therefore, our results are important for the interpretation of SAR images acquired by spaceborne SAR sensors at C-band (e.g., by those flown on the ERS, Envisat, and Radarsat satellites). That is, our results are suitable for the explanation of radar signatures of rain cells over the ocean, when its surface is covered by slicks or by mineral oil spills. However, in order to allow better knowledge of the influence of oceanic surface films on the imaging of strong rain events (and *vice versa*) additional experiments, particularly with lower rain rates and at different radar frequencies, are proposed.

5 References

Bliven LF, Sobieski PW, Craeye C (1997) Rain-generated ring waves: measurements and modelling for remote sensing. Int J Remote Sensing 18: 221–228

Braun N (1998) Laboruntersuchungen zum Einfluß von künstlichem Regen auf eine Wasseroberfläche mit Hilfe von Wellendraht-, Laser-, und Radarsonden. Diplomarbeit, Universität Hamburg, 99 pp

Braun N, Gade M, Lange PA (2002) The effect of artificial rain on wave spectra and multi-polarisation X band radar backscatter. Int J Remote Sensing 23: 4305-4322

Gade M, Alpers W, Ermakov SA, Hühnerfuss H, Lange PA (1998) Laboratory measurements of bound and freely propagating small gravity-capillary waves. J Geophys Res 103: 21697-21710

Laws JO (1941) Measurement of the fall-velocity of water-drops and raindrops. Trans Am Geophys Union 24: 452–460

Melsheimer C, Alpers W, Gade M (1998) Investigation of multi-frequency/multi-polarization radar signatures of rain cells, derived from SIR-C/X-SAR data. J Geophys Res 103: 18867-18884

Imaging surfactant concentration distribution at the air/water interface
Part 1: Surfactant concentration gradient on a laminar channel flow

Gerald M. Korenowski[1], Elizabeth A. van Wagenen[1] and Amir Hirsa[2]

[1]Department of Chemistry
[2]Department of Mechanical Engineering, Aeronautical Engineering, and Mechanics, Rensselaer Polytechnic Institute, Troy, NY, USA

Abstract. The surface specific spectroscopic probes of reflected second harmonic generation (SHG) and reflected sum frequency generation (SFG) have been successfully employed to measure surfactant monolayer concentration gradients on the ocean surface. Reflected SHG was adapted for areal measurements of monolayer concentrations using an intensified pulse gated CCD camera for detection and a dichromatic image splitter to allow for signal normalisation and scaling. As a preliminary test prior to field use, the imaging probe was used to measure the surfactant concentration gradients for an insoluble monolayer on a channel flow downstream of the Reynolds ridge. The resulting concentration measurements had a temporal resolution of 3 nanoseconds and spatial resolution of 0.21 millimetres or less per pixel.

1 Introduction

Over the last thirty or so years, the ocean science and ocean engineering communities have slowly come to recognise the importance of natural ocean surfactants in modifying the physicochemical properties and processes at the ocean/air interface. It is now the belief of many individuals in these communities that all of the ocean surfaces should be viewed as surfactant influenced to some degree or another (Liss et al. 1997). This growing interest has stimulated a new generation of scientific research directed at the ocean microlayer. Our own research is a part of this renewed scientific interest. We have worked at adapting reflected second-harmonic generation (SHG) and reflected sum-frequency generation (SFG) as nonintrusive *in situ* techniques for measuring surfactant concentration distributions

on the ocean surface (Frysinger et al. 1992, Korenowski et al. 1993, Korenowski 1997).

2 Background

Over the last twenty years, reflected SHG and reflected SFG have emerged as important new laboratory probes for studying the one or two molecular layers that comprise an interface. These techniques have been reviewed elsewhere and the reader is directed to several of these reviews for more detailed information (Shen 1989, Korenowski 1997) and a text on the subject of nonlinear optics is referenced (Shen 1984). It will suffice to say here that SHG and SFG are laser based second order nonlinear optical interactions (nonlinear dependence on the incident optical field). In general, SHG and SFG occur when the electric field from the pump laser light beam (SHG) or beams (SFG) drive the electrons in a condensed medium to oscillate in response to the sinusoidal varying electric field, but with an anharmonic component because of the strong electric field or fields. These electrons radiate light not only at the pump laser or laser frequencies but also at the harmonic and sum frequencies. For an isotropic medium, SHG and SFG are forbidden optical processes (electric dipole approximation). For a liquid medium such as water, the random molecular ordering in the bulk is sufficient to qualify the medium as isotropic. Only at the interface, where the isotropy is necessarily broken because of the interface, is there enough molecular ordering to permit SHG and SFG. Consequently, any SHG or SFG signal generated in transmission or reflection is the result of the optical interaction in the interfacial layer of molecules. When reflection occurs into an essentially non-dispersive (optical) medium like atmospheric pressure air, the conservation of momentum requires that the reflected pump laser beam at optical frequency ω (wavelength λ) be collinear with the reflected SHG signal at optical frequency 2ω (wavelength $\lambda/2$). The magnitude of this reflected nonlinear optical signal is dependent upon the vibronic (vibrational and electronic) structure of the interfacial molecules. When either the pump optical frequency or that of the nonlinear signal matches an allowed vibronic transition in the interfacial molecules, the resonance occurs and the signal increases. For strong resonances, the signal increase may be many orders of magnitude. Tuning the optical probe to a vibronic resonance of a surfactant molecule, enables one to monitor surfactant concentrations along with the much smaller signal from the interfacial water molecules (not in optical resonance). Any small potential for heating or photochemical degradation of the surfactant is not a problem when only a single laser pulse is used to record the signal or when

the probe beam is scanned across the surface (each footprint is on a fresh section of surface.)

The above characteristics of the reflected SHG and SFG probes were exploited by our group in developing these processes as *in situ* probes for natural ocean surfactants. The instantaneous nature of the signal (time scale for the duration of the incident laser pulse of either 5 to 3 nanoseconds), the extremely narrow spectral spread of the signal (essential the same spectral bandwidth as the pump laser which is less than 0.01 nm), the squared dependence of signal intensity on pump laser intensity, and the nondestructive nature of the optical processes were all invaluable in enabling us to use these probes in the field successfully. Tuning the laser wavelength to where we expect some form of resonance or preresonance (vibronic) for almost any organic surfactant, we were able to enhance the surfactant signal well above the background water signal. The temporal response of the signal, the pump laser intensity dependence, and its narrow spectral width made it easily identified and isolated from the ambient background light. In addition, the collinear nature of the signal and reflected pump laser allowed us to correct or scale the signal for fraction of signal collected. This is especially important, when surface waves create angular spreading in the surface reflection (Frysinger et al. 1993).

Figure 1 is an example of a time series SFG signal (532 nm and 355 nm pump beams and SFG at 213 nm) generated from surfactant gradients on the ocean surface (Korenowski et al. 1993, Korenowski 1997). The experiment was carried out during the SLIX 89 experiment just off the coast of California in the vicinity of Santa Rosa Island. The increases in the SFG signal correspond with visible records of crossing through a series of banded surface slicks. The increasing signal while crossing the banded slicks indicates an increase in surfactant concentration in the first molecular layer of the surface (The SFG and SHG signals increase quadratically with surfactant concentration). The largest signal occurs at the upwind edge of the banded slick and sharply decreases upon exiting the slick in the upwind direction. The variation of surfactant concentration is a maximum at the upwind edge decreasing to a minimum at the leeward edge. Such a concentration distribution would be consistent with the wind assisting the natural spreading tendencies of a surfactant monolayer downwind and opposing spreading on the upwind edge leading to compaction of the slick and a more abrupt change in concentration. Unfortunately, no information was available about any subsurface flow and its potential role in creating this concentration distribution. Another interesting feature occurs between 22 and 30 minutes in the data. A visible slick was observed but only a modest increase in the SFG signal occurred (slightly larger than background). This indicates only a small surface concentration of surfactant in

this region. Yet this small concentration of surfactant was enough to alter the interfacial rheology dramatically leading to suppressed wind-wave coupling and increased wave damping in this region. There are, however, limitations with the technique. The nonlinear response from different surfactants does vary. Consequently, for complex mixtures of surfactants like those found on the ocean surface, the probe only provides a general idea of when surfactant concentrations are increasing or decreasing when profiling the ocean surface. Spectral scanning of the pump lasers, however, would allow for some chemical speciation potential.

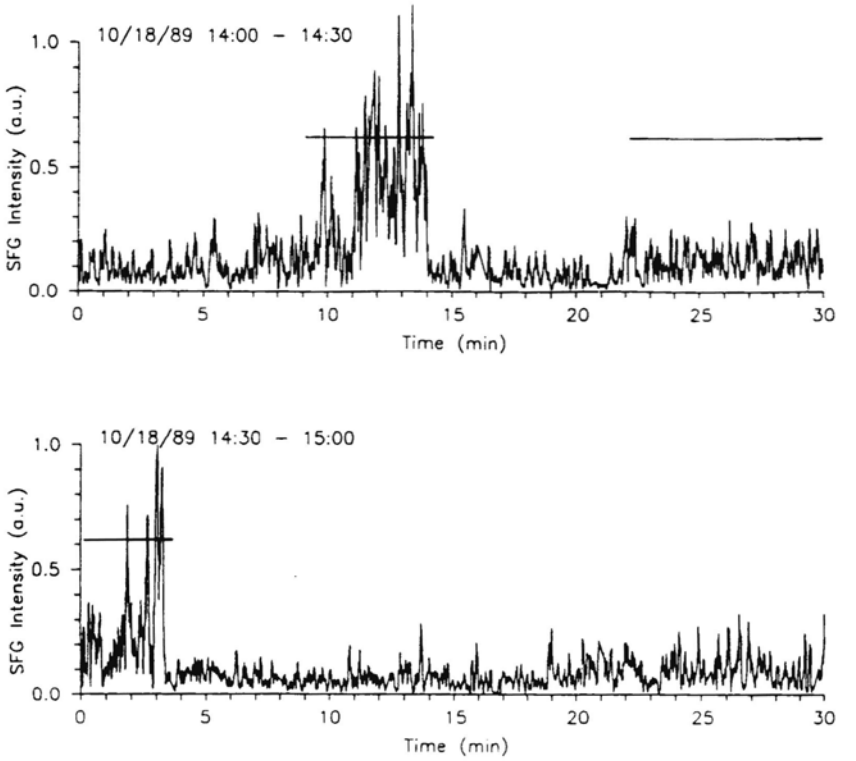

Fig. 1. The 213 nm SFG signal measured during a transect of a series of banded slicks. Signal maximums occur at the upwind edges of the banded slicks. Horizontal lines indicate regions visibly identified with banded slicks.

While these measurements provide a wealth of information on the gross structure of surfactant concentration gradients, the point sampling (2.5 cm in diameter sampling footprint) nature of the measurement technique; the 1 to 2 meter per second speed of the ship serving as the platform; and the 20 Hz repetition rate (20 laser pulses per second) of the laser make it difficult

to resolve the fine structure within the concentration gradients. In particular, it is especially important to obtain millimetre spatial resolution with these surfactant measurements. Millimetre spatial resolution would provide detailed information of the surfactant gradients on capillary-gravity (CG) and capillary waves where surfactants have their largest impact on wave damping and wind-wave coupling. With this goal in mind, we explored the possibility of making single laser pulse SHG and SFG measurements using a CCD camera to record an image of the surfactant based signal.

3 Experimental

Figure 2 is a schematic of the imaging experiment. An unfocussed 6 millimetre diameter 532 nm second harmonic beam from a high repetition rate (100 Hz) Coherent Infinity Nd:YAG laser was made incident at 60 degrees from normal on a water surface in a channel. An insoluble monolayer of a hemicyanine surfactant, 4-[4-(dimethylamino)-styryl]-1-docosyl-pyridinium bromide, was spread on the distilled water surface. The hemicyanine surfactant is a model surfactant system that we have found useful in preliminary laboratory studies (Hirsa et al. 1997). (Hemicyanine is a model surfactant for which we have synthesised derivatives with varying degrees of solubility ranging from derivatives that form insoluble monolayers to soluble surfactant versions). The water in the channel was subjected to a laminar flow of nominal velocity 20 cm s^{-1}. Details of the fluid measurements were presented elsewhere (Hirsa, et al., 2001). At the end of the channel a surface barrier was placed across the channel perpendicular to the flow direction. The SHG signal and the collinear reflected pump laser beam were collect in the direction of reflection. The collinear beams were passed through a dichroic image splitter to separate the green pump beam (532 nm) and the 266 nm second harmonic signal beam. The green pump laser beam was passed through a series of neutral density (ND) filters to limit the detected intensity. The UV SHG signal was passed through a 7-54 colour glass filter to eliminate any residual green pump laser light. The two beams are recombined side by side and sent through a Nikon quartz lens to image the two beams on the photocathode of the pulse gated microchannel plate image intensifier. This image is amplified and optically transferred via a fiber optic coupler to the chip of a CCD camera (Princeton Instruments now named Roper Scientific). The KG-1 filter was used in the pump beam path to eliminate any spurious 266 nm light from the pump beam.

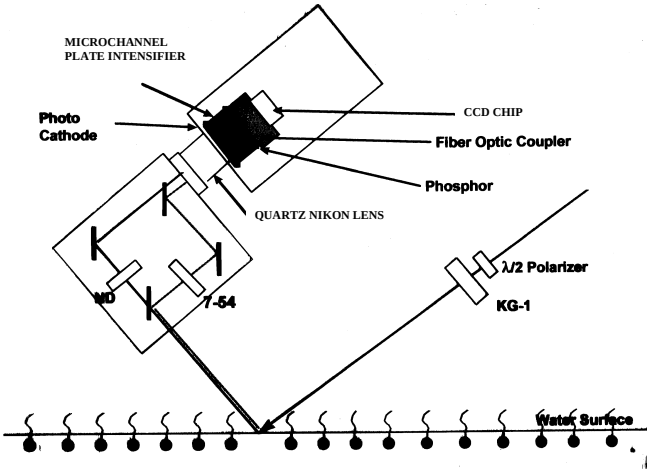

Fig. 2. A schematic drawing of the second harmonic imaging experiment and apparatus. KG-1 and 7-54 are coloured glass filters. The 266 nm signal follows the path through the 7-54 filter and the probe beam follows the path through the neutral density filters (ND)

4 Discussion of results

In the experiment, second harmonic measurements were taken at various positions down stream of the Reynolds ridge. An image of the surfactant distribution was recorded for each laser pulse. The intensity profile of the probe laser beam is quasi-Gaussian in cross-section, so each SHG image must be corrected for the intensity squared dependence on pump intensity. For each frame, a correlation between each of the pixels of the SHG image and those of the reflected pump laser was established. This (i, j) correlation between image pixels was then used to correct for spatial variations in pump laser intensity pixel by pixel. Prior to initiating flow in the channel, SHG measurements were made for a range of hemicyanine surface concentrations. This set of scaled SHG images served as a basis set for establishing SHG intensity as a function of surfactant concentration. This allowed one to determine an absolute value for the surfactant concentration at each pixel location. With the standard concentrations recorded, flow was initiated in the channel and images were obtained for the surfactant gradients downstream of the Reynolds ridge which formed in the channel. A portion of one image is shown in Figure 3 after intensity correction and conversion of the signal intensity to an absolute surfactant surface concentration. The

measurement of Figure 3 was carried out using one 532 nm laser pulse of slightly less than 3 nanoseconds in duration. The 60 degree angle of incidence used for the pump laser beam led to an elliptical footprint that accounts for the two spatial resolutions of 0.21 mm per pixel and 0.07 mm per pixel in the measurement.

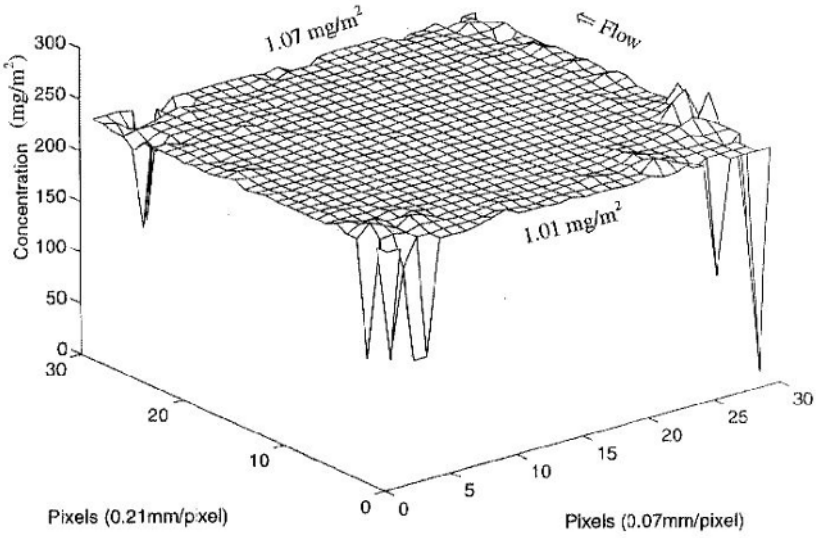

Fig. 3. Absolute hemicyanine monolayer concentrations just downstream of a Reynolds ridge in a laminar channel flow. The concentration gradient was determined using reflected SHG imaging

5 Conclusions

While past work established that SHG and SFG are important and viable *in situ* probes capable of measuring surfactant concentration gradients on the ocean surface, the spatial resolution was limited in these experiments. In order to resolve concentration gradient features of 1 cm or less in extent, an areal SHG measuring technique was developed using a CCD camera as the detector. An image splitting optical separator is key to this measurement technique allowing one to capture both the reflected SHG signal image along with the image of the reflected pump beam which allows us to correct for the intensity variations in the pump beam. The technique is capable of measuring surfactant concentrations with a spatial resolution of less than 1 millimetre and a temporal resolution of less than 3 nano-

seconds. In Part 2, we will discuss the application of this technique to the measurement of surfactant concentrations at the peak and trough of capillary waves.

Acknowledgements. The authors would like to acknowledge support from the Office of Naval Research (N000149710707 and N000149611071).

6 References

Frysinger GS, Asher WE, Korenowski GM, Barger WR, Klusty MA, Frew NM and Nelson RK (1992) Studies of ocean slicks by nonlinear laser processes, Part 1: Second-harmonic generation. J Geophys Res 97 5253-69

Hirsa, A, Korenowski, G. M., Logory, L. M. & Judd, C. D. (1997) "Determination of surface viscosities by surfactant concentration and velocity measurements for an insoluble monolayer". Langmuir, 13, 3813-3822.

Hirsa A, Vogel MJ, Kelley JS and Korenowski GM (2001) Simultaneous measurement of free surface velocity and surfactant concentration via common laser probe. Rev Scientific Instruments 72: 1502-1509

Korenowski GM, Frysinger GS and Asher WE (1993) Noninvasive probing of the ocean surface using laser-based nonlinear optical methods. Photogrammetric Engineering and Remote Sensing 59: 363-369

Korenowski GM (1997) Applications of laser technology and laser spectroscopy in studies of the ocean microlayer. In *The Sea Surface and Global Change*, ed. P. S. Liss and R. A. Duce, pp.445-470. Cambridge, U.K.

Liss PS, Watson AJ, Bock EJ, Jähne B, Asher WE, Frew NM, Hasse L, Korenowski GM, Merlivat L, Phillips LF, Schluessel P and Woolfe DK (1997) Physical processes in the microlayer and the air-sea exchange of trace gases. In The Sea Surface and Global Change, ed. Liss PS and Duce RA, pp. 1-33. Cambridge, U.K.

Shen YR (1984) *The Principles of Nonlinear Optics*, John Wiley, New York, N.Y.

Shen YR (1989) Surface properties probed by second-harmonic generation and sum-frequency generation. Nature 337: 519-525

Imaging surfactant concentration distributions at the air/water interface
Part 2: Insoluble monolayer concentrations on standing capillary waves

Gerald M. Korenowski[1], John R. Saylor[2], Elizabeth A. van Wagenen[1], Joseph S. Kelley[1] **,** Mark E. Anderson[1], and Elizabeth J. Edwards[1]

[1]Department of Chemistry, Rensselaer Polytechnic Institute, Troy, NY, USA
[2]Naval Research Laboratory, Washington, D.C., USA

Abstract. Surfactant concentrations at the peaks and troughs of a standing capillary wave field were measured using a reflected second harmonic generation (SHG) imaging technique. The results revealed behaviour that is consistent with a compaction of the insoluble monolayer at the crests of the capillary waves and a dilation of the monolayer in the troughs. Each measurement was obtained using a single 3 nanosecond laser pulse, providing essentially instantaneous measurements of surfactant concentrations.

1 Introduction

In Part 1, we reviewed the utility of reflected second harmonic generation (SHG) and reflected sum frequency generation (SFG) as ocean surface probes. We have adapted these laboratory probes to give us the first spectroscopic techniques capable of studying the top one or two molecular layers of the ocean surface *in situ*. The method has been demonstrated in field studies where we measured surfactant concentration gradients on the ocean surface (Frysinger et al. 1992, Korenowski et al. 1993, Korenowski 1997). This ability to measure and determine the chemical composition of the first two molecular layers is particularly important because surface tension, interfacial elasticity, and interfacial viscosity are a function of the composition in these layers. While these SHG and SFG probes have proven to be highly useful, nondestructive, and nonintrusive ocean surface probes, there are restrictions. In particular, there is a limitation on the spatial resolution when performing single point measurements on the ocean. The natural divergence in the laser beams and the limited repetition rates (100 Hz or

less) for solid state Q-switched lasers (high peak intensities needed to generate the SHG and SFG signals) coupled with the one to two metre per second speeds (slowest speed while maintaining steerage) of a research vessel, limit surface resolution to about a centimetre. While this is excellent for general surface profiling, millimetre or finer spatial resolution is needed to resolve variations in surfactant concentrations on the surface of capillary-gravity (CG) waves and capillary waves. Such measurements are important since surface tension gradients, interfacial viscosity, and interfacial elasticity strongly affect the CG and capillary waves, and wind-wave coupling and wave damping are dramatically altered for these waves when there are small changes in the interfacial chemical composition at the air-ocean interface.

The system, which we presented in Part 1, was an imaging detection apparatus for use with the reflected SHG and SFG probes. It was applied to the measurement of a gradient in an insoluble surfactant monolayer on a laminar channel flow. A two-dimensional surfactant gradient map was obtained (0.2 millimetre or better spatial resolution) from this flat, surfactant-covered surface. In this paper, we apply this reflected SHG imaging technique to the measurement of surfactant concentrations at the crest and trough of a standing capillary wave field. It is expected that insoluble surfactant monolayers will undergo compression and dilation on a capillary wave surface (e.g. MacIntyre 1971). The expansion of the compressed portion of the monolayer and the contraction of the dilated portion give rise to additional interfacial forces instrumental in wave damping and the reduction of wind-wave coupling (Levich 1962). In this paper we present a direct measurement of this capillary wave induced compression and dilation of an insoluble monolayer.

2 Experimental

Measurements of surfactant concentrations on travelling capillary waves is complicated by the rapid decay rate of these waves, necessitating measurements close to the source of wave generation. To avoid this complication, we utilized a field of standing capillary waves. The wave tank was a circular (6.99 cm, inner diameter) glass vessel. The inner wall was coated with paraffin to avoid loss of the surfactant to the tank side walls. Triply distilled water was used as the substrate. The tank was overflowed to clean the surface prior to spreading the insoluble hemicyanine surfactant monolayer at a surface concentration of 0.288 μg cm^{-2}. Hemicyanine, 4-[4-(dimethylamino)styrl]-1-docosyl-pyridinium bromide, is a stilbazolium dye molecule to which is attached on one end a saturated twenty two car-

bon chain making it an insoluble surfactant. A monolayer was spread from a 3.644 mg mL^{-1} stock solution of hemicyanine in HPLC grade chloroform. Using a microlitre syringe, the stock solution was applied to the water surface and allowed 20 minutes for solvent evaporation and monolayer equilibration prior to use. The spreading concentration of 0.288 μg cm^{-2} will be referred to as the equilibrium concentration, meaning the concentration in the absence of the circular wave field. (After each ten to thirty laser pulses, the surface was cleaned and a new monolayer was spread throughout the series of experiments.)

The tank was mounted on a shaker to impart a vertical vibration for producing the circular capillary wave field. A laser slope gauge consisting of a HeNe laser and a position sensitive detector, was used to measure the wave slope at the tank centre, and to trigger the SHG probe laser. This made it possible to obtain single laser pulse images with the centre of the tank either at a maximum (peak) or minimum (trough). The wavelength of the capillary wave used was 2.0 millimetres (frequency of 240 Hz which matched the frequency of the electromechanical shaker). This frequency was chosen because it produced a small enough wavelength wave where several crests and troughs could be imaged with the existing optical system. The maximum amplitude of 28 microns occurred at the centre of the tank and successive standing wave extrema decreased in amplitude with radial distance from the tank centre. When viewed with the human eye, the wave field appeared as a series of concentric rings. A detailed analysis of the wave field has been presented elsewhere (Saylor et al. 2000).

The incident probe pulse was the 532 nm second harmonic beam from a Coherent Infinity Nd:YAG laser. The 3 nanosecond laser pulse was oriented 60 degrees from the water surface normal direction. The 6 millimetre diameter laser beam was not focussed, and the beam energy was 85 mJ per pulse. The imaging detection system described in Part 1 was used in this experiment; it consisted of a dichroic image splitter, quartz Nikon camera lens, and a pulsed gated, intensified CCD camera (Roper Scientific formerly Princeton Instruments).

3 Discussion of results

In the following discussion, a frame is defined as the recorded output from the CCD detection system as generated by a single pulse from the pump laser. Within each frame there are two related images. One image is the reflected 532 nm pump laser surface reflection and the second is the 266 nm SHG surface signal. There was no averaging of frames from different pump laser pulses. Consequently, each SHG image obtained in the experi-

ments contains a 3 nanosecond snapshot of the surfactant layer concentration on the wave surface. In order to extract this concentration map from the raw images, a correction was applied to account for intensity variations across the laser beam profile. This correction process is now described.

The SHG signal intensity has a quadratic dependence on the incident laser pump intensity (Shen 1989). This quadratic dependence makes it especially important to correct for any variations in laser intensity across the SHG image carefully. The pump laser beam possesses a quasi-Gaussian intensity in spatial profile in addition to small random intensity fluctuations. In order to obtain an accurate surface concentration map, these intensity variations must be recorded and the resulting SHG image appropriately scaled.

We first determined the correct (i,j) offset between a pixel in the 532 nm image and its corresponding pixel in the SHG image for each frame. This (i,j) offset between the two images was determined by finding the best correlation between the three most intense pixels in the 532 nm image with those in the 266 nm SHG image. This (i, j) offset only varied by plus or minus one pixel over all the frames analysed. Consequently, we believe the resulting image scaling yields reliable surfactant concentration measurements.

With the (i, j) offset determined, each pixel in the SHG image was scaled to correct for the pump laser intensity variations. The scaled second harmonic image corresponds to a relative concentration map of the surfactant monolayer. In order to convert this relative surface concentration to an absolute concentration, images from flat (no waves) surfactant-covered surfaces (surfactant concentration of 0.288 $\mu g\ cm^{-2}$) were recorded using the same laser intensity. The scaled pixel intensities from these standard images were used as a scale for converting the relative concentrations from the capillary wave images to an absolute surface concentration map. Because the optical system is aligned to collect an optical signal only from the regions of zero wave slope (flat regions), only those regions which correspond to the crest or trough of the standing capillary wave field provide sufficient signal to convert into a concentration value. A portion of one such concentration map is shown in Figure 1 below.

Each pixel in the crest or trough of the image is a point measurement of surfactant concentration. These point concentration measurements are subject to small perturbations and inhomogeneities in the wave field as well as the noise inherent to the SHG measurement (detector noise, etc.). In order to obtain a more precise measure of the surfactant concentration along a given crest or trough, averaging along the individual crests and troughs of the image was performed. In the table below the averaged concentrations along the crests and troughs are listed along with their 95 % confidence

limits for the image of Figure 1. The regions of zero slope (crest and troughs) in the image (detection system aligned to accept the specular reflection from a flat surface) were determined from the complimentary image of the reflected incident pump laser beam footprint and timing from the wave slope detector.

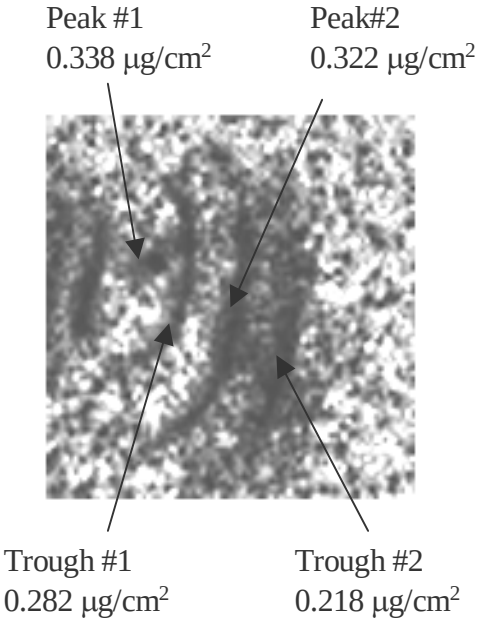

Fig. 1. An intensity scaled SHG image of surfactant concentration on a 2.0 mm wavelength standing circular capillary wave is shown above using a grey scale with darker indicating a stronger signal. The equilibrium (no waves) surfactant concentration was 0.288 μg cm^{-2}. The image was obtained with a single 3 nanosecond laser pulse and the imaging system was optically aligned to capture the signal from the regions of zero slope (crests and troughs-the darker bands in the image). The image is 80 by 80 pixels on edge (0.81 mm/pixel in the y axis and 0.22 mm/pixel in the x axis due to the 60 degree angle of incidence). Indicated on the image are regions corresponding to peaks and troughs of the wave. For each of these regions, concentrations of the insoluble hemicyanine monolayer are indicated. These concentrations are obtained by averaging the individual pixel concentrations along the crest or trough for that particular extremum. The region indicated as 'Peak #1,' is the tank centre.

All of the individual frames analysed in these experiment show trends in surfactant concentration variation: an increase in surfactant concentration at the crest of the wave and a decrease in surfactant concentration at the

trough. Deviations from the equilibrium surface concentrations are at a maximum at the centre of the circular wave field where wave amplitudes are at a maximum. Excursions from the equilibrium surfactant coverage (0.288 μg cm^{-2}) for crests or troughs converge toward the equilibrium concentration at large distances from the centre of the tank. This behaviour is expected since the standing circular capillary wave field in the experiment exhibits a maximum amplitude at the centre. Wave amplitudes decreased as one moved outward from the centre. Images recorded when the centre is a trough, rather than a crest, exhibit the opposite trend from that presented in Table 1. The surfactant concentration was less than the equilibrium value in the centre, and then alternating positive/negative excursions from the equilibrium value. Consequently, the SHG imaging technique presented here is measuring surfactant concentrations that are consistent with a compression and dilation of the monolayer in the peaks and troughs, respectively.

Table 1. Surfactant surface concentration (μg cm^{-2}) and 95 % confidence limits for the image in Figure 1

	Surfactant Concentration [μg cm^{-2}]
Crest (Centre)	0.338 ± 0.197
Trough 1	0.282 ± 0.051
Crest 2	0.322 ± 0.073
Trough 2	0.218 ± 0.046

While these results are intriguing, we need to address the large confidence limits for the measurements obtained at the tank centre. There are two primary reasons for this large confidence limit. The first is that there are very few pixels to average over for the centre crest or trough (in comparison to other crests or troughs). With the optical system aligned to collect signal from regions of zero wave slope only, the image of the central crest (or trough) has the fewest number of pixels available for averaging. We included as many pixels as possible in the averaging process for the central portion of the wave field. This may have included pixels in the image not necessarily corresponding to exactly a slope of zero, and which were not necessarily focused in the image plane. This was compounded by the fact that there are small deviations or irregularities in the diameter of the tank resulting from manufacturing and paraffin coating of the inner walls. These diameter deviations are small. Nevertheless, they affect the waves resulting in an approximation, albeit a good approximation, to a true standing wave with slight distortions. The wave field is generated at the

tank walls by the vertical shaking motion creating an inward travelling circular wave that is reflected at the centre (now an outward travelling wave) with the net result a quasi-circular standing wave field. These edge deviation effects are not discernable in the outer portions of the field near the tank edge but are magnified near the centre of the tank where the wave field is focused. This effect appears as a distorted central crest (or trough). Nevertheless, image after image shows a consistent concentration increase for a centre crest and a concentration decrease for a central trough albeit with a large confidence limit. Consequently, we believe the measurement is capturing the correct change in concentration for this region. The slight distortion in the wave field may also account for slight deviations from the expected absolute surfactant concentrations measured in moving from the centre of the field outward. The overall trends recorded are, however, consistent with the insoluble monolayer under compression at the wave crest and dilated at the wave trough. In future experiments we will expand the incident probe laser beam to encompass more of the wave field in the imaging.

The existing measurements of the crest and trough surfactant concentrations are precise and accurate enough to demonstrate that the reflected SHG imaging technique can measure capillary wave generated surfactant concentration gradients. The measurements obtained in these experiments will be subjected to a comparison with theoretical predictions in a future publication. In addition, experimental work on the technique and its application to capillary wave induced surfactant concentration gradients continues as well as work adapting the method for *in situ* ocean work.

4 Conclusions

We have demonstrated that capillary waves do induce concentration gradients for an insoluble surfactant monolayer on a water surface. In the experiments described above, reflected SHG imaging was shown to provide a direct measurement of these surfactant concentration gradients with a temporal resolution of 3 nanoseconds. As far as we know, this is the first such direct, nonintrusive measurement of these monolayer concentration gradients on a capillary wave field which does not require mechanical contact with the system under study. Elegant surface potential measurements were used in similar experiments but this latter technique requires part of the measuring device to be located under the water and in close proximity to the water surface that may affect the subsurface motion associated with the wave (Hühnerfuss et al. 1985, Hühnerfuss et al. 1985, Lange et al. 1986). In these surface potential measurements, a travelling wave was used which

can result in a phase shift with respect to the position of maximum compression and dilation of the monolayer on the wave surface. For this reason, the experiments reported here employed a standing wave field (or nearly so) in an attempt to simplify the experiment by eliminating or minimising any phase shift so that maximum compress and dilation should occur (according to theory) at the wave crest and trough, respectively.

Applications of this nonlinear laser imaging technique holds the promise of directly studying the effect that capillary wave stresses exert upon the surfactant layer as well as those exerted by the surfactant on the water surface. The importance of capillary wave/surfactant dynamics at the ocean underscores the importance of these experiments and suggests that further efforts directed toward extending these experimental techniques to *in situ* ocean studies would be most useful.

Acknowledgements. The authors would like to acknowledge support from the Office of Naval Research (N000149710707 and N000149611071) and the Naval Research Laboratory.

5 References

Frysinger G S, Asher WE, Korenowski GM, Barger WR, Klusty MA, Frew NM and Nelson RK (1992) Studies of ocean slicks by nonlinear laser processes, Part 1: Second-harmonic generation. J Geophys Res 97: 5253-69

Hühnerfuss H, Lange PA, and Walter W (1985) Relaxation effects in monolayers and their contribution to water wave damping. Part I: Wave induced phase shifts. J Colloid Interface Sci 108: 430-441

Hühnerfuss H, Lange PA, and Walter W (1985) Relaxation effects in monolayers and their contribution to water wave damping. Part II: The Marangoni phenomenon and gravity wave attenuation. J Colloid Interface Sci 108: 442-450

Lange PA and Hühnerfuss H (1986) Use of an electrical surface potential probe for the measurement of capillary and gravity water waves. Rev Sci Instrum 57, 926-932.

Korenowski GM, Frysinger GS, and Asher WE (1993) Noninvasive probing of the ocean surface using laser-based nonlinear optical methods. Photogrammatic Engineering and Remote Sensing, 59: 363-369.

Korenowski GM (1997) Applications of laser technology and laser spectroscopy in studies of the ocean microlayer. In The Sea Surface and Global Change, ed. P. S. Liss and R. A. Duce, pp.445-470. Cambridge, U.K.

Levich VG (1962) Chapter 9 “Waves on a Liquid Surface”. In *Physicochemical Hydrodynamics*, pp 591-668, Prentice-Hall, U.S.A. and the references therein.

Liss PS, Watson AJ, Bock E J, Jähne B, Asher WE, Frew NM, Hasse L, Korenowski GM, Merlivat L, Phillips LF, Schluessel P, and Woolfe DK (1997) Physical processes in the microlayer and the air-sea exchange of trace gases.

In *The Sea Surface and Global Change*, ed. P. S. Liss and R. A. Duce, pp.1-33. Cambridge, U.K.

MacIntyre F (1971) Enhyancement of gas transfer by interfacial ripples. Phys Fluids, 14, pp.1596-1604

Saylor JR, Szeri AJ, and Foulks GP (2000) Measurement of surfactant properties using a standing circular capillary wave field. Experiment in Fluids (in press)

Shen YR (1989) Surface properties probed by second-harmonic generation and sum-frequency generation. Nature 337: 519-25.

Chapter 3:

Modelling and Air-Sea Interactions

Variability of the wave number spectra of short surface waves in the ocean and their modulation due to internal waves and natural slicks

Paul A. Hwang

Oceanography Division (on assignment of Remote Sensing Division),
Naval Research Laboratory, Washington DC, USA

Abstract. Spatial measurements of capillary-gravity (CG) waves in the ocean are collected using a scanning slope sensor mounted on a free-drifting, wave-following buoy. The spectral analysis of spatial measurements yields wave number resolution directly. The range of wavelengths resolved from the optical sensor is from 0.4 to 6.2 cm. This paper investigates the variability of the spectral densities of these capillary-gravity waves under natural field conditions. For mild to medium wind speeds, the variation factor (to be further defined in the text) is typically between 1.5 and 2.5 in the short gravity wave regime, and between 2 and 4 in the capillary wave regime. The quantitative enhancement of the roughness contrast by natural slicks and surface current strains induced by internal waves is also presented.

1 Introduction

Acquisition of capillary-gravity wave data in the ocean has been a difficult task due to several reasons. (1) High Doppler frequency shift of short waves by surface currents, rendering interpretation of point measurements difficult. (2) Spatial measurements using wave gauge array suffer the limitation of frequency response and contamination from meniscus effect. (3) Spatial measurements using imaging techniques are complicated by the convolution process of image formation and optical scattering from a complicated surface, the nonuniform ambient lighting condition also contributes to the uncertainty of results. (4) Short waves are sensitive to variations of environmental parameters, either natural or manmade, thus flow disturbance of instrument mounting platform represents a serious source of signal contamination.

In order to alleviate these problems, several solutions are available. Spatial scanning techniques can be applied to the design of laser slope gauge to eliminate the problem associated with Doppler shift and still maintain high frequency response (e.g., Hwang et al. 1993, 1996, Li et al. 1993, Bock and Hara 1995). In order to reduce flow disturbance, Hwang et al. (1996) initiated the design of free-drifting deployment. The instruments are mounted on an open-frame structure, which also serves as a free drifting wave-following buoy such that the relative velocity between flow and instruments can be reduced to minimize disturbance to the sensing area.

The scanning slope sensor buoy (SSSB) participated in the HiRes II Field Experiment onboard R/V Columbus Iselin in June 1993. The average wave number spectra are reported by Hwang et al. (1996). The results indicate that (1) a pronounced peak at the wave number k = 9 rad cm^{-1} is evident in the curvature spectra for wind speeds below 6 m s^{-1}; (2) the slopes of the curvature spectra are 1 and -1 on the two sides of the spectral peak; (3) the spectral density and mean square roughness properties increase linearly with wind speed; and (4) these observations suggest a spectral function of the form $\chi(k) = Au_* c^{-2} c_m k_m k^{-4}$, which is proportional to $u_* k^{-3}$ in the short gravity wave region and $u_* k^{-5}$ in the capillary wave region, where u_* is the wind friction velocity, c_m the minimum phase velocity of surface waves, and k_m the corresponding wave number. In this paper, the variability of spectral intensity under natural field conditions and the modulation due to internal waves are studied. Section 2 describes the field experiment and the measurements. Section 3 presents the analysis procedure and the results of spectral variation. Section 4 is a summary.

2 Field experiment

2.1 Measurements

The key instrument for CG wave measurements is the scanning slope sensor. In the present design, a laser beam scans a two-dimensional pattern of eight linear segments spaced 0.5 cm apart. Each linear segment, 10 cm in length, is sampled at 50 positions with an equal spacing of 0.2 cm. The duration to sample the 50 positions is 2.5 ms, and the mechanical flyback time of the scanning mirror facets to generate two consecutive scan lines is 4.3 ms. In addition to the scanning slope sensor, other data collected from the wave-following SSSB include wind speed and direction at 1.32 m above mean water level (MWL), air temperature (0.97 m above MWL), water temperature (0.47 m below MWL), long wave induced acceleration

of the platform, depth of water above the laser scanner projector, the compass orientation of the platform, and the ambient light intensity.

In field measurements, monitoring of the ambient light is an important task. Due to the limited laser power (8 mW output, 670 nm wavelength), the signal intensity deteriorates markedly under bright sunlight although narrow band-passed filters are used. An analysis of the effect of ambient light on the slope measurements was presented by Hwang et al. (1996). It was shown that the ambient light causes an attenuation of the slope signal. The attenuation factor is a function of the ambient level normalized by the laser intensity (denoted as N/S). Experiments carried out in the laboratory confirm the analytical calculation. From these results, the data segments with ambient light intensity $N/S<2$ can be compensated with reasonable confidence. The ambient intensities of the data selected for analysis presented in this paper, with $N/S<0.76$, are much less than the critical level. During the data processing, the ambient light intensity is updated every 10 s.

2.2 Environmental conditions

The SSSB is deployed in the Atlantic Ocean approximately 40 km northeast of Cape Hatteras (Case 1413) at 35° 26.16' N, 75° 2.90' W and retrieved at 35° 24' N, 75° 4' W. The data collection period is from 13:59:29.14 (t = 0) to 16:09:22.03 (t =7783.15s) UTC. The data for the first 14 minutes or so are onboard the research vessel and not used. On this day, two long internal wave bands several kilometres long and approximately 2 to 4 kilometres apart are spotted on the water surface. The buoy is released into water at 14:13 UTC. The sky is partly cloudy. At 14:49 ($t \approx$ 3000 s) the ship is in a large dark cloudy area. The buoy records a sharp drop in the ambient light at t >2500 s. The dual surface slick bands are visible throughout the morning. The buoy obviously crosses one of them at $t \approx$ 3100 s when a dip of 0.1°C water temperatures is recorded (Fig. 1b). Visual confirmation of this encounter is not available due to the large distance between the ship and the buoy. However, similar surface temperature drops (from Jim Edson's onboard met-sensor display) occur when ship crosses slick bands in a few other occasions.

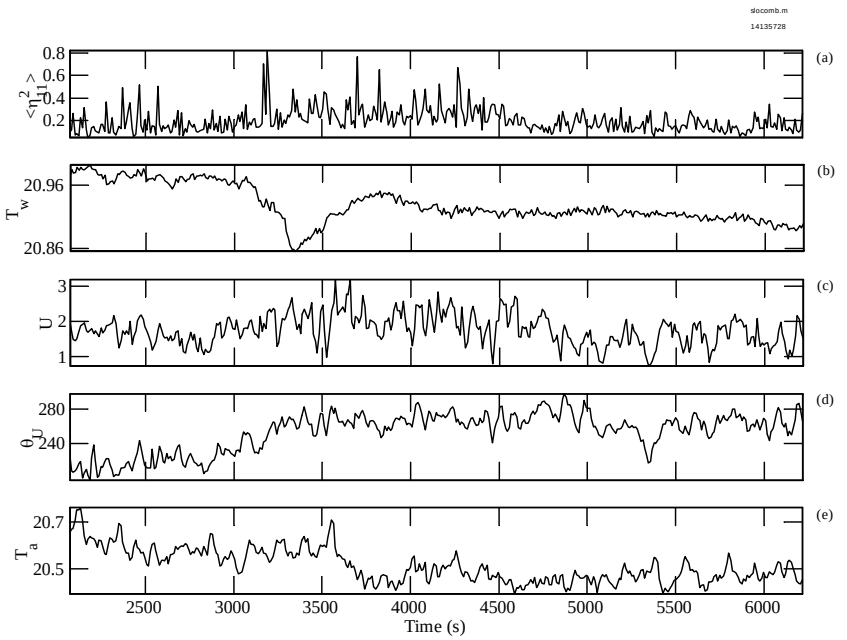

Fig. 1. Case 1413, buoy encountered internal wave soliton and slick bands. (a) Mean square curvature, (b) surface water temperature, (c) wind speed, (d) wind direction, and (e) air temperature

Wind readings from shipboard display indicate northerly in the first hour after deployment. The wind speed increased from 3.5 m s^{-1} at 14:00 ($t \approx 30$ s) to 5 m s^{-1} at 15:00 ($t \approx 3630$ s). The wind started shifting clockwise and gradually decreased to 3 m s^{-1} from 30° at 15:37 ($t \approx 5850$ s), then increased to 5 m s^{-1} from 30° at 16:00 ($t \approx 7230$ s). In the afternoon, wind continued shifting and speed reached 9 m s^{-1} from 75° at 17:00 ($t \approx 10830$ s). Similar fluctuation of wind velocities was recorded at the drifting buoy (Figs. 1c, d). There are some apparent differences between the ship observation and the buoy recording. Because the buoy was too far away from the ship, we are able to establish only semi-quantitative correlation between ship observations and buoy recording. The time difference can be attributed to the spatial distance of the ship and the buoy. From radar tracking, the distance was approximately 2 km at 14:49 and the buoy was barely visible from the ship by unaided eyes. (In fact, the buoy was too far away at the end of the experiment it disappeared from the ship radar. NRL P3 aircraft and R/V Bartlett had to be summoned to help searching and recovering the buoy.) The wind direction output shown in Fig. 1 is not cali-

brated and has an unknown bias. The magnitude of wind shifting, however, is accurate.

3 Analysis procedure and result discussion

Hwang et al. (1996) reconfirmed the linear correlation between (long-term averaged) wind speeds and surface roughness established from sun glitter measurements by Cox and Munk (1954). Hwang (1977) compiled available field data sets, included the mean square slopes derived from the sun glitter measurements (Cox and Munk 1954), surface slope measurements by a laser slope gauge mounted 10 m ahead of a ship's bow (Hughes et al. 1977), surface slope measurements by a laser slope gauge mounted on a mechanical wave-follower (Tang and Shemdin 1983, Hwang and Shemdin 1988), and the data from the scanning slope sensor buoy (Hwang et al. 1996). The combined measurements show that the scatter of data points from these various sources is primarily confined within the factor-of-two envelope of the mean trend. For wind speed exceeding a threshold condition, the functional relationship of mean square curvature in the downwind direction, $<\eta_{11}^2>$, on wind speed, U_{10}, is empirically determined to be

$$\left\langle \eta_{11}^{\ 2} \right\rangle = 9 \times 10^{-2} U_{10} \qquad (1)$$

In order to investigate the spectral variability, wave number spectra from optical scanning slope sensor were processed in 10-s segments. The resulting spectrum of each segment is the average of 1800 raw spectra. As illustrated in Fig. 1a, the 10-s processing preserves many fine features of the structure of ocean surface roughness. Notably, the two sets of spikes in the mean square curvature (Fig. 1a) at the leading (t ~ 3200 s) and trailing (t ~ 3750 s) edges of the internal wave event are well resolved. Associated with this internal wave event (suggested by the water temperature record (Fig. 1b) and visual observations during the experiment) are regions of low surface roughness, presumably caused by the slick bands observed in the region throughout the whole period of experiment. The data analysis is complicated by the large variation in the wind field (Fig. 1c, d) during the same period.

Based on Eq. (1), a ratio $r = <\eta_{11}^2>/(0.09U_{10})$ is used to sort out data segments into three classes (I, II, and III) according to $r \le 1/\sqrt{2}$, $1/\sqrt{2} < r \le \sqrt{2}$, and $r > \sqrt{2}$. Subsets of class I with $r < 2$ (Ib) and of class III with $r > 2$ (class IIIb) are also produced. The three classes will be referred to as sub-normal, normal, and super-normal conditions in the following.

Figure 2 shows an enlarged section of the internal wave event and the associated 10-s average mean square curvature (Fig. 2a) and wind speed

(Fig. 2b). Different plotting symbols are used to identify sub-normal (circles and down triangles) and super-normal (pluses and up triangles) from the normal segments (crosses).

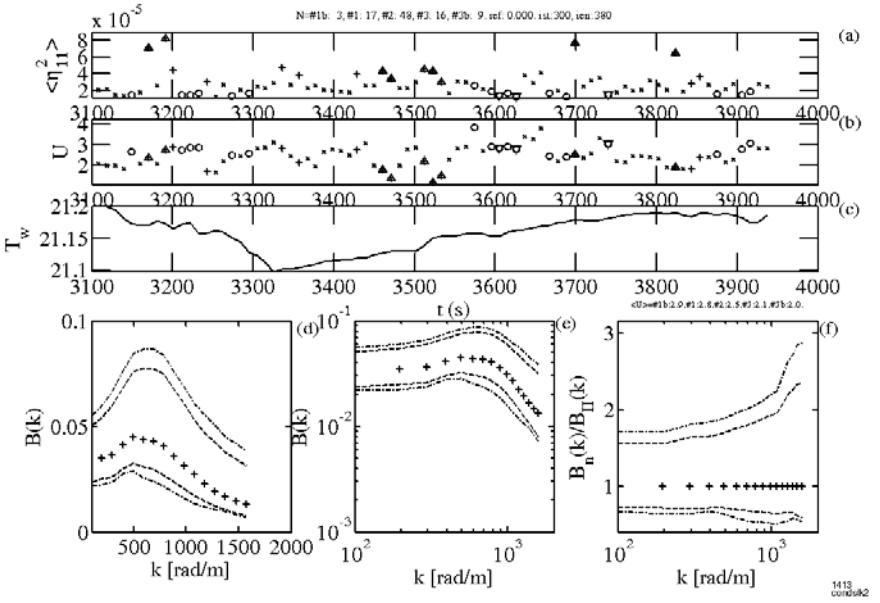

Fig. 2: Enlarged plots of the segments near the internal wave event. (a) Mean square curvature (×: normal, + and Δ: super-normal, 1.5 and 3 dB, respectively, o and ∇: subnormal, -1.5 and -3 dB, respectively), (b) wind speed (symbols are the same as those in (a)), (c) surface water temperature, (d) dimensionless wave number spectra, $B(k)$, (e) same as (d) but in logarithmic scales, (f) normalized spectra. In (d-f), the mean spectrum is shown by pluses, the dashed curves are the 3 dB envelops, and the dash-and-dotted curves are the 6 dB envelops

Three groups of enhanced roughness can be identified. (1) At the leading edge of the internal wave, $t \approx 3190$ s, there are two closely spaced roughness spikes. Using the average drift velocity of the buoy, 0.31 m s^{-1} computed from the retrieval and deployment locations, the separation distance of the two spikes was approximately 3 m. (2) At the trailing edge there are another two spikes more widely separated, at $t \approx 3700$ and 3820 s. The distance of separation calculated with the mean drift velocity was 36 m. (3) Between these two sets of roughness spikes, a region (between $t \approx$ 3460 and 3530 s) of super-normal roughness with very low wind speeds but above-average surface roughness was observed. The water temperature profile indicates some noticeable perturbations (see fig. 1a for a better per-

spective) and suggests that the straining of the surface current field, not the wind, was responsible for the presence of this roughness patch.

Regions of suppressed roughness occurred at both edges of the internal wave event. These suppressed regions tend to be more contiguous. At the leading edge, two subnormal bands occurred on both sides of the enhanced roughness (at $t \approx 3190$ s). The water temperature showed a prominent fluctuation signature (Fig. 1b provides a better perspective) associated with this roughness enhancement event. The temperature dropped significantly (at $t \approx 3250$ s) following the subsequent roughness suppression. The second group of roughness suppression that occurred at the trailing edge was more spread out. A long contiguous region near $t \approx 3600$ s was coincident with a plateau of the water temperature time series. Surface wind speed in this segment was above average of the whole episode. The significance of these correlations of the surface temperature microstructure and the surface roughness may provide interesting insights of the dynamics of short waves on the ocean surface. Because surface temperature is a much easier quantity to measure than the near-surface current, it may serve as a surrogate parameter to represent the near surface turbulence and current strain. The correlation to the surface roughness then allows radar or other remote sensors to monitor the near-surface turbulence structure.

The dimensionless spectral density (the degree of saturation, $B(k)=k\chi_1(k)$, defined by Phillips, 1985) of the three classes and two subclasses are shown in Figs. 2d and 2e in linear and logarithmic scales, respectively. The maximum of $B(k)$ occurred at $k\approx 7$ rad cm^{-1}. Using the mean spectral density of the class II segments as the normalization factor, the normalized spectra are shown in Fig. 2f. The envelope formed by the super- and sub-normal spectra is a representation of the roughness contrast of the ocean surface. Environmental parameters contributing to the roughness contrast include wind-induced turbulence fluctuation and surface or internal wave modulation. The range of spectral variations in the short gravity wave range ($1 \leq k \leq 5$ rad cm^{-1}) was relatively constant, and increased steadily toward short capillary waves with higher wave numbers.

The same analysis is applied to three other cases without internal waves. The mean wind speeds were 1.3 (case 2422), 3.5 (case 1310) and 5.7 (case 1223) m s^{-1}, as compared to 2.1 m s^{-1} for the internal wave case (case 1413) just described. The spectral variability as a function of wave number is calculated by the ratio of $B_{III}(k)/B_I(k)$, where subscripts I and III denote class I and class III, respectively. The results are plotted in Fig. 3, showing a monotonic increase in the variation level with increasing wind speed and wave number. The spectral variability can be interpreted as a measure of the modulation amplitude. The modulation level of the internal wave seg-

ment in case 1413 is considerably higher than that of the segment with similar wind speed but in the absence of internal waves or surface slicks (Fig. 3).

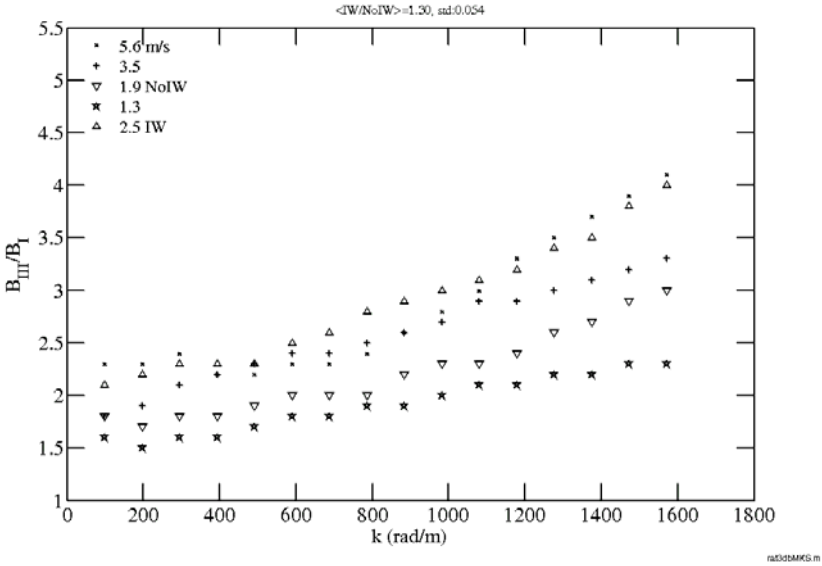

Fig. 3: The ratio $B_{III}(k)/B_I(k)$, as a representation of the modulation amplitude, plotted as a function of k.

4 Discussion and conclusions

Using a free-drifting scanning slope sensor system, the wave number spectra of surface roughness in the vicinity of an internal wave soliton were measured. Associated with the internal wave event were two persistent linear slick bands. The surface roughness responded to the surface current strain induced by the internal wave and displayed high roughness spikes at the leading and trailing edges of the soliton. The response of the observed roughness modulation has certain similarities with observations of internal waves by synthetic aperture radars (Hughes and Gower 1983, Hughes and Dawson 1988, Thompson and Gasparovic 1986). It is believed that the primary mechanism is the modulation of short waves by straining of surface current induced by the internal waves.

Interestingly, the amplitude of spectral modulation increased toward higher wind speed and wave number (Fig. 3). This trend is opposite to the prediction of the relaxation theory that assumes a monotonic increase in

the relaxation rate with increasing u_*/c (e.g., Keller and Wright 1975, Hughes 1978, Plant 1982). Based on the relaxation theory, in a non-resonant system (comprised of the modulating current field, the modulated wave component, and the associated wind generation and breaking dissipation) the spectral density fluctuation (thus the contrast of radar backscatter) is larger if the relaxation rate is slower (longer wavelength, lower wind speed, or faster convection of the modulating current field). The modulus of relaxation can be expressed as (Hwang and Shemdin 1990)

$$M_n = \frac{s + r}{\sqrt{\left(\beta_r / \Omega_n\right)^2 + \left(1 - c_g / C_n\right)^2}} \tag{2}$$

where Ω_n and C_n are the n-th harmonic of the characteristic angular frequency and the phase velocity of the modulating current field, r the ratio of the group velocity, c_g, and the phase velocity, c, of the modulated short wave component, s the slope of the wave number spectrum in the vicinity of the modulated short wave component, and β_r the relaxation rate, which is approximately proportional to the growth rate, β, of the modulated short waves. Hwang (1999) presented an analysis of laboratory measurements of the hydrodynamic modulation of capillary-gravity waves. The result showed that the theoretical predictions were in excellent agreement with the upper bound of the experimental data. This is a logical conclusion because in a wind-generated wave system, growth and decay of short waves are continuous processes. The interaction time or interaction distance between a particular modulated wave number component and the modulating long waves is variable. Therefore, the measurements represent modulation results at different stages of interaction. Hwang and Shemdin (1990) illustrated with numerical computations that the modulus of hydrodynamic modulation increases monotonically with interaction duration or interaction distance.

Although the ratio of $B_{III}(k)/B_I(k)$ presented in the last section is not the same as the modulus of hydrodynamic modulation, one expects that the two quantities to be proportional. The increasing trend of hydrodynamic modulation of short CG waves has important implications in radar remote sensing. The results suggest that high contrast of sea return can be obtained from radars of shorter wavelengths, making implementation on spacecraft or aircraft much easier to accommodate. It is noted that similarly surprising results have been reported for much longer Bragg waves of L- and X-band radars (about 25 and 3 cm wavelengths). These results suggest that the hydrodynamic properties of short surface waves (decimetre to millimetre scales) are very different from those of longer gravity waves (greater than ~10 m) that have been studied extensively. For example, one of the

well-documented observations is the parasitic capillary waves phase-locked with short and steep gravity waves (e.g., Cox 1958, Ebuchi et al. 1987, Perlin et al. 1993). Longuet-Higgins (1963, 1992, 1995) presented theoretical analyses describing a physical mechanism that produces parasitic capillary waves. The steep curvature near the crest of a short gravity wave produces localized surface tension force that serves as the generator of capillary waves. The capillary waves can maintain phase-locked with the short gravity wave when their propagation speeds match. These capillary waves decay very fast and the evolution processes are frequently completed at the front phase of the crest of the short gravity wave. The modulation properties of these waves are controlled by the viscous dissipation rather than wind forcing or breaking dissipation (Hwang 2002). This feature is starting to be integrated into the study of surface wave spectral models (e.g., Makin and Kudryavtsev 1999, Kudryavtsev et al. 1999). More research remains to be carried out on short gravity and capillary-gravity waves to gain a better understanding of their dynamics and evolution in the open ocean.

Acknowledgements. Support of this research was sponsored by the Office of Naval Research. [NRL Contribution PP/7330-98-0048].

5 References

Alpers W, Hasselmann K (1978) The two-frequency microwave technique for measuring ocean wave spectra from an airplane or satellite. Bound Layer Meteorol 13: 215-230

Bock EJ, Hara T (1995) Optical measurements of capillary-gravity wave spectra using a scanning laser slope gauge, J Atm Oceanic Tech 12: 395-403

Cox CS (1958) Measurements of slopes of high-frequency wind waves. J Mar Res. 16: 199-225

Cox CS, Munk W (1954) Statistics of the sea surface derived from sun glitter. J Mar Res 13: 198-227

Ebuchi N, Kawamura H, Toba Y (1987) Fine structure of laboratory wind-wave surface studied using an optical method. Bound Layer Meteorol 29: 133-151

Hughes BA (1978) The effect of internal waves on surface wind waves. 2. Theoretical analysis. J Geophys Res 83: 455-465

Hughes BA, Grant HL (1978) The effect of internal waves on surface wind waves. 1. Experimental measurements. J Geophys Res 83: 443-454

Hughes BA, Gower JTR (1983) SAR imagery and surface truth comparisons of internal waves in Georgia Strait, British Columbia, Canada. J Geophys Res 88: 1809-1824

Hughes BA, Dawson TW (1988) Joint Canada-U.S. Ocean Wave Investigation Project: An overview of the Georgia Strait Experiment. J Geophys Res 93: 12219-12234

Hughes BA, Grant GL, Chappell RW (1977) A fast response surface-wave slope meter and measured wind-wave moments. Deep-Sea Res 24: 1211-1223

Hwang PA (1997) A study of the wavenumber spectra of short water waves in the ocean. Part II: Spectral model and mean square slope. J Atm Oceanic Tech 14: 1174-1186

Hwang PA (1999) Microstructure of ocean surface roughness: A study of spatial measurement and laboratory investigation of modulation analysis. J Atm Oceanic Tech 16: 1619-1629

Hwang PA (2002) Phase distribution of small scale ocean surface roughness. J Phys Oceanogr 32: 2977-2987

Hwang PA, Shemdin OH (1988) The dependence of sea surface slope on atmospheric stability and swell condition. J Geophys Res 93: 13903-13912

Hwang PA, Shemdin OH (1990) Modulation of short waves by surface currents - A numerical solution. J Geophys Res 95: 16311-16318

Hwang PA, Trizna DB, Wu J (1993) Spatial measurements of short wind waves using a scanning slope sensor. Dyn Atm Oceans 20: 1-23

Hwang PA, Atakturk S, Sletten MA, Trizna DB (1996) A study of the wavenumber spectra of short water waves in the ocean. J Phys Oceanogr 26: 1266-1285

Kudryavtsev VN, Makin VK, Chapron B (1999) Coupled sea surface-atmosphere model. 2. Spectrum of short wind waves. J Geophys Res 104: 7625-7639

Li Q, Shiao M, Tang S, Sun S, Wu J (1993) Two-dimensional scanning laser slope gauge: measurements of ocean-ripple structures. Appl Optics 32: 4590-4597

Longuet-Higgins MS (1963) The generation of capillary gravity waves by steep gravity waves. J Fluid Mech 16: 138-159

Longuet-Higgins MS (1992) Capillary rollers and bores. J Fluid Mech 240: 659-679

Longuet-Higgins MS (1995) Parasitic capillary waves: a direction calculation. J Fluid Mech 301: 79-107

Makin VK, Kudryavtsev VN (1999) Coupled sea surface-atmosphere model. 1. Wind over waves coupling. J Geophys Res 104: 7613-7623

Perlin M, Lin H, Ting CL (1993) On parasitic capillary waves generated by steep gravity waves: an experimental investigation with spatial and temporal measurements. J Fluid Mech 255: 597-620

Phillips OM (1985) Spectral and statistical properties of the equilibrium range in wind-generated gravity waves. J Fluid Mech 156: 505-531

Plant WJ (1982) A relationship between wind stress and wave slope. J Geophys Res 87: 1961-1967

Tang S, Shemdin OH (1983) Measurement of high frequency waves using a wave follower. J Geophys Res 88: 9832-9840

Thompson DR, Gasparovic RF (1986) Intensity modulation in SAR images of internal waves. Nature 320: 345-348

On the imaging of biogenic and anthropogenic surface films on the sea by radar sensors

Martin Gade

Institute of Oceanography, University of Hamburg, Hamburg, Germany

Abstract. Radar signatures of sea surface films of different origin are investigated, which have been acquired by airborne and spaceborne multi-frequency/multi-polarisation microwave sensors during the *Spaceborne Imaging Radar-C/X-Band Synthetic Aperture Radar* (SIR-C/X-SAR), missions in 1994, as well as by the ERS SAR in 1996-98. During SIR-C/X-SAR, controlled surface film experiments were performed in the German Bight by deploying various quasi-biogenic substances and mineral oil on the sea surface, in order to study the radar signatures caused by surface films of different visco-elastic properties. In general, our results show that multi-frequency capabilities, rather than multi-polarisation capabilities, are needed for a radar-based system for the discrimination of marine surface films. We show that, under high wind conditions (> 10 m s^{-1}), a discrimination between the different kinds of surface films is very difficult, whereas at low to moderate wind speeds (≤ 5 m s^{-1}) a discrimination seems to be possible. This finding is supported analytically by means of a new model for the wave number-dependent radar contrast at high wind speeds (> 10 m s^{-1}) and statistically through the analyses of more than 700 ERS SAR images. In addition, results of laboratory experiments are presented that were carried out in the wind-wave tank of the University of Hamburg. At certain wind-speed ranges a different damping of bound and freely propagating surface waves by monomolecular surface films is observed, which may explain the high radar contrasts measured by the microwave sensors.

1 Introduction

The damping of short gravity-capillary ocean surface waves by biogenic and anthropogenic surface films is a well known phenomenon and has been subject of various investigations (Gade et al. 1998a, and literature cited therein). At oblique incidence angles short ocean surface waves are responsible for the backscattering of microwaves of comparable wave-

lengths (Bragg scattering, see Valenzuela 1978), thus, wave damping by oceanic surface films causes a reduction of the measured radar backscatter. For this reason, dark patches visible on synthetic aperture radar (SAR) images of the ocean surface can often be related to oil spills or natural slicks floating on the sea surface.

The layer thickness of a mineral oil spill is much larger than that of a monomolecular sea slick, which results in different visco-elastic properties and, therefore, in a different damping of the ocean surface waves (Alpers and Hühnerfuss 1988). Results of laboratory experiments showed that Marangoni damping is the dominant mechanism for the damping of short sinusoidal gravity waves by monomolecular slicks (Hühnerfuss 1986). Following Marangoni damping theory, monomolecular surface films exhibit a resonance-like damping behaviour (at wave numbers of about 100 $radm^{-1}$), whereas this distinct damping maximum is missing for (thick) mineral oil spills.

Since the application of a single-frequency, fixed incidence radar system (like the C-band SAR aboard the ERS satellites) can provide information on the damping of ocean surface waves at only one single Bragg wavelength, multi-frequency radar techniques have already been used to obtain more extended information on the damping behaviour of the detected surface films (e.g., Gade et al. 1998c). However, during recent field experiments with artificial monomolecular surface films, a distinct damping-maximum at intermediate wave numbers was not measured (Gade et al. 1998c). Thus, additional terms describing the energy fluxes on the water surface, like the energy input by the wind, wave breaking, and non-linear wave-wave interaction, have to be taken into account for the development of theoretical models that can explain the measured damping of small ocean surface waves by different surface films.

During the two Shuttle Imaging Radar C-/X-Band Synthetic Aperture Radar (SIR-C/X-SAR) missions in April and October, 1994, surface films of different visco-elastic properties were deployed in the German Bight of the North Sea, in order to simulate different biogenic and anthropogenic ocean surface films. The aim of these experiments was to investigate whether active microwave techniques are capable of yielding information, on the one hand, on the damping behaviour of different surface films and, on the other hand, on the damping behaviour of one substance under different environmental conditions. Here we briefly present the results of these experiments obtained by a 5-frequency/multi-polarisation scatterometer, and by the 3-frequency/multi-polarisation SIR-C/X-SAR. They are complemented by statistical analyses of more than 700 ERS SAR images acquired over different parts of European coastal waters and by results of laboratory studies performed in a wind-wave tank. For a more de-

tailed description of these results the reader is referred to Gade (1996) and to the papers by Gade et al. (1998a,b,c).

2 Results obtained from measurements with HELISCAT

During the two SIR-C/X-SAR missions in April and October, 1994, radar backscatter measurements were carried out with a 5-frequency/multi-polarisation scatterometer flown on a helicopter. This scatterometer, called HELISCAT, works at 1.25, 2.4, 5.3, 10.0, and 15.0 GHz (L-, S-, C-, X-, and Ku-band, respectively) and is capable of performing radar backscatter measurements at different incidence angles.

During all measurements, monomolecular slicks consisting of oleyl alcohol (OLA) were deployed, thus allowing for an investigation of the dependence of the damping behaviour on different environmental conditions, in particular, on wind speed. Even though it is known to simulate biogenic slicks not optimally, this substance was already deployed during several earlier campaigns, because its strong damping capabilities make it easy to be detected by microwave sensors. In addition to OLA, slicks consisting of oleic acid methyl ester (OLME) and triolein (TOLG) were deployed, which both represent compounds of natural surface films. Because of their molecular structure, these substances form monomolecular surface films (i.e., slicks with a thickness of only one molecule). Depending on wind and wave conditions, however, these slicks may be locally disrupted, thus causing a large scatter in the measured radar contrast (Figures 1 and 2). The measurements were performed shortly after the slick deployment, when the slicks were fully spread, in order to avoid any data spoiling by slick aging effects. The measured damping ratios (i.e., the ratios of the relative backscattered radar power from a slick-free and a slick-covered water surface) are shown in Figure 1.

It can be concluded that, under all wind speed conditions, the measured damping ratios increase with increasing Bragg wave number and that the maximum damping decreases with increasing wind speed. These two findings cannot be explained by pure Marangoni damping theory which describes the damping of small sinusoidal water surface waves by monomolecular slicks and which predicts a distinct damping maximum at intermediate wave numbers of approx. 100 rad m^{-1} (Hühnerfuss 1986). In addition, wind-induced effects, primarily the energy input into the wave spectrum, have to be considered, as well.

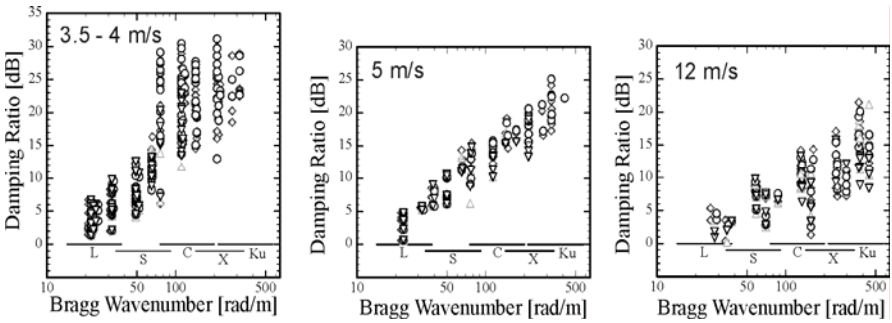

Fig. 1. Damping ratios measured by HELISCAT over an oleyl alcohol (OLA) slick at different wind speeds (**left:** 3.5–4 m s^{-1}; **middle**: 5 m s^{-1}, **right:** 12 m s^{-1}). Diamonds, circles, and grey triangles denote HH, VV, and VH/HV polarisation, respectively

In order to explain their experimental results obtained at high wind speeds (12 m s^{-1}, where the energy input by the wind is larger than the viscous dissipation in the whole Bragg wave number range) quantitatively Gade et al. (1998c) developed an analytical model for the damping ratios that is based on the assumption that the spectral action is balanced (Hasselmann 1960), i.e.

$$\frac{\sigma^{(0)}(k)}{\sigma^{(s)}(k)} = \frac{\Psi_0(k)}{\Psi_s(k)} = \frac{N_0(k)}{N_s(k)} = \frac{S_{wi}^{(s)} - S_{vd}^{(s)}}{S_{wi}^{(0)} - S_{vd}^{(0)}} \cdot \frac{S_{br}^{(0)} - S_{nl}^{(0)}}{S_{br}^{(s)} - S_{nl}^{(s)}} \tag{1}$$

where σ is the radar backscattering at a (Bragg) wave number k, $\Psi(k)$ is the wave spectrum, $N(k)$ is the wave action, and S_{wi}, S_{vd}, S_{br}, and S_{nl} are the source terms for the wind input, viscous dissipation, wave breaking, and nonlinear interaction, respectively. The indices "0" and "s" denote a slick-free and a slick-covered water surface. Gade et al. (1998c) included analytical expressions for the wind input (Phillips 1985) and the wave breaking (Donelan and Pierson 1987) and assumed that the nonlinear interaction is much smaller than the energy flux caused by wave breaking (which should be the case under high wind conditions). They found the following expression for the measured damping ratios:

$$\frac{\sigma^{(0)}(k)}{\sigma^{(s)}(k)} \approx \frac{\beta_s - 2\Delta_s c_g}{\beta_0 - 2\Delta_0 c_g} \cdot m^{\Delta n - 4} \left(2u_* \cdot \sqrt{\frac{|\cos\varphi| k}{g}} \right)^{\Delta n} \tag{2}$$

where β is the coefficient for the wind energy input given by Plant (1982), Δ is the coefficient for viscous dissipation, c_g is the group velocity of the water waves, u_* is the wind friction velocity, φ is the azimuth angle be-

tween wind and wave propagation direction, and g is the acceleration of gravity. The parameters m and Δn describe the reduction of u_* and of the wave breaking, respectively, in the presence of a slick (for more details see Gade et al. (1998c)):

$$m = u_*^{(s)} / u_*^{(0)}$$
$$\Delta n = n_0 - n_s \tag{3}$$

where n_i are the exponents in the analytical description of the wave breaking source term, $S_{br} \sim (k^4 \Psi)^n$. Following the results of earlier field measurements performed by Stolte (pers. commun.), m was set to 0.7 and 0.9 for the strong (leeward) and weak (windward) damping parts of the surface films, respectively. Considering the different impact of the weak and strong damping parts of a surface film on wave breaking the parameter Δn is ranging from 0.7 (weak damping substance oleic acid methyl ester) to 3.5 (strong damping substance oleyl alcohol).

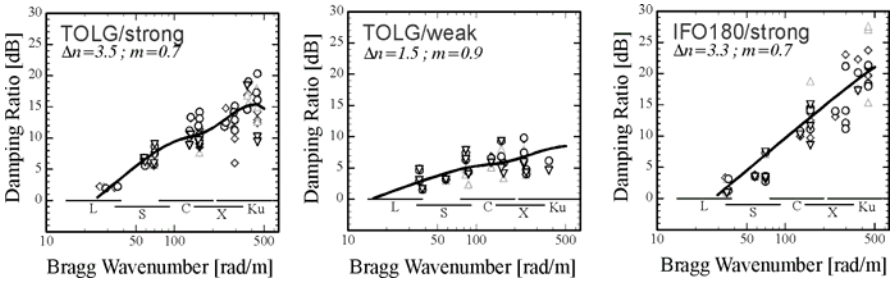

Fig. 2. Same as Figure 1, but for the strong (**left**) and weak (**middle**) damping parts of a triolein (TOLG) slick and the strong damping parts of a mineral oil (IFO180, **right**) spill under high wind conditions (12 m s^{-1}). The solid lines added into each diagram denote model results (see (1)) using the respective parameters m and Δn given in the panels. Diamonds, circles, and grey triangles denote HH, VV, and VH/HV polarisation, respectively

Note that in this parameterisation m and Δn describe the reduction, but not the absolute value, of the source terms for wind input and wave breaking, respectively.

Deploying their model Gade et al. (1998c) were able to explain the continuous increase in the measured damping ratios with Bragg wave number. A comparison of some experimental and model results is shown in Figure 2.

It is obvious that this model can well reproduce the measured damping ratios and, moreover, that the absence of the expected Marangoni damping maximum at intermediate Bragg wave numbers (approx. 100 rad m^{-1}) can

be interpreted. Furthermore, the model can explain the similarities between the results obtained from quasi-biogenic (TOLG) and anthropogenic (IFO180) surface films under high wind conditions.

3 Results obtained from analyses of SIR-C/X-SAR data

Various SIR-C/X-SAR images showing biogenic and anthropogenic surface films at different parts of the world's oceans were analysed, in order to investigate whether or not SIR-C/X-SAR is capable of discriminating between biogenic and anthropogenic oceanic surface films. Using SAR images of the surface film experiments in the German Bight of the North Sea, again, we found that the measured damping ratios strongly depend on the wind speed, which is in accordance with the results obtained by HELISCAT (see Figure 1). The results obtained from SAR images of various biogenic and anthropogenic surface films are shown in Figures 3 and 4, respectively. The classification between biogenic and anthropogenic surface films was made based on the shape and the size of the observed surface films. E.g., the SAR images shown in Figure 3 show typical signatures of biogenic surface films encountered in large sea areas during ongoing algal blooms: the surface-active material accumulates on the water surface and the long, narrow, dark streaks follow the surface currents. In contrary, signatures caused by spilled mineral oil look different: the dark elongated patch in Figure 4 is very likely caused by an oil spill, because of its irregular shape and the fact, that its contrast is independent of the different wind speed on either sides of the varying wind speed in that very area. In general, however, no sampling of any film material was done for our studies.

It is obvious that biogenic surface slicks cause a strong damping at L-band (Figure 3), whereas anthropogenic oil spills cause low L-band damping ratios (Figure 4). Considering the large scatter of the data, the observed damping ratios at C- and X-band are similar, which, particularly at C-band, is due to an insufficient signal-to-noise ratio of the SIR-C/X-SAR system.

The presented results, however, show that multi-frequency SAR imagery yields more information about the damping characteristics of oceanic surface films than single-frequency SAR imagery. This is, in turn, needed for a better discrimination between different kinds of surface films, particularly under low to moderate wind conditions. Moreover, our results show that L-band data is crucial for a successful discrimination of different surface films. Although OLA represents natural slicks, its damping ratios look similar to those of mineral oil spills. A possible reason for this is the limited spatial extent of these films. In contrast, natural slicks usually

cover large areas of the sea surface, thus being more effective in damping even longer (metre) waves.

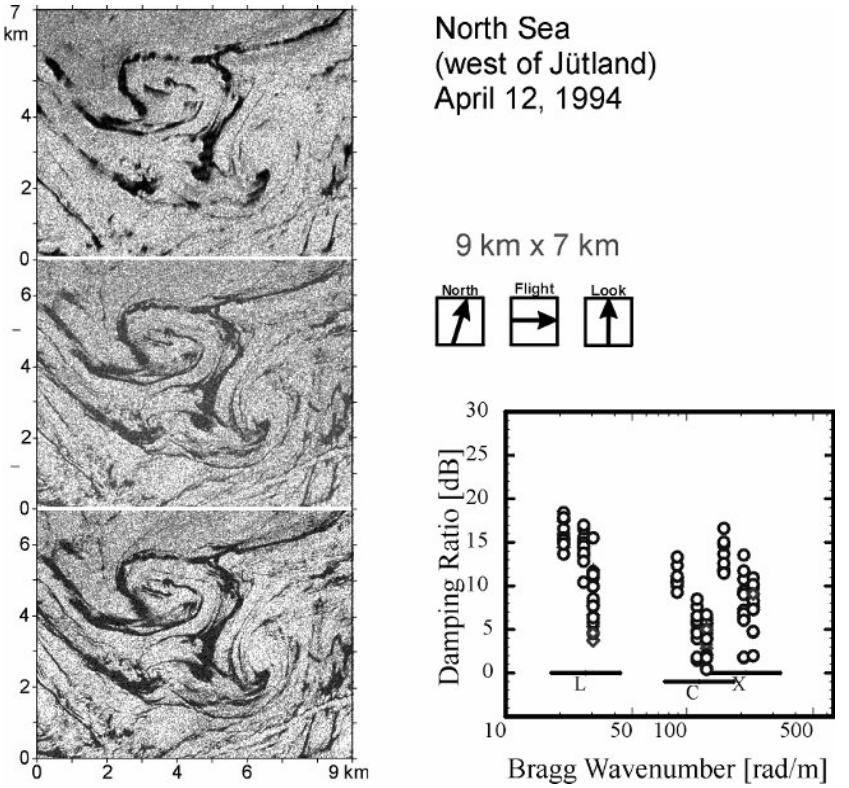

Fig. 3. Left side: SIR-C/X-SAR images of the same spot of the North Sea acquired during the first shuttle mission on April 12th, 1994, and showing signatures of natural surface films (image dimensions 7 by 9 km). The images were acquired at L-, C-, and X-band (from **top to bottom**), VV-polarisation. On the **bottom right**, damping ratios obtained from SIR-C/X-SAR images of various natural slicks at low to moderate wind speeds (< 7 m s^{-1}) are shown. Diamonds and circles denote HH and VV polarisation, respectively

In summary, multi-frequency SAR imagery is advantageous to the recognition and classification of oceanic surface films; that is, important additional information can be inferred from these SAR data. The evidence shows that under low to moderate wind conditions, multi-frequency radar techniques are capable of discriminating between the different kinds of surface films, whereas at high wind conditions a discrimination (on a basis of damping measurements) is impossible (for examples for high wind speed see the paper by Gade et al. (1998b)).

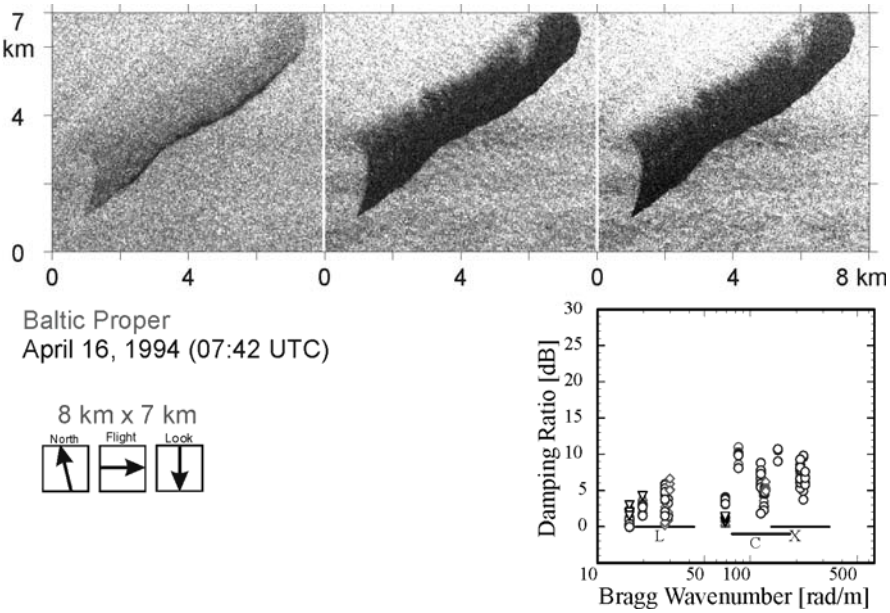

Fig. 4. Upper row: SIR-C/X-SAR images of the same spot of the Baltic Proper acquired during the first shuttle mission on April 16th, 1994, and showing signatures of a mineral oil spill (image dimensions 8 by 7 km). The images were acquired at L-, C-, and X-band (from left to right), VV-polarisation. On the **bottom right**, damping ratios obtained from SIR-C/X-SAR images of various mineral oil spills at low to moderate wind speeds (< 7 m s^{-1}) are shown. Diamonds, circles, and triangles denote HH, VV, and HV/VH polarisation, respectively

4 Statistical Analysis of ERS SAR Data

Gade et al. (2000) analysed more than 700 ERS SAR images of European marginal waters (acquired between December 1996 and November 1998 over the Baltic Sea, the North Sea, and the northwestern Mediterranean Sea) with respect to the detectability of marine oil pollution. Model wind speeds provided by the Deutscher Wetterdienst (DWD, German Weather Service) were used to get an estimate of the influence of the mean local meteorological conditions (namely of the wind speed) on the overall detectability of marine oil pollution. The model results for the three test areas, each for the entire period of SAR image acquisition (December 1996 until November 1998), are shown in Figure 5. The upper row contains the values calculated for the summer periods (April – September) and the

lower row contains the values calculated for the winter periods (October – March). The maximum mean wind speed in the Baltic Sea test area (left column of Figure 5) lies between 8 and 9 m s^{-1} during summer and between 9 and 10 m s^{-1} during winter. The corresponding values for the North Sea test area (middle column) are 7 and 8 m s^{-1} (summer) and 10 and 11 m s^{-1} (winter), and for the northwestern Mediterranean Sea test area they are 6 and 7 m s^{-1} (summer) and 8 and 9 m s^{-1} (winter), respectively. Thus, on average, oil spill detection using SAR techniques should be most successful in the northwestern Mediterranean Sea during the summer period, and it should be least successful in the North Sea test area during winter period.

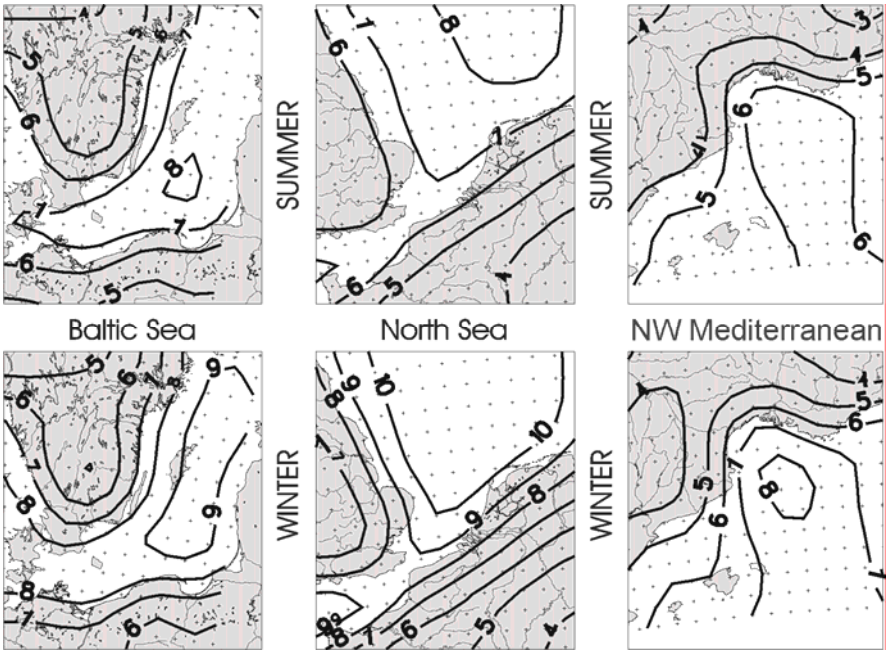

Fig. 5. Mean wind speeds for the three test areas, as derived from a numerical model driven by the DWD. In the upper row the mean wind speeds are shown for summer periods (April – September) and in the lower row for winter periods (October – March)

Gade and Redondo (1999) used the same data set to derive areas of mean oil pollution by taking into account those dark patches in the SAR images that show a significant reduction of the radar backscatter. In all three regions they found more oil pollution during summer months (April – September) than during winter months (October – March), which they

explained by the overall higher wind speeds in all test areas during winter time. Moreover, the northwestern Mediterranean Sea seemed to be the test area with highest detected oil pollution, whereas the pollution seemed to be lowest in the Baltic Sea. They concluded that this might be caused by the difference in mean wind speed, which in turn causes a different visibility of oil pollution in SAR images. (However, it is of course also possible that the northwestern Mediterranean Sea is simply the most polluted test area.)

For our improved statistical analysis we included the mean local windspeed, as derived from interpolated values of the DWD model. As a first step we calculated the distribution of the detected oil spills with wind speed. As shown in the upper left panel of Figure 6 most oil spills were detected at mean (modelled) wind speeds between 3 m s^{-1} and 4 m s^{-1}. The upper right panel of Figure 6 shows the wind speed distribution of the DWD model with a maximum between 5 m s^{-1} and 6 m s^{-1}. The lower panel of Figure 6 shows the "normalised oil spill visibility" (NOSV) calculated as the (normalised) ratio of the two above.

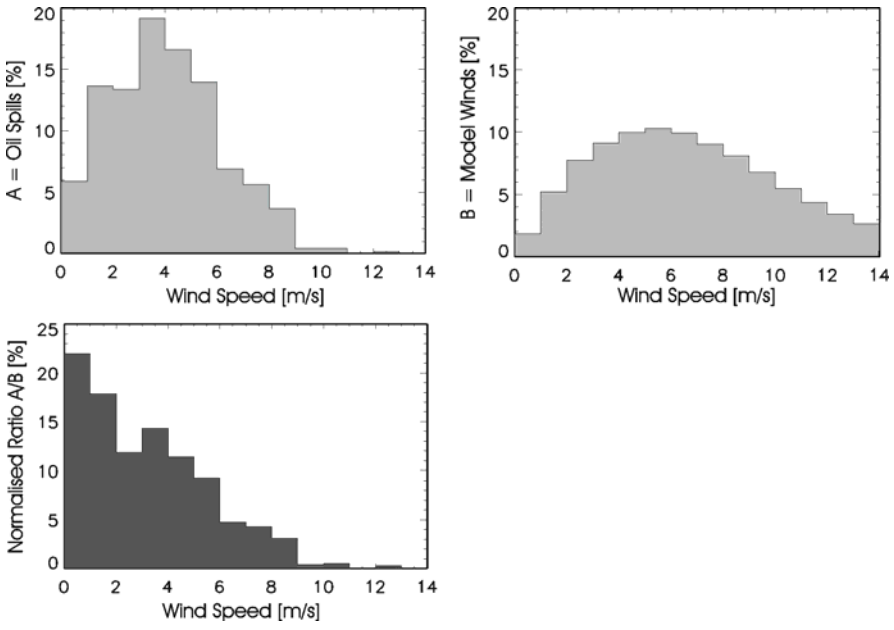

Fig. 6. upper left: histogram of the distribution of detected oil pollution as function of wind speed; **upper right:** distribution of the DWD model winds; **lower left:** "normalised oil spill visibility" calculated as the ratio of the histograms for oil spills and model winds

The NOSV gives a better estimate of the detectability of marine oil pollution, independently of the local wind conditions of this particular study. These results show that higher wind speeds cause lower detectability of oil pollution, and the maximum (model) wind speed where oil spill detection in European coastal waters can be inferred. In particular, at wind speeds below 7 m s^{-1} oil spills are well detectable, whereas above 10 m s^{-1} wind speed the definite detection of marine oil pollution seems to be almost impossible. At wind speeds between 7 and 10 m s^{-1} the detectability of oil spills is rather low. These results can explain why less oil pollution was detected in the northern test areas during winter time. E.g., the mean wind speed in the central North Sea during winter time lies above 10 m s^{-1} (Figure 5), thus making it unlikely that every oil spill in that area was detectable by SAR sensors.

5 Results obtained from laboratory measurements

In order to complement the results of the radar backscatter measurements on the open sea, laboratory measurements of the wave amplitude and slope and of the radar backscatter at X- and Ka-band were carried out in a wind-wave tank with mechanically generated gravity waves as well as with wind-generated waves on a slick-free and a slick-covered water surface. In this paper, we concentrate on the results of the radar measurements with wind-generated waves. For a full description of the obtained results the reader is referred to Gade et al. (1998c).

The measurements were carried out in the wind-wave tank of the University of Hamburg, which is 26 m long and 1 m wide. The mean water depth is 0.5 m, the wind tunnel height is 1 m, and the effective fetch is 19.5 m. The measurement area was at a fetch of 15.5 m. The scatterometers used for the present investigation are working at 9.8 GHz (X-band) and 37 GHz (Ka-band) and the measurements were carried out with upwind looking radar antennae and at VV-polarisation.

Figure 7 shows the measured radar Doppler shifts, both at X- and Ka-band, for the entire wind speed range. The solid and dashed lines in both panels denote theoretical Doppler shifts assuming freely propagating Bragg waves and Bragg waves bound to the dominant wind waves, respectively. We can conclude that the X-band backscattering from a slick-free water surface at low wind speeds (up to approximately 4.5 m s^{-1}) and long fetches (15.5 m in our investigation) is determined mainly by bound waves, whereas the Ka-band backscatter is caused by both bound and freely propagating Bragg waves. For wind speeds higher than 4.5 m s^{-1} the X-band backscattering in our experiments is caused by both parasitic har-

monics and freely propagating Bragg waves, whereas the Ka-band backscatter is caused mainly by freely propagating Bragg waves. In particular, the generation of freely propagating wind waves results in a reduction of the X-band Doppler shift at wind speeds of 4.5-5 m s^{-1}, which is less distinct at Ka-band.

When comparing the results obtained by different authors, one has to take into account the different experimental set-ups, which may lead to different results. In particular, the existence of bound (Bragg) waves does not only depend on the wind speed and frequency of the gravity waves but also, for example, on the fetch length and the wave age (which may strongly differ in different experimental set-ups). Therefore, we suspect that on the open ocean X- and Ka-band Bragg waves are encountered that are both freely propagating and bound to gravity waves (which in turn may be modulated by the long ocean waves).

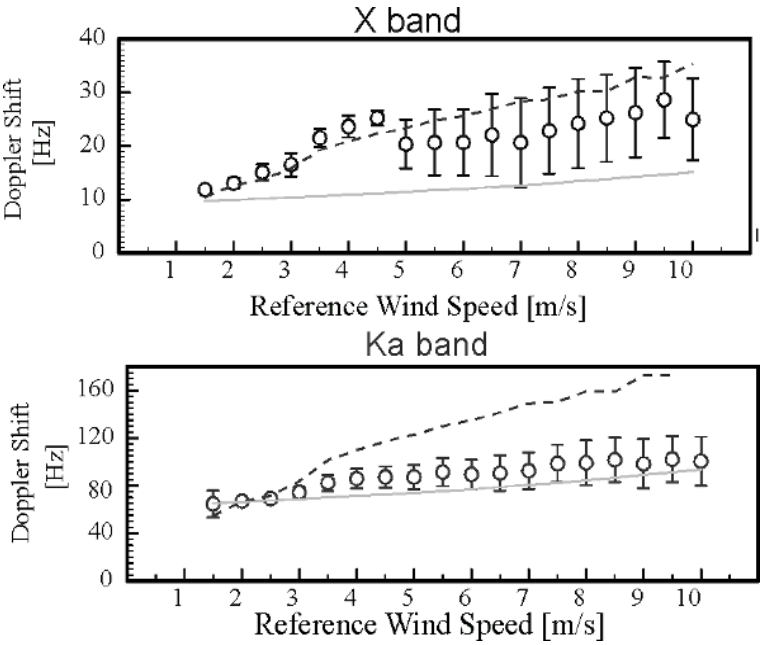

Fig. 7. Measured X- and Ka-band Doppler shifts as function of the reference wind speed. The measurements were performed with a slick-free water surface. Additionally inserted into each diagram are the theoretical curves assuming bound (dashed line) and freely propagating (solid line) Bragg waves

The X- and Ka-band Doppler shifts measured from wind-generated waves on a water surface covered with oleyl alcohol (OLA) are shown in Figure 8. It is obvious that the coverage of the water surface with a sur-

face-active substance has a strong influence on the generation of bound waves at the crests of the gravity waves. At intermediate wind speeds of approximately 6 m s^{-1} the X-band backscatter is mainly caused by bound Bragg waves, and the Ka-band backscatter is caused by both bound and freely propagating Bragg waves. In the wind speed range between 7 and 9 m s^{-1}, where the short gravity waves are strongly damped by the OLA slick, both the X- and Ka-band backscatter are caused only by freely propagating waves. This wave damping behaviour of the OLA slick can explain the strong damping of the radar backscatter in this particular wind speed range as well as the fact that the measured wave damping exceeds the values predicted by Marangoni damping theory for this (water wave) frequency range.

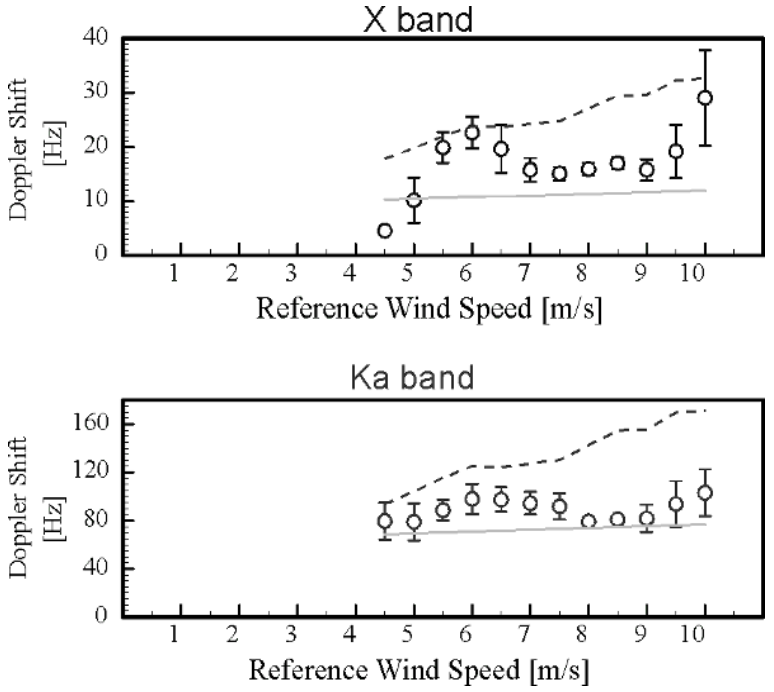

Fig. 8. Same as Figure 7, but for a water surface covered with oleyl alcohol (OLA). The minimum wind speed for the excitation of ripple waves on a slick-covered water surface is about 4.5 m s^{-1}

These results obtained from a slick-covered water surface are of great importance for the interpretation of measured reductions of the radar backscattering by oceanic surface films (see the preceding sections). However, we also note that results obtained from wind-wave tank experiments can-

not be readily transferred to the open ocean. Moreover, the described effects are obviously strongly dependent on the experimental conditions (i.e., on the fetch and the tank dimensions), so that only field experiments (e.g., similar measurements of the radar backscattering performed on the open ocean) can prove our assumption that bound Bragg waves have an important impact on the measured radar signal from the ocean surface. At least, taking our results into account, we can expect reductions of the radar backscatter at X-, Ku-, and Ka-band that are higher than those predicted by Marangoni damping theory. This has indeed been observed.

6 Summary and Conclusions

The results obtained by HELISCAT showed that the damping behaviour (i.e., the ratio of the radar backscatter from a slick-free and a slick-covered water surface) of the same substance strongly depends on the wind speed, which can be explained by means of the source terms of the action balance equation. Thus, we developed a model to simulate measured damping ratios for different surface films at high wind speeds (> 10 m s^{-1}, where the energy input by the wind is larger than the viscous dissipation). The simulated values are in good agreement with the experimental results.

We have analysed SIR-C/X-SAR images from natural surface films and mineral oil spills and have compared the measured damping ratios. It turns out that the radar signatures are most different at L-band (where the signal-to-noise-ratio is sufficiently high). For mineral oil spills the damping ratio increases with Bragg wave number, whereas for natural surface films a minimum of the damping behaviour is measured at C-band (even when the signal-to-noise ratio very often is insufficient).

No significant dependence of the radar contrast on the polarisation was found, whereas it strongly depends on radar frequency. Thus, multi-frequency capabilities are recommended for any radar-based system for the discrimination of oceanic surface films, but not multi-polarisation capabilities. Furthermore, we conclude that the discrimination of natural and man-made surface films seems to be possible at low to moderate wind speeds whereas it is impossible at high wind speeds (see the results obtained at 12 m s^{-1} wind speed, Figures 1 and 2).

It is remarkable that, over each surface film deployed during our field experiments, SIR-C/X-SAR measured lower damping ratios than HELISCAT (Figure 9). These differences are independent of the deployed substance and of wind speed, but not of Bragg wave number. Possible explanations for this finding may include different resolution scales (25 m for the SAR system, the footprint dimensions of the HELISCAT systems are

between a few meters and about 100 m, depending on incidence angle and radar band), while time differences and state of evolution of the slick in our opinion play a minor role. Additional systematic investigations are required in order to answer these questions.

The analysis of a large number of ERS SAR data revealed improved statistical information on the oil pollution of European marginal waters. The results show that the consideration of local environmental conditions (namely the local wind speed) improves the statistical results significantly: the Baltic Sea seems to be only slightly less polluted than the northwestern Mediterranean, which is not in accordance with results from earlier studies where local wind speeds had not been taken into account.

The results from the wind-wave tank measurements show that at X- and Ka-band the radar backscattering from a slick-free water surface is caused by bound as well as by free propagating ripples. In the presence of a monomolecular surface film at certain wind speeds only bound or only free propagating ripples are responsible for the backscattering at X-band, which can explain higher measured damping ratios.

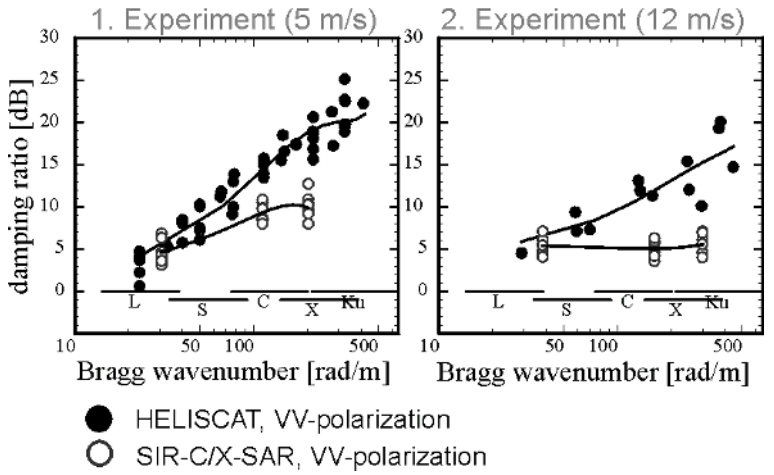

Fig. 9. Comparison of the radar contrast caused by the deployed OLA slicks during both shuttle missions in April (**left panel**) and October (**right panel**), 1994. The solid circles denote results obtained by HELISCAT, the open circles denote results obtained from SIR-C/X-SAR data. Note that in both cases, SIR-C/X-SAR measured lower damping ratios than HELISCAT

7 References

Alpers W and Hühnerfuss H (1988) Radar signatures of oil films floating on the sea and the Marangoni effect. J Geophys Res 93: 3642–3648

Donelan MA and Pierson WJ (1987) Radar scattering and equilibrium ranges in wind-generated waves with application to scatterometry. J Geophys Res 92: 4971–5029

Gade M (1996) Untersuchungen zur Abbildung biogener und anthropogener Oberflächenfilme auf dem Meer mit Hilfe von Radarsensoren. Dissertation, Univ. of Hamburg; Shaker, Aachen, 176 pp

Gade M and Redondo JM (1999) Marine pollution in European coastal waters monitored by the ERS-2 SAR: a comprehensive statistical analysis, Proceed Intern Geosci Remote Sens Sympos (IGARSS) '99, IEEE, Piscataway, NJ, USA, 1375-1377

Gade M, Alpers W, Hühnerfuss H, Masuko H and Kobayashi T (1998a) The imaging of biogenic and anthropogenic surface films by a multi-frequency multi-polarization synthetic aperture radar measured during the SIR-C/X-SAR missions. J Geophys Res 103: 18851–18866

Gade M, Alpers W, Ermakov SA, Hühnerfuss H and Lange PA (1998b) Wind-wave tank measurements of bound and freely propagating gravity-capillary waves. J Geophys Res 103: 21997–22010

Gade M, Alpers W, Hühnerfuss H, Wismann VR, and Lange PA (1998c) On the reduction of the radar backscatter by oceanic surface films: scatterometer measurements and their theoretical interpretation. Remote Sens Environ 66: 52-70

Gade M, Scholz J and v.Viebahn C (2000) On the detectability of marine oil pollution in European marginal waters by means of ERS SAR imagery. Proceed Intern Geosci Remote Sens Sympos (IGARSS) '00, IEEE, Piscataway, NJ, USA, 2510-2512

Hasselmann K (1960) Grundgleichungen der Seegangsvoraussage. Schiffstechn 7: 191-195

Hühnerfuss H (1986) The molecular structure of the system water/monomolecular surface film and its influence on water wave damping. Habilitationsschrift, Univ. Hamburg, Dept. of Chemistry, Hamburg, Germany, 245 pp

Phillips OM (1985) Spectral and statistical properties of the equilibrium range in wind-generated gravity waves. J Fluid Mech 156: 505–531

Plant WJ (1982) A relationship between wind stress and wave slope. J Geophys Res 87: 1961–1967

Valenzuela G (1978) Theories for the interaction of electromagnetic and oceanic waves - a review. Bound Layer Meteorol 13: 61–85

Slick radar image modelling with an extended “VIERS-1” wave spectrum

Harm Greidanus

TNO Physics and Electronics Laboratory, Den Haag, The Netherlands
present address: European Commission Joint Research Centre, Ispra, Italy

Abstract. The VIERS-1 model (Janssen et al. 1998) was originally devised to describe ERS scatterometer measurements over the sea on a physical basis. This model is extended to include the saturation range, and it is used to derive equilibrium wave spectra and formulations for the relaxation toward that equilibrium, with and without slicks present. It was attempted to derive actual relaxation rates from the model, but this was only successful on part of the spectral range. The extended VIERS model is combined with a radar imaging model originally designed for radar bathymetry, to yield quantitative computations of radar contrast along transects through slicks. The resulting model shows an apparent size increase of the slick and a smoothing of its edges, due to the finite relaxation time of the slick-dampened, backscattering surface roughness. The present work offers no validation by observed images, but the trend in frequency and polarisation dependence of the radar contrast is supported by published measurements.

1 Introduction

Radar is a valuable sensor for the maritime environment. It can provide information about a great variety of features and processes, such as wind, waves, currents, ships, bathymetry and natural and man-made slicks. When oil spills are at issue, the pertinent questions are location, extent, thickness, type and age, and the prediction of these. Some of these questions may be answered on the basis of imaging radar data. At the same time, also natural slicks alter the radar properties of the sea surface, thereby complicating the interpretation of radar imagery when the interest is aimed at other features. Therefore, it is necessary to understand the characteristics of slicks, both man-made and natural, in radar images.

This contribution presents some results of research into the modelling of the radar imaging of slicks, which are here assumed to be in the form of surface films. The research was aimed at assembling a numerical, physics-based model to calculate the radar image of a slick on the sea surface, and at improving the consistency of the elements of this model. The elements of the model are:

1. Equilibrium surface wave spectra, based on the balancing of the spectral energy source and sink terms, both for clean and slick-covered water;
2. Relaxation rates prescribing the time scales of evolution of the surface waves toward the equilibrium;
3. A model that calculates the actual local ocean surface wave spectrum, based on relaxation towards the equilibrium spectrum; and
4. A radar backscatter model that yields normalised radar cross section (NRCS), given a local ocean surface wave spectrum.

Concerning the first element, the equilibrium wave spectra, the literature offers several forms, such as the Phillips, Pierson-Moskowitch or JONSWAP spectra, the Donelan-Banner-Jähne spectra (Apel 1994) or the spectra proposed by Romeiser et al. (1997). Most of these are parameterised functions of wind speed, based on measurements, and have only a limited basis in physical processes. Not all of them adequately describe the short gravity-capillary waves which are the primary ones that radar is sensitive to, and none of them are amenable to including slicks. Also for the relaxation rate (the second element), the literature offers several parameterisations, such as Hughes (1978), Plant and Wright (1977) or Hsiao and Shemdin (1983). Again, the effects of slicks cannot be included. In this work, we have, therefore, sought to extend the ocean backscatter model called "VIERS-1" of Janssen et al. (1998), who compute a gravity-capillary equilibrium spectrum based on physics with parameterisations for 'unresolved' physical (sub-) processes. This ocean backscatter model was originally developed for ERS scatterometry. Our aim was to obtain a consistent modelling of both the equilibrium spectrum and the relaxation rates, also in the presence of slicks.

Concerning the third element, the relaxation model, a radar imaging model that was originally developed for bathymetry and ship wakes was used. This is a quasi-two dimensional wave-current interaction model, along the lines of e.g. Lyzenga and Bennett (1988) and Vogelzang (1989). Parts of it have been described in Greidanus (1994). It has been validated on radar bathymetry measurements and performs quite well (Greidanus et al. 1997). The basis of the modelling is that water wave energy packets are traced while their action changes by processes such as wind input, non-linear interactions and dissipation. This action change is modelled as a relaxation toward an equilibrium spectral value. For the present application,

the current field is set to zero. The outcome of this calculation is a full wave spectrum at a series of points along a cross cut over the water surface, that may be input into a radar backscatter algorithm (the fourth element) to give a radar backscatter (NRCS) profile. For the radar backscatter model a "standard" composite surface model was used.

In what follows, the above elements will successively be discussed. In section 2, the VIERS-1 equilibrium spectrum will be briefly described, followed by a discussion of the extensions that have been implemented in order to be able to better use it for the present purpose of slick modelling. In section 3, an attempt is made to derive relaxation rates from this spectrum, and the form of the net restoring source term when out of equilibrium is established. In section 4, the radar image modelling will be discussed. Section 5, finally, discusses and summarises the results.

2 Equilibrium spectrum

2.1 The VIERS-1 spectrum

The VIERS-1 model (Janssen et al. 1998) is a physically based theoretical ocean backscatter model for intermediate incidence angles. It comprises an ocean wave equilibrium spectral model and a radar backscatter model. It was developed in particular to model the relation between ambient ocean parameters and observed radar backscatter from the ERS C-band scatterometer, in order to be able to derive more accurate wind fields from that instrument. Because a number of physical processes are included in the modelling, it lends itself for rather general use as a tool in interpreting maritime radar backscatter. The main effects that are taken into account in the wave spectral part include: wind speed, fetch (or wave age), air and sea temperature (and difference), surface tension, viscosity, Marangoni effect (for surface slicks), wave breaking (dissipation), 3- and 4-wave non-linear interactions and wind input. The physical modelling, however, is only applied in the high wave number tail of the spectrum, i.e. in the capillary regime and the transition regime between capillary and gravity waves. At a low level, many of the effects mentioned are parameterised; for example, there is a parameter α_3 (function of wavelength) that describes the strength of the 3-wave interactions and an α_4 for the 4-wave interactions. While the parameters have been tuned to X-band scatterometer measurements in wave tanks and on the open sea, the fit to ERS C-band scatterometer data is almost as good as the fully empirical CMOD4, and even better at very low and very high winds.

Here, the VIERS-1 model is only briefly sketched; a more complete description can be found in Janssen et al. (1998) and Snoeij et al. (1993). The

spectral part of the model works as follows. The form of the equilibrium spectrum in the high wave number tail is found by postulating a spectral energy balance, i.e., by postulating that the total of all energy source (and sink) terms acting on a spectral ocean wave component is zero. The various energy source terms are wind input, viscous dissipation, Marangoni (slick) dissipation, wave breaking, and wave-wave non-linear interaction. Denoting these respective spectral source terms by a subscripted *S*, the energy balance reads:

$$S(\vec{k}) = S_{in}(\vec{k}) + S_{vis}(\vec{k}) + S_{slick}(\vec{k}) + S_{br}(\vec{k}) + S_{nl}(\vec{k}) = 0\,. \tag{1}$$

Wave number, wave number vector and wave angular frequency are denoted k, $\vec{k}$ and ω. The wave energy spectrum (divided by the water density ρ) is $E(\vec{k}) = \frac{\omega^2}{k} F(\vec{k})$, with F the wave height spectrum that has the wave variance as its integral.

Taking viscous and Marangoni dissipation together, and making the dependence of the source terms on the spectral energy level E explicit, the energy balance can be written as:

$$S(E) = \delta\omega(\frac{u_*}{c})^2 E - 4\nu M k^2 E - \beta(E) k E + S_{nl}(E) = 0\,, \tag{2}$$

where for wind input (first term) u_* is the friction velocity, c the surface wave phase speed, and the factor δ is a function of wave number in order to incorporate the quasi-linear effect. In the second term, ν is the kinematic viscosity of water, and M is the Marangoni relative damping ratio describing surfactant-induced wave damping (Alpers and Hühnerfuss 1989):

$$M = \frac{1 + X(\cos\delta_s - \sin\delta_s) + XY + Y\sin\delta_s}{1 + 2X(\cos\delta_s - \sin\delta_s) + 2X^2}, \tag{3}$$

$$X = \frac{|E_s| k^2}{\rho\sqrt{2\nu\omega^3}},\; Y = \frac{|E_s| k}{\rho 4\nu\omega}, \tag{4}$$

with $|E_s|, \delta_s$ the slick's dilational modulus and its phase angle, respectively. (In the absence of a slick, M = 1.) In the breaking (third) term, $\beta(E)$ is a prescribed function of integral properties of the spectrum. Finally, instead of writing the non-linear interaction (fourth) source term directly as

$$S_{nl}(E(\vec{k})) = \omega I_3(\vec{k}) + \omega I_4(\vec{k}) \tag{5}$$

with I_3 and I_4 the 3- and 4-wave action collision integrals (e.g., Hasselmann 1963 for the 4-wave interaction), it is written rather as the divergence of a spectral energy flux vector (Snoeij et al. 1993):

$$S_{nl}(E(\vec{k})) = -\vec{\nabla} \circ \vec{\in}(\vec{k}) . \tag{6}$$

The spectral energy flux vector has the form

$$\vec{\in}(\vec{k}) = \omega \vec{k} I_3(\vec{k}) + \omega \vec{k} I_4(\vec{k}) . \tag{7}$$

The collision integrals are written as

$$I_3(\vec{k}) = \alpha_3 N^2 k^5 c / c_g \;,\; I_4(\vec{k}) = \alpha_4 N^3 k^9 / c_g \;, \tag{8}$$

with $N = \dfrac{E}{\omega}$ the wave action, c_g the group speed of the surface waves, and α_3, α_4 parameters that can in general (on dimensional grounds) be functions of c/c_g. In the VIERS-1 model, α_3 goes to zero when c/c_g goes to 2 (i.e., for pure gravity waves), and α_4 is taken to be constant.

In spite of the relevance of angular structure in the spectrum (e.g., Komen et al. 1984), the radial dependence is integrated out, and the energy balance is solved only as a function of k. After angular integration, the non-linear source term becomes

$$S_{nl}(E(k)) = -\frac{1}{k} \in'(k) \tag{9}$$

(using the notation $f' = \dfrac{\mathrm{d}f}{\mathrm{d}k}$) and

$$\in(k) = \omega k^2 I_3(k) + \omega k^2 I_4(k) = \frac{c^4}{c_g} \left(\alpha_3 B^2(k) + \alpha_4 B^3(k) \right) \tag{10}$$

using the 'curvature spectrum' $B(k) = k^4 F(k)$.

This approach is similar to Kitaigorodskii's (1983), without, however, taking $\in(k)$ as constant.

The resulting energy balance is solved by numerically integrating the differential equation

$$\in'(k) = k \gamma E(k) \tag{11}$$

(where γE is the three source terms that are linear in E taken together), starting from some point k_0 in the spectrum with boundary value $E(k_0)$, towards higher wave numbers. At the lower wave numbers and the boundary, i.e. at $k \le k_0$, a JONSWAP-type spectrum is assumed. The exact value of k_0 depends on wind speed, but is around 80 rad m^{-1}. The saturation level in the gravity range is taken as $B(k) = \alpha_{Ph}/2$, with 'Phillips constant' $\alpha_{Ph} = 0.24\chi^{-1}$ a function of wave age χ. The wave age is in turn defined as $\chi = u_* / c_p$, with c_p the phase speed at the JONSWAP peak.

2.2 Low wave number extension to the VIERS-1 spectrum

The gravity region is not physically modelled in the VIERS-1 spectrum. As mentioned above, a JONSWAP spectrum is assumed there, which implies a k^{-4} saturation behaviour with a long wave cut-off (plus an enhancement of the spectral peak). The gravity region is, however, relevant for the modelling of the radar backscatter of slick-covered sea surface, directly via Bragg scattering when using longer radar wavelengths (order 10 cm or longer), or through tilt modulation by the longer waves that affects all radar wavelengths. Furthermore, in the next section it will be tried to derive relaxation rates, and for that a modelling of the spectrum is also needed. Therefore, it was attempted to extend the equilibrium spectral model into the saturation region, i.e. between the spectral peak and the gravity/capillary transition range, in a relatively simple and crude way.

The shape of the gravity wave spectrum in the saturation range has been debated in the literature (e.g., Kitaigorodskii 1983; Phillips 1985; Apel 1994). Arguments favour a flat curvature spectrum $B(k)$, or a curvature spectrum of the form $B(k) \propto k^{0.5}$ (in the absence of slicks). As the most recent equilibrium spectra from the literature (Apel 1994; Romeiser et al. 1997) seem to favour a flat curvature spectrum, we can adhere to the original VIERS approach which also takes on a flat curvature spectrum in the saturation range, as noted above. The VIERS approach will furthermore be followed by retaining the description of the non-linear interaction as in Eq. 9, and letting the 3-wave interaction coefficient go to zero in the saturation range. (In the original VIERS-1 modelling, this coefficient is already halved at k_0.) In the saturation range, then, in the absence of slicks, we are left with the energy balance (the viscous dissipation being small enough to neglect here):

$$S(E) = \delta\omega\left(\frac{u_*}{c}\right)^2 E - \beta(E)kE - \frac{1}{k}\in' = 0 \qquad (12)$$

and

$$\in = 2\alpha_4 c^3 B^3(k) = 2\alpha_4 \frac{k^9}{c^3} E^3(k). \tag{13}$$

For a constant value of α_4, as used in the original VIERS-1, this energy balance does not lead to the desired flat $B(k)$. Since α_4 is a parameter, one can try to solve for an $\alpha_4(k)$ that leads to a flat $B(k)$; while it is possible to find such an $\alpha_4(k)$, its shape does not seem to be realistic.

In order to force the energy balance to result in a flat curvature spectrum, the dissipation term $-\beta kE$ is replaced by a different one, $S_{sd}(E)$, the shape of which is chosen exactly so that it balances the energy input terms if $B(k)$ is flat. Although this is somewhat artificial, the same argument has been used by Phillips (1985) in his attempt to obtain a $k^{0.5}$ curvature spectrum. Reverting to a constant α_4, we obtain (in the saturation range):

$$S(E) = \delta\omega(\frac{u_*}{c})^2 E + 3\alpha_4 \frac{k^7}{c^3} E^3 + S_{sd}(E) = 0 \tag{14}$$

with:

$$S_{sd}(E) = -\delta\omega(\frac{u_*}{c})^2 E(\frac{E}{E_{sat}})^{p_1} - 3\alpha_4 \frac{k^7}{c^3} E^3 (\frac{E}{E_{sat}})^{p_2 - 2} \tag{15}$$

In this 'artificial' dissipation term, the extra factors $(E/E_{sat})^p = (B/(\alpha_{Ph}/2))^p$ provide a generalisation; but for any p, clearly, when $E = E_{sat}$, $S(E) = 0$.

Justification for a dissipation term of this shape may be sought by noting that, for $p_1 = p_2 = 0$, these terms conform to the general shape proposed by Komen et al. (1984). This general shape (their equation 2.7) that has parameters n and m can be rewritten into:

$$S_{dis}(\vec{k}) = -c(1.3)^{1-n}(\frac{0.24}{0.0081})^m \chi^{n-m-1} u_*^{n-1} g^{1-n/2} k^{n/2} E(\vec{k}). \tag{16}$$

Here, Komen et al.'s integral spectral parameters $\hat{\alpha}$ and $\overline{\omega}$ have been approximated by their Pierson-Moskowitz values of $\hat{\alpha}_{PM} = 0.56\alpha_{Ph}$ and $\overline{\omega}_{PM} = 1.3\omega_p$.

For $p_1 = p_2 = 0$, the dissipation term (Eq. 15) can be written as

$$S_{sd}(E) = -\delta\omega(\frac{u_*}{c})^2 E - 3\alpha_4 \frac{c^7}{k^3} E_{sat}^2 E = \\ = -\delta u_*^2 g^{-1/2} k^{3/2} E - 3\alpha_4 (0.24)^2 \chi^{-2} g^{1/2} k^{1/2} E \quad (17)$$

These terms conform to Komen et al.'s form for $n = 3$, $m = 2$ and $n = 1$, $m = 2$, respectively, and are also numerically quite close to Komen et al.'s results (their equation 4.2).

Furthermore, while the dissipation terms in Komen et al. are proportional to E, Phillips (1985) introduces a dissipation term proportional to E^3.

Concerning the actual choice of p_1 and p_2, it can be noted that $p_1 = 0$, $p_2 = 2$ would lead to a trivial equation for the energy balance. The next simplest choice is $p_1 = p_2 = 1$, and this will be used. This means that we take the dissipation in the saturation range proportional to E^2. (Calculations have been made for various combinations of p_1 and p_2 taken from 0, 1, 2, and they actually give rather similar results.)

2.3 Equilibrium spectrum over full spectral range

On the basis of the above arguments, the energy balance for the full range (saturation, gravity/capillary transition and capillary) becomes

$$S(E) = \delta\omega(\frac{u_*}{c})^2 E - 4\nu M k^2 E + S_{nl}(E) - (1-w)\beta(E)kE + wS_{sd}(E) \quad (18)$$

with $S_{nl}(E)$ as before according to Eqs. 9, 10, $S_{sd}(E)$ according to Eq. 15 with $p_1 = p_2 = 1$, and $w(k)$ a smooth transition function. Taking for $w(k)$ the 'inverse' of $\alpha_3(k)$, $w(k-k_0) = \alpha_3(k_0 - k)/\mathrm{Max}\{\alpha_3\}$, gives good results. The energy balance is numerically solved in the same way as before, by integrating Eq. 11, but now starting from $k_0 = \sqrt{3}k_p$.

The results are shown in Fig. 1. In this calculation, a neutrally stable atmosphere with $T_{air} = T_{sea} = 10$ ˚C is used, and the wave age is set at 25. No slicks are used. (In the standard VIERS-1 spectrum, a wind-dependent slick coverage is assumed.) The integration over the saturation range gives rise to a flat curvature spectrum, as it should, and the overall shape of the spectra is practically identical to the original VIERS-1 form.

For comparison, two other spectra from the literature are plotted in Fig. 2, the Donelan-Banner-Jähne (DBJ) spectrum (Apel 1994) and the Romeiser-Alpers-Wismann (RAW) spectrum (Romeiser et al. 1997). It can be seen that the behaviour of the VIERS-1 spectrum is somewhat in between these two.

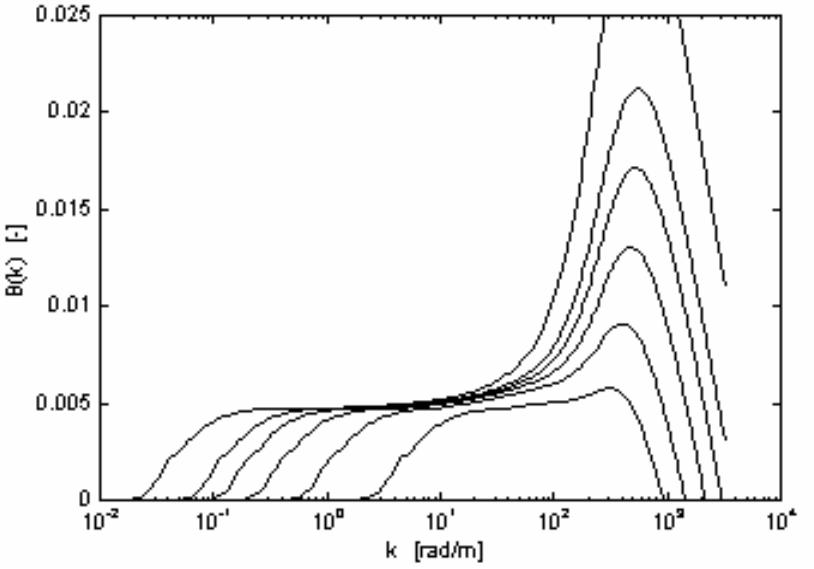

Fig. 1. Curvature spectrum $B(k)$ according to the present model for wind speeds U_{10} = 2, 4, 6, 8, 10, 15 m/s (lower to upper curves). Wave age is 25, no slick

Figure 3 shows the effects of a slick. As a typical example, the visco-elastic parameters for oleic acid ($|E_s|$ = 0.014 N/m, δ_s = 176°) were used (Alpers and Hühnerfuss 1989). The friction velocity u_* was lowered to 80 % of its clean surface value (Alpers and Hühnerfuss 1989), but disappearance of the surfactant as a result of mixing due to the sea state was not taken into account. It can be seen that the effect of the slick is most pronounced at shorter wavelengths, waves with k > 100 rad m^{-1} being very strongly suppressed. In the saturation/gravity range the spectral intensity is lowered but the curvature spectrum remains flat. This can be understood because this range of the spectrum (up to where the Marangoni damping M first begins to come into effect) is directly set by the boundary value $\varepsilon(k_0)$, which is only influenced by the lowered u_*.

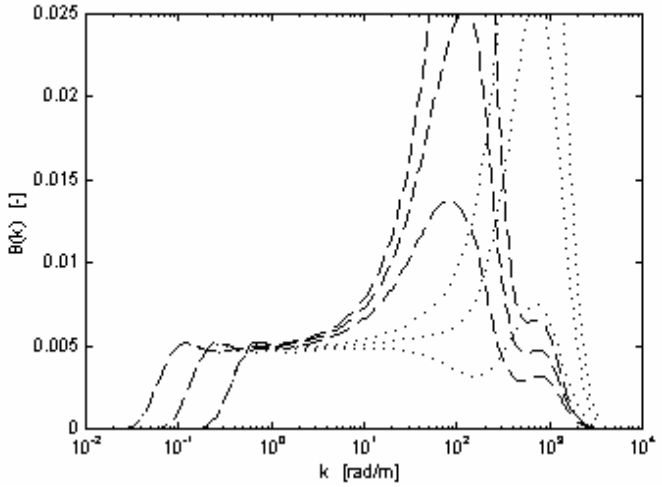

Fig. 2. Curvature spectrum $B(k)$ for wind speeds U_{10} = 6, 10, 15 m s^{-1}, according to the RAW model (dashed) and the DBJ model (dotted). The spectral level in the saturation range (half the 'Phillips constant') was set to the same value as in Fig. 1

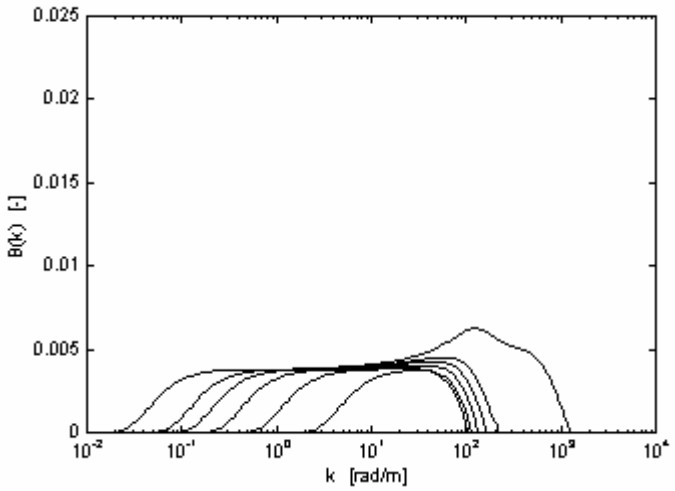

Fig. 3. Curvature spectrum $B(k)$ according to the present model with slick present (oleic acid), for wind speeds U_{10} = 2, 4, 6, 8, 10, 15 m s^{-1}. Spectral peak frequencies are chosen the same as in Fig. 1

3 Relaxation rates and total source term

In the relaxation model discussed in the introduction ('element 3'), the wave spectrum is calculated along a transect through the current field by tracing the waves through (*x*,*k*)-space, and integrating the wave action *N* along these rays. (In the present application, the current field is absent, implying that action *N* and energy *E* are actually equivalent.) In general for such a relaxation model, the action source term need not be specified in detail, but can be written as a deviation from an equilibrium:

$$\frac{\mathrm{d}N}{\mathrm{d}t} = S(N) \approx -\mu(N - N_{eq}) . \tag{19}$$

This is the start of a Taylor series expansion around $S(N_{eq}) = 0$, with

$$\mu = -\frac{\mathrm{d}S}{\mathrm{d}N}(N_{eq}) . \tag{20}$$

When, however, $S(N)$ can be written as

$$S(N) = f_1 N + f_2 N^2 + f_3 N^3 , \tag{21}$$

which is in fact the case here (Eq. 18), we can actually write exactly

$$S(N) = -f_1 (1 - \frac{N}{N_{eq}} \frac{f_3}{f_1} N_{eq}^2) \frac{N}{N_{eq}} (N - N_{eq}) , \tag{22}$$

which leads to the very good approximation

$$S(N) \approx -\mu \frac{N}{N_{eq}} (N - N_{eq}) \tag{23}$$

with

$$\mu = f_1 - f_3 N_{eq}^2 . \tag{24}$$

For a real (stable) equilibrium, one needs $\mu > 0$.

We are now in the situation that we can use for $N_{eq}(k, u_*)$ the equilibrium spectrum calculated in the previous section, but we also know the form of the total source term $S(N)$ (Eq. 23), and we can calculate the relaxation rates $\mu(k, u_*)$ since we have available f_1 and f_3. This approach of calculating the relaxation rate was also used by Trokhimovski (1993).

The results of calculating the relaxation rate are shown in Fig. 4. They are somewhat surprising, in that a negative value for the relaxation rate is found in the region where the curvature spectrum rises. This would indi-

cate an unstable solution, and hence one which would not be found in reality.

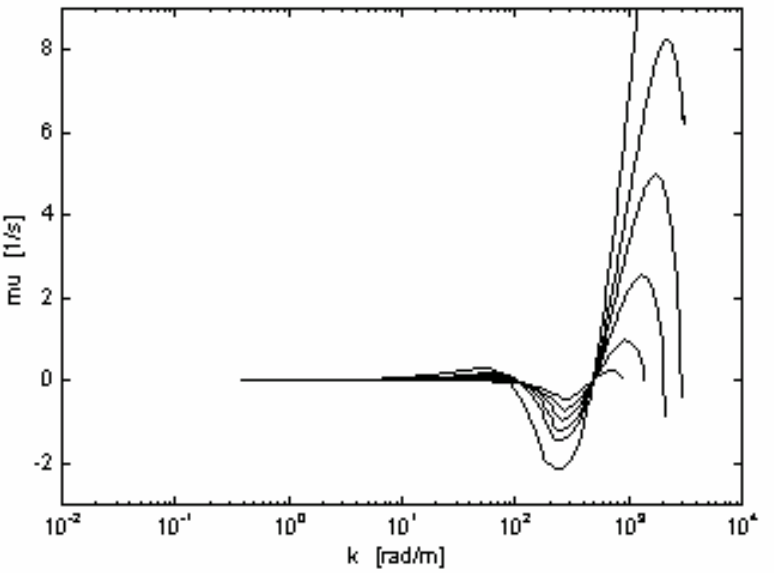

Fig. 4. Relaxation rates computed according to Eq. 24, for wind speeds U_{10} = 2, 4, 6, 8, 10, 15 m s^{-1}. No slicks present. The lowest wind speed curves show the smallest excursions and vice versa

In order to investigate the possibility that negative values for μ be a consequence of the numerical implementation of solving $S(E) = 0$ by integrating $\in'(k)$ (Eq. 11), the action balance $S(N) = 0$ was also solved directly by solving the polynomial[1]

$$S(N) = f_1 N + f_2 N^2 + f_3 N^3 = 0 . \qquad (25)$$

This equation can have more than one positive solution N_{eq}. If there are two positive solutions, one is stable ($dS/dN < 0$) and the other one unstable. In such cases, the integration method always finds the stable solution. In those cases where an unstable solution is found, there exists no second positive solution. So the integration method works well in that respect. As a further check, the relaxation rate was also computed numerically as $\Delta S/\Delta N$. This led to the same numbers as the ones found previously from Eq. 24.

[1] Note that f_1 and f_2 contain $B'(k)$; the $B'(k)$ values used here are those obtained from the integration procedure.

In order to further assess the values of the relaxation rate found here, we compare them with Plant and Wright's (1977) parameterisation which is often used. (Other parameterisations are roughly similar, but can deviate by factors of up to 4.) The comparison is plotted in Fig. 5. It can be seen that in the saturation/gravity range and in the far capillary range, the values found here are quite realistic. Only in the intermediate range, where the negative μ-values are found, is a significant deviation present.

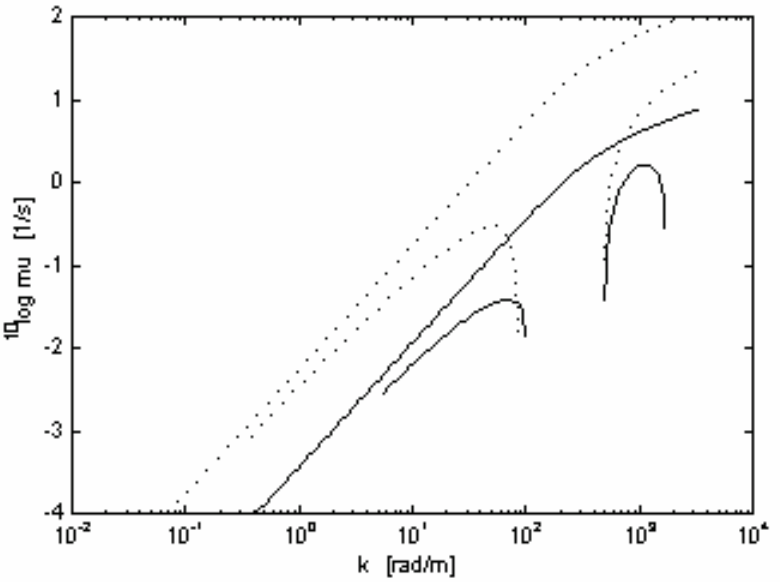

Fig. 5. Computed relaxation rates (discontinued curves) compared to Plant and Wright relaxation rates (continuous curves) on a logarithmic scale, for wind speeds U_{10} = 5 m/s (drawn) and 10 m/s (dotted). Clean surface

The fact that in the saturation range the computed relaxation rate is realistic, means that the choice of $p_1 = p_2 = 1$ in Eqs. 15, 18 appears to be justified. The values of p_1 and p_2 determine to which of the coefficients f_1, f_2 or f_3 the breaking terms S_{sd} (that were introduced, Eq. 15, to force a flat saturation spectrum) contribute, thereby directly influencing μ.

As a last check to assess the validity of the method used, it is applied to Phillips' (1985) saturation spectrum. In Phillips' effort to derive a saturation spectrum (in his case $B(k) \propto k^{0.5}$), he defines forms for three source terms in the energy balance equation, *viz.* wind input, non-linear interaction and dissipation. When written in the form of Eq. 21, his energy balance has $f_2 = 0$. In that case, Eq. 24 can actually be further reduced to $\mu = 2 f_1$. Save for a factor of 2, this yields the Plant and Wright relaxation

rate. So the methodology used here for deriving a relaxation rate seems to be valid.

Figures 6 and 7 show the effect of a slick on the computed relaxation rate. The same slick as for Fig. 3 was used. In the saturation range, the presence of the slick lowers the relaxation rate by the same order of magnitude as it lowers the spectrum. Around k = 100 rad m^{-1}, the slick leads to a more stable spectrum. In the capillary range (k > 200 rad m^{-1}) the relaxation rate is reduced by exactly the same factor as the spectrum, regardless whether μ is positive or negative.

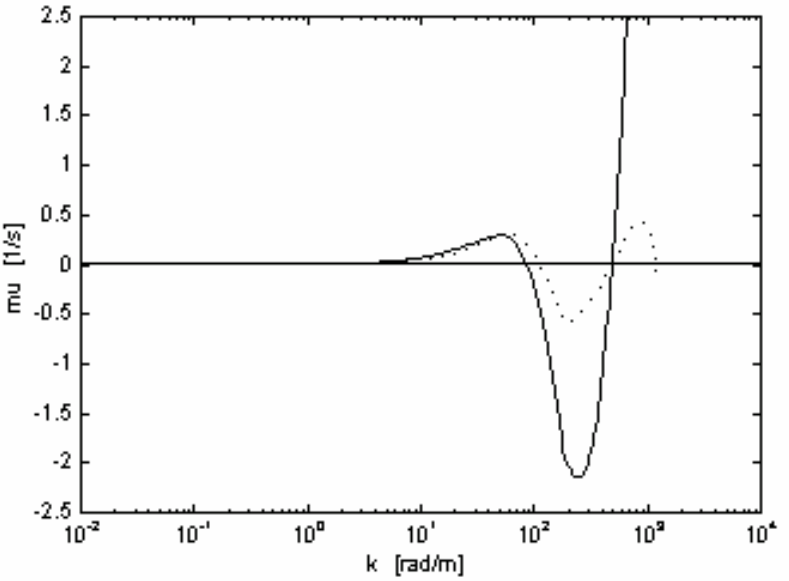

Fig. 6. Computed relaxation rates for a clean surface (drawn) and with oleic acid slick present (dotted), for wind speed U_{10} = 15 m/s

4 Radar image modelling

On the basis of the extended VIERS wave spectral model presented above, it was attempted to calculate the radar backscatter along a transect through a slick on the sea surface. A slick of 50 m diameter of the same substance as used in the previous sections (oleic acid) was taken, and the radar backscatter was calculated along a 150 m section centred on the slick. A wind speed at 10 m height (U_{10}) of 5 m/s was used and the radar look direction was downwind.

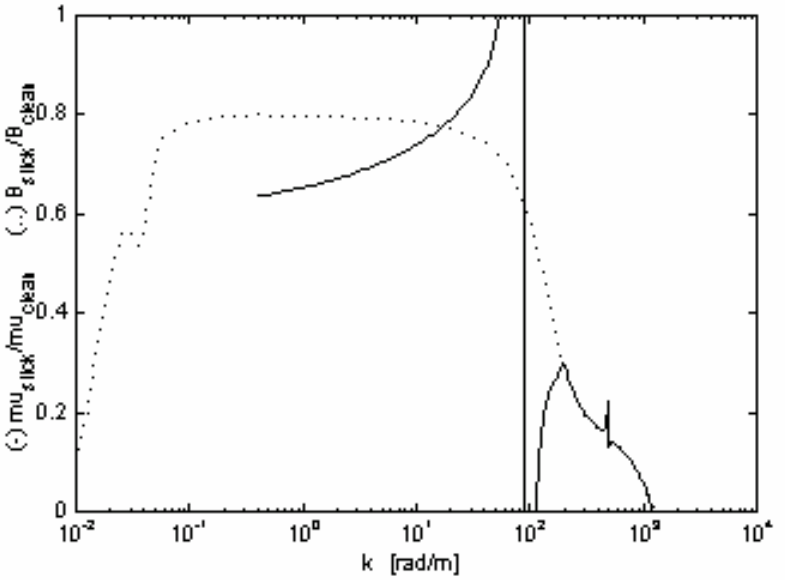

Fig. 7. Ratio of slick-covered relaxation rate to clean surface relaxation rate (drawn), compared to ratio of spectral values (dotted), for wind speed U_{10} = 15 m/s

As a first step, the equilibrium wave spectra were calculated for the slick-free and slick covered surfaces, respectively (Figs. 1 and 3). Because of the negative values occurring in the relaxation rates calculated in section 3, these could not be used in the radar modelling. It was therefore necessary to resort to the Plant and Wright relaxation rates again. With the equilibrium spectra, the form of the source term (Eq. 23) and the relaxation rates available, the actual spectral values of all wave components were calculated by integrating the action balance equation along the cross cut, i.e., by integrating

$$\frac{\mathrm{d}N}{\mathrm{d}x} = -\frac{1}{c_g}\mu\frac{N}{N_{eq}}(N - N_{eq}), \tag{26}$$

starting at $x = 0$ with $N = N_{eq}$. This yields the wave spectrum at each point along the cross cut. For this the relaxation model mentioned in the introduction (‘element 3’) was used with a zero current field.

From these calculated wave spectra, the normalised radar cross sections (σ^0) were calculated using the VIERS-1 radar backscatter module (Janssen et al. 1998). This is a more or less ‘standard’ composite model which includes the two-scale effect (Bragg backscatter influenced by longer wave

tilting) and a specular component (only important at steeper incidence angles) (e.g., Valenzuela 1978).

The results are shown in Fig. 8, for several radar wavelengths and incidence angles. For reference, the Bragg wavelengths of the radar configurations used are listed in Table 1. Only the results for VV polarisation are shown, those for HH are quite similar. It can be seen that at high Bragg wave numbers, the radar contrast is very large; there is practically no radar reflection from the slick. In C-band, when going from typical airborne incidence angles ($\geq 40°$) to the ERS case (23°), the radar backscatter damping is substantially reduced. This is mostly a consequence of the shape of the wave spectrum, that has on the slick still appreciable energy at $k = 87$ rad m^{-1} but much less at $k \geq 143$ rad m^{-1} (at 5 m s^{-1} wind), but also the result of the specular contributions to the backscatter, that come into play at 23°. Since the long waves are damped much less than the shorter ones, L- and P-band contrasts are low, with especially in P-band the maximum contrast not being reached on account of the small slick size with respect to the relaxation distance.

The lower damping at the long water wavelengths also reduces the contrast at the shorter radar wavelengths via the two-scale effect: when only Bragg backscatter is taken into account, the expected C-band contrasts would be much larger.

Table 1. Radar configurations used in Fig. 8, their Bragg wave numbers and maximum damping ratios attained.

Radar band	Radar wavelength [cm]	Incidence angle [°]	Bragg wavenumber [rad m^{-1}]	Maximum damping [dB]
X	3.3	55	312	40
C	5.7	40	143	13.7
C	5.7	23	87	2.7
L	24	55	43	1.5
P	68	55	15	0.3

The finite relaxation rate smoothes the edges of the slick in the modelled radar image. For strong damping, this effect is stronger on the leeward side of the slick than on the windward side. This is due to the factor N/N_{eq} in the source term producing smaller relaxation rates at lower absolute spectral levels. Because this form of the source term derives from the analysis of section 3, this should be a realistic effect. (In reality, one may expect additional effects from the wind action on the slick distribution on the water surface that may also give rise to different radar profiles for the leeward and windward sides.) Because of this, the apparent size of the slick is increased. For example, if one would take as the criterion for the extent of

the slick its –3 dB contour, the apparent size of the slick at C-band 40° would be 65 m instead of 50 m. A further consequence is that the location of the slick will appear to be displaced in the wind direction. All these effects become more pronounced at lower wind speeds.

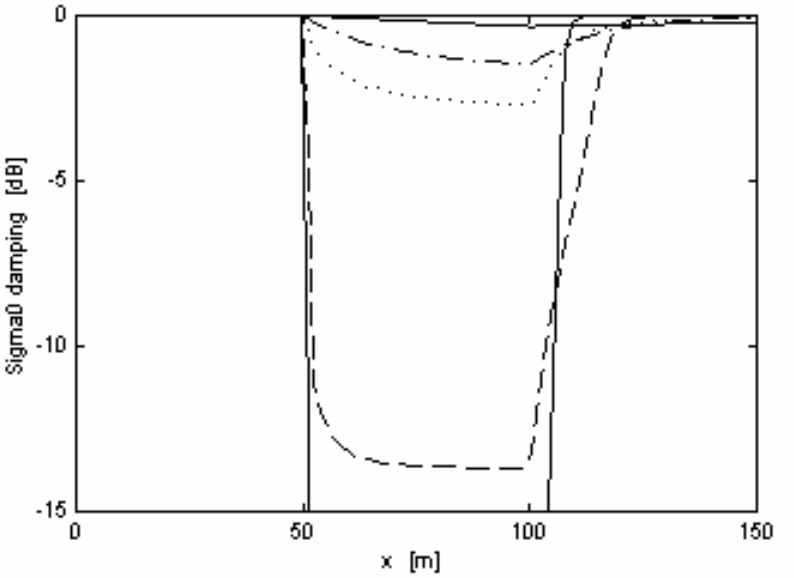

Fig. 8. Computed radar contrasts across a slick (oleic acid) that occupies 50 m < x < 100 m. X-band 55˚ incidence (drawn), C-band 40˚ (dashed), C-band 23˚ (dotted), L-band 55˚ (dash-dot) and P-band 55˚ (drawn). Radar look direction is downwind, VV polarisation, wind speed U_{10} = 5 m/s, neutrally stable atmosphere

5 Discussion and conclusions

The VIERS-1 wave spectral physical model, which is based on an energy flux divergence formulation, has been extended to include the saturation range by introducing a dissipation term proportional to wave energy squared. This leads to a physics-based wave spectral model in which the effects of slicks can be taken into account over the full saturation, gravity/capillary transition and capillary ranges. The model is not completely closed, however, because it needs to be supplied with a boundary energy flux value from the spectral peak, which is not included in the physical modelling but retains a JONSWAP parameterisation.

The form of the non-equilibrium net source term was derived from the spectral model. Also relaxation rates were derived, which in the saturation/gravity and far capillary ranges led to good results, but produced negative values in the short gravity/near capillary transition range. Negative relaxation rates are unacceptable as they will not lead to an equilibrium. Nevertheless, the VIERS-1 spectrum has been validated by X- and C-band scatterometry and is similar in shape to other validated spectral models. Therefore, we accept the extended VIERS model for computation of the spectrum but at the same time conclude that it is not yet suitable to yield relaxation rates.

The final goal of constructing a consistent slick radar imaging model could, therefore, only partially be met. It was possible to derive three aspects in a consistent manner, *viz.* an equilibrium wave spectrum for a clean surface, one for a slick-covered surface, and the form of the source term (quadratic). A fourth aspect, the actual relaxation rates, could only be meaningfully derived on part of the spectral range. Relaxation rates, therefore, had to be supplied externally, which was achieved by using the Plant and Wright (1977) parameterisation. In combination with a composite radar backscatter model, this leads to a physically based model that is able to compute radar contrasts across slicks. Sample results of the model show that at high radar frequencies, the slick appears extended on the leeward side on account of the quadratic source term leading to a slower relaxation on that side. Especially at lower radar frequencies, relaxation effects give the slick smooth edges and make it appear to be displaced in the wind direction. These effects become larger at lower wind speeds.

The slick imaging model has not been validated with measurements. However, a provisional comparison with observations from the literature, e.g. Gade (2006), shows that the increase of damping ratio with Bragg wave number (Table 1) is indeed observed, as well as the very low sensitivity to polarisation.

Acknowledgements. The availability of parts of the VIERS-1 software is gratefully acknowledged. This work was partly funded by the EC MAST program, contract MAS3-CT95-0035.

6 References

Alpers W, Hühnerfuss H (1989) The damping of ocean waves by surface films: a new look at an old problem. J Geophys Res 94 (C5): 6251-6265

Apel JR (1994) An improved model of the ocean surface vector spectrum and its effects on radar backscatter. J Geophys Res 99 (C8): 16269-16291

Gade M (2006) On the imaging of biogenic and anthropogenic surface films on the sea by radar sensors. In: Gade M, Hühnerfuss H, Korenowski GM (eds) Marine Surface Films. Springer, Heidelberg (this volume)

Greidanus H (1994) Wave-current interaction modeling incorporating wave blocking. Proc. IGARSS ’94, 8-12 August 1994, Pasadena, pp 1739-1741

Greidanus H, Calkoen C, Hennings I, Romeiser R, Vogelzang J, Wensink GJ, (1997) Intercomparison and validation of bathymetry radar imaging models. Proc IGARSS ’97, 3-8 August 1997, Singapore, pp 1320-1322

Hasselmann K (1963) On the non-linear energy transfer in a gravity wave spectrum, Part 2. J Fluid Mech 15: 273-281

Hughes BA (1978) The effect of internal waves on surface wind waves. Part 2. J Geophys Res 83 (C1): 455-465

Hsiao SV, Shemdin OM (1983) Measurements of wind velocity and pressure with a wave follower during MARSEN. J Geophys Res 88 (C6): 9844-9849

Janssen PAEM, Wallbrink H, Calkoen CJ, van Halsema D, Oost WA, Snoeij P (1998) VIERS-1 scatterometer model. J Geophys Res 103 (C4): 7807-7831

Kitaigorodskii SA (1983) On the theory of the equilibrium range in the spectrum of wind-generated gravity waves. J Phys Oceanogr 13: 816-827

Komen GJ, Hasselmann S, Hasselmann K (1984) On the existence of a fully developed wind-sea spectrum. J. Phys. Oceanogr. 14: 1271-1285

Lyzenga DR, Bennett JR (1988) Full-spectrum modeling of synthetic aperture radar internal wave signatures. J Geophys Res 93 (C10): 12345-12354

Phillips OM (1985) Spectral and statistical properties of the equilibrium range in wind-generated gravity waves. J Fluid Mech 156: 505-531

Plant WJ, Wright JW (1977) Growth and equilibrium of short gravity waves in a wind-wave tank. J Fluid Mech 82: 767-793

Romeiser R, Alpers W, Wismann V (1997) An improved composite surface model for the radar backscattering cross section of the ocean surface, Part 1. J Geophys Res 102 (C11): 25237-25250

Snoeij P, van Halsema E, Vogelzang J, Waas S, Zecchetto S, Jansen H, Oost W, Jähne B, Calkoen Ch (1993) VIERS-1 final report phase 3. BCRS report 92-24, ISBN 90 5411 068 6

Trokhimovski Y (1993) The model for gravity-capillary waves modulation in IW current field and they application to radiophysical measurements. Proc IGARSS ’93, 18-21 August 1993, Tokyo, pp 500-502

Valenzuela GR (1978) Theories for the interaction of electromagnetic and ocean waves – a review. Bound Layer Meteor 13: 61-85

Vogelzang J (1989) The mapping of bottom topography with imaging radar. A comparison of the hydrodynamic modulation in some existing models. Int J Remote Sensing 10 (9): 1503

Thermal imagery of surface renewal phenomena

David K. Woolf[1] and Nicholas Ward[2]

[1]Centre for observation of Air-Sea Interactions and fluXes (CASIX), National Oceanography Centre, Southampton, United Kingdom
[2]School of Ocean and Earth Science, National Oceanography Centre, Southampton, United Kingdom

Abstract. Processes within the sea surface microlayer have been relatively little studied considering their major role in air-sea interaction, especially gas exchange. This state of affairs can be explained by the inaccessibility of this very thin layer to most methods. One of the few suitable tools is radiometry which can probe a surface layer of ~1-1000 micrometres according to the wavelength chosen. In particular, thermal imagery can be used to investigate turbulence impinging on the sea surface - "surface renewal patterns". Field measurements with thermal imaging cameras show evidence of fairly large-scale (~ 1 metre) organised turbulent structures. Thermal imagery is also a powerful tool in the study of breaking waves. Thermal images of breaking waves are characterised by a "hot" high-emissivity crest ahead of a warm patch. Interpretation of field observations remains difficult. Greater control on variables is possible in the laboratory. Laboratory experiments show that in dynamically weak situations (e.g., free convection), though the influence of eddies is readily apparent, these eddies do not appear to bring bulk water to the absolute surface. Even quite weak bubble plumes are highly effective in renewing the surface, suggesting that they will influence the thermal signature of the sea surface following breaking waves, and may be an effective agent of air-sea gas exchange. Surface-active materials both influence the nature of surface renewal and the measurement process (through alteration of emissivity).

1 Introduction

Sea surface renewal can be defined broadly as the manner in which sub-surface turbulence enhances the transport of water, heat and dissolved substances between the absolute sea surface and the upper ocean (Hasse 1997). Surface renewal has a major effect on the distribution of surface-active material at the sea surface. Also, surface-active material on the sea surface is expected to have a major effect on the structure of sub-surface turbulence and thus surface renewal rates (Tsai 1996).

The most urgent interest in surface renewal is founded in the relationship of surface renewal to the air-sea exchange of poorly soluble gases, including carbon dioxide. If these gases had to be transported through a stagnant layer of only 1mm thickness, then rates of ocean-atmosphere exchange would be impossibly slow. It is clear that in fact turbulence enhances mixing even within a millimetre of the surface, but a full description of this process is elusive. A number of models of the surface renewal process have been proposed; see for example: Jähne and Haussecker (1998). Here, we briefly review a selection of these models with particular emphasis on their implication for radiometric methods of estimating air-sea exchange. The term "surface renewal model" is often used more narrowly to describe models in which elements of the sea surface are occasionally directly replaced by water from the bulk, and exchange proceeds by this occasional replacement and molecular diffusion within the surface elements. We shall term these models as "absolute renewal models" to distinguish them from models in which only sub-surface elements are directly replaced from the bulk ("partial renewal"). Notable among partial renewal models is the surface penetration model of Harriott (1962) in which the nearest approach of an eddy to the surface is randomly distributed. A very different set of models ("turbulence-diffusion") describe diffusive transport by molecular diffusion and numerous eddies whose scale and intensity reduces asymptotically to zero as the surface is approached. Various absolute renewal models differ most significantly in their description of the statistical distribution of the time between successive replacements. Higbie (1935) originated (absolute) surface renewal models, but Danckwerts (1951) introduced the most popular form of the surface renewal model that assumes that the time between replacements will follow an exponential distribution. This is an appealing model for turbulent exchange in "forced convection conditions" since it follows directly from assuming that the probability of replacement of an element at an instant is independent of the time since the element was previously replaced. Turbulent processes are stochastic rather than purely random however, and a modified distribution may be set by the statistics of turbulence. Rao et al. (1971) described a log-

normal distribution for "bursting phenomenon", and this distribution has been supported by high resolution thermal imagery (Jähne and Haussecker 1998; Schimpf et al. 1999). Absolute renewal is questionable on energetic grounds (Hasse 1990) due to the difficulty of disrupting the surface against surface tension. Partial renewal and turbulence-diffusion models do not require turbulent replacement at the absolute surface.

In addition to limiting the transfer of gases and other dissolved substances across the microlayer, the relatively low mixing within the microlayer usually leads to a strong temperature gradient in the microlayer. The sea surface is usually slightly cooler than the water below due to a net heat loss to the atmosphere above (Hasse 1971). This temperature difference (typically a few tenths of a Kelvin) can be measured, as can the net heat flux from the sea surface to the atmosphere (some difficult calculations of the *effective* heat flux are also necessary, the calculation in daylight is particularly demanding). Surface temperatures can be estimated by radiometry. In the next section, we consider the utility of "radiometric methods" in studies of surface renewal and estimates of air-sea gas transfer velocities. In the following sections, we describe some observations in the field and the laboratory with a thermal imaging camera, which give some insight into the characteristics of surface renewal processes.

2 Radiometric methods

2.1 Large footprint radiometry

We consider first application of measurements of the ensemble average "cool skin effect' in known environmental conditions. The basic principle is that a "transfer velocity of heat", K_h can be calculated from the temperature difference across the microlayer, ΔT, by assuming the transport of heat from the bulk to the surface is in balance with the heat flux from the surface to the atmosphere, Q:

$$Q = -K_h \, C_p \, \rho \, \Delta T \tag{1}$$

where C_p is the specific heat of the water and ρ is the density of the water

The transfer velocity of another property (for example, a gas) can be estimated given a model of the analogous transport of heat and this other property. A simple turbulence-diffusion model of the homogenous transport of heat and gas through the microlayer gives a simple equation for the transfer velocity of a gas, K_g:

$$K_g = \left(\mathrm{Pr}/Sc\right)^n \, K_h \tag{2}$$

where *Pr* is the Prandtl number of heat in the water, *Sc* is the Schmidt number of the gas in the water, and *n* is a model-dependent exponent.

Traditional turbulence-diffusion models (based on the boundary layer adjoining a solid wall) imply that $n = 2/3$, but a value $n = 1/2$ is appropriate for a boundary layer adjoining a free surface (Jähne and Haussecker 1998). The appropriate value of n depends on the wind stress and the surfactant loading of the surface. Soloviev and Schluessel (1994) have described a procedure for estimating gas transfer velocities from measurements of heat transport, assuming that transport is adequately described by the classical (Danckwerts) surface renewal model. The key relationship can be written in the form:

$$K_g = \varphi \left(\mathrm{Pr}/Sc\right)^n \; K_h \tag{3}$$

where φ is a non-dimensional number, related to the distribution of surface temperature. A similar equation can be written for any surface renewal model but the value of φ is model dependent.

A major difficulty with applying large footprint measurements of the cool skin, is the question of homogeneity. The models described above require an assumption of horizontally homogenous distribution of heat flux and sub-surface turbulence within the footprint. Such an assumption is highly dubious, for example patches of relatively intense turbulence may be expected near breaking waves (Rapp and Melville 1990, Woolf 1995). The detrimental effect on our simple model can be understood from the following thought experiment: Consider turbulent exchange to be enhanced by a factor *N* over a fraction $1/N$ of the sea surface. For large N, we find that the air-sea exchange of a gas will be doubled, but the spatially averaged cool skin effect is barely altered.

In summary, large footprint measurements permit an estimate of gas transfer velocities, but these estimates are sensitive to model assumptions. Furthermore, large footprint measurements give no direct information on the characteristics of surface renewal. Also, the method is extremely sensitive to drift in the calibration of either the surface or the bulk temperature measurement.

2.2 Imagery and "surface thermometry"

In cool skin conditions, an eddy bringing sub-surface water to the surface will create a "warm anomaly" on the sea surface. Temperature fluctuations on the sea surface will be highly sensitive to the character of surface renewal. The turbulence-diffusion paradigm implies that the vertical scale of eddies diminishes asymptotically to molecular scales close to the surface,

so that associated temperature fluctuations are restricted to below the surface. By contrast, an absolute renewal model implies a distribution of surface temperatures with the bulk water temperature at one extreme. Partial renewal will produce less extreme variations in surface temperature than absolute renewal. In general, the distribution of surface temperature fluctuations is a function of both the frequency and character (i.e., absolute or partial) of renewing eddies.

Thermal imagery offers the possibility of directly measuring temperature fluctuations at the sea surface, and thereby inferring the character and intensity of surface renewal. The utility of thermal imagery is limited by its departure from an "ideal surface thermometer" and the extent to which apparent temperature fluctuations are forced by extraneous factors. We might wish that an imaging radiometer would solely measure heat radiated from the surface that it is focussed upon, but reality intervenes. Three factors that slightly degrade real radiometric measurements are surface reflectivity, penetration of thermal radiation through water, and atmospheric absorption and emission. The sea surface behaves approximately as a black body at low incidence angles, but a small fraction (~ 1%, depending on incidence angle and wavelength) of radiation received by an imager will have been reflected at the sea surface rather than emitted there. It is possible to see reflections of objects in thermal images of the water surface, and these can contribute to measured temperature fluctuations. Similarly, variations in the temperature of the sky reflected to the camera will contribute. Variations of the emissivity of the surface can be particularly important especially for relatively high incidence angles, and when the sky temperature is very low. Waves, whose slope alters the incidence angle, can cause significant variability in emissivity across an image. Some surfactants can significantly alter the intrinsic emissivity of the surface water. The penetration of thermal infrared radiation through sea water is wavelength dependent; it is only an approximation to assume that air-sea infrared radiation is radiated and absorbed at the absolute sea surface (this also has implications for how we model heat transport through the microlayer). Typically, a longwave (8-12 μm) thermal imager will receive radiation from approximately the top 20 μm of the sea. (It might be noted here also, that the assumption in most models of the thermal skin that heat transfer by radiation is insignificant below the absolute surface is also only an approximation. One notable consequence of finite radiative transfer within the surface skin is that the rate of change of surface temperature immediately following an absolute renewal event is also finite; thus while a practical measurement cannot normally capture surface temperatures exactly equal to the bulk temperature below, the rate of cooling following an absolute renewal should be sufficiently low for temperatures closely approach-

ing the bulk temperature to be captured). The radiation reaching the radiometer is modified also by the atmosphere between the instrument and the target. Each of the mechanisms described above can contribute errors in the estimated surface temperature at each point of ~ 100mK, which is a significant obstacle to this methodology.

Another factor that is difficult to eliminate is the direct effect of varying air-sea fluxes on surface temperature fluctuations. It is clear that a sustained horizontal variation in these fluxes (at the sea surface in the Lagrangian frame of the surface elements) will modify the surface temperature distribution. It may not always be possible to determine if a feature is essentially "oceanographic" (i.e., forced from below by surface renewal; which ultimately, but not directly, depends on atmospheric forcing), or "meteorological" (i.e., directly associated with variability in atmospheric fluxes).

In spite of the limitations described above, we can be certain that if a subsurface eddy is apparent in a thermal image of the sea surface, then that eddy has some finite influence on exchange across the microlayer. Thus, imagery at least must have a role in identifying significant processes. It should also be possible in some cases to demonstrate that a process does not absolutely renew the surface. The observations reported in the following sections address these issues and are largely qualitative, but we hope they will be useful in constructing more complete quantitative models of sea surface renewal.

3 Field observations

Images were taken from a fixed platform, Meetpost Noordwijk, 9 km off the Dutch Coast in May and June 1996. The region is influenced by the Rhine river plume, and surface slicks and other features associated with surfactants and freshwater were often observed. We report the analysis of data from late (night time) on 3rd of June. The instrument used was a scanning thermal imager sensitive at longwave (8-12 μm) set up at an elevation of 16.5 m on an overhanging platform on the North side of the platform. The camera was pointed at a cardinal angle of 030^{o} and at 45^{o} to the vertical. Heat flux components and standard meteorological and oceanographic variables were measured (and recorded in most cases as ten-minute averages). The ten-metre-elevation wind was 6-8 m s^{-1} from the Southwest (unfortunately wind and waves will have been distorted by the North West corner of the platform). The current was carrying water towards the imager at up to 0.5 m s^{-1}. The sky was clear as far as can be established. The resulting net infrared heat loss (30-90 Wm^{-2} within the data

period described here) was the most important component of the heat flux, forcing a cool skin. Relative humidity varied in the range 69-77 %, adding a latent heat flux to the net heat loss. Air and water temperatures were similar, and consequently the sensible heat flux was quite small. The thermal noise of each pixel (= 80 mK) obscures all but the strongest features At moderate wind speeds, by far the greatest signal is associated with the crests of actively breaking waves, but these were fairly rare. It is also apparent that the wakes of these breaking waves are relatively warm. An image of a relatively large breaking wave is shown below (Figure 1).

The original images do not usually show any distinct features apart from an occasional breaking wave. In order to extract more information, we have processed the images as follows. The image is warped (with the greatest possible preservation of individual pixels) to a 128 x 128 pixel, 6.4 m x 6.4 m subsample at the centre of the original image. Warping is necessary, but the mapping was carefully designed to remain as close as possible to mapping one original pixel to a single final pixel. Linear horizontal gradients are eliminated (de-trended images). Very large scale (>3 m) variability which can not be sampled satisfactorily is removed. The total standard deviation within these images is dominated by the 80 mK "white noise" of the instrument (a natural limit of the sensing element at its normal operating temperature). The variation with time of the standard deviation of temperature within each image is shown in Figure 2 (upper left). The remaining signal is highly variable. Dramatic increases and then falls in standard deviation are observed on time scales of 10 minutes and less. A few isolated values can be attributed to special features; for example the breaking wave featured in Figure 1 is responsible for a single high value at ~2151 UTC. The slower variation (gradual increase followed by decrease) follows the trend in heat flux, but the excursions are unexpected. The small-scale (0.1-1 metre) fluctuations slightly exceed the instrumental noise, but generally any coherent fluctuations at these scales are not sufficiently large to extract from the white noise. The standard deviation within images is separated according to spectral range. The variability in two spectral ranges is highly correlated over time periods of a few minutes (e.g., Figure 2, lower left), but the two sets of values are not simply proportional (straight line in figure) as might be expected if each was proportional to the instantaneous heat flux or reflectivity. Larger scale variability contributes disproportionately to the rapid excursions in standard deviation.

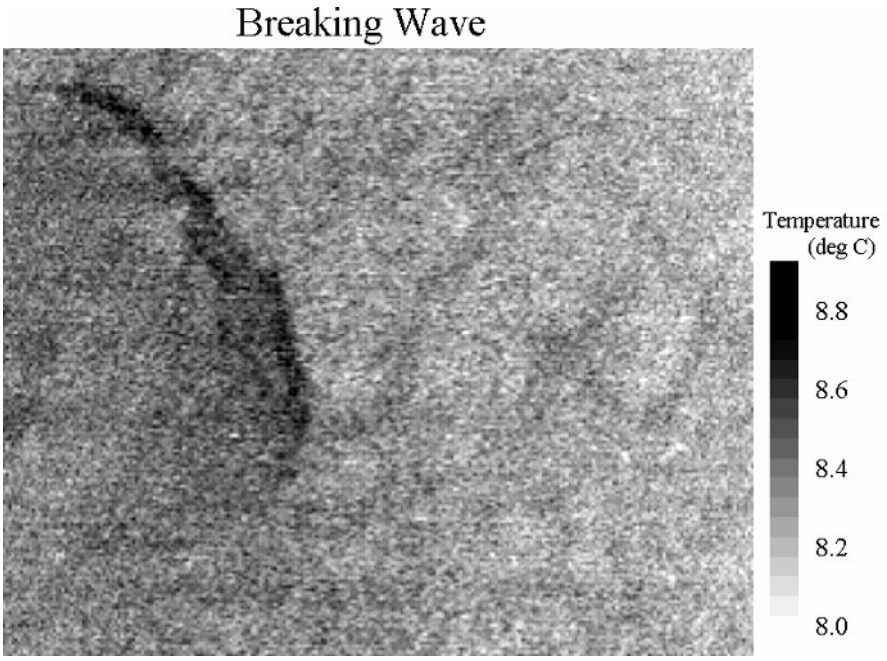

Fig. 9. A raw thermal image. These images cover ~10 x 10m of sea surface but are geometrically distorted. The bottom of the image is closest to the viewing point, and the image is foreshortened in the vertical due to the oblique (45^o) view. The breaking wave was propagating from left to right. (Images similar to this one have been described by Jessup et al. (1997a). The highest temperatures are associated with the high emissivity crest of the breaking wave, while warm water behind the crest is indicative of a turbulent wake)

Images are then low-pass filtered to remove high wave number noise while retaining low wave number information (low-pass images). One low-pass image is shown in Figure 2 (right); the features in this particular image are typical in form, but relatively intense. Since ancillary measurements were only recorded at 5-minute or 10-minute intervals, we do not know if there were large changes in wind forcing or atmospheric heat fluxes coincident to the excursions in thermal signal. However, it is difficult to see how the features apparent in the low-pass images can be a direct response to meteorological forcing. Variations in emissivity of the sea surface and reflected features in the sky are also candidate explanations. The variability in emissivity associated with the slope of waves would be the most likely of these, but the orientation of the features seen in the processed images is contradictory to this explanation, and the strength and the variability are also rather too high to be explained in this way.

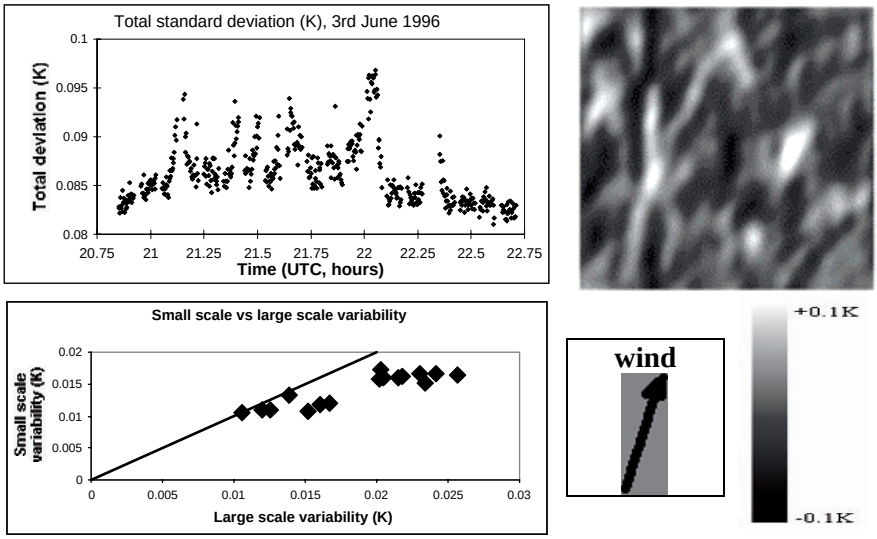

Fig. 10. Upper left: Standard deviation of temperature in the de-trended images plotted against time for a two hour subset of the data. Lower left: the variability at a larger scale (~1- 3 m) against the variability at a smaller scale (~0.1 – 1 m) in a 150 second period of the large excursion at ~2200 UTC. **Right**: A low-pass processed image at ~ 2200 UTC near the peak in variability. The image covers a 6.4m x 6.4 m area of sea surface. The approximate wind direction and temperature anomaly scale are shown below. Features preferentially aligned with the wind and spaced ~ 1 metre apart are apparent

In general patterns appear to be the result of a complicated pattern of embedded vortices, preferentially aligned approximately in the direction of the wind, with the addition of a few relatively extreme fluctuations in patches. It seems most likely that vortices in the upper ocean imprint temperature fluctuations on the surface by partial renewal. Reorganisation of surfactants on the surface, and resulting variability in emissivity, by vortices may also play a role in their imaging. During the excursion at ~2200 UTC, there is a trend in the skewness of temperature within images, with extreme hot values predominating over extreme cold values early in the excursion. There appears to be highly variable mixing phenomena at play, but a full interpretation is beyond us.

4 Laboratory observations

The interpretation of field data on surface images is often made more difficult by limitations in the absolute measurement of both surface and bulk

temperature. For example, under a cold sky a radiometric measurement of surface temperature is quite sensitive to the assumed emissivity of the surface, and this is invariably quite uncertain due to the sensitivity of emissivity to surface films and surface roughness. Thus, it is not always clear if the warmest water at the sea surface is at precisely the temperature of the bulk water (as implied by absolute renewal). Also, our field measurements are very restricted in resolution. We have resorted to small-scale laboratory experiments in which we can resolve even millimetre-scale fluctuations by viewing at short distances, and are able to diminish errors in temperature measurement greatly. These were simple experiments using tap water, with no effort to remove the inevitable surfactant loading of the water. Measurements were made at low-incidence angles (usually 30^{o}) in order to decrease reflection, and in most cases with a background temperature close to the water temperature (this greatly reduces the error associated with uncertainty or variability in emissivity). We have conducted a large variety of experiments in free and forced convection conditions. A general observation is that water of bulk temperature (within experimental uncertainty) is only observed to outcrop at the surface in the more energetic cases. Here, we feature a single experiment designed to investigate the effect of bubble plumes on surface renewal.

It is thought that large enhancements of air-sea gas exchange are likely as a result of “whitecapping” breaking waves (Woolf 1997). Transfer will be enhanced by exchange across the surface of bubbles and by additional exchange across the sea surface, notably in the wake of the breaking waves. The simplest description of mass, heat and momentum exchange in the wake zone simply considers an enhanced level of turbulence. Within these patches, bubbles contribute buoyancy and alter significantly the behaviour of the turbulent plumes. In addition, when bubbles surface and burst, they will disrupt the surface microlayer.

A basic appreciation of the effect of bubble plumes on the sea surface can be reached through simple laboratory measurements. An open container of water at approximately room temperature will usually be cooled at the surface by vapour loss to the laboratory, resulting in a surface “skin temperature” up to ~1K cooler than the bulk of the water. We have conducted experiments in a temperature-controlled laboratory using a container with a thermally insulated base and walls, but open at the top and filled with tap water. The effect on surface temperature of surfacing bubbles was measured with a thermal camera, calibrated *via* reference targets in the field of view. Bubbles were generated by pumping air from the laboratory through a peristaltic pump to a simple aquarium "air stone" in the base of the container.

Figure 3 shows the mean temperature of a rectangular area of the water surface during an experiment. Images were acquired once every 0.8 seconds. Initially, the laboratory is unventilated and the surface temperature is very close to both the bulk water temperature and the room temperature (images 0 – 180). When the laboratory is ventilated by dry air the mean temperature drops rapidly until the surface heat loss is balanced by heat supplied to the surface by free convection within the container. (There are fluctuations in surface temperature associated with free convection patterns, but in common with numerous other observations of free convection, every surface element is much cooler than the underlying water). At image 328, the peristaltic pump was switched on and bubbles began to surface near the centre of the selected area. The temperature rose steadily as the region disrupted by the surfacing bubbles expanded, until this region encompassed the entire selected area. Thereafter the surface temperature decreased as a result of heat loss, which was enhanced by the bursting bubbles.

Fig. 11. Temperature of water surface in the course of an experiment

Examination of individual frames of thermal and video imagery reveals details of disruption processes. Individual bubbles produce local warming, indicating some disturbance of the surface microlayer, but only partial renewal of the surface. A plume of bubbles acts in concert to produce rapid surface renewal within a well-defined area of the surface. The area affected by the plume expands well beyond the region where bubbles are surfacing.

It is important to note that the particular experiment described here was conducted with a very low airflow into the bubble generator yielding a bubble plume that was barely perceptible in close-up video images of the water surface. Stronger airflow and a substantial bubble plume produced

rapid and dramatic disruption of the thermal skin across the entire surface of the container. By contrast, when we used the same pump and tubing to pump water, there was only a significant surface effect if the flow was strong and the outlet was close to the water surface.

5 Discussion and conclusions

Infrared imagery of the sea surface is a powerful technique for investigating surface renewal processes at the sea surface, including the modulation of these phenomena by wind stress, wave breaking, slicks and other environmental variables. Thermal imaging techniques have shown to be effective in the study of large and small breaking waves (Jessup *et al*. $1997_{a,b}$); and Jaehne and co-workers (Jähne and Haussecker 1998; Schimpf et al. 1999) have exploited small-scale temperature fluctuations to estimate gas transfer velocities. It should be noted in caution that infrared cameras are not "ideal surface thermometers" and, therefore, interpretation of an image is not always straightforward.

Night-time measurements with the thermal IR camera in a moderate wind (6-8 m s^{-1}) show evidence of the importance of fairly large-scale (~ 1 metre) organised turbulent structures, and suggest that the process of air-sea exchange is remarkably dynamic. The amplitude of the metre-scale fluctuations varies enormously on time scales of a few minutes. It seems likely that the variations in metre-scale fluctuations have a dynamical origin within the water column – perhaps associated with wave breaking which also varies greatly on these time scales. Images show evidence of vortices aligned with the wind. These vortices may be part of a spectrum of similar motions extending from large-scale Langmuir circulation down to much smaller scales (Melville et al. 1998). The smaller scale motions are likely to be more directly significant to surface renewal and air-sea gas exchange, but it may be possible to investigate small-scale surface renewal indirectly by measuring the related large-scale fluctuations (requiring less spatial resolution). Patches at relatively high temperature may result from the action of small breaking waves (with or without air entrainment, but we can not quantify this process).

At the sea surface, we may expect surfacing bubble plumes to contribute to surface renewal in the wake of breaking waves. This surface renewal will necessarily enhance air-sea gas exchange. It is our experience that only a small flux of bubbles is necessary to transform surface renewal, but this is difficult to quantify. It seems likely that bubbles are significant to surface renewal by small breaking waves, even when there is no obvious “whitecap”.

In general, observations of temperature fluctuations at the sea surface support a “surface renewal” paradigm rather than “turbulence-diffusion”. Further, high-resolution measurements support an absolute renewal model with a log-normal distribution of surface replacement (Jähne and Haussecker 1998; Schimpf et al. 1999). We wish to stress the continuing need for a more complete description of sea surface renewal. We note the variety of processes contributing to surface renewal and query whether “absolute renewal” is common. It is not possible to say that surface water is exactly at bulk temperature, but there are instances where it is clear that bulk water is not brought to the absolute surface. We observe that partial renewal is common, even in fairly energetic conditions, and may be more typical than absolute renewal. It is also apparent that transport through the microlayer may be achieved through the action of numerous eddies (following the turbulence-diffusion paradigm) rather than a single replacement action. Both the “surface renewal” and “turbulence-diffusion” paradigms are idealisations, and a more complete model should include elements of both. Note that while similarities of heat and gas transfer are implied by any model, the exact relationship is model dependent. For example, Atmane et al. (2004) have recently noted the implications of substituting a replacement model (Harriott 1962) for a standard surface renewal model. A quantitative description of surface renewal, mass and heat transport should include a description of turbulent transport by various processes.

Acknowledgments. Experiments were undertaken in the framework of ASGAMAGE (MAST III Programme, MAS3-CT95-0044) and LUMINY (Environment and Climate Programme, ENV4-CT95-0080) supported by the European Commission. We thank our fellow participants in these projects. This research is currently supported by the UK Natural Environment Research Council, through the Centre for observation of Air-Sea Interactions and fluXes (CASIX).

6 References

Atmane MA, Asher WE, Jessup AT (2004) On the use of the active infrared technique to infer heat and gas transfer velocities at the air-water free surface. J Geophys Res 109: C08S14

Danckwerts PV (1951) Significance of liquid-film coefficients in gas absorption. Ind Engng Chem 43: 1460-1467

Harriott P (1962) A random eddy modification of the penetration theory. Chem Eng Sci 17: 149-154

Hasse L (1971) The sea surface temperature deviation and the heat flow at the sea-air interface. Bound Layer Meteor 1: 368-379

Hasse L (1990) On the mechanism of gas exchange at the air-sea interface. Tellus 42B: 250-253

Hasse L (1997) Transport processes in the sea-surface microlayer. In *The Sea Surface and Global Change*, eds PS Liss and RA Duce, Cambridge University Press, pp 93-119

Higbie R (1935) The role of absorption of a pure gas into a still liquid during short periods of exposure. Trans Am Inst Chem Engr 35: 365-373

Jähne B, Haussecker H (1998) Air-water gas exchange. Ann Rev Fluid Mech 30: 443-468

Jessup AT, Zappa CJ, Loewen MR, Hesany V (1997a) Infrared remote sensing of breaking waves. Nature 385: 52-55

Jessup AT, Zappa CJ, Yeh H (1997b) Defining and quantifying microscale wave breaking with infrared imagery. J Geophys Res 102: 23145-23153

Melville WK, Shear R, Veron F (1998) Laboratory measurements of the generation and evolution of Langmuir circulations. J Fluid Mech 364: 31-58

Rao KN, Narasimha R, Narayanan B (1971) The bursting phenomenon in a turbulent boundary layer. J Fluid Mech 48: 339-352

Rapp RJ, Melville WK (1990) Laboratory measurements of deep-water breaking waves. Philos Trans Roy Soc London A331: 735-800

Schimpf U, Haussecker H, Jähne B (1999) Studies of air-sea gas transfer and micro-turbulence at the ocean surface using passive thermography. In *The Wind-Driven Air-Sea Interface*, ed ML Banner, University of New South Wales, pp 345-352

Soloviev AV, Schluessel P (1994) Parameterization of the cool skin of the ocean and of the air-ocean gas transfer on the basis of modelling surface renewal. J Phys Oceanogr 1339-1346

Tsai WT (1996) Impact of surfactant on turbulent shear layer under the air-sea interface. J Geophys Res 101: 28557-28568

Woolf DK (1995) Energy dissipation through wave breaking and the air-sea exchange of gases. In *Air-Water Gas Transfe*r, ed B Jaehne and EC Monahan, pp 185-195, Hanau, Germany: AEON

Woolf DK (1997) Bubbles and their role in air-sea gas exchange. In *The Sea Surface and Global Change*, eds PS Liss and RA Duce, Cambridge University Press, pp 173-205

Infrared imaging: a novel tool to investigate the influence of surface slicks on air-sea gas transfer

Uwe Schimpf [1], Nelson M. Frew [2] and Bernd Jähne [1,3]

[1] Institute of Environmental Physics, University of Heidelberg, Germany
[2] Woods Hole Oceanographic Institution, Woods Hole, MA, USA
[3] Interdisciplinary Center for Scientific Computing, University of Heidelberg, Germany

Abstract. The influence of surface films on air-sea gas exchange at low and moderate wind speeds is investigated. Observations were made in the small Heidelberg circular wind-wave facility and in coastal and offshore waters south of Cape Cod, New England. The passive controlled flux technique was used to investigate the micro turbulence very near the water surface, which controls the rate of transfer of momentum, heat, and mass across the air-sea interface. The analysis of infrared image sequences allows the estimation of the net heat flux at the water surface, the skin-bulk temperature difference across the thermal sublayer and thus the heat transfer velocity. Using Schmidt number scaling, estimates of the gas transfer velocity are obtained. Experimental evidence shows that increased surface film concentrations suppress near surface turbulence and thus decrease the gas exchange compared to a slick-free ocean interface. If a surfactant is present, turbulent mixing is dampened and direct renewal of the surface is inhibited. A surface slick changes the hydrodynamic boundary conditions in that the length scales of near surface turbulence controlling air sea gas exchange are modified. The micro-scale temperature fluctuations at the water surface indicate that at low wind speeds the transport process is dominated by large-scale turbulence, whereas at higher wind speeds the smallest observed scales dominate the transport.

1 Introduction

The oceans cover two-thirds of the earth's surface. Driven by the wind and heated by solar radiation, this moving bulk of water directly affects earth's climate (e.g., the impact of the North Atlantic circulation on West Europe's climate). These huge amounts of flowing water have an enor-

mous capacity to absorb and release both heat and gases. The oceans play an important role as sink for carbon (the yearly absorption capacity is about three Gigatons of carbon). In recent years, global climate change and the growing pollution in atmosphere and oceans have drawn the attention to small-scale transfer processes at the air/water interface.

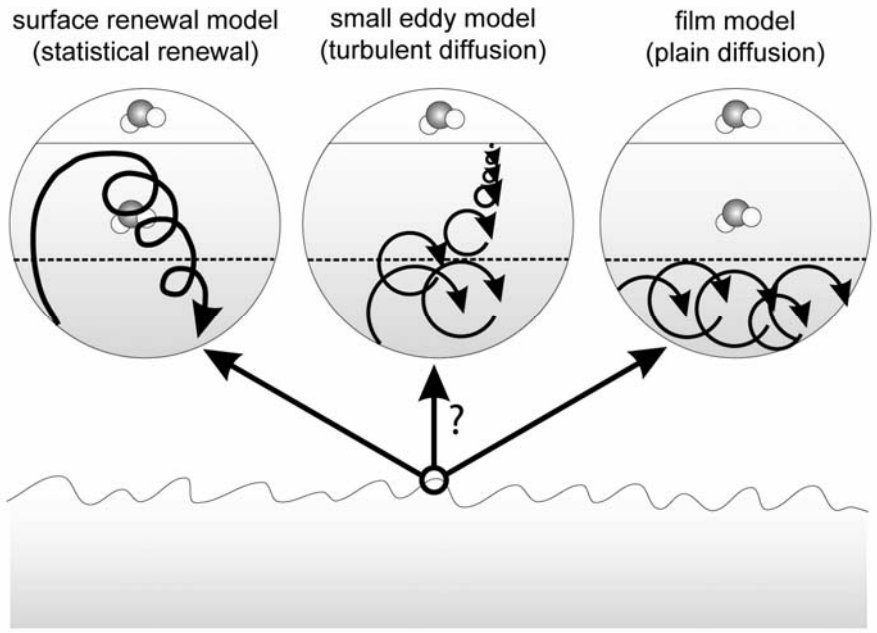

Fig. 1. Which of the three commonly used models best describes the mass transfer across the aqueous boundary layer: surface renewal, turbulent diffusion or molecular diffusion?

The exchange of inert gases including greenhouse gases (e.g., carbon dioxide, methane) is governed by the interplay of turbulent transport and molecular diffusion in the aqueous boundary layer. This 20-300 μm thick layer constitutes the bottleneck for the exchange of gases between atmosphere and ocean. Although the underlying turbulent transport mechanisms are extremely complex and difficult to quantify, knowledge about the environmental parameters influencing air-sea gas exchange has increased considerably in recent years. Nevertheless, the commonly used semi-empirical parameterisations of the gas exchange rate with wind speed (e.g., Liss and Merlivat 1986, Wanninkhof 1992, Wanninkhof and McGillis 1999) predict a global carbon uptake that differ by a factor of three (Donelan and Wanninkhof 2002). Theoretical gas exchange models (surface renewal and

small eddy model, see Fig. 1) differ in the prediction of concentration profiles, but not in the dependence on environmental parameters such as wind speed.

In order to gain insight into the transport mechanisms, new techniques for the quantitative investigation of gas exchange have been developed, e.g., boundary layer visualization with laser induced fluorescence imaging (Münsterer and Jähne 1998), particle tracking velocimetry (Siddiqui et al. 2004) and infrared imaging (Schimpf et al. 1999), but only lately progressed to a state where quantitative measurements of relevant turbulent properties are feasible. By using novel visualization and image processing techniques, it is possible for the first time to get an insight into the mechanism of these dynamic processes (Haußecker et al. 1998) and to investigate turbulent processes that underlie the transport mechanisms across the aqueous boundary layer. Despite experimental and theoretical effort, there is still a lack of understanding how other processes, e.g. rain, wave breaking, and intermittent meteorological conditions affect the transport processes.

In the following discussion, the *Controlled Flux Technique* (Jähne et al., 1989) is presented, using heat as a proxy tracer for gases. The high spatial and temporal resolution of this unique technique allows the study of key questions about transfer processes. Detailed laboratory measurements were carried out in the Heidelberg wind wave facility and during the 1997 Coastal Ocean Processes Study in the Atlantic Ocean. Experimental evidence shows that a surface film decreases the gas exchange rate and modifies the length scales of near surface turbulence in comparison to a clean interface.

2 Heat as a proxy tracer for gases

Typical mass balance methods to measure the air-sea gas transfer have one major drawback: the response time is of the order of hours to days, making a parameterisation with parameters such as wind forcing, wave field, or surface chemical enrichments nearly impossible. The controlled flux technique uses heat as a proxy tracer for gases to measure the air-sea gas transfer rate locally and with a temporal resolution of less than a minute. This method offers an entirely new approach to measure the air-sea gas fluxes in conjunction with investigation of the wave field, surface chemical enrichments and the surface micro turbulence at the water surface. The principle of this technique is very simple: a heat flux is forced onto the water surface and the skin-bulk temperature difference across the thermal sublayer is measured.

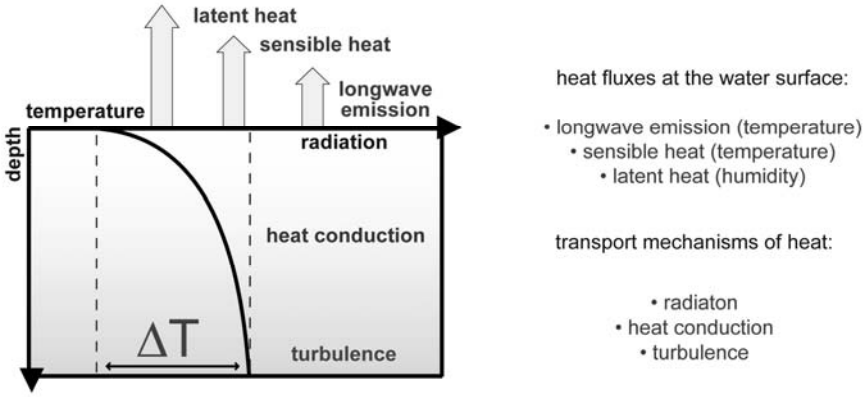

Fig. 2. Naturally occurring heat fluxes at the ocean surface and transport mechanisms of heat in the thermal sublayer

In a first realization, Jähne et al. (1989) forced a periodical heat flux density onto the water surface using a chopped heat source above the water surface. The temperature response at the water surface was detected with point measuring radiometer. In a further implementation of this technique, Haußecker (1996) developed the so-called passive controlled flux method that estimates the skin-bulk temperature difference under natural heat flux conditions assuming a surface renewal model. The naturally occurring heat fluxes at the ocean surface (latent, sensible and long wave radiative heat flux) cause the surface temperature to decrease or increase depending on the direction of these fluxes. The net heat flux forces a skin-bulk temperature difference ΔT across the thermal sublayer, commonly referred to as the "cool skin" of the ocean (compare Fig. 2).

The high temperature resolution of state-of-the-art infrared imagers allows measurements of the temperature fluctuations at the ocean surface even under low natural net heat flux conditions (Schimpf et al. 1999). The net heat flux density j_h, skin-bulk temperature difference ΔT and the characteristic time constant t^* of the transfer process are related by the transfer velocity for heat, k_h, according to (Jähne et al. 1989):

$$k_h = \frac{j_h}{\rho\, c_p \Delta T} = \sqrt{\frac{D_h}{t_*}}\,, \tag{1.1}$$

where D_h denotes the molecular diffusion coefficient for heat in water. Given the net heat flux density, the local heat transfer velocity is determined by measuring the skin-bulk temperature difference across the ther-

mal sublayer. From the heat transfer velocity, the transfer velocity of an arbitrary gas is estimated using the so-called "Schmidt number scaling" (Jähne and Haußecker 1998):

$$\frac{k_g}{k_h} = \left(\frac{Sc_h}{Sc_g} \right)^n \tag{1.2}$$

with the Schmidt numbers Sc_h (heat) and Sc_g (gas) and the Schmidt number exponent n (2/3 for a smooth surface, 1/2 for a wavy). The large difference in the Schmidt numbers of heat (Sc = 7) and gas (Sc = 600 for carbon dioxide) might cast doubt whether the extrapolation is valid. However, detailed laboratory measurements have shown that the extrapolation is correct within a relative error of 10% provided that the uncertainty in the diffusion coefficient of the gas is less than 5% and the Schmidt number exponent is known with an absolute error less than 0.02 (Jähne et al. 1987).

3 Experimental Setup

The laboratory measurements were carried out in the small circular wind-wave facility (Fig. 3), located in the Institute of Environmental Physics, University of Heidelberg. This facility is gas tight and equipped with a ventilation system that controls the flush rate of the air space independently of the wind speed. The outer diameter of the flume is 4 m and the channel width is 30 cm. The flume is loaded with 872 litres of deionised water which corresponds to a water depth of 30 cm. Wind is generated up to 12 m/s by a rotating paddle wheel under the ceiling. A detailed description of the facility can be found by Schmundt et al. (1995). The water surface is observed via a mirror by the infrared camera system (see Fig. 1.3) and the imaged footprint at the water surface has a size of 20 by 20 cm. The infrared camera (Amber Radiance, Raytheon, Goleta, CA) has a 256 x 256 focal plane array and is sensitive in the wavelength regime from 3 to 5 μm with a noise equivalent temperature difference of 26 mK.

The field measurements were carried out in coastal and offshore waters south of Cape Cod, New England in July 1997 in the framework of the NSF-sponsored Coastal Ocean Processes study (CoOP97) conducted onboard the RV Oceanus. The main part of the setup combined an infrared camera, an infrared carbon dioxide laser and a temperature calibration device (Fig. 4).

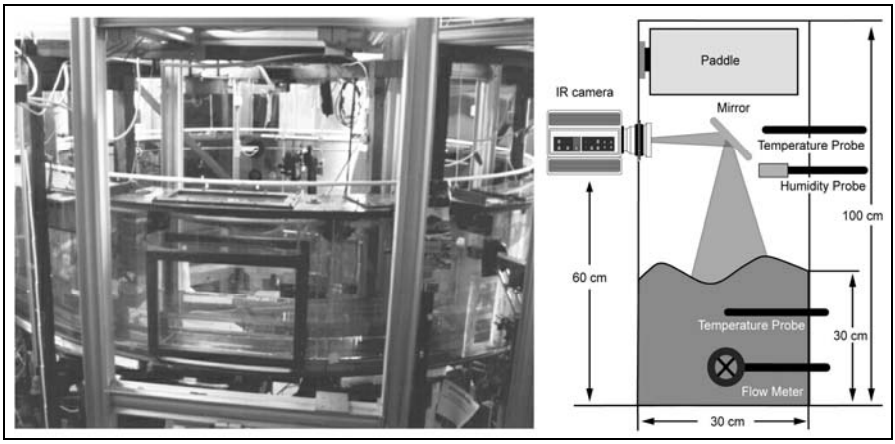

Fig. 3. Wind wave facility at the Institute of Environmental Physics, University of Heidelberg and schematic setup of the infrared imager at the flume

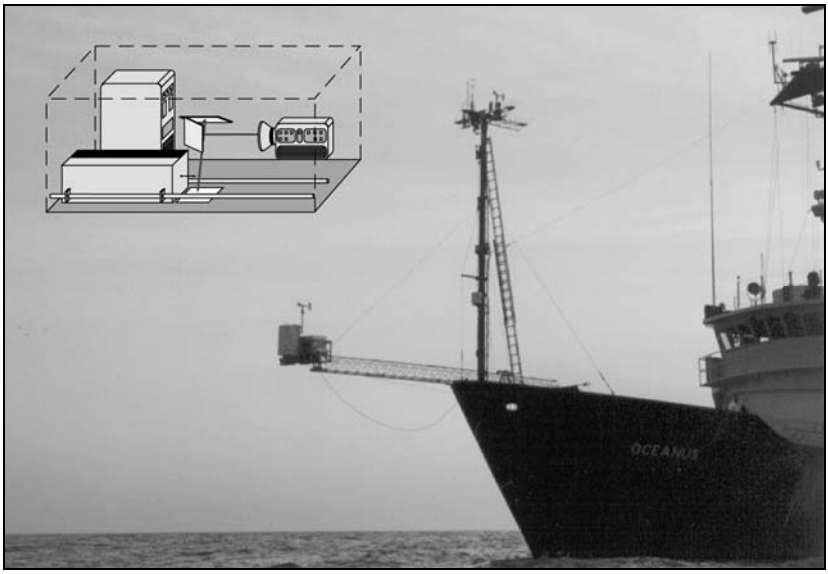

Fig. 4. Setup during the 1997 Coastal Ocean Processes Experiment in the Atlantic Ocean. The instrumentation was mounted on a boom at the bow of the research vessel

In order to achieve a reliable temperature resolution of 26 mK, the infrared camera had to be carefully calibrated with special designed blackbody. The geometrical arrangement of three different temperature standards and the reference bodies made the calibration box behave like an ideal black-

body. With this setup a relative temperature calibration was performed with a relative accuracy of the temperature measurement of approximately 30 mK (Schimpf, 2000). The entire instrumentation was mounted on a boom at the bow of the research vessel (Fig. 4).

4 Estimation of the skin-bulk temperature difference

In closed air circulation mode, no heat exchange between water and air is present. The relative humidity reaches nearly 100%, and the latent heat flux vanishes. The temperature in the air space of the facility quickly (approximately 1 minute) adjusts to the water temperature so that, in addition, the sensible heat flux is eliminated. Thus no net heat flux at the water surface is present and the bulk temperature is equal to the surface temperature (see Fig. 5).

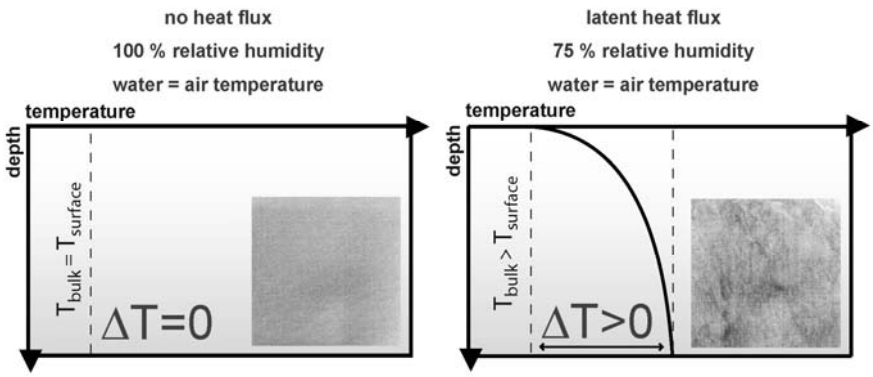

Fig. 5. Schematic of the two operational modes of the wind wave facility to estimate the skin-bulk temperature difference across the thermal sublayer

If the air space of the wind-wave flume is flushed with dry air (relative humidity approximately 75%), a latent heat flux is established through evaporation. The surface temperature drops a few tenth of a degree ("cool skin") and skin-bulk temperature difference is forced across the thermal sublayer.

For a duration of 50 minutes every 5 minutes, the air conditioning system of the facility is switched between these two conditions. Thus it is possible to determine an averaged skin-bulk temperature difference every 10 minutes. In the first mode the infrared imager records the bulk temperature, and in the second mode the surface temperature.

In the field, experimental problems arise from the fact that the net heat flux density at the water surface cannot be artificially controlled and thus only the surface temperature is directly accessible with the infrared camera and not the skin-bulk temperature difference required for estimating the transfer coefficient for heat. Practical implementations use the statistical properties of the sea surface temperature distribution assuming a surface renewal model (Schimpf et al. 1999) in order to estimate the skin-bulk temperature difference.

5 Results

Two conditions were realized in the wind wave facility: in the first set of experiments the interface was clean, whereas in the second set a surfactant (Triton-X-100, concentration: 3 ppm) was used. Image sequences of duration of 1 second (60 frames at 60 Hz) were recorded every 10 seconds for a time period of 50 minutes. This procedure was repeated at four different wind speeds. Using the controllable air ventilation system in the wind wave facility, the latent heat flux was switched on and off every 5 minutes. The net loss of heat at the water surface was determined by the rate of change of the overall water bulk temperature (Schimpf 2000).

Figure 6 shows the mean surface temperature (left) and variance of temperature (right) of the imaged footprint at the water surface versus time. When there is no heat exchange between water and air phase (closed air circulation mode), the temperature increases and temperature fluctuations at the surface no longer occur. The infrared camera detects the bulk temperature. The variance of the surface temperature is of the order of the noise level of the infrared imager. Immediately after the latent heat flux is switched on (open air circulation mode), the surface temperature drops down a few tenths of a degree and the patterns of near surface turbulence appear in the images. The variance in the temperature increases and is significantly above the noise level of the infrared imager (26 mK). The infrared camera now detects the surface temperature.

If a surfactant is present, the values of the skin-bulk temperature difference are higher than for a clean surface (Fig. 7, right). This is due to the fact that near surface turbulent mixing is generally dampened in presence of a surfactant. The values of the skin-bulk temperature difference also show a significant trend, decreasing rapidly with increasing wind speed, in line with the formation of capillary waves (Schimpf 2000). If the interface is clean, the values of the temperature gradient all are below 0.1 Kelvin and they do not alter significantly as the wind speed increases. This is the result of two competing effects at higher wind speed: enhanced turbulent

mixing (decreasing the skin-bulk temperature difference), and increasing net heat flux density at the water surface (increasing the skin-bulk temperature difference).

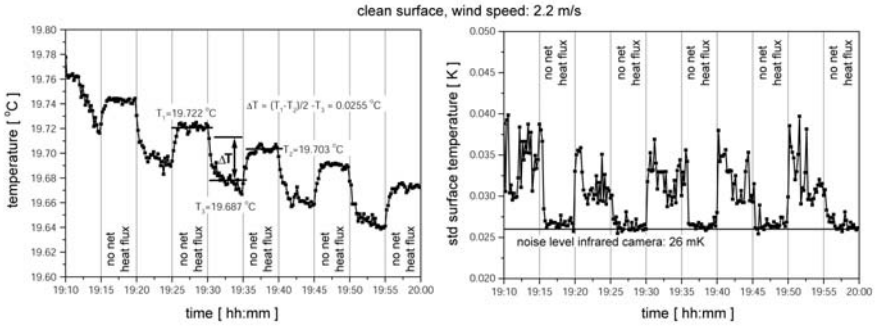

Fig. 6. Mean surface temperature (left) and variance (right) of the imaged footprint during one run of a duration of 50 minutes

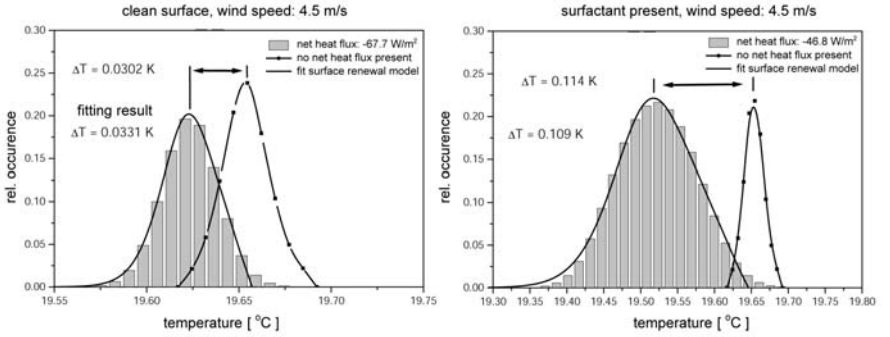

Fig. 7. Estimates of the skin-bulk temperature based on latent heat flux switching method and prediction of a fit assuming a surface renewal model

Given the net heat flux density at the water surface and the skin-bulk temperature difference across the thermal sublayer the heat transfer velocity was estimated according to Eq. 1.1. From heat transfer coefficients, gas transfer velocities were calculated using a Schmidt number of Sc = 600 (carbon dioxide at 20°C and Sc = 7 (heat at 20°C in Eq. 1.2). Figure 8 (left) shows the gas exchange rates in the Heidelberg wind wave facility plotted versus wind speed. The results are in good agreement with previous mass balance method (Eichkorn 1997), (Kandelbinder 1994) deployed

in the same facility and with the semi-empirical relationships from Liss and Merlivat (1986), and Wanninkhof (1992).

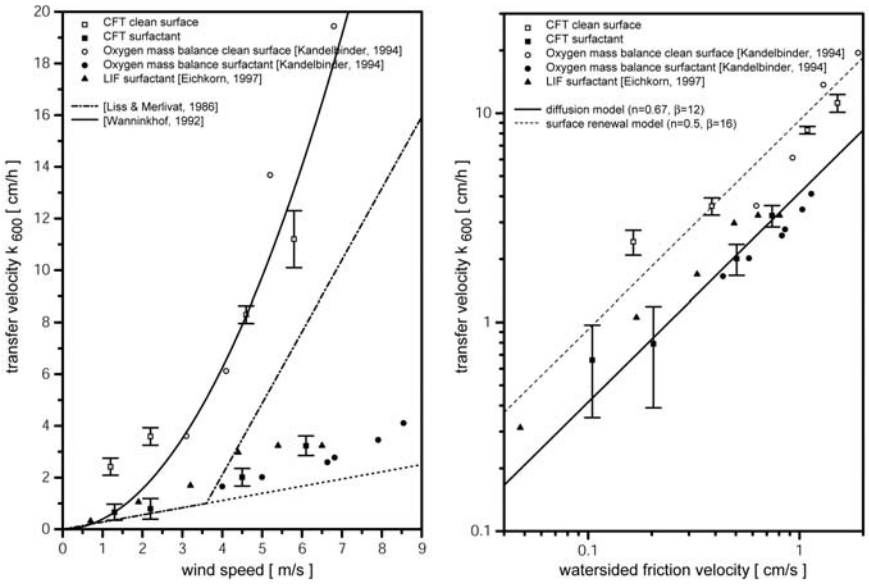

Fig. 8. Gas exchange rates in the Heidelberg wind wave facility: rates obtained from the passive controlled flux method compared with previous measurements

In Figure 8 (right) the transfer coefficients are plotted as a function of the waterside friction velocity. The theoretical curves for a smooth surface based on a diffusion model (Deacon 1977) and for a rough surface based on a surface renewal model (Danckwerts 1970) are also included. The theoretical curve for a smooth surface (no waves were visually observed) is in good agreement with the measurements when a surfactant was present. For a clean interface, the transfer coefficient follows the theoretical curve for a surface renewal model with a wavy surface.

The micro-scale temperature fluctuations at the water surface give a direct insight into the turbulent transport mechanism and the influence of surface chemical enrichments on near surface turbulence. Figure 9 shows two sequences of three consecutive infrared images of the water surface recorded at a wind speed of 2.2 m s^{-1}; one sequence was taken while the interface was clean, and the other while a surfactant was present. The formation of stationary temperature streaks at the water surface which are oriented parallel to the wind direction occur in both cases and result from organized turbulent structures close to the interface. In presence of the surfactant the “temperature” streaks seem to be more regularly oriented in the

wind direction in comparison to a clean interface (see figure 9). A strong surface film inhibits direct renewal of the water surface and modifies the length scale and orientation of near surface turbulence (Schimpf et al. 2004).

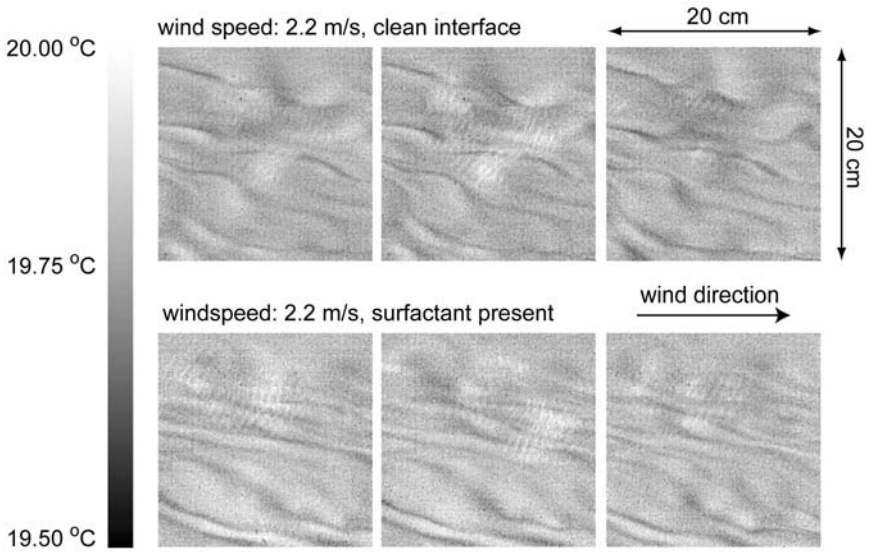

Fig. 9. Examples of the formation of stationary temperature streaks at the water surface which oriented parallel to the wind direction

Infrared observations of the effects of surface films on heat and gas transfer have been made *in situ* (Frew et al. 2004). Figure 10 (upper) shows the instrumented air-sea interaction catamaran LADAS operating within a banded surface slick during the CoOP97 study. Simultaneous infrared imaging and measurements of wave slope and surfactants outside and inside of the slick determined that, when the slick was entered, the surface temperature distribution shifted toward lower temperatures and the spatial scales of the temperature fluctuations at the sea surface increased (Fig. 10, lower), characteristic of reduced surface renewal and an attenuation of mixing in the aqueous boundary layer. The estimated temperature gradient increased from 0.13 Kelvin to 0.24 Kelvin and the net heat flux dropped from 77.2 Watt m^{-2} to 36.5 Watt m^{-2}. The 80% increase in ΔT and a 50% decrease in the heat flux lead to a decrease in the estimated heat transfer velocity from 49.7 cm h^{-1} to 13.1 cm h^{-1}.

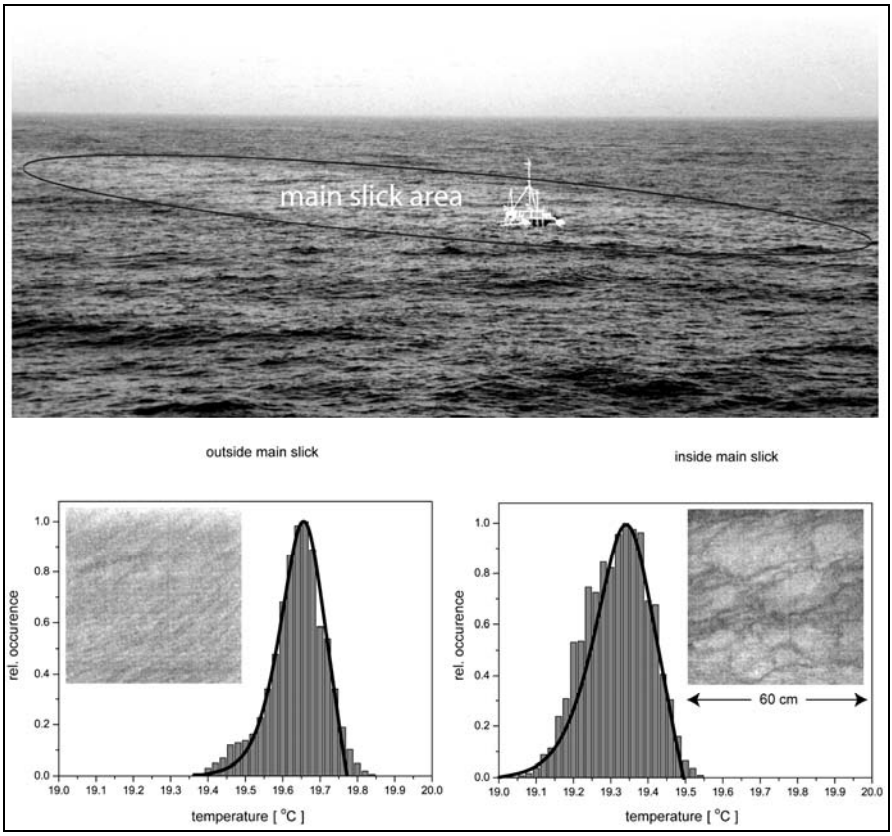

Fig. 10. LADAS catamaran is crossing a banded slick during the field measurements. Comparison of the temperature distributions of the two infrared images inside and outside the main slick

Schmidt number scaling of the heat transfer velocities according to Eq. 1.2 suggests nearly an order of magnitude reduction in the gas transfer velocity due to the slick (5.1 cm h^{-1} and 0.64 cm h^{-1} outside and inside the slick respectively) at a wind speed of 4 m s^{-1}.

6 Conclusions

Studies of the air-water gas exchange process by infrared imaging techniques enable local and fast measurements of the heat transfer velocity. Applying Schmidt number scaling, the obtained gas transfer velocities are consistent with mass balance methods and are in good agreement for the

theoretical prediction of the diffusion model for a film covered surface and a surface renewal model in case of a clean and wavy interface.

The transport of heat as is insensitive to bubble-mediated gas transfer, i.e., it measures the transfer rate of a gas with high solubility. In conjunction with measurement of other trace gases this feature might allow distinguishing between the different transport mechanisms governing air-water gas transfer.

Using heat as a proxy tracer for gases not only delivers the transfer coefficient at high spatial and temporal resolution but also gives direct insight into the spatial structure of near surface turbulence enabling detailed investigations of the influence of surface chemical enrichments on the gas transfer velocity and the turbulent transport mechanisms.

7 References

Danckwerts PV (1970) Gas-liquid reactions, McGraw-Hill, New York

Deacon EL (1977) Gas Transfer to and across an Air-Water Interface. Tellus 29: 363-374

Donelan MA and Wanninkhof R (2002) Gas Transfer at Water Surfaces – Concepts and Issues, in Gas Transfer at Water Surfaces, edited by M. A. Donelan, W. M. Drennan, E. S. Saltzman, and R. Wanninkhof, Geophysical Monograph 127, 1-10, American Geophysical Union

Eichkorn S (1997) Visualisierung und Quantifizierung des CO_2 Gasaustausches mittels laserinduzierter Fluoreszenz (LIF), master thesis, Institute for Environmental Physics, University of Heidelberg

Frew NM, Bock EJ, Schimpf U, Hara T, Haußecker H, Edson JB, McGillis WR, Nelson RK, McKenna SP, Uz BM and Jähne B (2004) Air-sea gas transfer: its dependence on wind stress, small-scale roughness and surface films. J Geophys Res 109: C08S17

Haußecker H (1996) Measurements and simulation of small scale exchange processes at the ocean surface, PhD thesis, University of Heidelberg

Haußecker H, Schimpf U, and Jähne B (1998) Measurements of the air-sea gas transfer and its mechanism by active and passive thermography. Proc. IGARSS '98, sensing and managing the environment, Seattle, WA, IEEE

Jähne B and Haußecker H (1998) Air Water Gas Exchange. Annual Reviews Fluid Mechanics 30: 443-468

Jähne B, Münnich KO, Bösinger R, Dutzi A, Huber W, and Libner P (1987) On the Parameters Influencing Air-Water Gas Exchange. J Geophys Res 92: 1937-1949

Jähne B, Libner P, Fischer R, Billen T and Plate EJ (1989) Investigating the transfer processes across the free aqueous viscous boundary layer by the controlled flux method. Tellus 41B: 177-195

Kandlbinder T (1994) Gasaustauschmessungen mit Sauerstoff, master thesis, Institute for Environmental Physics, University of Heidelberg

Liss PS and Merlivat L (1986) Air-sea gas exchange rates: Introduction and synthesis, in The Role of Air Sea Exchange in Geochemical Cycling, edited by P. Buat-Menard, 113-127, D. Reidel Publshing Co., Hingham, MA

Münsterer T and Jähne B (1998) LIF measurements of concentration profiles in the aqueous mass boundary layer. Experiments in Fluids 25: 190-196

Schimpf U (200) Investigations of Gas Exchange and Micro turbulence at the sea surface using infrared imaging. PhD thesis, University of Heidelberg

Schimpf U, Haußecker H and Jähne B (1999) Studies of Air-Sea Gas Transfer and Micro Turbulence at the Ocean Surface using Passive Thermography, in The Wind-Driven Air-Sea Interface, edited by M. L. Banner, University of New South Wales, 345-352

Schimpf U, Garbe S, and Jähne B (2004) Investigation of the transport process across the sea-surface microlayer by infrared imagery. J Geophys Res 109: C08S13

Schmundt D, Münsterer T, Lauer H and Jähne B (1995) The circular wind-wave facility at the University of Heidelberg, in selected papers from the third international symposium on air-water gas transfer, edited by B. Jähne and E.C. Monahan, Aeon Verlag & Studio, Hanau, Germany

Siddiqui MH, Loewen MR, Asher WE and Jessup AT (2004) Coherent Structures Beneath Wind Waves and their Influence on Air-Water Gas Transfer. J Geophys Res 109: C03024

Wanninkhof R (1992) Relationship between Gas Exchange and Wind Speed over the Ocean. J Geophys Res 97: 7373-7381

Wanninkhof R. and McGillis WR (1999) A cubic relationship between gas transfer and wind speed. Geophys Res Lett 26: 1889-1893

Chapter 4:

Remote Sensing Applications

Detection of oil spills by airborne sensors

Oliver Zielinski[1], Theo Hengstermann[2] and Nils Robbe[2]

[1]University of Applied Sciences Bremerhaven, Faculty of Technology, Marine Technology, Bremerhaven, Germany
[2]OPTIMARE Sensorsysteme AG, Bremerhaven, Germany

Abstract. Aerial surveillance of marine oil spills has become a multinational effort, especially for the deterrence of potential polluters and support of oil spill clean-up crews. For many years, the main effort has been directed towards developing sensors with enhanced spill monitoring capabilities. These sensors can be divided into different classes, namely basic sensors and advanced sensors including thermal imagers with active laser illumination. Recently, more attention has been paid to the automated derivation of high-level information from airborne remotely sensed multispectral oil spill data. In this paper, we present an algorithmic framework for automated analysis and fusion of multi-spectral oil spill data acquired by a near range sensor suite. It is shown how infrared/ultraviolet, microwave radiometer and imaging laser fluorosensor data can be converted into high-level information using single-sensor data processing and multi-sensor data fusion. It is also explained how this knowledge can, in combination with external information processing, improve the usability of the maritime surveillance system.

1 Introduction

Marine pollution by oil spills or harmful chemicals is still one of the major environmental problems to be faced. Besides the accidental releases of pollutants the main source is assumed from the controlled release by ship traffic and oil production platforms. Since accidents or violations of regulations can never be completely excluded, precautions and instruments are needed to detect and combat maritime pollutions and a crucial element of this framework is airborne surveillance. Like no other system, airborne pollution control is capable

a) to detect possible oil spills by radar sensors,

b) to verify, quantify and qualify reported pollutions by different near-range sensors,
c) to secure evidence against polluters and
d) to coordinate clean-up operation of ships.

Many nations have established such kind of airborne surveillance and also dense networks of international co-operations, since oil spills are not restricted to national borders. One example is the Bonn agreement of 1983, establishing a trans-border observation between the North-Sea adjacent states (see http://www.bonnagreement.org/).

During the last three decades airborne remote sensors have evolved into common instruments for the operational surveillance of oil pollutions (Goodman 1994, Fingas and Brown 2002, Zielinski 2003). Today's mostly used sensor suites include a side looking airborne radar and an infrared/ ultraviolet detector together with visual observation and video systems.

In addition to this standard, there are more sophisticated sensors like the laser fluorosensor or the microwave radiometer that allow an advanced analysis of oil spills concerning the remote identification of oil species and the estimation of film thickness. Recently thermal imaging systems with a covert action laser illuminator or an image intensifier started operation, enabling the operator to read the ships name in the absence of daylight or investigate areas of specific interest. This thermal imaging capability brings an important step towards night operation and polluter identification. Within this paper status and perspectives of airborne oil pollution monitoring and its available sensors will be presented. This includes the description of synergetic effects that arise from the use of a multi-sensor system and the combination with external information sources.

2 Basic airborne sensor equipment

The simplest and most direct method of surveillance and tracking oil spills is visual observation and hand plotting of the data on a map. It requires no costly installations, however, it is not suitable for night operation and needs skilled observers. Since the spectral characteristics of oil differ from the surrounding water especially in the ultraviolet and above 3 µm (mid-infrared) up to 30 cm (radar) wavelength, remote sensing equipment mainly focuses on the non-visible electromagnetic regions.

The most commonly used sensor arrangement includes a SLAR (side looking airborne radar) and an IR/UV (infrared/ultraviolet) detector. In order to give an example from 2004: Among the 8 contracting parties of the Bonn agreement, contributing 14 aircrafts in total, all platforms were

equipped with a SLAR and all but one were using IR/UV sensors for the near-range investigation.

The SLAR sends out X-band radar pulses to the left and right hand side of the aircraft and receives their reflection from small gravity and capillary waves up to a distance of typically 40 km, depending on wind conditions and aircraft altitude. These small waves are suppressed when an oil-film is on the surface (Figure 1). Yet a number of other conditions can lead to false returns that are difficult to distinguish from that of oil on the water, among them algae blooms, freshwater fronts, sand banks and wind shadows. These natural sea slicks are discussed in detail within Hühnerfuss et al. (1986), their potential discrimination by multi-frequency radar is discussed for example in Hühnerfuss et al. (1994) or Gade et al. (1998). These possible false returns are also one reason why satellite observations are not sufficient as a stand-alone tool and it is the task of the near range sensors to identify the origin of the missing radar signal area.

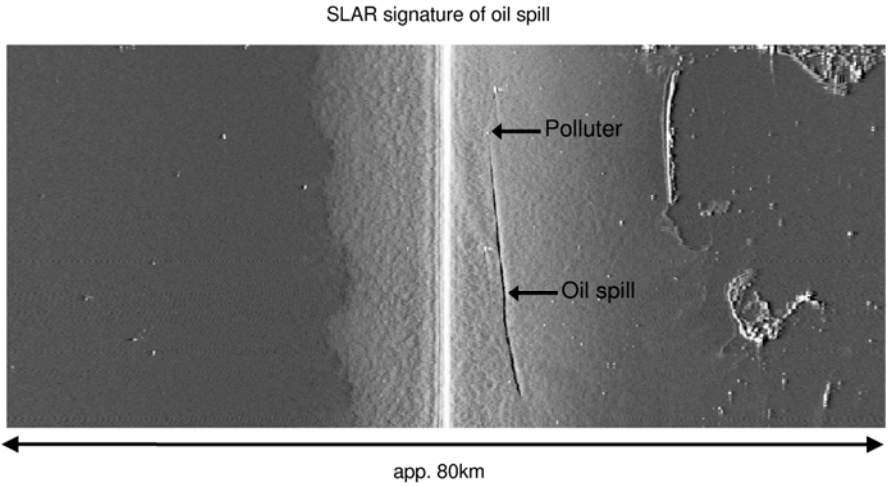

Fig. 1. Non-rectified SLAR image of a sea area showing an oil spill as well as the corresponding polluter. The aircraft track is in the middle of the image

The basic near range sensors are the infrared and ultraviolet detectors, often coming together as IR/UV-sensor, in most cases in a line-scanner (LS) assembly. The IR/UV-LS is a passive bi-spectral remote sensor that is sensitive in the thermal infrared (TIR) between 8 and 14 μm and in the near ultraviolet (NUV) between 0.32 and 0.38 μm. At an aircraft altitude of 300 m its swath width amounts to approximately 500 m. This sensor on the one hand is used to measure the thermal emission of the sea surface in the TIR and on the other hand serves for the detection of highly reflecting

features of the sea surface in the NUV. In general, the oil/air interface exhibits a lower integral emissivity in the TIR than the water/air interface. For this reason those areas of an oil spill, being in thermal equilibrium with the underlying water surface and slightly exceeding a specific limit of detection, appear colder in the TIR than the surrounding sea surface. However, very thick oil layers may be heated by the sun and thus appear as hot spots in TIR images. The infrared line-scanner can be used during both day and night time. By the way of contrast, the usability of the ultraviolet sensor requires daylight conditions because it measures the global NUV radiation reflected by the sea surface. The detection of oil spills in the NUV is based on the fact that the oil/air interface shows a higher integral NUV reflectivity than the water/air interface. The lower TIR and NUV detection limits of oil on water differ substantially. While in the NUV the minimum detectable oil thickness lies in the sub-micron range, the corresponding thickness threshold in the TIR amounts to a few tens of microns. For this reason the IR/UV-LS is used to map the total extent of the oil spill and those portions that are of intermediate or large oil thickness (Figure 2). The IR/UV-LS is probably the most important near-range remote sensor for the oil spill operator since it provides high-resolution imagery information on relative oil thickness.

3 Advanced sensors

In addition to the above described standard there are more sophisticated sensors like the laser fluorosensor (LFS) or the microwave radiometer (MWR) that allow an advanced analysis of oil spills concerning the remote identification of oil species and the quantification of film thickness. The two German maritime surveillance aircrafts are examples of operationally used pollution control systems incorporating the above-mentioned wide range of remote sensors (Figure 3). Other nations operate comparable systems or are at the step of defining new airborne systems, incorporating these advanced sensors for the second generation of maritime surveillance aircraft.

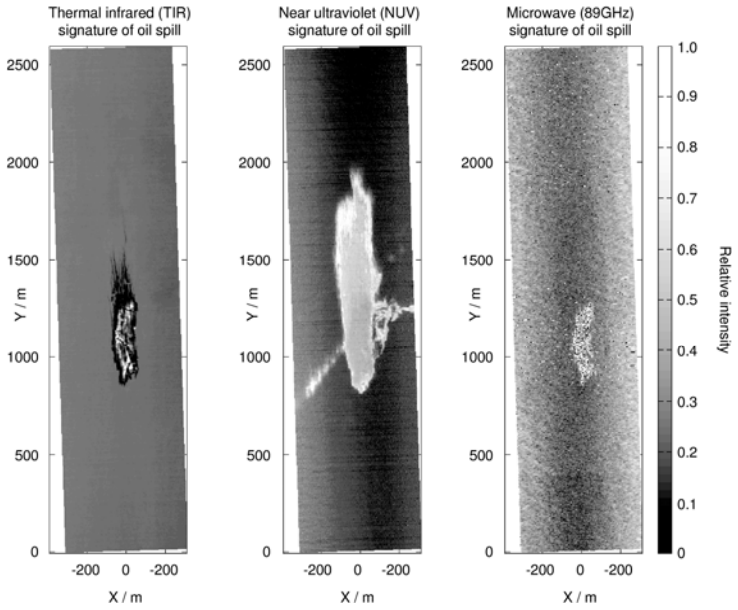

Fig. 2. From left to right: Thermal infrared, near ultraviolet and passive microwave (89 GHz) signatures of an oil spill (all data rectified)

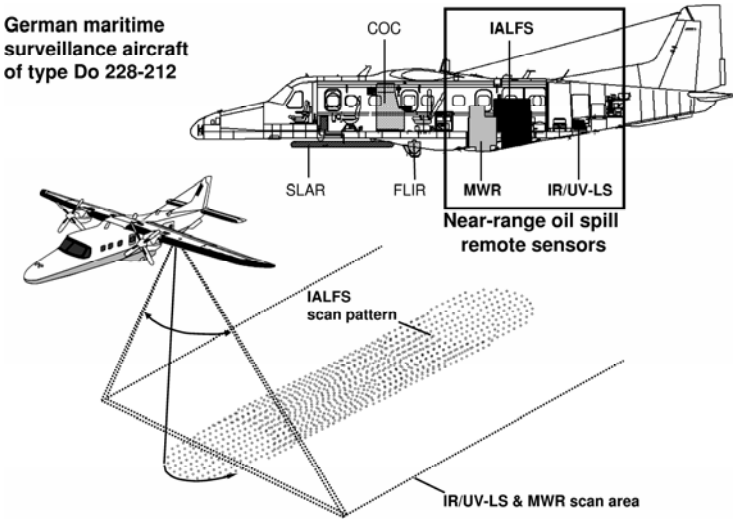

Fig. 3. Near-range remote sensors of the German maritime surveillance aircraft and their spatial coverage. Also shown are the SLAR as a far-range sensor, the central operating console (COC) and the forward-looking infrared imaging system (FLIR) for ship identification

The Imaging Airborne Laser Fluorosensor (named IALFS) as one of the most complex and also quantitatively measuring remote sensing instruments operated on an aircraft is an active laser-based sensor which sends short (~20 ns) high energy UV laser pulses towards the water surface (Hengstermann and Reuter 1990). This device is based on a XeCl excimer laser with an output wavelength of 308 nm. The laser-induced scattering and fluorescence is detected using a 20 cm telescope and spectrally separated into 12 channels (Figure 4). The IALFS performs a conical scan of the sea surface and thus provides information on the spatial distribution of fluorescent and attenuating matter. At a platform altitude of 300 m this device has a swath width of app. 180 m. The fundamental principle of laser fluorosensing of oil spills is given by the fact that crude oils and various refined crude oil products can be photochemically excited by UV radiation and classified by (remotely) analysing the spectral distribution of the resulting fluorescence. Laser fluorosensors are still the only instruments that can accomplish a remote classification of oil spills. Another feature of these instruments is the estimation of oil thickness in the range between app. 0.1 and 10 µm, depending on the type of oil and other parameters. In addition, the laser fluorosensor may be used for hydrographical measurements (Zielinski et al. 2000).

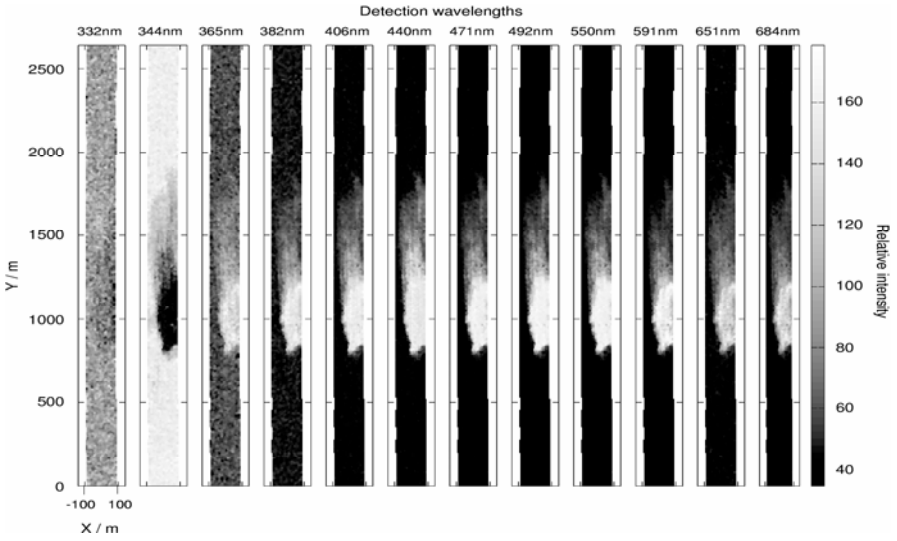

Fig. 4. 12-channel imaging airborne laser fluorosensor signature of spilled crude oil (all data rectified). The channel #2 (344 nanometres) shows the suppression of the laser-induced water Raman backscatter signal through the strongly absorbing oil film. This information can be used for thickness estimation

The line scanning Microwave Radiometer (MWR) enables quantitative assessments of detected oil spills by analysing the radiant emission from the sea surface and oil spills at two or three frequencies (for example 18.7, 36.5 and 89 GHz, see also Figure 2). The microwave emissivity of the oil/air interface is higher than that of the water/air interface and depends on the microwave frequency, oil thickness, and sea state. The three-channel information acquired by the MWR can be used to calculate a thickness estimate for very thick oil layers being of the order of millimetres in thickness (between 50 µm and 5 mm, Grüner et al. 1991). This information is absolutely necessary for clean up operations and the guiding of oil combat vessels. Since microwaves can penetrate clouds, rain, fog and drizzle, the MWR is an all-weather remote sensor with a high potential for multi-mission reconnaissance and surveillance applications.

4 Thermal imaging

Since thermal imagers, also known as Forward Looking Infrared (FLIR) devices, became commercially available, they are increasingly installed into smaller and mid-size aircraft. In 2004 a StarSAFIRE thermal imaging system with a newly developed covert action laser illuminator (CALI) started operation as part of the second German surveillance aircraft, enabling the operator to read the ships name in the absence of daylight or investigate areas of specific interest. This thermal imaging capability brings an important step towards night operation and polluter identification. The FLIR is also a sensor with a wide range of application, like search-and-rescue or border patrol, making it a perfect device for multi-role aircraft, sometimes only equipped with basic maritime surveillance sensors.

The covert illuminator is a 2 Watt laser diode inside the FLIR turret, radiating around 800 to 820 nm @ 25°C. Therefore the CALI is not illuminating the thermal camera detector (which is using the 3-5 µm mid-IR region), but the NIR sensitivity of the inbuilt CCD camera. These cameras normally use an IR-cut filter during daytime, blocking unwanted NIR radiation from its detector. During nighttime and in combination with the CALI, this NIR cut filter is removed and the laser illumination is available up to a distance of 1500 m (Figure 5).

FLIR devices can be divided in two classes by their detecting waveband. Mid-IR detectors, like the StarSAFIRE series mentioned above, are commonly used in humid environments since they show less signal depression by water vapour. However the detection of oil spills shows variable results and is not favourable as a stand-alone sensor for this purpose. Long-IR detectors (8-14 µm, sometimes realised by QWIP detectors with smaller

bandwidth) show nearly comparable detection capabilities as infrared line-scanners. In combination with geo-referencing and geo-locate-and-hold features offered by state off the art devices, they provide a high quality video guidance for the airborne operator and, via data-downlink, for the spill combating vessel. Used in nadir mode, long-IR FLIR devices can even be used as a virtual IR line-scanner. This combination of a SLAR long range detection and a FLIR with oil detection capabilities, its video cameras, autotracking and positioning features as well as (digital) video recording is a two-device approach that is particularly of interest for smaller and mid-size aircraft.

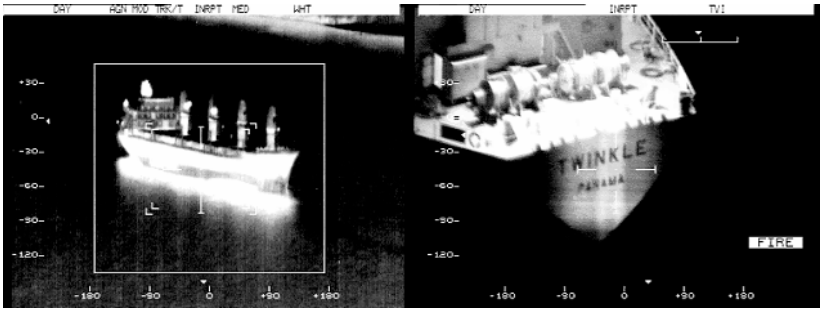

Fig. 5. Results from the covert action laser illuminator (CALI) inside a FLIR turret in combination with a NIR-sensitive CCD camera. **Left:** Approaching the vessel using the thermal camera (mid-IR) and the autotracker. **Right:** Laser-illuminated stern of the ship, supplied by the CCD camera with disabled NIR-cut filter. The images were taken during an exercise in Portland, Oregon with ships abiding by the regulations

5 Automated scene analysis and data fusion

Routine oil pollution monitoring with advanced remote sensing equipment requires a complex network and communication structure to be operated by a single operator. The combination of different data sources towards higher-level products is crucial in two ways: First, the operator is struck by the amount of data to evaluate and needs guidelines, alarm triggers and synergetic overviews. Second, the combination of different sensors increases the probability of qualitative and quantitative predictions of the substances observed. Both aspects, combined with the incorporation of external data sources, will lead the way to the third generation of airborne maritime surveillance systems.

One of the major problems to overcome is the diversity of different sensors, resulting in varying sampling rates, different sensor geometries, swath widths and different data formats. The direct comparison of sensors like IR/UV and laser fluorosensor for the evaluation of an oil spill or in the case of larger quantities, IR/UV and microwave radiometer requires a good understanding of the sensor characteristics, capabilities and restrictions. Such an understanding may not be suitable for the routine operation by none-scientifically trained personnel. Therefore, it is intended to evaluate sensor data automatically and create results in such a way that an assessment may be accomplished by operators that are not necessarily familiar with all sensor characteristics and details. One step forward in such a concept is the generation of a synthetic image from the various sensor images which allows much faster interpretation of sensor data because there is only one image visually describing the whole and often complex situation over an oil spill. It is important to provide such investigative tools in real time because it is obvious that evaluation and assessment of damages, resulting in possible clean up operations, have to be made immediately.

5.1 Internal data processing

Next, the Oil Spill Scene Analysis System (OSSAS) is presented (Robbe and Zielinski 2004, Robbe 2005). The task of OSSAS is the fully-automated generation of the requested high-level information onboard the surveillance aircraft. This kind of data processing is hereby defined as *internal data processing*. In the case of the present application, the term 'end-user' comprises the airborne sensor operator, the response crew at sea and responsible authorities. Any further use of the internally derived high-level information outside the surveillance aircraft is defined as *external information processing*.

The overall functional diagram in Figure 6 illustrates the principal structure of OSSAS. According to the diagram, IR/UV-LS data are of central importance for the function of the analysis system. This is true because the IR/UV-LS is probably the most important near-range remote sensor for the oil spill operator since it provides high-resolution imagery information on relative oil thickness. While the thermal infrared (TIR) component of the IR/UV-LS is used for visualizing thick oil, the corresponding NUV component is used for mapping the total extent of the oil spill. IR/UV-LS data are, therefore, considered as primary input for OSSAS. MWR and IALFS data as well as external model input and data originating from other sensors are considered as secondary input for the analysis system. The output of OSSAS is shown in the bottom part of the overall functional diagram. It includes the desired set of high-level information.

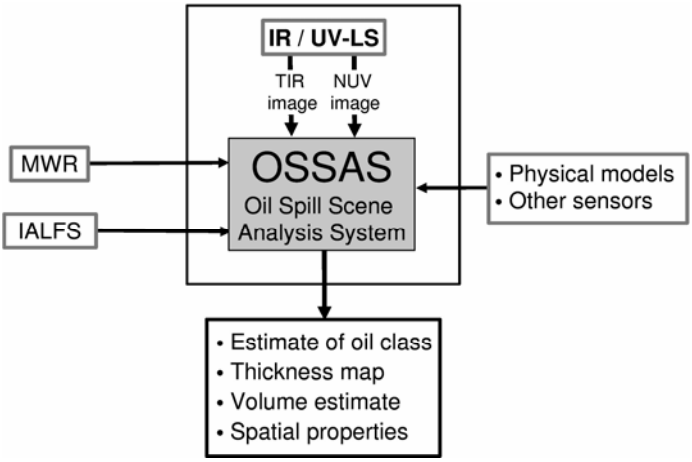

Fig. 6. Overall functional diagram of the Oil Spill Scene Analysis System (OSSAS)

5.2 Feature extraction and spatial analysis

The most important part of OSSAS is a processing chain for the robust extraction of oil spill features from IR/UV-LS data (TIR and NUV images). This processing chain consists of four steps (Figure 7 from top to bottom). The first step is an image enhancement applied to the original images prior to the subsequent image segmentation. The segmentation of the enhanced images (second step) is performed using the extended 2 D *locally excitatory globally inhibitory oscillator network* (LEGION) algorithm (Chen et al. 2000). Originally, LEGION was motivated by neurophysical concepts on brain functions and feature binding (Terman and Wang 1995). Chen et al. (2000) introduced an extended version of LEGION that is based on a specific weight adaptation scheme. They successfully applied their version of LEGION to artificially created images as well as to satellite images for the extraction of hydrographic features and magnetic resonance images.

The feature extraction chain of OSSAS is based on this version of LEGION. The image enhancement (first step) turned out to be necessary because the LEGION algorithm tends to extract high intensity features such as hot spots in TIR images and highly reflecting sheens of oil in NUV images. The fourth step is responsible for the labelling of the different subsegments 'recognised' by LEGION. The labelling step is based on the segmentation program 'region' by Koethe (2003). In connection with this labelling process all sub-segments are related to their mean pixel value. Finally, the well-known unsupervised K-means clustering algorithm is used

for assigning the sub-segments to either the signature of the oil spill or the residual area. The results of the feature extraction chain are binary representations of the associated raw images. These binary images hence are called *segment maps*.

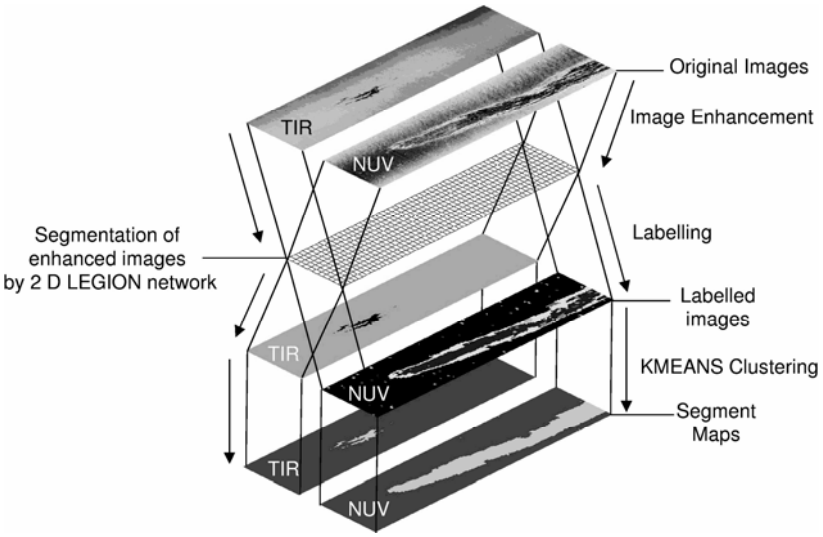

Fig. 7. Feature extraction chain (from top to bottom) of the Oil Spill Scene Analysis System

The extracted spill segments can be easily analysed concerning their spatial properties. The spatial characterisation implemented in OSSAS is capable of computing the area, the centre of area, the tilt and the length/ width ratio of each segment. The latter two properties are especially useful for describing an oil spill in terms of its spreading direction and shape, respectively. They are determined by fitting ellipses to the convex hulls of the segments. The algorithms used for this purpose are robust and documented (Barber et al. 1996, Fitzgibbon et al. 1999). Moreover, the fusion of the TIR and NUV segment maps allows the detection of thermal hot spots (due to thick oil) and the automated discrimination between thermal hot spots and ships. This kind of classification is possible because ships are usually poor reflectors in the NUV. On the basis of modelled and reported detection limits (Robbe 2005) the extracted thermal and ultraviolet features are used for the calculation of a minimum volume estimate. This estimate is part of a decision scheme for volume estimation based on IR/UV-LS, MWR, IALFS and fused NUV/IALFS information.

5.3 NUV/IALFS fusion and composite image generation

The NUV signature of an oil spill exhibits more or less intense brightness gradients that are correlated with the thickness and the complex refractive index of the spilled oil. A spatially inhomogeneous optical thickness of the oil spill is associated with a spatially inhomogeneous transmission of the water-leaving radiance through the oil film. In addition, changes in the surface reflectance of the oil film may also contribute to the observed brightness gradients. It was shown on the basis of field data that NUV images can be calibrated with IALFS data to give the *lidar optical thickness* $\kappa_{o,\,l}$ of the oil spill (Robbe and Zielinski 2004, Robbe 2005). The lidar optical thickness $\kappa_{o,\,l}$ is directly proportional to the thickness of the oil film. The IALFS-based measurement of $\kappa_{o,\,l}$ corresponds to an excitation wavelength of 308 nm and a detection wavelength of 344 nm (centre wavelength of the water Raman band). So far, information on lidar optical thickness has only been available within the field of view (FOV) of the IALFS, i.e. FOV = 28.4°. The proposed calibration procedure extends the measurement and visualisation of lidar optical thickness to the FOV of the IR/UV-LS, i.e., FOV = 87.3°. This is not only beneficial for visualisation, but also for enhanced volume estimation. Figure 8 shows a fused NUV/ IALFS image of lidar optical thickness overlaid with extracted thermal and ultraviolet features. This is the thickness map generated by OSSAS; all essential information required by the airborne sensor operator is integrated in a single map.

6 External information processing

The high-level information products derived onboard the surveillance aircraft are not only useful for the airborne sensor operator. They are also beneficial for decision and response mechanisms on shore and at sea. The use of the internally derived high-level information outside the surveillance aircraft is defined as *external information processing*. The relay of tactical information to ground stations is possible via data downlink. In this context, it is beneficial that the generated high-level information requires much less memory than the original raw data.

6.1 Internet-based GIS in airborne oil spill remote sensing

Geographical Information Systems (GIS) are instruments for management, display and statistical analysis of geographic information. They turned out to be useful for many scientific and commercial applications. The use of GIS technology for the visualisation of remote sensing data and associated

information products is predestined for oil spill response. However, it is important that the pollution information is available to all parties involved in the response mechanism. This leads directly to the use of internet-based GIS. The development of an internet-based GIS as a decision support tool for marine monitoring of water quality and pollution has been subject of the European RTD project DISMAR from 2002 to 2005. The first prototype is an OpenGIS compliant marine information management system called DISPRO. Figure 9 shows an orthorectified SLAR image displayed on the Web Map Server interface. The SLAR image was acquired by the German maritime surveillance aircraft, serial number 57+01, over the Meldorf Bight area, Northern German Wadden Sea. The DISPRO system is capable of integrating any type of georeferenced information. Examples are remote sensing data (satellite, aircraft, etc.), *in situ* data (e.g., autonomous moored and drifting platforms), model simulations (oil drift, phytoplankton blooms, etc.) and associated information products.

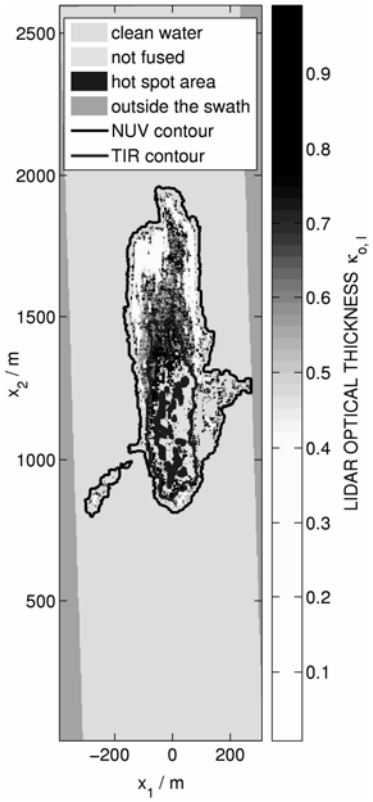

Fig. 8. Fused NUV/IALFS image of lidar optical thickness overlaid with extracted thermal and ultraviolet features (all data rectified)

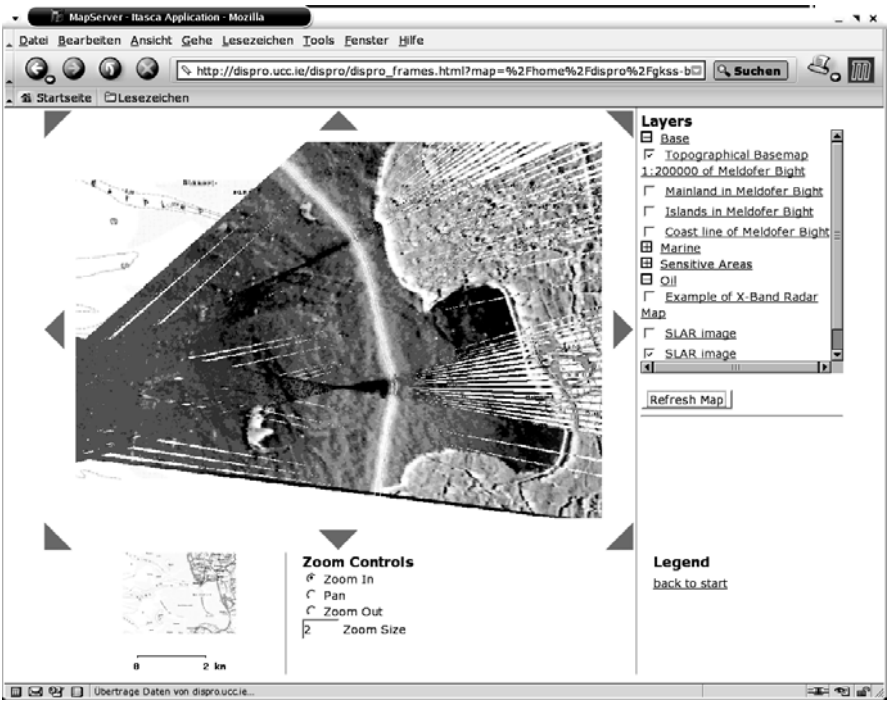

Fig. 9. Web map server interface showing an orthorectified SLAR image

6.2 AIS – automated identification systems

Automatic Identification Systems (AIS) were introduced for vessel traffic control and represent a ship-based broadcast system operating in the VHF maritime band. Apart from ship-to-ship and ship-to-shore AIS systems there are airborne AIS transponders that make dynamic vessel information available to airborne surveillance platforms. Examples of information provided by airborne AIS are: time, position, heading, course, speed, IMO number, destination, type of cargo and estimated time of arrival. This information is of general interest in airborne maritime surveillance, including search and rescue operation and oil spill monitoring. Especially the GIS integration of AIS information as well as its online visualisation onboard the surveillance aircraft are considered beneficial for oil spill response since it allows the identification of potential polluters.

7 Conclusions

Looking at the present state of marine pollution remote sensing it was outlined that basic and advanced sensors are available for an effective airborne surveillance. While the basic sensors (SLAR, IR/UV) are currently installed in nearly every platform, the advanced sensors (LFS, MWR) are only present at a few, dedicated aircraft. However this is likely to change, since several nations are at the step of defining new sensor systems in the next years. Within these system upgrades, FLIR thermal imagers with a laser illuminator will be prominent, since they offer

a direct support in securing evidence against polluters at night and
a wide range of applications, making them perfect for multi-role aircraft.

The need for operator support by means of data reduction and fusion was identified and steps towards this approach have already been accomplished by the Oil Spill Scene Analysis System (OSSAS). The overall objective of this research project is to develop an advanced (intelligent) information system for monitoring and forecasting the marine environment to improved management of pollution crises in coastal and ocean regions of Europe. It brings all types and sources of data together (satellites, aircraft, costal radar, ships) in one IT platform and provides (fusion) tools for the extraction of value-added information. On a bigger scale this reflects also the future of airborne surveillance. Utilising improved bi-directional communication links, database information from harbours together with latest satellite reports will be available online. Increased computational resources on-board and advanced algorithms will support the operator in its complex tasks, providing the basis for rapid man-made but machine-aided decisions. And in return, using feature extraction and fused images, preanalysed airborne sensor information on oil quantities, types and possible origins can be transmitted while in flight to land or ship based command centres, supporting the combat against the dangers of world-wide ship traffic.

Acknowledgements. The authors thank the German Ministry of Transport, the Central Command for Maritime Emergencies and the Federal Institute for Hydrology for their support and express their gratitude towards the co-operative staff of the 3rd Naval Air Wing „Graf Zeppelin“. This work was supported by the EU project DISMAR under contract number IST-2001-37657.

8 References

Barber CB, Dobkin DP, Huhdanpaa H (1996) The Quickhull Algorithm for Convex Hulls. ACM Transactions on Mathematical Software 22: 469-483

Chen K, Wang D, Liu X (2000) Weight Adaption and Oscillatory Correlation for Image Segmentation. IEEE Transactions on Neural Networks 11: 1106-1123

Fingas MF, Brown CE (2002) Review of oil spill remote sensors. Proceedings of the 7th International Conference on Remote Sensing for Marine and Coastal Environments, Miami, Florida

Fitzgibbon W, Pilu M, Fisher RB (1999) Direct least-squares fitting of ellipses. IEEE Transactions on Pattern Analysis and Machine Intelligence 21: 476-480

Gade M, Alpers W, Hühnerfuss H, Masuko H, Kobayashi T (1998) Imaging of biogenic and anthropogenic ocean surface films by the multifrequency/multipolarization SIR-C/X-SAR. J Geophys Res 103: 18851-18866

Goodman R (1994) Overview and Future Trends in Oil Spill Remote Sensing. Spill Science & Technology Bulletin 1: 11-21

Grüner K, Reuter R, Smid H (1991) A New Sensor System for Airborne Measurements of Maritime Pollution and of Hydrographic Parameters. GeoJournal 24: 103-117

Hengstermann T, Reuter R (1990) Lidar Fluorosensing of Mineral Oil Spills on the Sea Surface. Applied Optics 29**:** 3218-3227

Hühnerfuss H, Alpers W, Richter K (1986) On the discrimination between crude oil spills and monomolecular sea slicks by airborne radar and infrared radiometer - possibilities and limitations. Int J Remote Sensing 7: 1001-1013

Hühnerfuss H, Garrett WD, Hoge FE (1986) The discrimination between crude oil spills and monomolecular sea slicks by an airborne lidar. Int J Remote Sensing 7: 137-150

Hühnerfuss H, Gericke A, Alpers A, Theis R, Wismann V, Lange PA (1994) Classification of sea slicks by multi-frequency radar techniques: new chemical insights and their geophysical implications. J Geophys Res 99: 9835-9845

Koethe U (2003) Generic Programming for Computer Vision. The Vigra Computer Vision Library Version 1.2.0, Cognitive Systems Group, University of Hamburg, Germany

Robbe N (2005) Airborne Oil Spill Remote Sensing: Modelling, Analysis and Fusion of Multi-spectral Data. Institute of Experimental Physics, PhD Thesis, University of Hamburg, Germany

Robbe N, Hengstermann T, Zielinski O, Cembella B (2005) Automated analysis and fusion of multi-spectral data in airborne oil spill remote sensing. Proceedings of the 8th International Conference on Remote Sensing for Marine and Coastal Environments, Halifax, Canada

Robbe N, Zielinski O (2004) Airborne remote sensing of oil spills – analysis and fusion of multi-spectral near-range data. J Mar Sci Enviro C.2: 19-27

Terman D, Wang D (1995) Locally excitatory globally inhibitory oscillator networks. IEEE Transactions on Neural Networks 6: 148-176

Zielinski O (2003) Airborne pollution surveillance using multi-sensor systems. Sea Technology 44: 28-32

Zielinski O, Andrews R, Göbel J, Hanslik M, Hunsänger T, Reuter R (2000) Operational Airborne Hydrographic Laser Fluorosensing. Proceedings of the 4th EARSeL Workshop on Lidar Remote Sensing of Land and Sea, Dresden

Zielinski O, Hengstermann T, Mach D, Wagner P, Steinhage A, Winkel C (2001) Multispectral information in operational marine pollution monitoring: A data fusion approach. Proceedings of the 5th International Airborne Remote Sensing Conference, San Francisco

Satellite monitoring of accidental and deliberate marine oil pollution

Guido Ferraro, Dario Tarchi, Joaquim Fortuny, and Alois Sieber

European Commission - Directorate General Joint Research Centre,
Ispra, Italy

Abstract. The present activities of the Joint Research Centre (JRC), a Directorate General of the European Commission, in the field of monitoring sea-based oil pollution are described. The methodology used to process and interpret a massive set of satellite images (i.e., mosaics over all European Seas) and the relevant legal framework are briefly introduced. Both the issues of accidental and deliberate oil discharges are addressed. The presentation then focuses on JRC experience acquired on the use of satellite images during the Prestige accident emergency in 2002. At that time, the JRC provided technical assistance on the interpretation of the satellite images to the EC Civil Protection Mechanism and interested EU Member States. In addition to this task, JRC is carrying out a systematic mapping of the illicit vessel discharges using mosaics of satellite images over all the European Seas. These maps and the associated statistics are repeated on an annual basis in order to assess its evolution. The results obtained for the Mediterranean and the Black Sea are of special interest due to the lack of a regular aerial surveillance as that in the North and in the Baltic Sea. This action helped to reveal for the first time the dimension of the oil pollution problem, thus stressing the need for more concerted international actions. Finally, a strategy to tackle this issue is presented. In this context, the need for additional research efforts involving the competent regional/national authorities and the importance of securing the role of space-borne sensors in support to aerial and naval means are outlined. The proposed strategy is based on the involvement of the end-users. Consequently, the JRC together with DG Environment has established a permanent Group of Experts on satellite monitoring of sea-based oil pollution.

1 Setting the scene

1.1 The use of satellite imagery to detect oil pollution at sea

Oil spills originated from land-based or sea-based sources are causing damage to the marine environment. Sea-based sources are discharges coming from ships or offshore platforms. Among the different tools for monitoring such oil spills are the use of airplanes and also images from satellites equipped with Synthetic Aperture Radar (SAR).

In the context of monitoring of marine oil pollution, satellite images are currently used for the following applications:

1. Support response operations in case of maritime accidents (see as an example the Prestige case);
2. Providing an early warning of possible threats to coastal areas in time to take counter-measures;
3. Detecting and deterring illegal discharges from sea-based sources;
4. Measuring the state of European seas - means, variations, trends, to inform policymaking and assess the success or otherwise of action taken.

It must be noted that the first three applications are complementary to aerial surveillance traditionally used by national Coast Guards and require a near real time service (i.e., “dynamic” use of the images), while for the fourth one, the images can be analysed in a “static” way.

1.2 Identification of Oil Spills in SAR Images

The possibility of detecting an oil spill in a SAR image relies on the fact that the oil film decreases the backscattering of the sea surface (Alpers and Hühnerfuss 1989) resulting in a dark feature that contrasts the brightness of the surrounding spill-free sea. The analysis of this basic fact needs to start from a description of the different mechanisms responsible for the sea surface radar backscattering, which strongly depends on the incidence angle of the radar platform. In a quite large range of angles, approximately from 20 to 85 deg, the angular span of particular interest for space-borne observations, the main agent of radar backscattering are the wind-generated short gravity-capillary waves. The oil film has a dampening effect on these waves locally decreasing the backscattering and finally the brightness in the image. It is implicitly assumed that a light wind field exists in order to activate short gravity-capillary waves. The minimum wind speed is in fact depending on the frequency of observation and the incidence angle. For operational satellites operating in C-band, a minimum wind field of 2-3 m s^{-1} creates sufficient brightness in the image and makes the oil film visible (Donelan and Pierson 1987). On the other end, when the wind speed is too high, it causes the spill to disappear. First, because the short

waves receive enough energy to counterbalance the dumping effect of the oil film. Then, when the sea-state is fully developed, the turbulence of the upper sea layer may break and/or sink the spill or a part of it.

As a consequence of the above brief discussion the identification of an oil spill in a SAR image includes always as first and basic step the detection of dark features. Typically, a SAR image may show some dark features that are not oil spills (i.e., in most cases due to both meteorological and/or oceanographic effects). These look-alike features pose a fundamental problem to the identification of oil spills and require the intervention of an experienced radar image analyst. In general terms the problem can be approached in different ways, through an automatic system, completely relying on dedicated image analysis software tools, or in a semi-automatic mode, where the most critical decisions are taken by an experienced operator, able to understand and correctly interpret the images.

The basic functions of a system for automatic identification of oil spills can be described as follows:

1. Isolation and contouring of all dark signatures, through appropriate threshold and segmentation processing of the image.
2. Extraction of key parameters for each candidate signature, which usually are related to its shape, internal structure and radar backscattering contrast.
3. Test of the extracted parameters against predefined values, which characterise man-made oil spills, usually determined through phenomenological considerations and statistical assessments.
4. Computation of probabilities for each candidate signature.

The approach can be also more sophisticated taking into account relevant environmental parameters having an impact on the spill shape, such as the time history of wind fields and currents (Espedal and Wahl 1999). While the two first steps do not require too much assistance from the image analyst, the two last steps, basically concerning the discrimination of oil spills from other look-alike, strongly rely on the experience and ability of the operator.

1.3 Legal aspects concerning sea-based oil pollution

Not all oil spills detected by using satellite images are necessarily illegal. In fact, we have to distinguish between spills outside special areas and spills inside special areas. Moreover, different rules apply to discharges coming from ships or offshore platforms.

Special areas are defined according to the International Convention for the Prevention of Pollution from Ships (MARPOL 73/78), which in its Annex 1 deals specifically with prevention of pollution by oil. Almost all

seas around Europe (Figure 1) have been designated Special Areas according to Annex 1 of MARPOL 73/78. Only the Norwegian Sea, the Bay of Biscay and the Iberian Coast are not covered by the Special Area status.

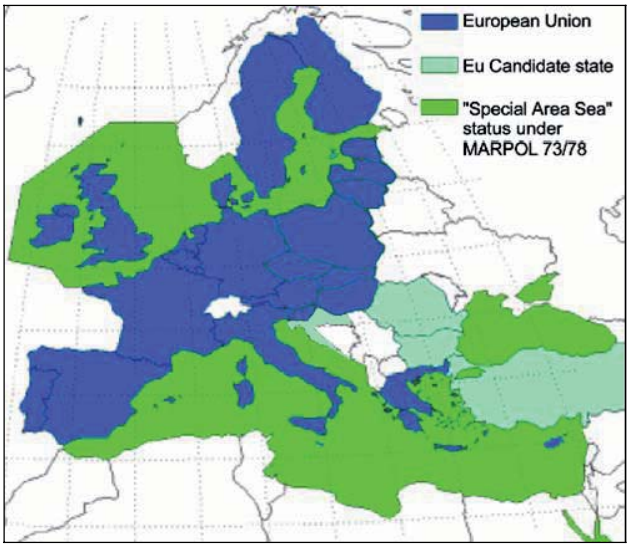

Fig. 1. Special Areas according to MARPOL 73/78

These areas are considered to be so vulnerable to pollution that discharges from ships within them have been completely prohibited, with minor and well-defined exceptions. Without entering into details, we can say that discharges are allowed when the oil content of the discharged effluent does not exceed 15 ppm (parts per million).

It should also be noted that satellite-borne SAR images do not allow the detection of oil spills, if the sea surface is too rough or too smooth, i.e., in the case of winds below 2 m s^{-1} and above 15 m s^{-1}. Last, not least, at present, satellites SAR images are unable to identify the pollution culprit (i.e., the name of the ship that polluted); satellite can at best identify the position of the probable pollution culprit.

2 JRC's experience in the field of oil spill monitoring

2.1 Experience in the field of accidental pollution (the Prestige case, see ref. Fortuny)

Right after the accident of the Prestige tanker, the Monitoring and Information Centre of the European Commission, in coordination with the

Spanish authorities, activated the CHARTER (see ref. CHARTER; International Charter Space and Major Disasters) on November 14th, 2002. The authorised users while the CHARTER was active were the Spanish Authorities (Fomento Ministry), the French Navy, Le Cedre (France), and the EC JRC. The CHARTER was closed on 3 December 2002, two weeks after its activation.

On behalf of the Directorate General Environment (DG ENV), the Joint Research Centre provided support to the interpretation of radar satellite images over the areas affected by the Prestige Tanker accident (Atlantic Coast of Galicia, Cantabrian Coast and the Bay of Biscay). In support of the operational phase, the following working scheme was adopted:

Provision of radar images through the Charter (first phase, in the period 14/11/2002 to 5/12/2002) and then directly from the European Space Agency (second phase, in the period 6/12/2002 to 5/3/2003).

Interpretation of images by the JRC and delivery of relevant information to DG-ENV;

Distribution of the interpreted images by DG-ENV, as annex to Infosheets on the Prestige accident, to all Member States.

The activity concerning the satellite image processing and interpretation in support to the management of the emergency phase consisted of the following tasks:

Image geo-location (i.e., transforming the image from a radar internal reference system to a geographical one (lat-long));

Image equalisation to correct for the incidence angle dependence of the sea surface radar backscatter;

Image segmentation to identify dark features.

Image interpretation identifying possible oil spill signatures.

The final product was a geo-located radar image with the indication of likely spilled areas (Figure 2), for each of which a level of confidence (low-medium-high) was also provided. When possible, in order to ease the image interpretation, suitable geographical reference points (e.g., towns or other clearly recognizable geographical features) were also indicated. Out of the 169 images provided to JRC about 30 were identified as being of interest (a possible oil spill signature was present with at least a low level of confidence) and then delivered to DG-ENV. On average the time delay from the image acquisition to the delivery of the final results to DG-ENV was about 9 hours. In practice, the bottleneck in this process was the delivery of the images by the image provider. It must be noted that a great number of the images were acquired be the ESA ENVISAT satellite, which was in its commissioning phase and the image delivery scheme was not yet fully operational. Consequently, it can be concluded that the overall efficiency was quite good.

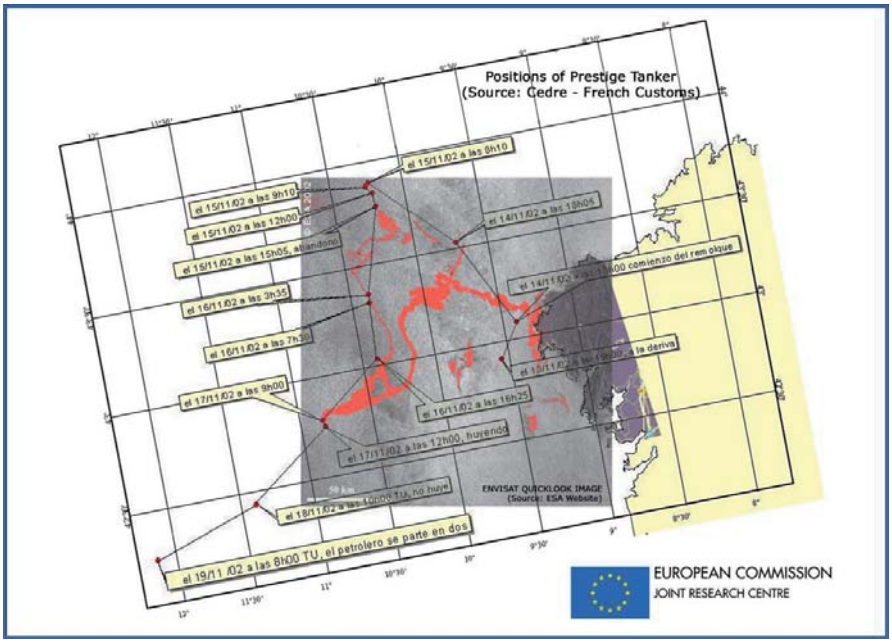

Fig. 2. First satellite image interpretation produced at the JRC for the Prestige accident

The Prestige Tanker accident has been characterised by a number of peculiar aspects, most of them previously not encountered or even unknown. They basically concern the type of discharged oil, the amount of discharged oil, the extent of the affected area, the time period of persistence of oil at sea, as well as the mutual interactions between them.

Such a complex context has to be taken into account when drawing the conclusions on the use of satellite SAR images in support to the emergency phase. In addition we want to distinguish the technical/scientific aspects from the operational one.

Concerning the first aspect the following general comments can be made:

Satellite observations provided useful information due to their capability to cover large and remote areas;

no information has been provided in some cases due to the well known limitations of the sensor (i.e., unfavourable sea conditions);

positive and/or negative identification of pollution not confirmed by other observations.

The last point has many different explanations such as the misinterpretation due to complex situations, the lack of knowledge of the charac-

teristics and of the behaviour of the discharged oil, the lack of experience in dealing with accidental spills and the lack of contextual information at the time of image interpretation.

The Prestige case highlighted a number of technical/scientific needs, where additional investigations and technical improvements are necessary. Many of them are not specific for the oil pollution identification in case of accidental spilling but are a part of the general problem of detecting and identifying marine oil pollution from vessels.

Concerning the operational aspect it should be noted that in most cases the information extracted from satellite images has been delivered to the end-user in a time largely unsatisfactory. Consequently, even images providing useful information loose their operational value.

The aspect of minimising the time delay from image acquisition and delivery of information to the final user is fundamental, and substantial improvements to meet the operational requirements are possible. From a technical point of view, today it is possible to deliver the interpreted image to the user within one hour from the satellite pass. Such a time delay may be acceptable in case of accidental pollution. Then the problem is essentially of organisational nature.

2.2 Experience in the field of operational pollution (mapping of the oil spills for the seas around Europe)

In the past few years, attention has been given to accidental pollution, which indeed is a major visible threat. On the contrary, the pollution problems caused from routine ship operations were not highlighted with the proper emphasis. In the field of monitoring operational oil pollution, JRC has acquired in the past years a unique experience via an institutional project “Monitoring of Illicit Discharges from Vessels” (MIDIV, see ref. MIDIV) and via the participation in competitive actions (such as AMED, RAPSODI, MARSAIS, OCEANIDES, ERUNET, WIN) with different partners.

Concerning operational pollution, data for the seas around Europe are not homogeneous. In the North Sea and in the Baltic Sea, regular aerial surveillance is executed (Figure 3, which reports the results of the aerial surveillance for the year 2000).

By the way of contrast, there is a lack of data for the other seas. Hereunder the results of JRC activities in the different seas are presented. The JRC activity has been focused on zones that are defined “special areas” according to annex I of the MARPOL convention (see above 1.3), for this reason the Norwegian Sea, the Bay of Biscay and the Iberian Coast are not covered. The data type used in these studies was un-calibrated low-resolu-

tion images (except the data concerning the summer campaign 2004 in the Adriatic Sea), since this is the most targeted and cheap product for this application. Recent studies (Gade and Redondo 1999, Gade et al. 2000) have shown that a pixel size of 50 m (resolution of 100 m) is sufficient for statistical investigations of marine oil pollution.

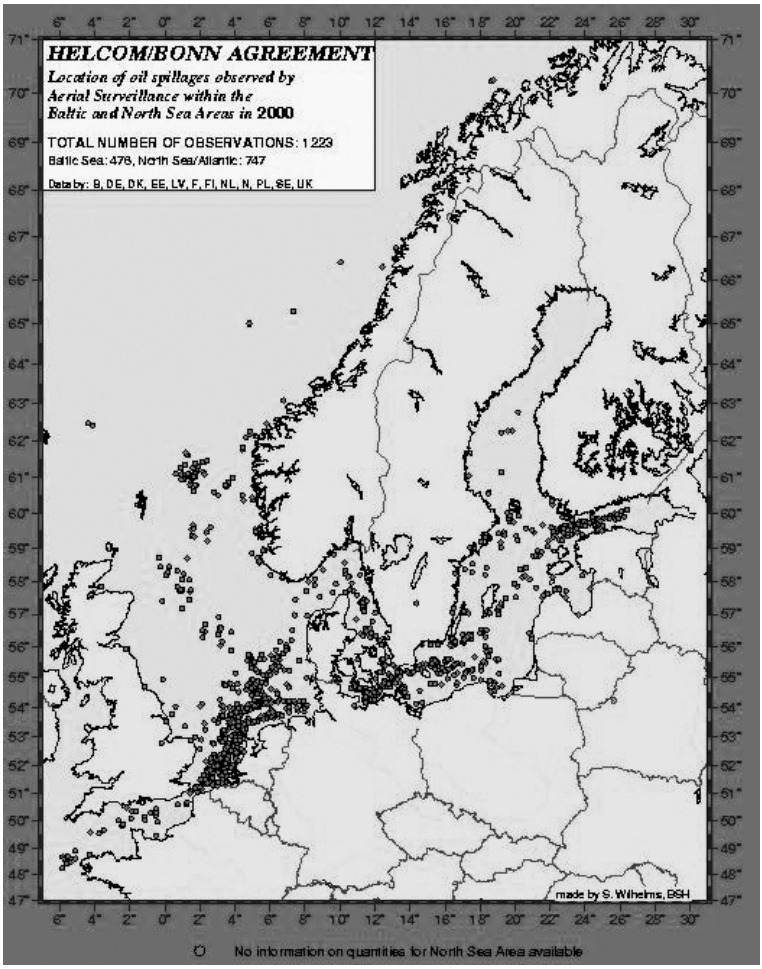

Fig. 3. Aerial surveillance in the Baltic and in the North Sea in the year 2000

For securing to the maximum possible degree that the detected spills were due to man-made activities and not to *look-alike* manifestations of natural phenomena, all the images were interpreted carefully through visual inspection. Each identified spill was registered in a database, together with information concerning its geographic position, the date and time of

detection, the spilled area, its average contrast strength, and a vector describing its shape.

2.3 The Mediterranean Sea

The results presented here concern the reconnaissance studies carried out over the entire Mediterranean region for the year 1999, 2000, and 2001, plus a specific campaign in the Adriatic Sea in the summer 2004. In the year 1999, a set of 1600 SAR images (ERS-1 and ERS-2) was used. In the year 2000, a larger set of 3500 ERS-2 SAR images was analysed. In the year 2001, a set of 2900 ERS-2 SAR images was analysed. Although these results are incomplete, they yield the first comprehensive picture of the dimension of the problem.

It should be stressed that the spatial distribution of the images is not totally homogenous. For example, a low number of images was available along the Libyan coast; on the contrary many images were available over the seas surrounding the Italian peninsula, so the results are somehow biased towards these areas.

For the year 1999, with a set of the 1600 images, the total amount of detected spills was 1638. For the year 2000, with a set of the 3500 images, the total amount of detected spills was 2350. And finally for the year 2001, with a set of the 2900 images, the total amount of detected spills was 1640. For the year 1999, the total spilled area of the 1638 detected spills was estimated to be 17,141 Km^2. Of great interest for the competent authorities, is the amount of oil represented by the spillage. However, an accurate estimation cannot be achieved, since it requires accurate knowledge of the spill thickness, which is not obtained by the SAR sensor alone (Mullin et al. 1995). Nevertheless, some reasonable assumptions can be made, which may help to obtain a gross idea of the spilled amount. For example, experimental investigations (Parker and Cormack 1984) of controlled mineral oil spills in the open sea concluded that a spill thickness of 0.1 microns was a threshold for imaging it with an airborne SLAR (Side Looking Airborne Radar). Spills of such thickness are considered by the operational people as very thin, and appear on the empirical graphs of spill thickness against colour, as thinner than the barely visible ones. Therefore, making the extreme assumption that all the detected spills in the present study were such thin and also uniform in thickness, we obtain as a minimum estimate 1,540 metric tons. In order to approximate a more realistic figure, we may follow as a rule of thumb, the conclusions of other studies (Hollinger and Menella 1984), 90 % of the oil remains usually in the thicker parts of the spill, which represent only the 10 % of its total area. Then, through such a consideration we obtain 13,860 metric tons. While the experience may sug-

gest, that even this figure is a rather conservative estimation, it is however four times greater, than the average amount spilled in the region by ship accidents.

In their vast majority the detected spills were of linear shapes, either straight or angular. In a first order classification we separated them in 5 categories (Figure 4). 1) Narrow straight linear spills, with a tapered front. 2) Straight linear spills without tapered front. 3) Angular spills with a tapered front. 4) Distorted broad spills without tapered front. 5) Amorphous. A very small number, about 2 % of the total, showed discontinuities. Such spills were classified in accordance to their overall shape in the previous categories. The first two classes indicate fresh spills. The third category may include also fresh spills, result from moving ships during a manoeuvring course. But, their angular shape may equally indicate spilling over a long time from a moving ship, during which, changes of the wind and the sea currents occurred. The fourth class is considered as old spills in their total.

As it is shown in the maps (Figure 5, which reports the oil spills detected by satellite imagery) and could have been easily supposed, enhanced spill concentrations appear along major maritime routes, such as those crossing the Ionian Sea towards the Adriatic Sea, towards the Messina Straits and towards the Sicily Straits. Concentrations along maritime routes appear also in the Ligurian Sea and the Gulf of Lion as well as very close to the east coast of Corsica. Here the spilling appears to be localised and frequent. All over the region, however, the spillages show considerable spatial dispersion.

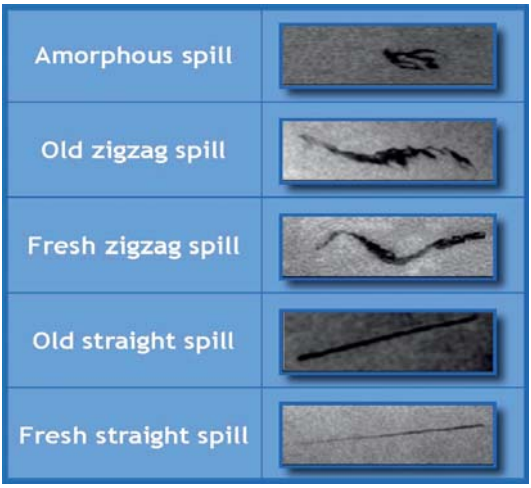

Fig. 4. Possible classification of detected spills in terms of their shape

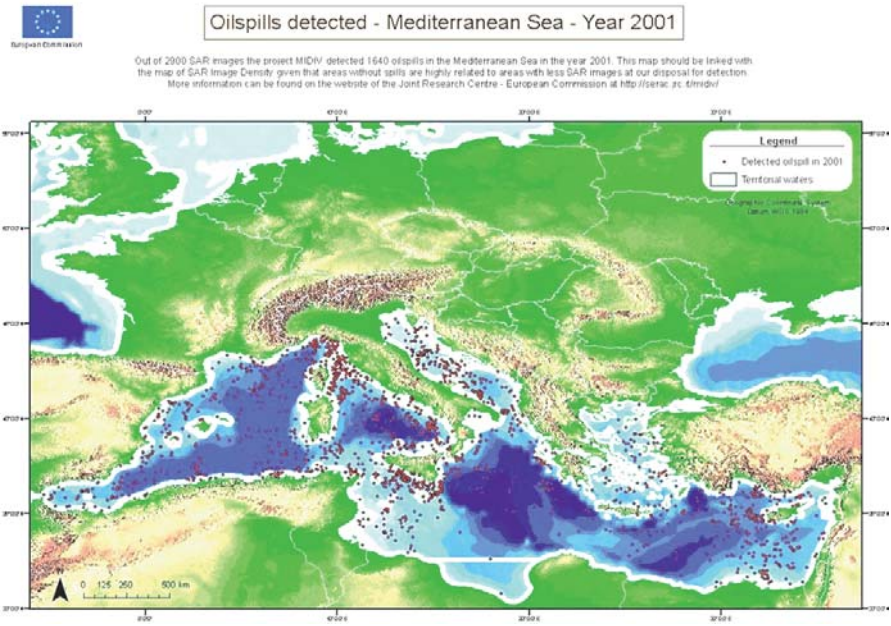

Fig. 5. Oil pollution in the Mediterranean Sea in the year 2001; 2900 images were analysed and 1640 spills were detected

From the analysis of the maps of the Mediterranean Sea in the year 1999, 2000 and 2001 some additional observations can be made:

"Luckily" the ratio between number of images and number of spills of 1999 of 1 spill per image was not kept in the year 2000 and 2001. In fact, in the year 2000 the number of images analysed was more than twice larger (3500 images) but the number of oil spills detected increased only of 50 % (2350 spills);

In the year 2000, the number of spills around Italy was analysed on a monthly basis. This demonstrated a relevant number of spills during the summer months on the routes to Sardinia and Corsica. This is a general trend previously identified by Gade et al. (2000). During summer the mean wind speed is lower, thus causing a higher visibility of oil pollution (and other marine surface films).

Moreover JRC in collaboration with the Regional Marine Pollution Emergency Response Centre for the Mediterranean Sea (REMPEC; see ref REMPEC) developed a specific sub-regional analysis detecting oil spills in the Adriatic Sea in the summer 2004. In this frame, JRC ordered 80 images (medium resolution) for the period July – September 2004. 75 images were

delivered in October and the total amount of detected (with high confidence) oil spills was 80.

2.4 The Black Sea

Concerning the Black Sea, JRC produced the maps of oil spills for the years 2000, 2001 and 2002. In 2000, 800 images were analysed and 205 spills were detected. In 2001, 700 images were analysed and 122 spills were detected. In 2002, 500 images were analysed and 139 spills were detected.

It is difficult to infer a possible trend of the prevalence of oil spills after an analysis period of three years only, each with a different number of images. As a first relevant parameter, we can say that approximately on average it was possible to detect an oil spill: in 2000 every 4 images, in 2001 every 6 and in 2002 every 3.5 images. The analysis of the images of the Black Sea revealed an evident concentration of oil spills along the main maritime routes: Odessa – Istanbul and Novorossiysk – Istanbul. Moreover a concentration of oil spills was detected in the area north of the Bosphorus Strait.

2.5 The Baltic Sea

The results obtained analysing 1300 images for the year 2000 of the Baltic Sea are unsatisfactory. In fact only 100 oil spills were detected. This number of oil spills seems too low compared with data obtained from aerial surveillance in the framework of the Helsinki Convention (see ref. HELCOM). In particular, in the year 2000, 476 oil spills were detected by aerial surveillance (4809 flight hours). In the following years, the number of spills detected by aerial surveillance shows a positive decrease, 389 in 2001, 344 in 2002, 292 in 2003.

One of the possible explanations, of the result of the analysis of the Baltic Sea images is related to the type of images used. As mentioned above the study was developed using un-calibrated low-resolution images and probably this type of images is not appropriate to detect oil spills in the Baltic region. In particular, we have to remind that the Baltic Sea has particular weather condition (in particular, icy waters in the northern part) during a long part of the year and low resolution images could not be the best tool to detect oil spills under these conditions.

2.6 The North Sea

In 2000, a total of 520 oil spills were detected from the analysis of 1500 images of the North Sea (Figure 6). First of all, it is interesting to compare this data with the data available in the framework of the Bonn Agreement (see ref. Bonnagreement). In particular, in the year 2000, 747 spills were detected by aerial surveillance (3426 flight hours). In the following years, the number of spills detected by aerial surveillance shows an uncertain trend, 596 in 2001, 510 in 2002, and 611 in 2003.

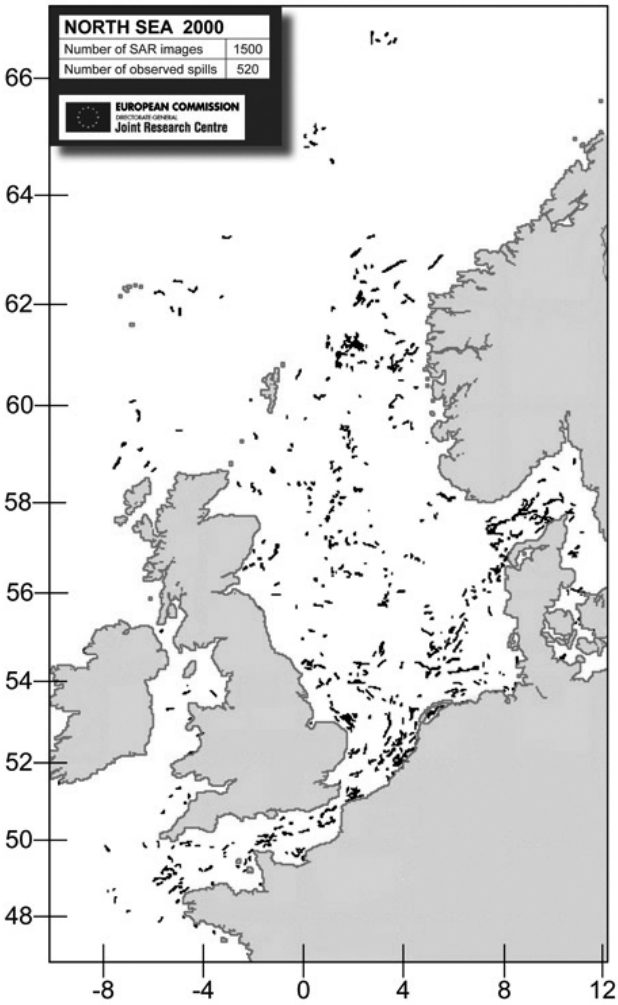

Fig. 6. Oil pollution in the North Sea in the year 2000; 1500 images were analysed and 520 spills were detected

The comparison of the data obtained from the analysis of satellite images with the data coming from aerial surveillance (Figure 3) reveals a number of interesting conclusions. There is a strong coincidence of the areas were a concentration of oil spills are detected, these areas can be recognised with the main maritime routes and areas where offshore platforms are installed. Due to the fact that images were probably covering more homogenously the North Sea compared to aerial surveillance that is mainly focusing on specific routes, it could be estimated that aerial surveillance is correctly carried out over the most sensitive areas.

Concerning the possibility to correlate the oil spills detected by satellite with spills observed by aircraft, a specific study has been developed by JRC. However, the number of matching possibilities does not have a solid scientific basis because there is too much uncertainty on the persistence and drifting of an oil spill.

3 A possible way forward

In summary, we recognised a clear need for additional research efforts and the need to involve the regional and national authorities deeply that are competent in the field of monitoring sea-based oil pollution. Concerning the additional research efforts, space-borne sensors will have to secure their role in support to aerial and naval means for the monitoring of sea-based oil pollution by (among others):

Refinement of methodologies to improve the reliability of the identification of oil spills (reduction of the false positives and false negatives rate). Possible research directions include the refinement of tools for the analysis of images acquired by a number of different sensors, such as RADAR, IR, UV, Passive Microwave, the fusion of information from different sensors as well as the integration of auxiliary data (meteo and oceanographic data).

Integration of data from different space borne sensors to improve the retrieval of oil spill thickness, the detection of submersed oil, and the type of the oil. These aspects are particularly important when heavy oil is discharged, as in the case of the Erika and Prestige accidents. In order to estimate the volume and the type of the discharged oil it is essential to assess the impact on the environment.

Refinement of methodologies for the prediction of oil spills movement, including oil dispersion model and ocean circulation models. This is a crucial aspect in case of accidents, but also in case of deliberate spilling close to the coastline.

Providing over the whole extension of the European Seas a reliable operational real-time service.

Defining a common data policy (affordable cost of the image);

Assuring the sustainability of the process (future missions).

Moreover, JRC will continue to collect and distribute results from satellite data, producing maps of all the seas around Europe.

Following these aims, JRC together with DG ENV launched the initiative of a permanent Group of Experts on satellite monitoring of sea-based oil pollution. The primary objective of this Group will be a comprehensive exchange of information, knowledge and expertise about the Satellite monitoring of sea-based oil pollution at European level. Moreover, the Group will have the following tasks:

Information exchange on R&D projects;

Technical support of the European Commission and in particular the Management Committee on Marine Pollution (MCMP), in the field of oil pollution detection and tracking by satellite monitoring;

Analyse and support the process towards standardisation, for re-porting system, and for agreement on best practice;

Make available to all countries the results of passed or ongoing studies or projects related to satellite tracking of oil pollution;

Allow for a joint thought on how to secure the continuous access of information for oil spill monitoring by satellite imagery, and how to enhance the coverage of all European Seas in time and space.

4 References

Alpers W and Hühnerfuss H (1989) The damping of ocean waves by surface films: A new look at an old problem. J Geophys Res 94: 6251-6265

Bonnagreement: http://www.bonnagreement.org ; Data concerning aerial surveillance are reported on: http://www.bonnagreement.org/eng/html/welcome.html

Brown C, Fruhwirth M, Fingus M, Vaudreuil G, Monchalin J, Choquet M, Heon R, Padioleau C, Goodman R, Mullin J (1995) Oil Slick Thickness Measurement: A Possible Solution to a Long-Standing Problem. Proceedings of the Eighteenth Arctic Marine Oil Spill Program Technical Seminar, Environment Canada, Ottawa, Ontario, pp 427-440

CHARTER: The Charter, through its partners Organizations (ESA, CNES, CSA, ISRO, NOAA, CONAE), aims at supporting the emergency management due to natural or man-made disasters providing the acquisition and fast delivery of space data of interest: http://www.disasterscharter.org/main_e.html

Donelan M A and Pierson WJ Jr (1987) Radar scattering and equilibrium ranges in wind-generated waves with application to scatterometry. J Geophys Res 92: 4971-5029

Espedal H A and Wahl T (1999) Satellite SAR oil spill detection using wind speed history information. Int J Remote Sensing 20: 49-65

Fortuny J, Tarchi D, Ferraro G and Sieber A (2004) *The Use of Satellite Radar Imagery in the Prestige Accident*, paper submitted to Interspill 2004, 14-17 June, Trondheim, Norway
Available on: http://serac.jrc.it/midiv/pub/interspill-2004-JRC.pdf

Gade M and Redondo JM (1999) Marine pollution in European coastal waters monitored by the ERS-2 SAR: a comprehensive statistical analysis. Proceedings of the International Geoscience and Remote Sensing Symposium, IGARSS '99, 2: 1375 - 1377

Gade M, Scholz J and von Viebahn C (2000) On the detectability of marine oil pollution in European marginal waters by means of ERS SAR imagery, Proceedings of the International Geoscience and Remote Sensing Symposium, IGARSS 2000, 6: 2510 - 2512

HELCOM: http://www.helcom.fi. Data concerning aerial surveillance are reported on: http://www.helcom.fi/manandsea/shipping/oilpollution.html

Hollinger JP and Mennella RA (1984) Measurements of the distribution and volume of sea-surface oil spills using multifrequency microwave radiometry, in *Remote Sensing for the Control of marine pollution*, Jean-Marie Massin ed., NATO Challenges of modern Society, Vol. 6 1984, Plenum Press

MIDIV: The first study of JRC was specifically devoted to the Mediterranean Sea: Pavalakis P, Tarchi D, Sieber A, Ferraro G and Vincent G (2001) On the Monitoring of Illicit Discharges – A Reconnaissance Study in the Mediterranean Sea" Available on: http://serac.jrc.it/midiv/pub/jrc_illicit_study.pdf; For more info on these projects: http://serac.jrc.it/midiv/

Parker H D and Cormack D (1984) Evaluation of Infrared Line Scan (IRLS) and Side Looking Airborne Radar (SLAR) over controlled oil spills in the North Sea, in *Remote Sensing for Control of Marine Pollution*, Jean-Marie Massin ed., NATO-Challenges of Modern Society Vol. 6, pp 237-256

REMPEC: For the Regional Marine Pollution Emergency Response Centre for the Mediterranean Sea (REMPEC) see: http://www.rempec.org

Long-term microwave radar monitoring of ocean slicks at low grazing angles

Christine P Gommenginger and Simon R Boxall

Ocean Circulation and Climate Division, National Oceanography Centre, Southampton, United Kingdom

Abstract. This paper proposes the use of a digital microwave marine radar system for the detection and monitoring of surfactant slicks at sea. The spatial, temporal and radiometric resolutions of this low grazing angle instrument are compared to those of satellite and airborne radars traditionally used for oil pollution monitoring. Experimental evidence is presented in two artificial surfactant releases in the coastal zone which were successfully detected and tracked with a shore-based marine radar. The information contained in a long-term time-series of NRCS images is explored and its synergistic use with traditional satellite- and air-borne radar data discussed.

1 Introduction

The detection of ocean surface slicks by microwave radars at intermediate incidence angles is well established. The all-weather day-and-night capabilities of microwave remote-sensing has resulted in its wide operational use by harbour authorities for the control of oil pollution in the coastal zone (Attema and Hoogeboom 1978, Sherman 1992). In research, microwave radars can also help further our understanding of air-sea interactions and hydrodynamic processes by providing extensive synoptic two-dimensional maps of the slicks' spatial distribution (Espedal et al. 1996, da Silva et al. 1998).

The reduction of ocean backscatter power by slicks has been attributed to the damping of the small scale waves predominantly responsible for the radar returns from the sea surface (Alpers and Hühnerfuss 1988). Successful slick imaging relies on good spatial and radiometric resolution to ensure sufficient contrast with the backscatter from the surrounding "clean" sea. At low grazing angles, the level of backscatter becomes very low as different scattering mechanisms such as shadowing become dominant

(Valenzuela 1978, Wetzel 1990) and as such the detectability of oil spills and sea slicks remains questionable; the conditions yielding adequate contrast levels are not well documented.

In this paper, the capabilities for slick detection at low grazing angles are examined with the use of a standard marine radar system chosen to represent the typical performance of this low cost technology. The resolution and data quality achieved with this kind of instrument are briefly reviewed and compared with those of traditional satellite and airborne radar systems. Two examples of the successful detection in the coastal zone of controlled surfactant slicks with a marine radar system are presented to illustrate the potential for operational and research applications. Finally, the information contained in long-term radar monitoring of a specific area is explored.

2 Spatial and temporal resolution

The digital marine radar system used in this study consists of a standard X-band (9.4 GHz) Racal Decca marine radar attached to an off-the-shelf PC-based digital capture board. A detailed description of the system and its operation can be found in Robinson et al. (1999). The radar is fitted with a horizontally polarised linear radar antenna with a 1 degree horizontal beamwidth which rotates at a period of 2.4 s. The microwave energy is emitted as pulses of fixed duration which determine the radar's spatial resolution in range. The pulse peak power and pulse repetition rate (PRR) is determined by the pulse length setting, so that on short pulse setting for example, the radial dimension of the emitted pulse is 12 m with a nominal peak power of 7.0kW.

On reception, the radar signal is log-amplified and intercepted by the digital capture board. The capture board includes a facility to integrate a number of successive returns to produce multi-look backscatter measurements and thus reduce the speckle in the digital images. The number of "looks" together with the PRR and the antenna rotation speed determine the images' resolution in azimuth. The integrated multi-look backscatter signal is then sampled at a rate of 20, 10 or 5 MHz resulting in a pixel resolution in range respectively equal to 7.5, 15 or 30 meters. The spatial resolution in the images is generally chosen to coincide with the physical dimensions of the pulsed antenna footprint. Typical values of the system's spatial resolution are summarised in Table 1.

The capture board allows pre-determined areas of the marine radar's view field to be extracted and stored as 8-bit images on the PC. The coverage of the digital image is controlled by various capture parameters described in detail in Robinson et al. (1999). In the present case, the maxi-

mum coverage is limited to a 180 degrees sweep in azimuth with an 8 km interval in range. These parameters are, however, specific to this board and may easily be extended. The system also enables the acquisition of time-series of images in specific areas separated by 2.4, 4.8 or 9.6 seconds. This facility allows 2D maps of the backscatter's statistical moments to be derived with later processing.

Table 1. Typical spatial and temporal resolutions for marine radar and airborne/ satellite systems

	Marine radar system	Airborne/satellite systems
Spatial resolution in range	10 - 130 m	10 to 100 m
Spatial resolution in azimuth	1 degree	10 to 100 m
Spatial coverage	8 km	10 - 150 km
Temporal resolution	2.4 seconds to minutes/hours/days	Airborne: hour to days Satellite: days
Temporal coverage	2.4 seconds to minutes/hours/days	-

3 Radiometric performance

The typical radiometric performance of marine radar systems was determined with an end-to-end calibration of the marine radar system described above. The object of this work was to use the performance of this particular low-cost technology to assess the applicability to the detection of slicks at sea.

Based on the classical Radar Equation, a normalising relationship between the pixel intensity, X, in the images and the Normalised Radar Cross Section (NRCS), σ^0, of the sea surface was established as:

$$\sigma^0(dB) = f_p(X) + 10\log_{10} R^4 - 10\log_{10} Ar - K_p \quad (1)$$

where R is the range of the pixel, Ar is the dimension of the antenna footprint at that range, f_p is the marine radar system transfer function relating the received backscatter power to the image intensity, and K_p is a constant representative of the system antenna properties. The accurate determination of f_p and K_p is presented in detail in Gommenginger et al. (1999). This calibration procedure also identified the system's noise floor and saturation level. The system's dynamic range thereby defined is presented in terms on NRCS in Figure 1 as a function of distance from the radar.

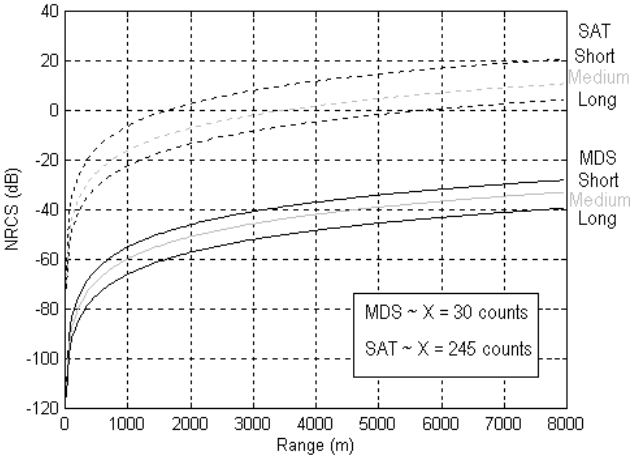

Fig. 1. Marine radar system noise floor (or Minimum Detectable Signal (MDS)) and saturation level expressed in their NRCS equivalents

The relative radiometric resolution of the instrument was derived from a detailed error analysis of (1) using theoretical estimates of the maximum error associated with each variable. The relative radiometric resolution was estimated for mean NRCS images obtained by averaging a variable number, N, of consecutive antenna sweeps. The derived resolution was thus found strongly dependent on N and on the pulse length setting (which governs the number of pulses integrated per pixel). A summary of the theoretical NRCS error is given in Table 2.

Table 2. Typical dynamic range and radiometric resolution for marine radar and airborne/satellite systems.

	Marine radar system			Airborne/Satellite systems
Dynamic range		~ 50 dB		50 - 70 dB
Relative NRCS error (dB)	Short	Medium	Long	
No. images averaged ≥ 4	0.6 dB	0.8 dB	1.1 dB	0.2 dB - 1 dB
No. images averaged ≥ 24	0.6 dB	0.6 dB	0.6 dB	

4 Comparing performances with traditional radars

Tables 1 and 2 present typical values for the spatial, temporal and radiometric resolutions of marine radar, airborne and satellite radar systems. The marine radar is found to provide a much reduced spatial coverage but

offers a resolution similar to that of other systems. Likewise, marine radar systems produce NRCS measurements of comparable quality with estimated relative NRCS errors generally of the order of 0.6 dB. The extended temporal coverage and flexible temporal resolution of the marine radar contrast sharply with the poor coverage and measurement repetitivity displayed by airborne and satellite systems. Overall, the comparison of these performances indicates that marine radar systems can provide reliable high-resolution NRCS images of specific areas with any chosen interval over extended periods of time. This type of information thus represents an ideal complement to interpret the large-scale snapshots obtained with satellite and airborne radars.

5 Controlled surfactant spill experiments

Results are presented for two controlled slicks carried out a few miles off the Isle of Portland on the south coast of the UK. The marine radar system was located on a cliff overlooking the sea to the west of the island at a height of approximately 60 meters above mean sea level. The surfactant deployed in these experiments consisted of a biodegradable chemical known as Emkarox, specifically developed for the Defence and Evaluation Research Agency (DERA), and designed to reproduce the visco-elastic properties of monomolecular natural films. In both cases, some information on the slicks' position, morphology and spreading was available through visual observations from the cliff top and the boat used for slick generation.

The first experiment took place in light wind and sea conditions (U_{10} = 4.5 m s^{-1} from the east; H_s = 1m). A sequence of marine radar images obtained during the deployment of the surfactant material is shown in Figure 2. The bright echoes in the middle of the images were produced by three instrumented buoys providing *in-situ* measurements of wind, wave and current conditions. The elongated bright echo seen in the upper part of the first image indicates the boat from which the surfactant was poured slowly and steadily while the boat travelled North. Some 20 minutes later, as the surfactant had spread sufficiently to form a coherent linear slick, a narrow line of reduced NRCS became visible to the east of the buoys. One hour after deployment of the surfactant, the radar image correctly indicated that the slick started to break up, presumably due to steady spreading and dispersion of the limited amount of surfactant deployed.

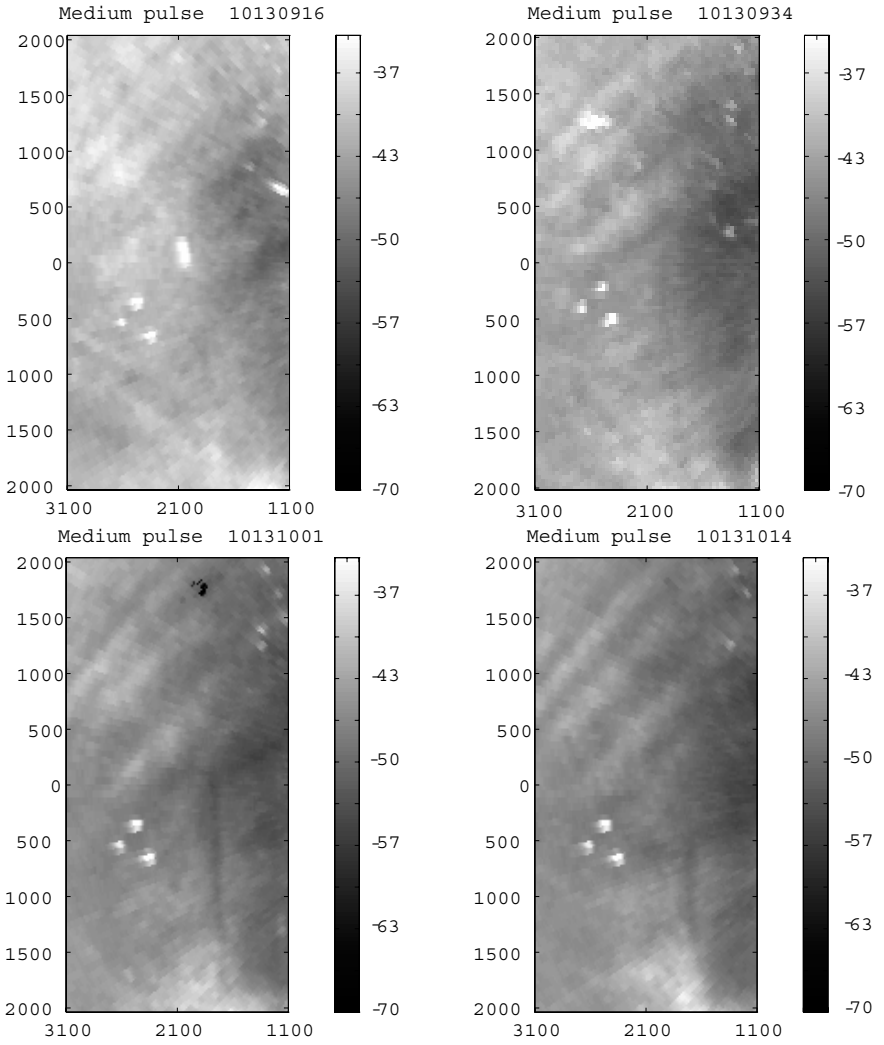

Fig. 2. Sequence of marine radar images in Portland Island during the deployment of a linear surfactant slick (Emkarox) to the east of the three instrumented buoys (indicated by bright echoes in the centre). Wind and sea conditions were light (U_{10} = 4.5m s^{-1} from east; $H_s \sim$ 1m)

The second experiment took place in stronger wind and sea conditions (U_{10} = 9 m s^{-1} from the west; H_s = 1.5 m) and is shown in Figure 3. The range scale of the image is now twice that used in Figure 2. The instrumented buoy echoes are not visible in these images due to the choppy sea state. The sequence of images corresponds to a period when the tide rapidly slacks from around 1.2 m s^{-1} for the first three images to practically 0 for

the last one. Three oceanographic features are pointed out in this figure: item (a) corresponds to an artificial slick deployed to the north-west of the covered area and is seen drifting south-easterly through the images in the sequence. Item (b) indicates a line of enhanced roughness collocated visually with a line of foam running along the bathymetric contour. It is thought that this feature indicates the position of a convergence zone. Finally item (c) displays the same reduced NRCS characteristic of the artificial slick but this time does not drift with the tide as indeed it relates to an underwater dip where the water depth sharply increases from 40 to 60 m. The observed reduced backscatter can thus be attributed to the hydrodynamic modulation of the short scale roughness by current gradients over the bathymetric dip (Alpers and Hennings 1984). Note how in the fourth image of the sequence, this latter feature disappears when the tidal current drops and the artificial slick has stopped drifting south-easterly.

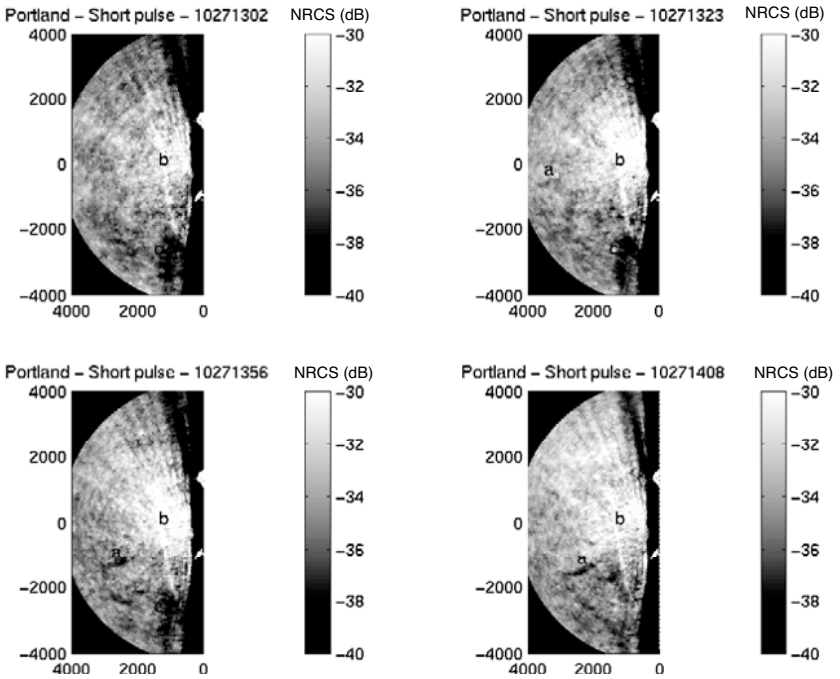

Fig. 3. Sequence of marine radar images in Portland Island showing **(a)** an artificial slick drifting with the tide, **(b)** an enhanced roughness line thought to indicate a zone of convergence and **(c)** the radar signature of an underwater dip from 40 to 60 meters water depth. Wind and sea conditions were moderate (U_{10} = 9 m s^{-1} from west; Hs ~ 1.5 m)

The NRCS reductions caused by (a) and (c) are better quantified in Figure 4 with transects taken across these features in the third radar image in the sequence. The transects AB across (a) and BC across (c) show NRCS reductions of similar magnitude (~ 3 dB) for both features with respect to the control transect (dashed line) taken in "clean" water immediately south of (a). The NRCS signature alone does thus not allow to differentiate (c) from an artificial slick, and only the time-sequence enables us to identify (c) with a stationary, bathymetry-related, process. The NRCS reduction across (a) is comparable to the damping ratios observed, for example, for biogenic slicks in SIR-C/X-SAR images (2 to 6 dB; see Gade et al. 1996). We note that the NRCS profile across (a) indicates a gradual NRCS decrease within the slick in the A to B direction, with maximum damping occurring at the eastern edge of the slick. This is consistent with a redistribution of the surfactant material within the slick under the action of the westerly wind.

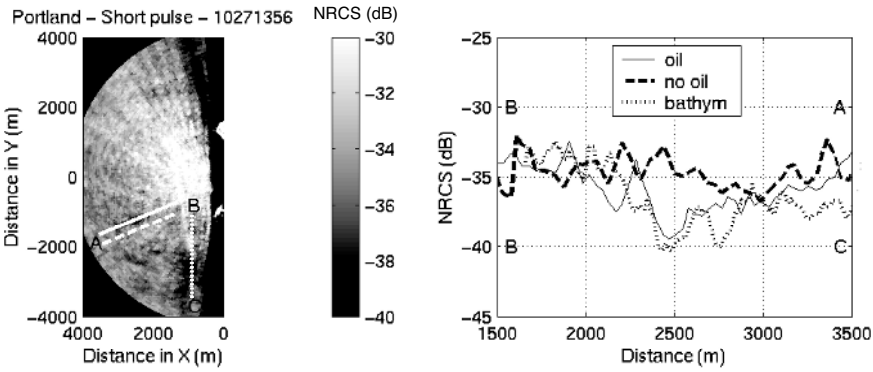

Fig. 4. NRCS transects taken across feature (a) and (c) as seen in the third radar image of the sequence shown in Figure 3. Transect AB (solid line) across the artificial slick (a) and transect BC (dotted line) across the underwater dip (c) show a similar NRCS reduction in excess of 3 dB, with respect to the transect across "clean" water (dashed line)

6 Discussion and conclusion

Results were presented of two surfactant slick detection experiments using a shore-based marine radar system. In both instances the slick was successfully detected and tracked at grazing angles less than 2 degrees in wind conditions ranging from light to moderate. Defining further the range of conditions favourable to slick detection with marine radar systems is a

complex problem. In particular, environmental and operational conditions strongly affect the microwave propagation mechanisms at low-grazing angles. These issues are outside the scope of this paper, but the reader is invited to consult Gommenginger (1997; Chapter 7 and 8) for further details on these problems.

Time-series of NRCS images were obtained and found able to provide information on the position, size, shape and surfactant distribution of the slicks as they evolved in time. Similarly, the sequence of images allowed bathymetric features with similar radar signatures to be rightly identified in view of their constant position in the images. It is expected that, in common with traditional radar systems, naturally occurring slicks would also produce this type of radar signatures, which would then be difficult to distinguish from artificial slicks. However, wind conditions conducive to biogenic slick formation (< 5 m s^{-1}) do not generally coincide with conditions needed to warrant sufficient backscatter contrast at low-grazing angles. Hence, biogenic slicks would be imaged only in exceptional circumstances (e.g., transient wind regime) when they would not be expected to persist.

These results confirm that marine radar systems can provide useful and reliable NRCS measurements in complex areas such as the coastal zone. These cost effective instruments provide a robust and reliable tool for long-term monitoring of sensitive coastal areas. The long-term monitoring facility suggests that these data may also be useful to interpret larger scale snapshots obtained from satellite or airborne radars.

Acknowledgements. We would like to thank Dr John Scott and Peter Dovey at DERA who provided access to the DERA cliff-top location on the Isle of Portland and enabled us to take part in the surfactant experiments. Many thanks also to Nicholas Ward for developing some of the radar image processing software used in this work.

7 References

Alpers W, Hennings I (1984) A theory of the imaging mechanism of underwater bottom topography by real and synthetic aperture radar. J Geophys Res 89: 10529-10546

Alpers W, Hühnerfuss H (1988) Radar signatures of oil films floating on the sea surface and the Marangoni effect. J Geophys Res 93: 3642-3648

Attema EPW, Hoogeboom IP (1978) Microwave measurements over sea in the Netherlands. pp 291-298 in, Surveillance of environmental pollution and resources by electromagnetic waves, eds T Lund

da Silva JCB, Ermakov SA, Robinson IS, Jeans DRG, Kijashko SV (1998) Role of surface films in ERS SAR signatures of internal waves on the shelf 1. Short-period internal waves. J Geophys Res 103: 8009-8031

Espedal HA, Johannessen OM, Knulst J (1996) Satellite detection of natural films on the ocean surface. Geophys Res Lett 23: 3151-3154

Gade M, Alpers W, Bao M, Hühnerfuss H (1996) Measurements of the radar backscattering of different oceanic surface films during the SIR-C/X-SAR campaigns. In Proc IEEE IGARSS'96

Gommenginger CP (1997) On the applicability of a conventional microwave marine radar system to quantitative measurements of the ocean surface roughness and oceanographic applications, PhD dissertation, Department of Oceanography University of Southampton

Gommenginger CP, Ward NP, Fisher G, Robinson IS, Boxall SR, (1999) Quantitative microwave backscatter measurements from the ocean surface using digital marine radar images. J Atm Ocean Eng 17: 665-678

Robinson IS, Ward NP, Gommenginger CP, Tenorio MA (1999) Coastal oceanography applications of digital image data from marine radar. J Atm Ocean Eng 17: 721-735

Sherman JW III (1992) Oil spill remote sensing - a perspective. pp 10-17 in, Sea Technology - Special Remote Sensing Report, August 1992

Valenzuela GR (1978) Theories for the interaction of electromagnetic and ocean waves - A review. Bound Layer Meteor 13: 61-85

Wetzel LB (1990) Electromagnetic scattering from the sea at low grazing angles. pp 109-171 in, Surface waves and fluxes, volume 2 - Remote Sensing. eds GL Geernaert and WL Plant

Oil spills on ALMAZ-1 and ERS-1 SAR images: results from the DOSE-91 experiment

Konstantin Litovchenko[1] and Andrei Ivanov[2]

[1]Space Research Institute, Russian Academy of Sciences, Moscow, Russia
[2]P.P.Shirshov Institute of Oceanology, Russian Academy of Sciences, Moscow, Russia

Abstract. This paper presents the results of the oil spill observations using Almaz-1 and ERS-1 SAR images collected in the Norwegian Sea during the Dedicated Oil Spill Experiment (DOSE-91) in 1991. Three artificial spills were released from a vessel in August 1991 and data on sea and weather conditions near the test area were determined. The analysis of the acquired SAR images shows that the reduction of the backscatter from oil-covered sea surface attained values of up to 10-15 dB. For the first time an effect of an intensification of wind waves both within the area of the spill and at the windward edge of the oil spill, expressed as a magnification of the SAR image brightness, was detected. The increase in relative backscatter power was up to 2.0 dB. It is concluded that both Almaz-1 and ERS-1 SARs are valuable tools for oil spill detection and localisation, but that the detectability essentially depended on wind speed, sea state and age of spills.

1 Introduction

It is well known that crude oil forms films of various thicknesses on the sea surface and that they locally dampen sea surface roughness. This fact gives a physical basis for the application of radars to oil spill detection and monitoring in the ocean. Since the launch of the first synthetic aperture radar (SAR) many cases of oil spill detection have been documented. In order to evaluate the capability of space imaging radars for oil pollution detection and to study the damping effect of oil films, a series of experiments has been recently conducted using the ERS-1 and SIR-C/X SAR aboard the space shuttle, where SAR image signatures and damping ratios of natural slicks and artificial slicks as well as oil spills have been studied (Oka-

moto et al. 1993, Masuko et al. 1995, Gade et al. 1998). It was shown that maximum damping by artificial films is encountered around the Bragg waves related to C-band (Gade et al. 1998).

However, radars' possibilities are limited by the respective conditions on the air-sea interface and depend on oil spill parameters. Different processes in the ocean-atmosphere system can result in similar SAR image signatures and equal contrasts. In order to discriminate between natural sea slicks and oil spills additional information is always required. Nevertheless, the ability of all-weather monitoring by radar makes it a powerful tool for ocean remote sensing.

The papers mentioned above did not include data obtained by the S-band SAR aboard the Russian Almaz-1 satellite. In order fill this gap we herein comparatively analyse the Almaz-1 and ERS-1 SAR imagery taken during the Dedicated Oil Spill Experiment-91 (DOSE-91) (Bern et al. 1992a, Ivanov et al. 1998). The S-band SAR aboard the Almaz-1 satellite was operating at 3.1 GHz (9.6 cm wavelength) at an orbital altitude between 300 and 400 km during the flight, horizontal polarisation of the signal (HH) for transmission and reception, resolution 10-15 m and variable incidence angles (25-60°). More detailed specifications of the Almaz-1 SAR can be found in Wilde et al. (1993).

2 Experiment and results

The DOSE-91 experiment was conducted between August 21 and September 2, 1991 in the Norwegian Sea, 100 km off the western coast of Norway around the Haltenbanken during simultaneous operation of the Almaz-1 and ERS-1 satellites. Twenty tons of artificial oil were spilled on the sea surface in a point with coordinates 64° 30′ N and 07° 30′ E (Figure 1) on August 21st (20:40 UTC), August 24th (19:05) and August 27th (19:00). Only the two first spills were imaged by either Almaz-1 or ERS-1 SAR and are considered here. The oil consisted of a mixture of 35 % Statfjord crude, 20 % Gullfaks crude and 45 % DUC crude (Bern et al. 1992a). Such mixture was selected because it does not form steady emulsions in the sea water and in this sense can be considered as ecologically safe (for details see Bern et al. 1992a, and Bern et al. 1992b). The spills existed in the sea between 3 and 5 days. In the area of the experiment three oceanographic buoys were installed to measure sea and wind parameters. The observations of the spill evolutions were also produced from a Norwegian aircraft equipped with SLAR, IR and UV sensors. Twelve data acquisitions from the Almaz-1 and 4 from the ERS-1 satellite were taken. However, the spills were only identified on four Almaz-1 and on two ERS-1 SAR im-

ages. More detailed experiment descriptions and analyses concerning the ERS-1 data acquired during the experiment can be found in Bern et al. (1992b).

Figure 1 shows how the spills (areas of reduced backscatter on SAR image) drifted during the observation period according to the SAR images. As inferred from the figure the drift of the spills was complicated and was affected by wind, waves and currents (for details see Bern et al. 1992b). Table 1 summarises the survey parameters, wind/wave conditions, age of oil spills and measured damping ratios.

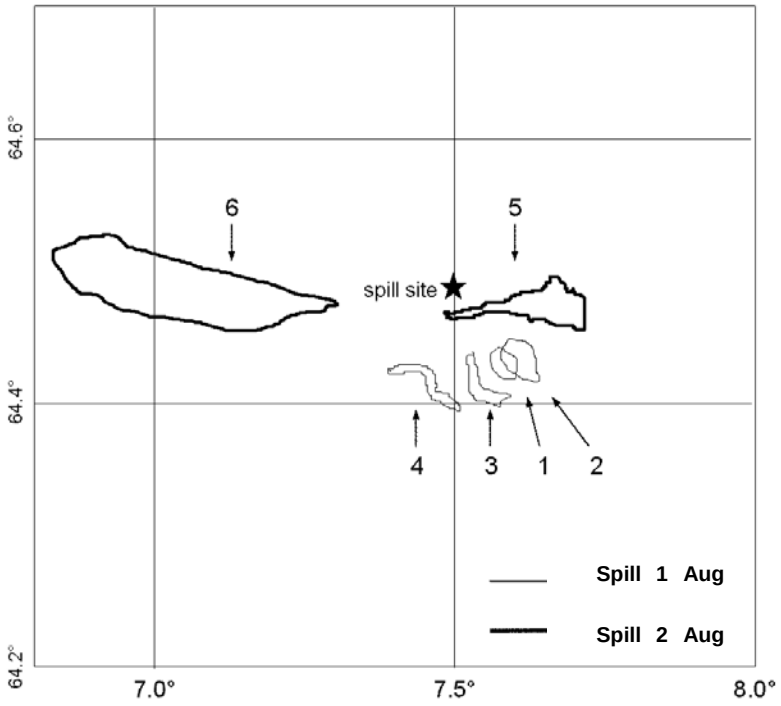

Fig. 1. The evolution of two oil spills deployed during the DOSE'91 Experiment. The numbers denote the spill contours delineated from the SAR images:

1 - ERS-1, 22.08, first spill, spill age 16 hrs
2 - Almaz-1, 22.08, first spill, spill age 22 hrs
3 - Almaz-1, 23.08, first spill, spill age 40 hrs
4 - ERS-1, Almaz-1, 25.08, first spill, spill age 88 hrs
5 - ERS-1, Almaz-1, 25.08, second spill, spill age 18 hrs
6 - Almaz-1, 27.08, second spill, spill age 72 hrs

Table 1. The parameters related with the SAR image acquisitions, environmental conditions and oil spills

Date of SAR survey, 1991		**Aug. 22**		**Aug. 23**	**Aug. 25**		**Aug. 27**
Satellite		ERS-1	Almaz-1	Almaz-1	ERS-1	Almaz-1	Almaz-1
Time, UTC		10:48	16:41	10:35	10:48	10:44	15:30
Incidence angle [deg]		23	35	27.4	23	52.6	35.3
Resonant surface wavelength [cm]		8.4	7.3	10.4	7.3	6.0	8.3
Wind speed [m s^{-1}]		5-7	2-3	7	2-3		12
Wind direction [deg]		190-200		170	200-240		220-230
Wave period [s]		9.5		9.5	7.9		12.5
Wave direction [deg]		245		260	305		265
Wave height [m]		2.8		2.8	1.7		3.1
Spill age [hr]	spill of August 21	16	22	40	88		
	spill of August 24				18		72
Damping ratio [dB]	spill of August 21	~1.2	2.5	2.2	9.5	~0.2	
	spill of August 24				15	~0.2	2.5

The standard SAR image processing which allows to delineate the processes on sea the surface includes, in particular, image section and NRCS contrast estimation. The wave damping ratio (the ratio of the spectral densities of Bragg waves (S) with wave number k or the normalised radar cross section (NRCS) (σ_0) of spill-free and spill-covered sea surface) or contrast:

$$K = S(k)/S_{sl}(k) = \sigma_0/\sigma_{0,sl} \quad (1)$$

The expression in dB is used as quantitative performance of the variability of wind waves in slick or spill areas.

Figures 2-5 show the ERS-1 and Almaz-1 SAR sub-images around observed oil spills and the NRCS sections through the spills. Note that thin white arrows show length and direction of the sections while thick black arrows indicate the wind direction. On the images of August 25 (Figure 4) both spills can be delineated.

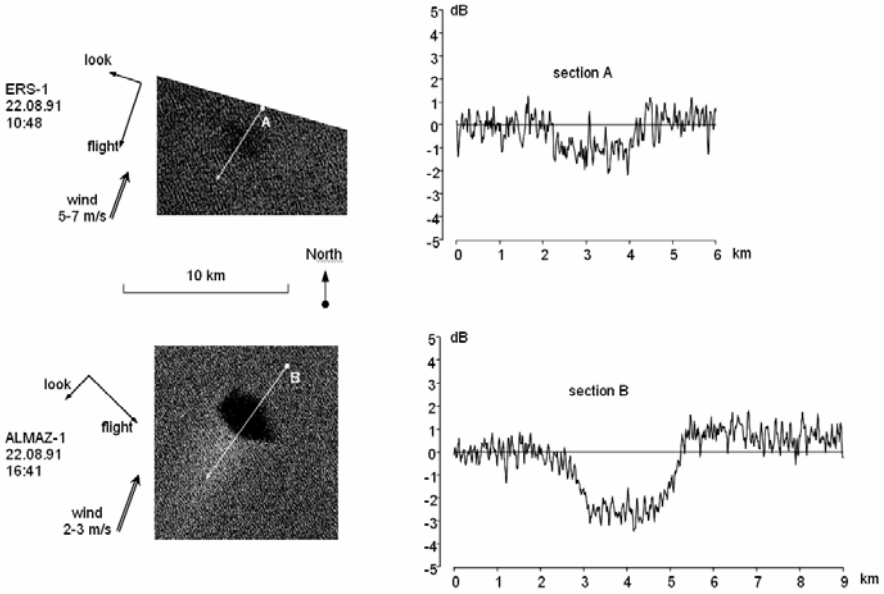

Fig. 2. ERS-1 and Almaz-1 SAR images of August 22nd, 1991, at 10:48 and 16:41 UTC showing the first oil spill released on August 21st (incidence angles 23° and 35°, wind speed 5-7 m s^{-1} and 2-3 m s^{-1}, spill age 16 hrs and 22 hrs respectively) (**left**). Variations of the radar backscatter along the scan lines are shown on the ERS-1 and Almaz-1 SAR images by white thin arrows (**right**), flight/look directions by thin black arrows, and wind direction by a double black arrow (image courtesy ESA and NPO Mashinostroenia)

The first pair of images was acquired on Aug. 22nd, 1991, at 10:48 (ERS-1) and 16:41 (Almaz-1) (Figure 2). The damping ratio in the ERS-1 image is low (1.2 dB), while in the Almaz-1 image acquired 6 hours later the damping ratio is 2.5 dB. In the latter image a wedge-shaped area of increased NRSC can be observed upwind from the spill's upwind border. It is located opposite to the wind direction and is ~1 dB brighter than the background. It follows from Table 1 that at the time of the ERS-1 overpass a south-westerly wind with 5-7 m s^{-1} speed and a westerly swell of 150 m

wavelength, 9.5 s period and 2.8 m waveheight was prevalent. At the time of the Almaz-1 overpass the wind speed had fallen down to 2-3 m s^{-1}. This can explain the higher damping ratio in the Almaz-1 case.

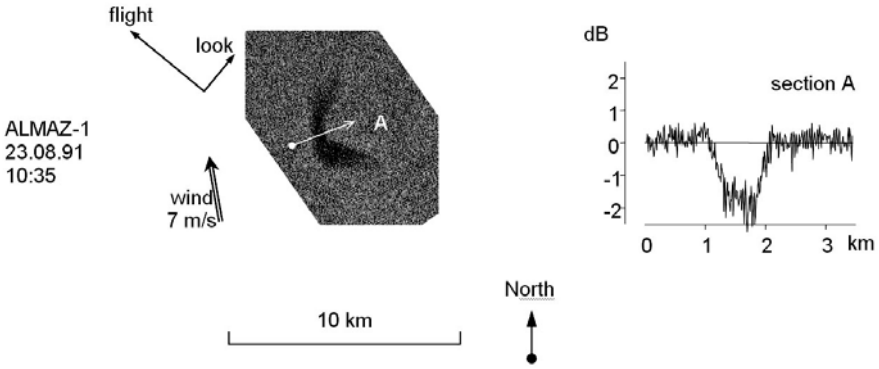

Fig. 3. Almaz-1 SAR image of August 23rd, 1991, at 10:35 UTC showing the first oil spill released on August 21st (incidence angle 27.4°, wind speed 7 m s^{-1}, spill age 40 hrs) (**left**). Variations of the radar backscatter along the scan line are shown on the Almaz-1 SAR image by white thin arrow (**right**), flight/look directions by thin black arrows, and wind direction by double black arrow (image courtesy NPO Mashinostroenia)

This spill was observed from RV *Svanaug Elise* on August 22nd at 10:30 as a blue shine and at 21:39 it was reported that the spill had been totally broken up and no emulsion was formed (Bern et al. 1992b). On August 23rd at 10:35 this spill was imaged again by the Almaz-1 SAR with lower damping ratio (Figure 3). The area covered by the spill almost did not change with age. As inferred from Table 1, the wave conditions were almost the same, too. The reason of the lower damping ratio compared to that of August 22nd could be the higher wind speed (7 m s^{-1}).

Another pair of images was acquired on Aug 25th, 1991 almost simultaneously at 10:44 (Almaz-1) and 10:48 (ERS-1) (Figure 4). Both images show the footprints of both spills. In that case, on the contrary, in the Almaz-1 image the damping ration is about 0, while in the ERS-1 image it is 9.5 dB for the older and 15 dB for the younger spill. Judging from the weather data, a weak wind (2-3 m s^{-1}) was observed. Such a wind is close to optimum for SAR image formation at vertical polarisation (Bern et al., 1992a). The very low damping ratio inferred from the Almaz-1 image can be apparently explained by the high incidence angle ~53º which is close to the critical value for receiving useful backscattering from the sea surface.

Thus, one can conclude that different SAR systems and their viewing geometry can result in highly different damping ratios of the same spill.

On two occasions (August 22nd and 25th) both satellites imaged the spills within a close time span. A comparison of the damping ratios for these two days shows that, among other factors, they highly depend on the viewing geometry, wind speed and sea state.

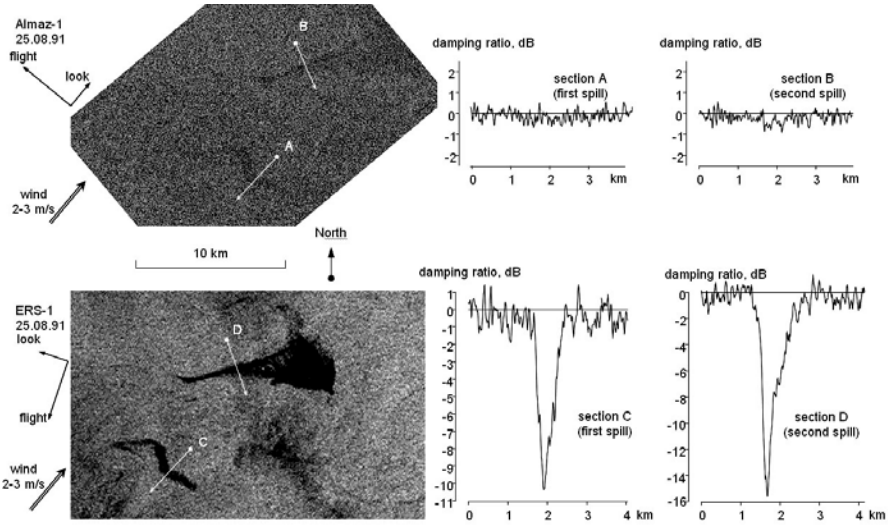

Fig. 4. Almaz-1 and ERS-1 SAR images of August 25th, 1991, at 10:44 and 10:48 UTC showing the first oil spill released on August 21st and the second oil spill of August 24th (incidence angles 52.6° and 23°, wind speed 2-3 m s^{-1}, spill age 88 hrs and 18 hrs, respectively) (**left**). Variations of the radar backscatter along the scan lines are shown on the Almaz-1 and ERS-1 SAR images by white thin arrows (**right**), flight/look directions by thin black arrows, and wind direction by a double black arrow (image courtesy NPO Mashinostroenia and ESA)

The last Almaz-1 SAR image of the second oil spill taken on August 27th at 15:29 UTC (Figure 5) shows an oil spill affected by wind and waves for about 3 days. The image was acquired when the wind speed was about 12 m s^{-1} and the significant waveheight about 3 m, wavelength about 200 m with a period of 12.5 s. This spill was positioned at 10:15 by an aircraft between 64° 38′ N, 08° 01′ E and 64° 36′ N, 07° 57′ E and was observed from RV *Svanaug Elise* at 16:45 as a pure blue shine (Bern et al. 1992b). It can be inferred from the image section that the NRSC contrast with respect to the background has alternate sign along the spill: some areas within it are even brighter than the oil-free surface. It probably shows that this oil spill was in a destruction stage.

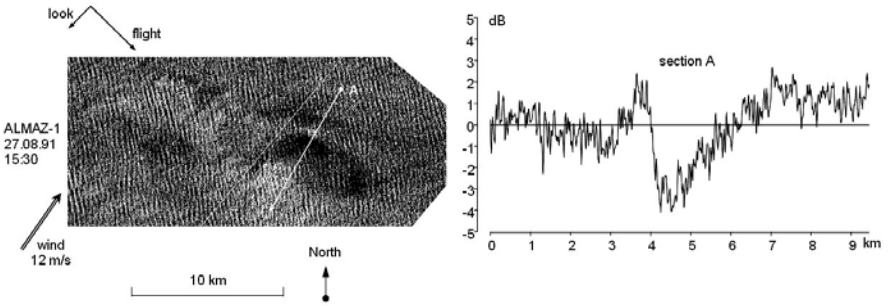

Fig. 5. Almaz-1 SAR image of August 27th, 1991, at 15:30 UTC showing the second oil spill released on August 24th (incidence angle 35.3°, wind speed 12 m s^{-1}, spill age 72 hrs) (**left**). Variations of the radar backscatter along the scan line are shown on the Almaz-1 SAR image by a white thin arrow (**right**), flight/look directions by thin black arrows, and the wind direction by a double black arrow (image courtesy NPO Mashinostroenia)

3 Discussion

It is well known that oil films floating on the sea surface attenuate Bragg waves. This gives rise to considerable reduction of SAR backscatter power. The Almaz-1 SAR was operated in S-band (3.1 GHz) under incidence angles of 25-60° that correspond to Bragg wavelengths between 6 and 14 cm. For ERS-1 this value is quasi-constant and equals 7.3 cm (see Table 1). Under the influence of crude oil films or surface-active substances the spectral density of ripples essentially decreases.

In order to study the capability of the SAR aboard the Almaz-1 satellite, a review of Almaz-1 SAR images showing oil spills was recently conducted (Ivanov 2000). It was shown that the Almaz-1 SAR, due to its high resolution and low orbit, allowed precise detection and localisation of oil spills and provided information on the dimensions, structure and dynamics of the spill. The ability of the Almaz-1 SAR to detect oil pollution on the sea surface depends on a number of environmental parameters, oil spill characteristics and technical parameters of SAR. The ERS-1 SAR has the similar performances (except for the incidence angle, which varies only across swath within limits 23 ± 0.5º) as proved by numerous publications. Therefore, the use of both systems for the imaging of the same spills or slicks is quite useful. Herein, a discussion on the potential influence of radar frequency, polarisation and viewing geometry on oil spill detection has

been omitted, because the number of available SAR images for comparison is too small.

The analysis of the present Almaz-1 and ERS-1 observations has shown that radar contrast of oil spills can depend on a number of parameters, firstly the wind speed and spill age, which in practice are usually unknown. Recent studies conducted with SIR-C/X show that radar contrasts weakly depend on oil type (Gade et al. 1998). The damping under different wind and sea state conditions will also be variable. Most observations support the conclusion of Bern et al. (1992a) that oil spill detectability strongly depends on wind conditions. Moreover, during the lifetime of oil at sea a number of physical and chemical processes, including natural oxidation and bacterial disintegration can lead to the deterioration of the oil spill with time (Kotova et al. 1998). Therefore, under the action of these processes, the damping also changes with time. In general, our results are in accordance with results reported by Singh et al. (1986) and Gade et al. (1998), where damping ratios between 5 and 8 dB were observed under moderate and strong winds for C-band with HH-polarization. In our experiments the damping under similar wind conditions varied between 0 and 2.5 dB and only once, at weak wind speeds, reached 10 dB and more (Figure 4, ERS-1). Our observations also support the idea that using the damping ratios for spill or slick classification is rather problematic.

The SAR image of a spill acquired at a wind speed of ~12 m s^{-1} (Figure 5) exhibits contrasts of alternating sign: in some places the spill areas are brighter than the background. It probably shows that this oil spill was in its disintegration stage. A paper by Okamoto et al. (1993) reports an observation of artificial slicks and spills in the ERS-1 SAR image at a wind speed of 11.7 m s^{-1}. The authors of this paper noted that at wind speed of 14 ms^{-1}, a spill on other ERS-1 SAR images had not been detected. Most probably, wind speed value between 12 and 14 m s^{-1} should be considered as wind speed limit for oil detection by spaceborne SAR.

By using the Almaz-1 SAR for the first time, an intensification of short waves at the windward edge of the oil spill is found. In the SAR image of August 22nd (Figure 2) an area of higher backscatter is stretched out opposite to the wind direction. At first glance, the positive contrast at the upwind side of the spill could be attributed to the non-linear interactions between wave components of the wave field. The mechanism of such interactions cannot be found without additional discussion. However, it is conceivable that the breach of wave equilibrium state under the influence of an oil film leads to the redistribution of wave energy in the spectrum (both within and beyond of oil film) which may lead to the local modification of wave field. In order to explain present observations, the action balance equation

$$dN/dt = S_{wind} + S_{nonlin} - S_{visdis} - S_{break} = 0 \quad (2)$$

has to be taken into account (Hasselmann 1960) as well; here N is the spectral action density of surface waves. As correctly noted by Gade et al. (1998) the source term for nonlinear wave/wave interaction (S_{nonlin}) is still poorly known and cannot easily be determined.

Let us analyse the case of August 22nd under a point of view that the effect was caused by a modification of the wave field. In suggestion that dominant wind waves can determine the phenomenon, one of the possible mechanisms is the «overshoot» effect in the generation of wind waves. In spill and slick areas short wind waves of cm- and partly dm-wavelengths are damped strongly and result in the damping of long dominant wind waves (Phillips 1977). A spill or a slick drifting due to the wind action leaves behind itself (i.e., at the upwind side) an area where wind waves start to develop. It is well known that wind waves reach their equilibrium state not monotonously, so that wind waves at short fetches exhibit higher amplitudes than in the equilibrium range (the overshoot effect). Characteristic fetches L at which long wind waves achieve maximum amplitudes are of the order of $10^3\lambda$ corresponding to characteristic times for the dominant wind waves of the order of τ:

$$\tau \approx L/C_{gr} = 4\pi g 10^3 \cdot \lambda T \quad (3)$$

where λ is the characteristic dominant wavelength, C_{gr} is the group velocity, g the gravity acceleration and T the period of the dominant waves. One can expect that long waves can be amplified at the upwind side of a spill due to the overshoot effect, if the characteristic drifting time

$$\tau_{drift} \approx I_{spill}/V_{drift} \approx I_{spill}/0.03W \quad (4)$$

l_{spill} is the characteristic scale of the spill, V_{drift} the drift velocity and W (the wind speed) is comparable with τ. The last condition is satisfied for moderate wind velocities (5-7 m s^{-1}) and spill scales of the order of several kilometres. The wind wave intensification due to the overshoot effect is about twice that at the equilibrium level; this is comparable with the positive contrasts observed at the upwind side of spills. Using the numbers given in the Table 1, τ_{drift} and τ can be determined. If, in our analysis, l_{spill} = 2.6 km, λ = 150 m, W = 5-7 m s^{-1}, T = 10.5 s and g = 9.81 m s^{-2}, then τ_{drift} = 3.4 - 4.8 hr and $\tau \approx$ 5.1 hr. Calculations using equations (3) and (4) show that the characteristic time of the spill drift τ_{drift} is comparable or smaller than the overshoot characteristic time τ. For this reason, the overshoot effect for waves travelling into the area left by the drifting spill is significant

and the wave amplification before the spill can be noticeable. Also these times are much smaller than the ages of observed oil spills. Most probably, in real sea conditions, the «picture» will be significantly complicated by surrounding waves propagating into the area of calm sea surface left behind the spill as well as by newly generated wind waves.

In the case of August 27th the effect is mainly attributed to breaking of the film, which can take place due to its ageing and the action of long waves. The local redistribution of oil matter also occurs in oil spills that drifted at sea for a longer time period. Thick films are usually inhomogeneous over the area and show fluctuations of their physical-chemical properties (Hühnerfuss et al. 1989). It is also well known that oil spills floating on the sea surface for a long time are slowly enriching surface-active compounds that are being formed by photo-oxidation and microbial transformation processes. According to Hühnerfuss et al. (1989) within thick oil films there are «holes» between thick patches, which are filled by surface-active substances (slick patches). If these areas contain concentrations of surface-active compounds considerably below monomolecular coverage, a ripple generation by wind is possible which, in turn, can lead to generation of short gravity waves and increased radar backscatter. Nevertheless, one can see the large area of the enhanced backscatter at the upwind edge of the oil spill (Figure 5) that can be also attributed to the overshoot effect. Hence in the SAR image of August 27th, an intensification of short-wave components occurs not only within the slick area, but also at edge of a spill where an increase of up to 1-2 dB in the NRCS contrast is observed.

It seems to be the first time that enhancements of the NRCS have been observed on the windward side of a spill in the sea. It is unclear why other researchers did not recognise this effect and whether or not these cases were a single peculiarity. Perhaps, this effect has been recognised for the first time due to a number of reasons, among them are: (1) the specific parameters of the Almaz-1 SAR, i.e., S-band, high resolution, low R/V (slant range/spacecraft velocity) ratio and HH-polarization versus those of the ERS-1 SAR; (2) specific conditions at the air-sea interface on August 22nd and 27th (Bern et al. 1992b), and (3) specific characteristics of the realised oil mixture (Bern et al. 1992a). In our opinion, the effect is governed by a combination of mentioned above factors.

Trying to find experimental and theoretical confirmations of the observed effect a survey of available literature has been carried out. Experiments conducted with small artificial and natural slicks in the sea have shown that in areas covered with surface-active compounds (slicks) the high-frequency energy in a spectrum noticeably decreases, while the long waves practically are not transformed (Ermakov et al. 1985, Ermakov et al. 1986). This effect is associated with damping of short waves by the slick.

Observations of large slicks show that the intensity of wind waves noticeably decreases both in the high- and the low frequency part of the spectrum (Hühnerfuss et al. 1981). The wind field above a slick is also transformed so that a small increase in the average wind speed is observed, which results in the modification of the energy transfer from wind to waves as well as between short and long waves (Barger et al. 1970). Summarising the results of reviewed papers, it is concluded that large slicks (>1 km of width) can essentially act on the long wave part of a spectrum (Barger et al. 1970, Hühnerfuss et al. 1981). Moreover, amplification of decimetre wind waves (wavelengths from 15 to 100 cm) in slicks was found which produces positive contrasts of 1.5-3.5 dB at winds of 5-7 m s^{-1} (Bravo-Zhivotovskii et al. 1984). The transformation (damping or intensification) of short wave components not only in slick but also around it can be associated with both the influence of surface films and the nonlinear interactions of spectral components of the wave field. Results of crude oil spill observations with the Almaz-1 SAR show that amplification of short wind waves can take place at the windward edge of a spill or within spills larger than a few km. Thus, these effects change somewhat our present view of spills and slicks as areas of wind wave damping only.

4 Conclusions

The SAR images obtained during the DOSE-91 experiment from the Almaz-1 and ERS-1 satellites were analysed with the purpose of comparing the potential of both SARs for detection of oil spills on the sea surface and measurement of their characteristics. Artificial crude oil spills were observed at low (2-3 m s^{-1}) to high (12 m s^{-1}) wind speeds. Analysis has shown that both SARs are able to detect oil spills on the sea surface in a wide range of environmental conditions, but that detection is not always possible. Below the conclusions are formulated.

1. Comparison of the Almaz-1 and ERS-1 SAR images has confirmed the results of previous findings that the ability of spaceborne SAR of oil spill detection depends on, firstly, environmental conditions (wind speed and sea state), and secondly, age of a spill, a parameter integrating a number of physical-chemical properties of an oil spill, which are changing under action of so-called weathering processes (Kotova et al. 1998) taking place during oil evolution in the sea. These processes impose definite limitations on classification of oil pollution using spaceborne SARs. Our study supports an idea that using damping ratio as a ratio of the NRCS of spill-free and of spill-covered sea surfaces for the classification is rather problematic, so it strongly depends on environmental

conditions and spill age. For these reasons, identical spills can exhibit different damping ratios on quasi-simultaneous Almaz-1 and ERS-1 SAR images.

2. Using high resolution Almaz-1 SAR images, for the first time an effect of an intensification of short waves at the upwind side, i.e., the windward edge of an oil spill, was found and a possible explanation is given. The overshoot effect can explain the intensification of short wave components at the windward edge. The increase in radar backscatter at the windward edge of the oil spill attained values between 1 and 2 dB. The effect found on the Almaz-1 SAR images requires a theoretical explanation as well as special additional experiments to understand these phenomena in detail. Another Almaz-1 SAR image displays the short waves intensification effect also within the spill area with increasing of the NRCS up to 1-1.5 dB against the background. On the one hand, the effect was stipulated by the change of the wave development and interaction regime (August 22nd; and, perhaps, August 27th). On the other hand, the amplification within the spill area may be explained by film disintegration as a result of ageing under the influence of environmental factors (August 27th).

To sum it up, the main conclusion is that the usual description of crude oil spills in SAR images in terms of damping ratios is not well enough understood. The radar signal damping in spills depends primarily on the wind speed and age, and effects leading to the transformation of oil properties, when a spill floats on the sea surface. Most of these factors are not usually known when spills are observed from space, and the effects mentioned are not sufficiently studied. All this imposes additional restrictions on the use of SAR for detection and classification of crude oil spills. The experimental facts also show that spaceborne imaging radars are not always able to detect crude oil spills in the ocean under low and high wind conditions.

Achnowledgements. The authors thank Dr. S. Ermakov for fruitful discussions of the paper, Mr. Terje Wahl of the Norwegian Defense Research Establishment (NDRE) and Mr. Knut Iden of the Norwegian Meteorological Institute (DNMI) for providing experimental data on weather and sea state. This work was supported by Russian Foundation for Basic Research (grant 97-05-64641) and by INTAS (grant 96-1665).

5 References

Barger WR, Garrett WD, Mollo-Christensen EL, Ruggles KW (1970) Effects of an artificial sea slick upon the atmosphere and the ocean. J Appl Meteor 9: 396-400

Bern T-I, Wahl T, Andersson T, Olsen R (1992a) Oil spill detection using satellite based SAR: Experience from a field experiment. Proc First ERS-1 Symposium, Cannes, France, 4-6 Nov. 1992, p.829-834

Bern T-I, Barstow S, Moen S (1992b) Oil spill detection using satellite-based SAR. Phase 0 and 1 1992, OCN R-92071. Marine Spill Response Corporation, Washington D.C. MSRC Technical Report Series 92-004, 108 p

Bravo-Zhivotovskii DM, Dolin LS, Ermakov SA, Zujkova AM, Luchinin AG, Titov VI (1984) The effect of decimeter wind wave amplification in the oil slick zone. Dokl Acad Sci USSR 276: 1243-1246 (in Russian)

Ermakov SA, Panchenko AR, Talipova TG (1985) Damping of high-frequency wind waves by artificial surface-active films. Izv Acad Sci USSR, FAO 21: 76-82 (in Russian)

Ermakov SA, Zujkova AM, Panchenko AR, Salashin SG, Talipova TG, Titov VI (1986) Surface film effect on short wind waves. Dyn Atmos Oceans 10: 31-50

Ermakov SA, Zujkova AM, Salashin SG (1987) Transformation of short wind wave spectra in film slicks. Izv Acad Sci USSR, FAO 23: 707-715 (in Russian)

Gade M, Alpers W, Hühnerfuss H, Masuko H, Kobayashi T (1998) Imaging of biogenic and anthropogenic ocean surface films by the multifrequency/multipolarization SIR-C/X-SAR. J Geophys Res 103: 18851-18866

Hasselmann K (1960) Grundgleichungen der Seegangsvorhersage. Schiffstechnol Z 1: 191-195

Hühnerfuss H, Alpers W, Jones WL, Lange PA, Richter K (1981) The damping of ocean surface waves by a monomolecular film measured by the wave staffs and microwave radars. J Geophys Res 86: 429-438

Hühnerfuss H, Alpers W, Witte F (1989) Layers of different thickness in mineral oil spills detected by grey level textures of real aperture radar images. Int J Remote Sensing 10: 1093-1099

Ivanov AYu (2000) Oil pollution of the sea on KOSMOS-1870 and ALMAZ-1 radar imagery. Earth Observation & Rem. Sensing, 15: 949-966

Ivanov AYu, Litovchenko KT, Ermakov SA (1998) Oil spill detection in the sea using Almaz-1 SAR. J Adv Mar Sci Tech Soci 4: 281-288

Kotova L, Espedal HA, Johannessen OM (1998) Oil spill detection using spaceborne SAR: A brief review. Proc 27th International Symposium on Remote Sensing Environmental, 8-12 June 1998, Tromsø, Norway, pp.791-794

Masuko H, Kobayashi T, Okamoto K, Alpers W (1995) Observation of artificial slicks with SIR-C/X-SAR around Japan. Proc IGARSS'95, Florence, Italy, 14-18 July 1995, 1, pp.227-229

Okamoto K, Masuko H, Ochiai S, Uratsuka S, Makamura K, Horie H, Fujita M, Shimada M, Nakai M, Shibata A (1993) Two year results of oil pollution de-

tection experiments in the sea adjacent to Japan by ERS-1 SAR. Proc 2nd ERS-1 Symposium, Hamburg, Germany, 11-14 Oct. 1993, pp.419-424

Phillips OM (1977) The Dynamics of the Upper Ocean. Cambridge University Press

Singh KP, Gray AL, Hawkins RK, O'Neil RA (1986) The influence of surface oil on C-and K_u-band ocean backscatter. IEEE Trans Geosci Remote Sens GE-24: 738-744

Wilde A, Brüning C, Alpers W, Etkin V, Litovchenko K, Ivanov A (1993) Comparison of ocean wave imaging by ERS-1 and Almaz-1 synthetic aperture radar. Proc. 2nd ERS-1 Symposium, Hamburg, Germany, 11-14 Oct. 1993, pp.239-245

Estimation of average surface currents from ERS SAR images of oil-tank cleaning spills

Leonid Mitnik[1], Kun-Shan Chen[2] and Chih-Tien Wang[2]

[1]V. I. Il'ichev Pacific Oceanological Institute,
FEB RAS, Vladivostok
[2]Center for Space and Remote Sensing Research,
National Central University, Taiwan

Abstract. Synthetic Aperture Radar (SAR) images from ERS-1/2 have been used to study current-induced perturbations of spill bands in the Kuroshio east of Taiwan, stemming from ballast water of several ships that had been dumped after the cleaning of tanks during the movement of the respective ship parallel to Taiwan's coast. Under weak winds, the variable surface currents normal to a ship's track were the main cause of the displacement of spills relative to a straight line. The currents were associated with the interaction of the Kuroshio with the island of Lutao and ocean bottom variations as well as with vortex structures of different scales, which were observed near the Kuroshio boundary. The average current velocity was determined by dividing the magnitude of the spill displacement by its residence time, which in turn was inferred from the distance of the spill from a ship and the supposed ship velocity. The current shear zones manifested themselves on the SAR images as narrow light lines. Sharp shifts in a spill were observed at its crossing lines. The estimates of current shear, based on the magnitude of the shifts, agree with published data. The width of a spill band observed on May 20th, 1994, at different distances from a ship, was found from the sections normal to it. The change in width as a function of the residence time may be well approximated by a power function with an exponent of about 0.86.

1 Introduction

It has now been universally accepted that radar imagery provides a wealth of information about the presence of surface features on the ocean surface associated with wind action, dynamic oceanic phenomena, slicks, natural and man-made oil pollution. ERS-1/2 SAR, operating at a wavelength of

5.6 cm, is capable of observing sea surface phenomena, including surface films through cloud cover, rain, and in the absence of daylight. The ability of SAR to detect films is due to the damping of small-scale roughness on the sea surface in areas covered by a film. These relatively smooth areas are characterized by decreased levels of backscattered signals (normalized radar cross section – NRCS – σ°), appearing darker on a radar image. Shipping traffic and legal and illegal ballast water discharges are constant sources of sea oil pollution. In order to study the effects of surface films, their relations with oceanic phenomena and to estimate the potential of different remote sensing instruments, including SAR, for their detection and monitoring special experiments were carried out (Alpers and Hühnerfuss 1989, Croswell et al. 1983, Espedal et al. 1998, Hollinger and Mennella 1973) and many ERS-1/2 SAR images of the Mediterranean, Baltic and others seas were analysed (Espedal et al. 1998, Fiscella et al. 2000, Gade and Alpers 1999, Girard-Ardhuin et al. 2003, Ivanov et al. 2004, Kostyanoy et al. 2004). Several automatic techniques have been developed to detect oil spills, ships and ship wakes in SAR images (Brekke and Solberg 2005, Del Frate et al. 2000, Eldhuset 1996, Girard-Ardhuin et al. 2004, Lin and Khoo 1997, Solberg et al. 1999, Wahl et al. 1993).

The radar contrasts of oil films and of ship wakes are a product of the environmental conditions at the time of imaging. The distribution of wind speed and direction is of decisive importance and determines the state of the ocean's upper layer: the roughness parameters, the presence, amount and distribution of wave breaking, the presence of organized structures in the surface roughness distribution. In turn, the state of the ocean surface determines the brightness of the background, the presence of structures in the σ° distribution and the level of speckle noise. For low winds ($W \leq 2–3$ ms^{-1}), no roughness over the unaffected sea surface is observed. Films look dark on a SAR image and their contrast to the surroundings is absent. On the other hand, during high winds ($W > 8–10$ ms^{-1}), the radar contrast of oil-polluted waters declines due to the increase in the brightness of the background and the level of speckle noise as well as the decrease in small-scale roughness damping by films, which are torn to small patches. This implies that the radar contrast of an oil film is a complicated function of wind characteristics and time (Alpers and Hühnerfuss 1989, Hamre and Espedal 1997, Espedal and Wahl 1999, Hühnerfuss et al. 1994, Brekke and Solberg 2005).

In this paper we will consider two simpler cases where radar contrast of a spill resulting from the discharge of ballast waters from a moving ship was high and the spill was clearly visible on a SAR image, without application of special transforms. The primary emphasis will focus on a detailed

consideration of the shape of the spill, or more accurately, on its displacement from the assumed ship course of a straight line. The displacement serves to estimate the average sea surface current. It is known that the shape as well as the drift and state (whether it is broken or not, etc.) of oil spill are determined by the wind and current history between the oil release and the time of SAR image acquisition (Espedal et al. 1998, Espedal and Wahl 1999, Reed et al. 1999). In the cases under study, a wind field in the spill area changed slightly during radar sensing, as follows from the SAR image brightness distribution. Moreover the surface analysis maps show that at the time of acquisition and 6 hours earlier, the sea east of Taiwan was in a low-gradient pressure field at the anticyclone periphery. Wind speed to the south and east of Taiwan was roughly 5 ms^{-1} and thus the wave breaking affecting the oil transport was absent. At such conditions the displacement from the assumed ship course allowed us to relate them to current patterns, reflecting in particular, the interaction of the Kuroshio Current with the bottom topography and an island.

The remainder of the paper is organized as follows. First, the features revealed on two ERS-1 SAR images, covering the sea southeast of Taiwan, are analysed, together with the bathymetry and the weather maps (section 2). The results of calculations of average surface currents based on the analysis of the geometry of the spills and also on estimates of wind drift are given in section 3. The spreading of the spill in the transverse direction and the dependence of the width of the band on time are considered in section 4. Additional data confirming the interpretation of disturbances in the spill shape and a discussion of the results of the analysis are presented in section 5.

2 Interpretation of the SAR signatures

A route east of Lutao, parallel to Taiwan is usual for ships (tankers) moving to and from Japan and South Korea. These ships have been regularly detected on the SAR images acquired by the Chung-Li (Taiwan) ground station. Some of the ships clean their tanks of oil along this route. As a result, spills from moving ships were observed on the SAR images.

Two kinds of theses spills have been detected. When the amount of oil in the cleaning waters was small (within permissible limits), a spill appeared as a narrow dark band, the width of which practically did not change, and its radar contrast decreased with the increase in distance from the ship (spill age). It may be assumed thus that only the amount of oil and its reduction due to evaporation were the factors inhibiting an increase in the width of a spill. The spread of oil (widening of a band) occurred as long as

the film thickness reached a threshold (undetectable) level (Fay 1969, Hoult 1972, MacDonald et al. 1993, Monin and Krasitskii 1985, Read et al. 1999).

Spill widening with the increase in the distance from a moving ship occurred when the amount of oil in the wastewater significantly exceeded the permissible limit and were observed rarer. It may be safely suggested on the basis of SAR image analysis that even in these cases the amount of oil per second spilled in the sea together with the cleaning waters and thus thickness of oil film were less than during ship accidents. At weak winds, the radar contrast of such spills can remain high in spite of width reaching 1-1.5 km or more after 2-3 h.

The variable surface currents, which are typical of the Kuroshio area (Hsu et al. 1997, 1998; Mitnik et al. 1996), produced the displacement of a spill of different scales relative to its initial position. The high spatial resolution of SAR data allowed us to detect both the mesoscale and small-scale disturbances of a spill's shape, interpreting them as current-induced.

The SAR images were acquired by the Chung-Li (Taiwan) ground station. They are precision processed images generated by the Centre for Space and Remote Sensing Research, National Central University at Chung-Li, Taiwan. The imaged area has an extent of 100 x 100 km. The images were provided on a digital CD-ROM.

Case 1.

The most pronounced feature in the radar image (Figure 1a) is a long dark band located about 40 km east of Taiwan. The dark tone of the band implies that the small-scale sea surface roughness, which determines the intensity of the radar backscattering σ°, was strongly reduced within the band. The shape of this twisting widening southward band will be investigated in the paper. The hatched area shows the band on the interpretation scheme (Figure 1b). The SAR image was acquired by ERS-1 on May 20, 1994, at 14:20 UTC (orbit 14874, frame 0459) during an ascending pass, when satellite was moving towards 347.2 °N and the SAR antenna was looking toward 77.2 °N.

The SAR image (Figure 1a) shows at the upper left the mountainous Taiwan coast and the island of Lutao south of it. Lutao extends approximately 7 km from northwest to southeast and rises at its highest point to 280 m above the mean sea level. The boundaries of the image are depicted on the weather map of the Japan Meteorological Agency (JMA) for 12:00 UTC (Figure 2). It can be inferred from the map that the wind characteristics east and southeast of Taiwan were determined by a high-pressure (1024 hPa) region cantered east of Honshu at about 37 °N, 145 °E.

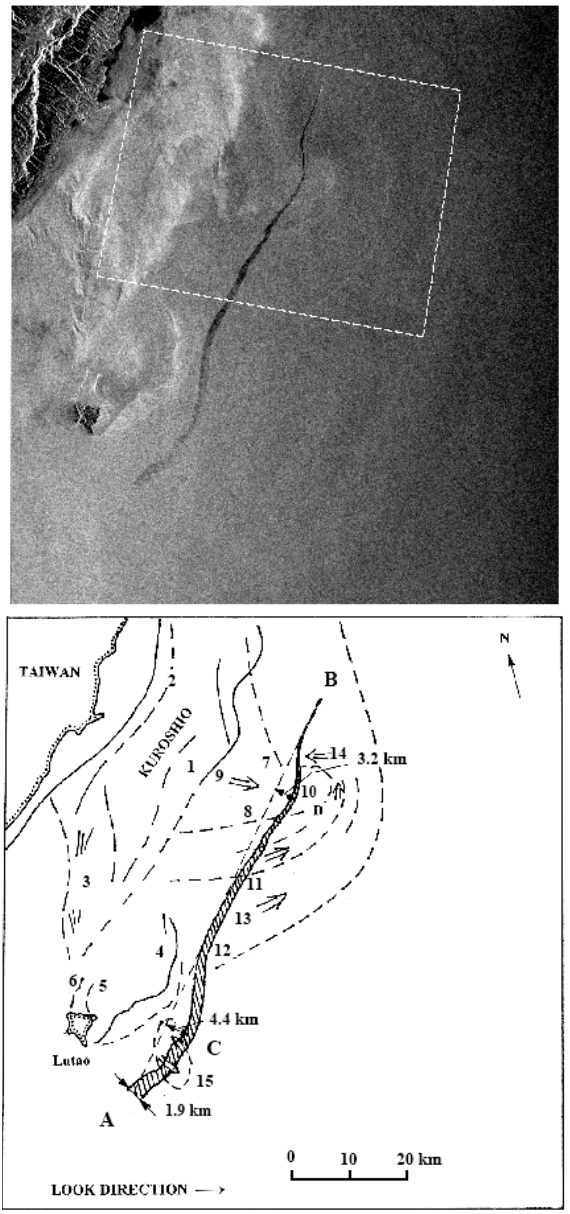

Fig. 1a, top. ERS-1 SAR image of the Kuroshio east of Taiwan acquired on May 20, 1994, at 14:20 UTC and **(b), bottom:** interpretive sketch of the contrast features appearing on the SAR image (copyright European Space Agency). Dashed rectangle marks the boundaries of fragment with mesoscale circulation shown in Figure 5

The pressure gradients at sea level were quite small and the wind speed was 5 ms^{-1} at two stations close to the area under study. The absence of pronounced sharp changes or organized structures in the surface wind field also follows from the brightness distribution of the SAR image. A wind shadow (darker area west of Lutao in Figure 1a) indicates that the wind direction, from east to west, was in agreement with the weather map (Figure 2).

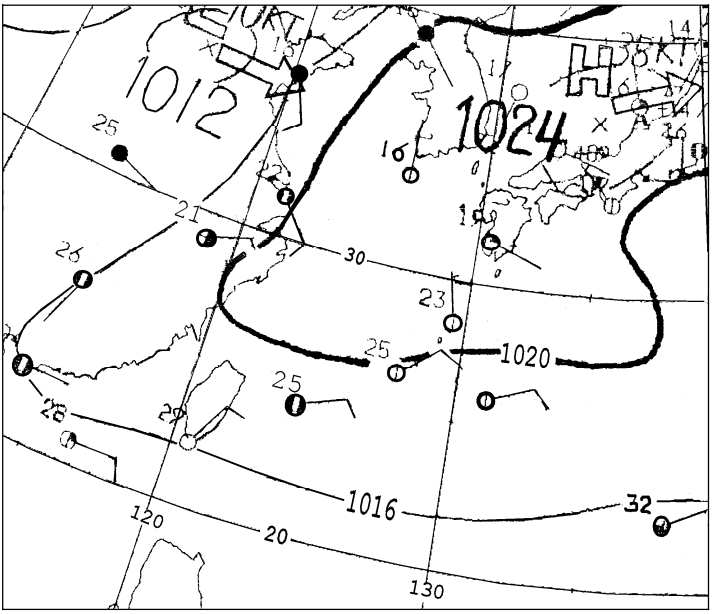

Fig. 2. Surface analysis map for 20 May 1994, at 12:00 UTC from the Japan Meteorological Agency

A large vessel (likely, a tanker) is clearly visible as a bright short line at the origin of the band. It can be assumed that the band was formed by a spill due to the cleaning of the oil-tanks and that the source of the polluted water was a point. Usually, such a spill (or turbulent ship wake) is observed as a straight line along the ship's heading. Variable winds and surface currents cause the drift of the film and disturbances of its shape (MacDonald et al. 1993, Espedal and Wahl 1999, Hamre and Espedal 1997, Monin and Krasitskii 1985, Ochadlick et al. 1992, Read et al. 1999). The magnitude of the perturbations increases as the time, wind speed and current velocity increase. Thus the shape of a spill represents an integral imprint of the joint action of wind and currents between the oil discharge and the time of SAR observation. Under low wind conditions, or with

enough *in situ* data, the perturbations in a spill's shape can be used to estimate mesoscale variations in surface currents or wind.

Several others features, which are important for the interpretation of the spill shape disturbances, are depicted in Figure 1b. The appearance of a part of them was associated with interaction of the Kuroshio Current with Lutao and the underwater relief (see the location of the SAR image on a bathymetry in Figure 3). The most distinctive bright features are: the Kuroshio fronts **1** and **2** and a broad band **3** located over a northward underwater ridge between Lutao and Taiwan (Figure 3). The wave-like features and darker patches within the band **3** are, likely, wakes, generated by underwater mountains. The depth of the sea over these mountains is between 20 and 120 m. Mariners have observed intensive wave breaking over this ridge and downstream from Lutao, and the corresponding marks are shown on the navigation maps. These features have been found on many SAR images of the region.

Lutao is an obstacle within the boundaries of the Kuroshio. The flow of Kuroshio waters around Lutao is accompanied by the formation of zones of current shift, **4-6** (Figure 1b), the origin of which are the downstream headlands of Lutao (Pattiaratchi et al. 1987). The zones are characterized by increased sea surface roughness (radar backscattering) and are well distinguished on the SAR image (Figure 1a). The location, length and shape of the current shift zones are determined by the characteristics of the Kuroshio flow and the complicated topography around Lutao. Since the topography does not change, variations in the radar signatures can be used to study the temporal variability of the Kuroshio in the considered area.

The Kuroshio and its fronts, **1** and **2,** are clearly observable on the SAR image due to their high radar contrast against the darker background. It is suggested that the increased σ^{o} values in the frontal areas were due to short gravity-wave/current interaction along the shear and/or convergence zones within the front. The Kuroshio front near the coast **2** was characterized by a somewhat lower radar contrast compared to frontal boundary **1,** located at a distance of about 20-25 km from the coast.

Near Taiwan, variations in the Kuroshio characteristics, such as the location of the axis, velocity, along-track width, flow separation, etc. are pronounced (Hwang 1996). The analysis of the SAR image strips of the Kuroshio, obtained during different seasons, has revealed a high variability in the location, shape and radar contrasts (both magnitude and sign) of the Kuroshio front (Mitnik et al. 1996, Hsu et al. 1997). The position of the Kuroshio boundaries **1** and **2** was consistent with available data on the behaviour of the Kuroshio during the spring.

Several low contrast features were also related to the disturbances of spill. The narrow light lines **7** and **8** are probably the boundaries of an east-

ward flow **9,** which crossed the spill. The shape of line **8** reflects the anticlockwise motion of the flow east of the spill and the formation of a cyclonic eddy **10,** when line **8** connects with line **7**. Two other light lines **11** and **12** were also formed at the boundaries of a north-eastward flow **13,** which flew along eddy **10**. The configuration of lines **7**, **8**, **11** and **12** and the step-like displacement of the spill at the locations of their crossing enable us to suggest that all these features represent the surface expressions of a mesoscale cyclonic circulation centred in area **10**.

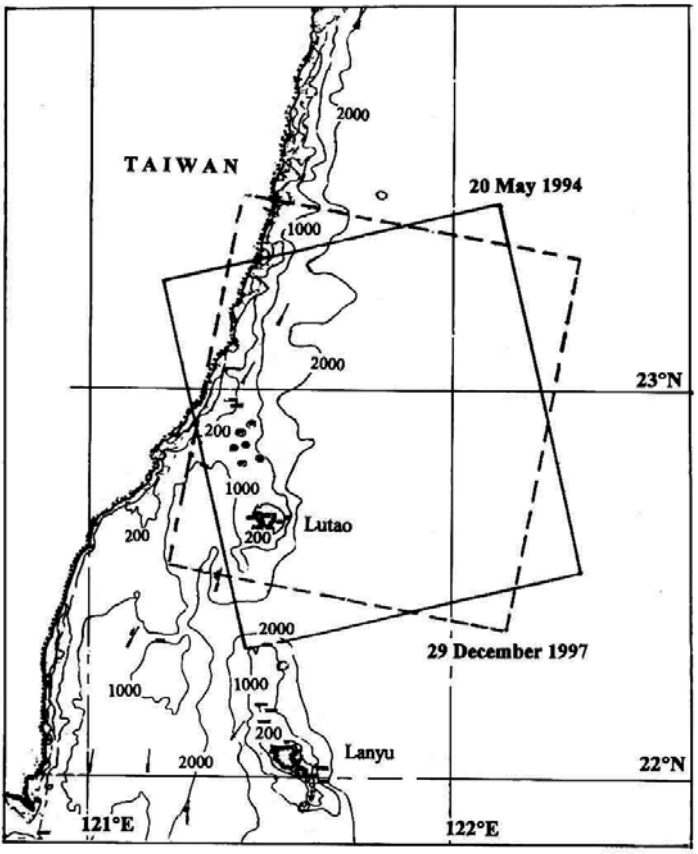

Fig. 3. Map of bathymetry of the Kuroshio area east of southern Taiwan. Isobaths are shown for 2000 m, 1000 m and 200 m. Solid and dashed rectangles note the boundaries of the SAR images acquired on May 20, 1994 and December 29, 1997, respectively, and arrow AB shows the location of ship course

The direction of the flow **9** is almost upwind and thus the relative wind speed over the flow was higher than over the surrounding waters, accord-

ing to the value of the current velocity. The area bound by the light lines **7** and **8** was characterized by a small positive radar contrast against the surrounding waters (Figure 1a), which supports this conclusion. The flow **13** bends around eddy **10** and turns to the west in area **14**. In this area the directions of the wind speed and surface current coincide. The relative wind speed here was lower and the area **14** looks darker in Figure 1a. Moreover, it should be noted that the brightness variations over the mesoscale eddy could be partly due to sea surface temperature variations and the corresponding variations in the stability of the boundary layer of the atmosphere. Likely, it was just these factors which would explain the positive radar contrast of the Kuroshio waters in Figure 1a (Mitnik and Lobanov 1992).

The step-like features in area **15** can also be interpreted as current-induced. The arrows in Figure 1b show the directions of surface currents in a small-scale elliptical eddy. These currents were responsible for the westward and eastward displacements of the spill band. This cyclonic eddy has a low radar contrast without distinct boundaries similar to the current shift lines **7** and **8**. The different scaled eddy-like structures and also the eddy streets were earlier detected in ERS SAR images of the Kuroshio east of Taiwan (Hsu et al. 1997 1998, Mitnik et al. 1996, Mitnik and Hsu 1998).

Case 2.

The ERS-2 SAR image shown in Figure 4 was acquired on December 29, 1997, at 02:26 UTC (orbit 14071, frame 3141) during a descending pass when the satellite was flying towards 192.9 °N and the SAR antenna was looking towards 282.9 °N. The mountainous Taiwan coast and the island of Lutao are clearly seen on the image.

On this day the seas surrounding Taiwan were under the influence of weak (3-6 ms^{-1}) northern winds, as shown in the weather maps of the JMA for 00:00 and 06:00 UTC. Two ships **1** and **2,** moving to the north and one ship **3** moving to the south are distinguishable in the upper right hand part of the image. Ship **1** was the cause of the appearance of a spill band **4**. A turbulent ship wake behind the ship and the northern part of the spill represented a straight line **5** parallel to the turbulent wake behind ship **2**.

A light (with increased σ° values) band **6** crosses the image from north to south. The band divides the warmer surface Kuroshio waters **7** from the colder waters **8** bordering the Taiwan coast. The difference in sea surface temperature between the Kuroshio and coastal waters is indicated by their brightness (the values of the NRCS). The higher NRCS values of the Kuroshio waters can be explained by the joint influence of two factors. The

first factor is associated with the formation of an unstable atmospheric boundary layer over the Kuroshio due to the change of sign in the difference between the air temperature T_a and the sea surface temperature T_s (Mitnik and Lobanov 1991, Beal et al. 1997). The linear structures with an alternating grey and light brightness, which are distinguishable in area **7** (Figure 4), support this suggestion. These features are imprints of the roll vortices that formed in the marine boundary layer of the atmosphere (Alpers and Brümmer 1994, Thompson et al. 1983). They indicate that the wind direction pointed from the north to the south, typical of the winter monsoon. An additional NRCS increment was due to an increase in the relative wind velocity over the northward (opposite the wind direction) Kuroshio flow. However, the resulting wind speed did not exceed 5-6 ms^{-1}, since it did not prevent the expression of such dynamic oceanic phenomena as the small-scale eddies **9-11** on the SAR image.

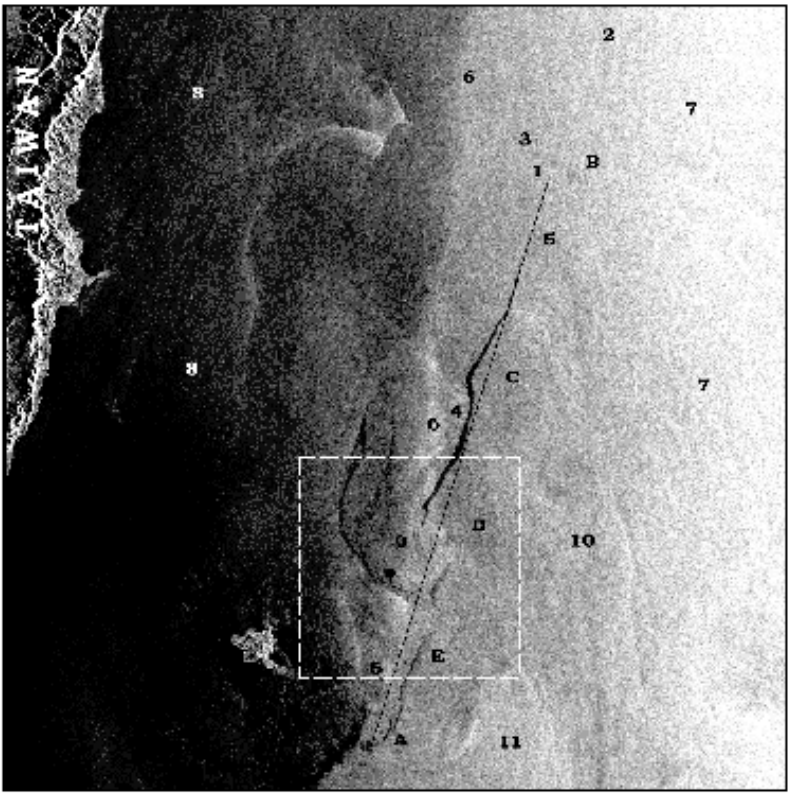

Fig. 4. ERS-2 SAR image of the Kuroshio east of Taiwan acquired on December 29, 1997, at 02:29 UTC (copyright European Space Agency). Dashed square marks the boundaries of fragment shown in Figure 6

The waters bordering Taiwan look darker in stable atmospheric conditions and decreasing of wind speed. The dark patches around Lutao indicate that the wind speed was about 3 ms^{-1} or less here. Contrary to Figure 1a, no radar signatures around Lutao or to the northwest of it were detected indicating the presence of current shift zones associated with the topography. However, filamentary slicks and bright narrow bands are probably the expressions of surface circulation in a cold water area **8**.

In order to estimate the surface currents, line **5** was extended to the south. It crossed the centre of eddy **9** and a dark patch (point **A**) near the lower boundary of the SAR image. The length of the line between the point **A** at the beginning of spill and point **B**, the location of ship **1**, is about 84 km. An increased amount of oil in the cleaning waters was observed in the middle part of the spill. The radar contrast of this part was high. In the southern part, the amount of oil was significantly less and the radar contrast of the spill decreased too. However, it was enough to determine its location reliably, and to observe the eastward displacement of polluted waters under the current's action. The northern part was characterized by a low radar contrast. Probably, the discharge of polluted waters had finished, and, therefore, the linear feature behind the ship represented a turbulent wake.

The ship's course was in the immediate vicinity of the dynamic Kuroshio boundary **6**. Most likely, this was the main cause of perturbations in a spill. There were several pronounced displacements of the spill relative to line **AB** both to the west and the east. The maximum westward component of the surface current was observed at a distance of 30 km behind the ship, where the drift of the oil-polluted waters was 2.2 km (area **C** in Figure 4).

The small-scale eddies **7**-**9** were observed on the SAR image shown in Figure 4 and also on the next SAR image covering the Kuroshio south of the considered area (frame 3158). The large displacements in area **D** were, most likely, caused by a small-scale vortex circulation **9** near the Kuroshio boundary **6**. The low contrast lines spiralling towards the brighter centre of the eddy provide a rough index of the current direction. The ship crossed the centre of this cyclonic vortex. The oppositely directed surface currents stretched the spill near the centre of the vortex so that it became almost undistinguishable against the background, since the amount of oil was small. The western and eastern parts of the spill separated at about 4.5 km. On both sides of the centre the oil film was in the main shifted rather than stretched. These parts of the spill are reliably distinguished against the background. Further south (area **E**), the eastward component of the current, caused by influence of the topography, predominated. The small-

scale deviations superimposed on the topography-induced shift reflected the influence of instabilities in the currents near the Kuroshio boundary.

3 Estimates of average current velocity and wind drift

Case 1

Estimates of average surface currents were obtained under the assumption that the ship in Figure 1b moved in a straight line **AB** (axis x), connecting point **A** at the beginning of the wastewater discharge and point **B**, its location during the SAR observations. This indicates that no wind- or current-induced drift were prevailing, only oil spreading was observed at point **A** during the ship's movement to point **B**. In such a case deviations of the spill from line **AB** were caused by the action of a single factor, the surface current, or more accurately, by a component of surface current normal to line **AB**. The average velocity of this normal component in point x can be found from the relation

$$V_c(x) = y(x)\left[\Delta t(x)\right]^{-1} \tag{1}$$

where $y(x)$ is the distance of the centre of the spill band from line **AB**, x is the distance of point x from point **A** and $\Delta t(x)$ is the time elapsed after the discharge of wastewater at point x.

Since $\Delta t(x) = (L - x)(V_s)^{-1}$, where L is the distance between points **A** and **B**, and V_s is the ship's velocity, the average current velocity can be rewritten as

$$V_c(x) = y(x)\left(L - x\right)^{-1} \cdot V_g \tag{2}$$

It is known that SAR observations of a moving target (ship) allow us to calculate the target's velocity. In a case under study, the radial component of the ship's velocity accounted for $0.4V_s$ and the eastward shift of the ship relative to its wake (spill) caused by this component was estimated with a large error, that hindered the accurate determination of ship velocity. Thus, assume that $V_s = 25$ km h^{-1}.

The maximum displacement from line **AB** was observed in area **C**, east of Lutao (Figure 1b). This displacement was most likely caused by an eastward component of the Kuroshio Current. The shape of the spill in area **C** is similar to the shape of feature **4**. The interaction of the Kuroshio flow with Lutao and underwater rising around it were responsible for the appearance of both feature **4** and the eastward component of the current. The change in velocity of this component with distance manifested itself as the shape of departure $y(x)$. The maximum displacement was found at a dis-

tance of x = 15 km from point **A** and equal to 4.5 km. The residence time of the spill here was 156 min. Assuming that the current velocity did not change during this time, we then find $V_c \approx 0.5$ ms^{-1}.

A weak cyclonic circulation associated with a small eddy **15** was superimposed on the eastward current in area **C** (Figure 1b). The size of the eddy between the boundaries, where the direction of the band changed, was about 8 km. The current in the southern part of the eddy shifted the spill south-eastward and the current in its northern part shifted it northwestward. The magnitude of these oppositely directed displacements was about ± 700-800 m. This corresponds to an average velocity of about 0.07-0.08 ms^{-1}, taking into account that the age of the spill in this region was 170 min.

The second large displacement of the spill occurred in area **D** at a distance of 13–25 km behind the ship. The ship had crossed this area 30–60 min earlier. An enlarged fragment of the SAR image covering area **D** is shown in Figure 5. As opposed to area **C**, sharp changes in the bottom topography are absent in this area (see Figure 3). The cause, which initiated the appearance of the flow **9** normal to the Kuroshio front and formation of cyclonic circulation **10,** is not clear at this time. The maximum displacement from line **AB** occurred in the central part of area **D**, where flow **9,** bounded by lines **7** and **8,** crossed the spill. The maximum average normal component of the flow velocity V_c, as calculated by equation (2), reached 1.2 ms^{-1}. The magnitude of the velocity vector should be still higher. The unclear boundaries and decreased darkness of the oil band in the central part of area **D** (Figures 1a and 5) were, probably, due to the fact that the spill was partly broken by strong surface currents.

As evident from Figure **5**, the profile $V_c(x)$ is not a smooth curve: several step-like changes in the current velocity have to be noted, corresponding to step-like shifts in the spill. Such features were observed in the places where the narrow light lines **7**, **8** and **11** crossed the spill, which may be interpreted as current shift zones (Johannessen et al. 1996, Marmorino and Trump 1994, Marmorino et al. 1994). The shift zones are often characterized by intensive wave breaking, and an increased concentration of foam, wastes, algae, etc. (Monin and Krasitskii 1985, Marmorino et al. 1994). Their width, as a rule, is small, typically ranging from several meters to several hundred meters. For example, the mean width of the shear zones **7** and **8** comprised values around 200 ± 25 m. The displacement of the band, where it was crossed by line **7,** was about 300 ± 25 m after about 34 min. This points to the existence of a differential current of about 0.15 ± 0.01 ms^{-1} across the band and an average shear of roughly (0.7–0.8)x10^{-3} s^{-1}. These values are in good agreement with the estimates obtained by Ochad-

lick et al. (1992) who used repeated airborne SAR observations of turbulent ship wakes to detect perturbations caused by surface currents. The magnitude of a wake's displacement and information about its age allowed them to estimate differential currents. The measured displacements were always co-located with natural filamentary slicks and not with the narrow light lines, as in Figures 1a and 4. This fact probably reflects differences in both the mechanisms of surface current formation and natural film concentration.

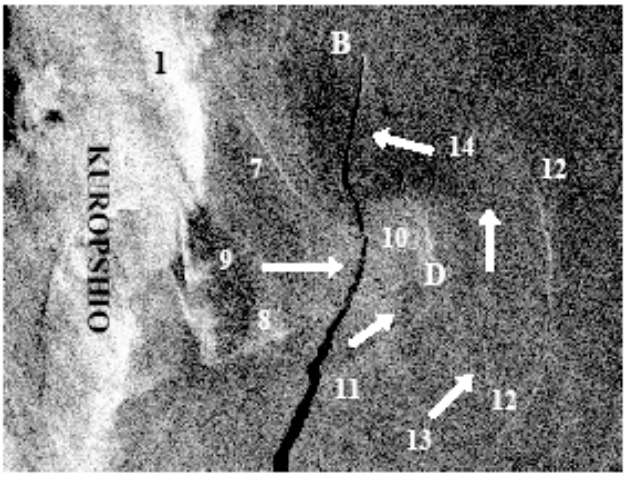

Fig. 5. Enlarged fragment (40 km x 50 km) of the ERS-1 SAR image obtained on May 20, 1994, at 14:20 UTC covering the area of the mesoscale cyclonic circulation east of Kuroshio boundary (copyright European Space Agency). The labels correspond to the labels in Figure 1b

Case 2

The same approach was used to estimate the surface current component normal to the spill in Figure 4. The maximum westward component of the surface current was observed in area **C** at a distance of 30 km behind the ship, where the shift was y = 2.2 km. This corresponds to an average current velocity of $V_c \approx -0.5$ ms^{-1}, assuming, as in the first case, that the ship's velocity was equal to 25 km h^{-1}. The maximum eastward component of current velocity in area **E** was about 0.43 ms^{-1} (a 4-km shift for 2 h 35 min).

An enlarged fragment of the SAR image, covering vortex **9** in area **D**, is shown in Figure 6. The velocities of the eastward (positive) and westward (negative) components of the vortex circulation were equal to ± 0.3 ms^{-1} (a ± 2.3 km shift for about 2 h 10 min).

Wind drift. Now let us estimate the probable influence of the wind drift on the advection of the oil spill. It is generally accepted that in offshore areas in light winds without wave breaking, the oil spill drift velocity is about 2-4 % of the wind speed *W* at a height of 10 m above the sea surface in the direction of the wind (Fay 1969, Reed et al. 1994, 1999). The analysis of the weather maps and the brightness distribution in the SAR images (Figures 1a and 4) supply evidence that the wind variations had only a small effect on shape variations in oil bands since the spill areas were located in low-gradient surface pressure field and the wind speeds did not exceed 5-6 m/s. Under these conditions, a rule of thumb is that spills move at 3 % of the wind speed *W*.

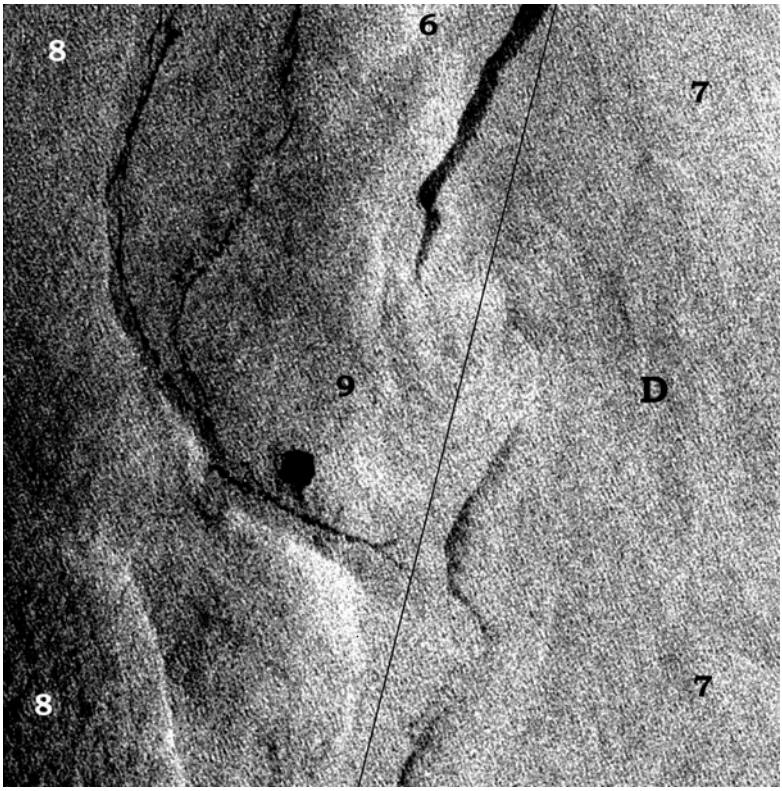

Fig. 6. Enlarged fragment (25 km x 25 km) of the ERS-2 SAR image obtained on December 29, 1997, at 02:29 UTC showing the discontinuity of the oil spill by eddy-like structures near the Kuroshio boundary (copyright European Space Agency). The labels correspond to the labels in Figure 4

The magnitude of the wind-induced drift in a direction normal to the ship's track (line **AB**) at distance x from point **A** (Figure 1b) can be estimated using a relationship

$$\Delta y_w(x) = 0.03W \cdot \Delta t(x) \sin\varphi = 0.03W \cdot (L - x) V_s^{-1} \sin\varphi \qquad (3)$$

where $\Delta t(x)$ is the residence time of the oil spill at point x, and φ is the angle between line **AB** and the wind vector.

The magnitude of the wind drift decreases linearly from its maximum value at point **A** (x = 0 km) to zero at point **B** ($x = L$ = 80 km). A westward shift was less than ≈ 0.5 - 0.8 km for area **C** (x = 8 - 25 km) and ≈ 0.15 - 0.3 km for area **D** (x = 55 - 67 km) at V_s = 25 km h^{-1} and W = 5 ms^{-1} from northeast to southwest ($\sin\varphi \le 0.5$). Even these maximum estimates are less than the spill's width in the areas under consideration and significantly less than the current-induced drift.

The eastward disturbances of the spill in Figure 4 caused by the wind have the same order as for case 1 since the component of the wind vector normal to the spill is about 0.5W (the angle between line **AB** and the wind vector is about 30°).

4 Development of the oil spill

The development of the oil spill in *case 1* was significant: near point **A** its width D reached about 1.9 km after about 3 h (Figure 1). Figures 7a and 7b show the profiles of radar backscatter (in counts) along two sections in the direction normal to the band at the distances of x = 2.7 km (the residence time Δt = 400 s) and 34.5 km (Δt = 4950 s) from point **B**. The profiles were obtained by averaging of the counts over 1000 m in the lateral direction and 50 m in the direction of the section lines by applying a running average procedure. The plots show that the width of the spill increased as the Δt increased. The $D(\Delta t)$ values were determined at a level of 0.5Δn, where Δn was the magnitude of the radar contrast (in counts) for a spill against the surrounding areas. Similar sections and estimates of the width were carried out for the other 15 sections.

The $D(\Delta t)$ values were approximated by a power function, $D(\Delta t) = a_o(\Delta t)^b$. The following values for the parameters were obtained: $a_o \approx 0.7$ m and $b \approx 0.86$. The correlation coefficient was 0.965. The scatter of the points relative to the approximating function could be caused by variations in the oil discharge rate associated, for example, with the variable amount of oil in cleaning waters pumped out from different tanks. The decreased width values in area **D** were, most likely, due to a spill's disturbance by a

strong surface current. When points from this area were removed from the data set, the parameters of the approximating power function, calculated from the remaining 13 points (Figure 8) changed: $a_o \approx 1$ m and $b \approx 0.82$. The correlation coefficient increased to 0.993. The function $1(\Delta t)^{0.82}$ is also shown in Figure 8 (smooth curve).

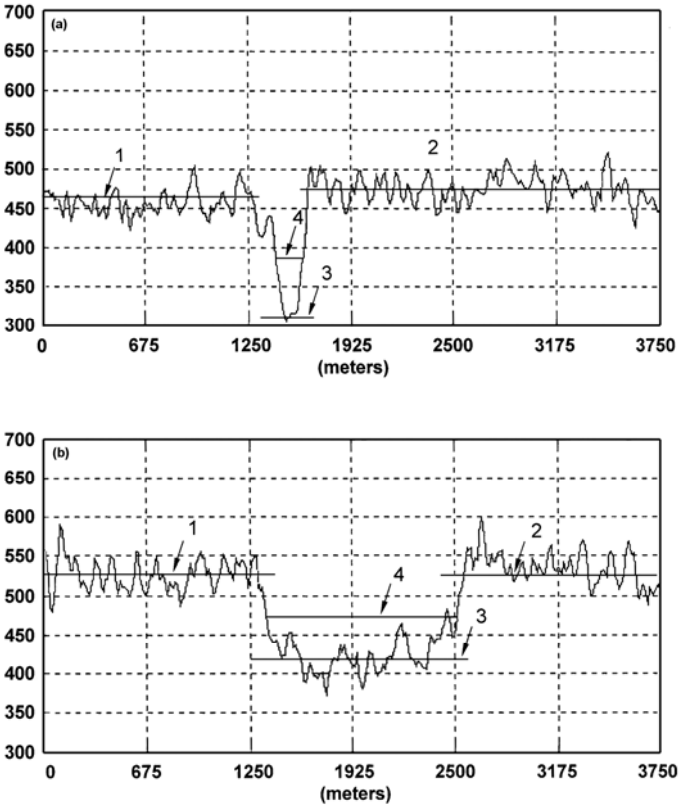

Fig. 7. Variation of SAR intensity (arbitrary units) along sections normal to the spill shown in Figure 1a at the distances of 2.7 km **(7a, top)** and 34.5 km **(7b, bottom)** from point B (from west to east), with cross-track average of 1 km and along-track average of 50 m. The decreased SAR intensity in the spill area is due to the damping of the small-scale roughness of the sea surface. The solid lines show average radar backscatter of the sea surface west (1) and east (2) of the spill, and in the spill area (3). The length of line 4 characterizes the width of the spill

A rough estimate of the volume of oil in the present ballast waters (*case 1*) was obtained by assuming that the oil discharge rate between points **A** and **B** was constant. In such a case, the width of the spill at point **B** at 192 min will be the same as near point **A** on the SAR image (Figure 1a). Since

the width of the spill continued to increase (Figure 8), the film thickness at point **A** did not reach the threshold of the detectable level d_o (the time needed to reach this level depends on the oil discharge rate and the degradation half-life of oil (MacDonald et al. 1993)). Typical values for the detectable thickness are d_o = 0.1-1 μm (MacDonald et al. 1993). Assume that the average thickness of the film d = 0.3 μm when D = 2 km. Then the volume of oil in wastewater will be $V = LDd = 8.0 \cdot 10^4 \cdot 2 \cdot 10^3 \cdot 3 \cdot 10^{-7}$ = 48.0 m^3 (15100$; 1 barrel = 50$).

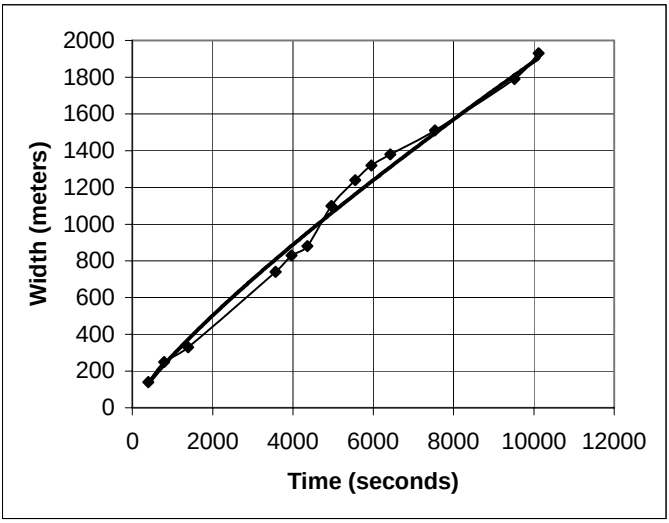

Fig. 8. Dependence of the width of the spill in Figure 1a on the residence time. The location of the dark squares show the measured width of the spreading oil spill (two sections are shown in Figure 7) as the distance from a ship (point B in Figure 1b) and thus the residence time of the spill increases. The solid smooth curve reflects the approximating function

5 Discussion and summary

The geometry of a surface film is formed under the influence of four factors: spreading/spilling procedure, currents, wind and time. In light winds, the spatial variability of currents becomes the main cause of a spill advection. In the two cases in question, the magnitude of the shift was measured relative to the supposed initial position of a ship's track on a SAR image. For the first approximation, the magnitude is a linear function of the average current velocity and the residence time of a given portion of the spill.

The residence time was estimated using the distance between a ship (she was visible on the SAR image) and the point under consideration and the assumed ship's velocity.

It was shown that the perturbations of the spills under consideration were imprints of the mesoscale and small-scale features of surface currents within and near the Kuroshio. They can give a better insight into the nature of current variability. A spill detected on the SAR image from May 20th, 1994, shows a bright expression of the mesoscale variability of surface currents caused by the interaction of the Kuroshio Current with the island of Lutao and the underwater bottom relief. The analysis of ERS-1/2 SAR images of this region has shown that the position of the contrast features **1-5** in Figure 1a is typical of the spring season. In particular, they were revealed in the SAR image from May 10th, 1994, at 0226 UTC. The presence of an eastward component of the current near Lutao (area **C** in Figure 1) was confirmed by the analysis of the location and the shape of the radar signatures on the other SAR images. An additional oil spill, resulting from pumping waste waters out of tanks, was detected on the two ERS-1 SAR images acquired on May 1st, 1995, at 1421 UTC (orbit 19870, frames 0441 and 0459) during an ascending pass. Winds blowing from south to north varied between 2.5 and 5 ms^{-1} however the brightness distribution around the spill area was uniform. A ship moved east of Lutao to the southwest. The amount of oil in the cleaning waters and the width of the spill were less than on May 20th, 1994 (Figure 1a), while the shape of the spill disturbance east of southern Taiwan was similar to that of the one in area **C** in Figure 1. This suggests that the disturbance was caused by an eastward current.

The cyclonic eddy-like structures, similar to eddies **10** and **15** (Figure 1a) and **9-11** (Figure 4), are typical of the Kuroshio Current area east of Taiwan. They have been detected on many ERS-1/2 SAR images; however, their position is variable. These eddies were observed due to their radar contrast against the background and/or the presence of definite structures (narrow spiral lines), resulting from the modulation of surface roughness by variable currents. Filamentary slicks were much less common here to favour their detection. Estimates of the current velocity for two eddies obtained by the analysis of the oil spill displacements were found to be 0.07-0.08 ms^{-1} and 0.3 ms^{-1}.

The narrow zones of current shear manifested themselves on the SAR images (Figures 1a and 4-6) as narrow bright (light) lines. Their shape and position reflected the surface current patterns, associated with the eddy formations which perturbed the oil band. The quantitative estimates of surface currents (0.4-1.2 ms^{-1}) and current shear (roughly (0.7–0.8)10^{-3} s^{-1})

calculated from the magnitudes of these perturbations over a definite time are in line with those of other investigators.

The spills of wastewater, and probably, the special-purpose man-made slicks, timed with satellite and airborne SAR observations, can be used to reveal and study the mesoscale and fine scale features of surface currents in this highly variable Kuroshio area during different seasons as well as in other dynamic oceanic areas.

Acknowledgements. This research was partly supported by the National Science Council under grant NSC-87-2811-m-008-0018. The authors wish to thank Maia Mitnik for processing the data on oil spreading (Figure 8). The ERS-1/2 SAR images collected by ESA satellites were received and processed by the Taiwan Ground Station.

6 References

Alpers W, and Hühnerfuss H (1989) The damping of ocean waves by surface films: A new look at an old problem. J Geophys Res 94: 6251-6265

Alpers W, and Brümmer B (1994) Atmospheric boundary layer rolls observed by thee synthetic aperture radar aboard the ERS-1 satellite. J Geophys Res 99: 12,613-12,621

Beal BC, Kudryavtsev VN, Thompson DR, Grodsky SA, Tilley DL, Dulov VA, and Graber HC (1997) The influence of the marine atmospheric boundary layer on ERS 1 synthetic aperture radar imagery of the Gulf Stream. J Geophys Res 102: 5799-5814

Brekke C, and Solberg AHS (2005) Oil spill detection by satellite remote sensing. Remote Sensing of Environment 95: 1 –13

Clemente-Colon P, Pichel W, and Yan X-H (1997) Evolution of oil slick patterns observed by SAR off the coast of Wales. Proceedings of the 3rd ERS Symposium Space at the service of our Environment, Florence, Italy, *ESA SP-414*, 3 Vols, I: 565-568

Croswell WF, Fedors JC, Hoge FE, Swift RN, and Johnson JC (1983) Ocean experiments and remote sensed images of chemically dispersed oil spills. IEEE Trans Geosci Rem Sens 21: 2-15

Del Frate F, Petrocchi A, Lichtenegger J, and Calabresi G (2000) Neural Networks for oil spill detection using ERS-SAR data. IEEE Trans Geosci Rem Sens 38: 2282-2287

Eldhuset K (1996) An automatic ship and ship wake detection system for spaceborne SAR images in coastal regions. IEEE Trans Geosci Rem Sens 34: 1010-1019

Espedal HA, Johannessen OM, Johannessen JA, Dano E, Lyzenga DR, and Knulst JC (1998) COASTWATCH'95: ERS 1/2 SAR detection of natural film on the ocean surface. J Geophys Res 103: 24969-24982

Espedal HA, and Wahl V (1999) Satellite SAR oil spill detection using wind history information. Int J Remote Sensing 20: 49-65

Fay JA (1969) The spread of oil on a calm sea. In: D. Hoult (Ed.), *Oil on the Sea*. Plenum Press, 53-63

Fiscella B, Giancaspro A, Nirchio F, Pavese P, and Trivero P (2000) Oil Spill Detecting Using Marine SAR Images. Int J Remote Sensing 12: 3561-3566

Gade M, and Alpers W (1999) Using ERS-2 SAR images for routine observation of marine pollution in European coastal waters. The Science of the Total Environment 237/238: 441-448

Girard-Ardhuin F, Mercier GG, and Garello R (2003) Oil slick detection by SAR imagery: potential and limitation. Proc OCEANS'2003 1: 164-169

Girard-Ardhuin F, Mercier G, Collard F, and Garello R (2004) Oil slick detection by SAR imagery: algorithms comparison. Proc. IGARSS'04

Hamre T, and Espedal HA (1997) Operational use of wind data for slick detection. Proc. 3rd ERS Symp. Space at the service of our Environment, Florence, Italy, *ESA SP-414*, III: 1417-1421

Hollinger JP, and Mennela RA (1973) Oil spills: Measurements of their distributions and volumes by multifrequency microwave radiometry. Science 181: 54-56

Hoult DP (1972) Oil spreading on the sea. Annual Rev of Fluid Mechan 341-368

Hsu M-K, Mitnik LM, Lobanov VB, Liu C-T, and Bulatov NV (1997) Kuroshio front and oceanic phenomena near Taiwan and in the southern Okhotsk Sea from ERS SAR data. Proc. 3rd ERS Symp. Space at the service of our Environment, Florence, Italy, *ESA SP-414*, III: 1259-1266

Hsu M-K, Mitnik LM, and Hu J-H (1998) Kuroshio near Taiwan on ERS SAR images. In *Remote Sensing of the Pacific Ocean by Satellites*. (R.A. Brown, Ed.), Earth Ocean & Space Publishing, pp. 111-123

Hühnerfuss H, Gericke A, Alpers W, Theis R, Wisman V, and Lange PA (1994) Classification of sea slicks by multifrequency radar techniques: New chemical insights and their geophysical implications. J Geophys Res 99: 9835-9845

Hwang C (1996) A study of Kuroshio's seasonal variability using an altimetric-gravimetric geoid and TOPEX/POSEIDON altimeter data. J Geophys Res 101: 6313-6335

Ivanov A, He M-H, and Fung M (2004) Experience of using ERS-1/2, Envisat and Radarsat SAR images for oil spill mapping in the waters of the Caspian, Yellow and East-China Sea. *Envisat Symp. Programme and Abstract Book. Envisat &ERS Symposium*, 6-10 September 2004, Salzburg, Austria

Johannessen JA, Shuchman RA, Digranes G, Lyzenga DR, Wackerman C, Johannessen OM, and Vachon PM (1996) Coastal fronts and eddies imaged with ERS 1 synthetic aperture radar. J Geophys Res 101: 6651-6667

Johannessen JA, Vachon PM, and Johannessen OM (1996) ERS-1 SAR imaging of marine boundary layer processes. *Earth Observation and Remote Sensing* (J. Russian Academy of Sciences), No. 3, 79-88

Kostyanoy AG, Lebedev SA, Litovchenko KTs, Stanichniy SV, and Pichuzhkina OE (2004), Satellite remote sensing of oil spill pollution in the southern Baltic Sea. *Gayana*, 68: pp. 327-332

Lin II, and Khoo V (1997) Computer-based algorithm for ship detection from ERS SAR imagery, Proc. 3rd ERS Symp. Space at the service of our Environment. Florence, Italy, *ESA SP-414*, III: 1411-1416

Lu J (2003) Marine oil spill detection, statistics and mapping with ERS SAR imagery in south-east Asia. Int J Remote Sensing 24: 3013-3032

MacDonald IR, Guinasso NL Jr, Ackleson SG, Amos JF, Duckworth R, Sassen R, and Brooks JM (1993) Natural oil slicks in the Gulf of Mexico visible from space. J Geophys Res 98: 16,351-16,364

Marmorino GO, and Trump CL (1994) A salinity front and rip near Cape Hatteras, North Caroline. J Geophys Res 99: 7627-7637

Marmorino, GO, Jansen RW, Valenzuela GR, Trump CL, Lee JS, and Kaiser JAC (1994) Gulf Stream surface convergence imaged by synthetic aperture radar. J Geophys Res 99: 18,315-18,328

Mitnik LM, Hsu M-K, and Liu C-T (1996) ERS-1 SAR observations of dynamic features in the southern East-China Sea. La mer 34: 215-225

Mitnik LM, and Hsu M-K (1998) Atmospheric and oceanic vortex streets: observations by satellite radar. J Advanced Marine Science and Technology 4: 241-248

Mitnik LM, and Lobanov VB (1991) Reflection of the oceanic fronts on the satellite radar images. In; *Oceanography of Asian Marginal Seas*. (K. Takano, Ed.), Elsevier, Amsterdam, Elsevier Oceanography Series, 54: 85-101

Monin AS, and Krasitskii VP (1985) *Phenomena on the Ocean Surface*. Hydrometeoizdat, Leningrad, 376 pp. (in Russian)

Ochadlick A, Cho P, and Evans-Morrgis J (1992) Synthetic aperture radar observations of current colocated with slicks. J Geophys Res 97: 5325-5330

Pavlakis P, Tarchi D, and Sieber AJ (2001) On the monitoring of illicit vessel discharges using spaceborn SAR remote sensing - a reconnaissance study in the Mediterranean Sea. Ann Telecommun 56: 700-718

Pattiaratchi C, James A, and Collins M (1987) Island wakes and headland eddies: a comparison between remotely sensed data and laboratory experiments. J Geophys Res 92: 783-794

Reed M, Turner C, and Odulo A (1994) The role of wind and emulsification in modelling oil spill and drifter trajectories. Spill Science & Technology Bulletin 1: 143-157

Reed M, Johansen Ø, Brandvik PJ, Daling P, Lewis A, Fiocco R, Mackay D, and Prentki R (1999) Oil spill modeling toward the close of the 20th century: Overview of the state of art. Spill Science & Technology Bulletin 5: 3-16

Thomson TW, Liu WT, and Weissman DE (1983) Synthetic radar observation of ocean roughness from rolls in unstable marine boundary layer. Geophys Res Lett 10: 1172-1175

Solberg AH, Storvik G, Solberg R, and Volden E (1999) Automatic detection of oil spills in ERS SAR images. IEEE Trans Geosci Rem Sens 37: 1916-1924

Wahl T, Eldhuset K, Skoelv A (1993) Ship traffic monitoring using the ERS-1 SAR. *Proc. First ERS-1 Symposium*, Cannes, France, 4-6 November 1992, *ESA SP-359*, 823-828

Subject Index